

Rheological Methods and Their Application To Biological Systems



Jonathan Louis Kaplan

Department of Engineering
University of Cambridge

This dissertation is submitted for the degree of
Doctor of Philosophy

Clare Hall

April 2019

Declaration

I hereby declare that except where specific reference is made to the work of others, the contents of this dissertation are original and have not been submitted in whole or in part for consideration for any other degree or qualification in this, or any other university. This dissertation is my own work and contains nothing which is the outcome of work done in collaboration with others, except as specified in the text and Acknowledgements. This dissertation contains fewer than 65,000 words including appendices, bibliography, footnotes, tables and equations and has fewer than 150 figures.

Jonathan Louis Kaplan

April 2019

Acknowledgements

There are a great many people to whom I owe thanks for their guidance and encouragement over the course of this project. Some will already know of my gratitude while others may not, and to those colleagues I would like to express my thanks explicitly.

Alexandre Kabla – thank you for your help, kindness and inspiration throughout, and for warmly welcoming me into your group for the last year and a half. Siobhan Braybrook – thank you for giving me a chance, allowing me to explore ideas, and all the guidance along the way.

I owe considerable thanks to all members of the Braybrook group. Firas, your consistent generosity towards me and others is truly admirable. Joanna, thank you for initiating me into the world of experimental biology and answering my many questions so patiently.

Again, I owe a great deal to all members of the Kabla group. To Alessandra, our resident fractional viscoelasticity expert, thank you not only for generously sharing your fractional viscoelastic wisdom, but also for your unwavering encouragement.

I am also grateful to my thesis examiners, Thierry Savin and Emad Moeendarbary. Thank you for reading through the original draft of this thesis with great care and providing valuable feedback.

I would like to thank the George and Lillian Schiff Foundation for their generous support of this PhD. The Schiff Fund's commitment to interdisciplinary research is laudable and I feel very fortunate to have been a beneficiary.

Last but by no means least, this PhD would certainly not have been completed without the constant support of Jess, Larry, Maryrose and Harriet. Thank you.

Abstract

Pectin is a major component of the primary plant cell wall and is known to play an important role in many physiological processes. It also has many uses in the food and biomedical industries as it is abundant, mechanochemically versatile and non-toxic. However, the relationship between its chemistry and mechanical properties is not fully understood. In this thesis, pectin *in vitro* and the pectin-rich outer cells of *Arabidopsis* seedlings are studied using an AFM methodology adapted from the animal rheology literature. The effects of the degree of methylation, and degree of blockiness on the viscoelastic properties of pectin are explored. Elastic and viscous properties of pectin are found to be negatively correlated with its degree of methylesterification, whilst elastic properties are positively correlated with its degree of blockiness. Mixed gels, composed of pectin with differing degrees of methylesterification are also investigated and their parameters are found to scale in accordance with their volume fraction. *In vivo* mechanical properties observed in the *Arabidopsis* hypocotyl are harder to disentangle, but a number of interesting differences between transverse and axial cell walls are observed. A modelling approach is taken, and although a model based on exponentially decaying terms is found to be adequate for the two material types studied, a fractional viscoelastic model is found to be far superior for pectin *in vitro*.

Fractional viscoelasticity is the use of fractional differential equations for the modelling of viscoelastic phenomena. In addition to its aforementioned use for pectin, its utility is evidenced here by re-analysis of data gathered from the biomechanical literature. In spite of the apparently simple qualitative behaviours they exhibit, there are a number of unique challenges associated with the selection and fitting of fractional viscoelastic models due to their mathematical complexity. This complexity may, in part, explain why fractional viscoelasticity has seen limited use thus far, even though it captures many of the qualitative behaviours commonly observed in biomaterials. This observation led to the development of an open-source rheology analysis software package, RHEOS, which has many of the common fractional and non-fractional viscoelastic models built-in. The architecture, features and implementation specifics of RHEOS are discussed.

Table of contents

| | |
|---|-------------|
| List of figures | xiii |
| List of tables | xvii |
| Nomenclature | xix |
| 1 Introduction | 1 |
| 1.1 Rheology and Its Application to Biology | 1 |
| 1.2 Purview and Structure of Thesis | 3 |
| 1.3 Main Aims of Thesis | 5 |
| 2 Mechanical Characterisation of Materials | 7 |
| 2.1 Overview of Chapter | 7 |
| 2.2 Fundamentals of Rheology | 8 |
| 2.2.1 Elastic Deformation | 8 |
| 2.2.2 Relaxation, Creep and Linear Viscoelasticity | 9 |
| 2.2.3 Arbitrary Loading and the Hereditary Integral | 11 |
| 2.2.4 Dynamic Mechanical Analysis | 14 |
| 2.2.5 Viscoelastic Models | 15 |
| 2.3 Experimental Methods in Plants and Pectin | 23 |
| 2.3.1 Main Testing Paradigms | 24 |
| 2.3.2 Atomic Force Microscopy | 26 |
| 2.3.3 Contact Models | 29 |
| 3 Mechanical Properties of Pectin <i>In vitro</i> and <i>In vivo</i> | 33 |
| 3.1 Author Contributions | 33 |
| 3.2 Overview of Chapter | 34 |
| 3.3 Introduction | 34 |
| 3.3.1 The Plant Cell Wall | 34 |

| | | |
|----------|--|-----------|
| 3.3.2 | Pectin <i>In vitro</i> and <i>In vivo</i> | 38 |
| 3.3.3 | Mechanical Testing of Pectin and the Plant Cell Wall | 46 |
| 3.4 | Overview of Experimental Work | 51 |
| 3.5 | Materials and Methods | 52 |
| 3.5.1 | Preparation of HG Gels | 52 |
| 3.5.2 | Preparation of Plant Material | 53 |
| 3.5.3 | AFM-based indentation tests | 53 |
| 3.5.4 | Hertz Contact Model for A Spherical Indenter | 55 |
| 3.5.5 | Computation of Viscoelastic Response | 56 |
| 3.5.6 | Viscoelastic/Poroelastic Framework Evaluation | 58 |
| 3.5.7 | Viscoelastic Models | 59 |
| 3.6 | Results and Discussion | 61 |
| 3.6.1 | Acquiring Force-Displacement Proxy Relationships | 61 |
| 3.6.2 | HG Is Linear Viscoelastic Under Micro-indentation | 63 |
| 3.6.3 | A Modelling Approach to <i>in vitro</i> Pectin Viscoelastic Analysis . . . | 65 |
| 3.6.4 | Elastic and Viscous SLS2 Parameters Are Inversely Correlated with DM | 67 |
| 3.6.5 | Pectin Strength vs. DM is Non-Linear – Consequences For Mixed DM Gels | 71 |
| 3.6.6 | Elasticity, Not Viscosity, Correlated with DB | 72 |
| 3.6.7 | The <i>Arabidopsis</i> Hypocotyl Cell Wall – From Elastic to Viscoelastic Analysis | 76 |
| 3.6.8 | <i>In muro</i> DM Negatively Correlated With ISS and Rate of Creep – Predicted Plateau Shear Stiffness Appears To Be Coupled In Axial/- Transverse Walls | 79 |
| 3.7 | Conclusion | 81 |
| 4 | The Utility of Fractional Viscoelasticity and Its Software Implementation | 87 |
| 4.1 | Author Contributions | 87 |
| 4.2 | Overview of Chapter | 87 |
| 4.3 | Fractional Viscoelasticity | 88 |
| 4.3.1 | Introduction | 88 |
| 4.3.2 | The Limitations of Spring and Dashpot Systems | 89 |
| 4.3.3 | The Springpot | 93 |
| 4.3.4 | Multi-element Fractional Models | 97 |
| 4.3.5 | Comparison with Empirical Moduli | 102 |
| 4.3.6 | Fractional Models for Biological Materials | 106 |

| | | |
|----------|---|------------|
| 4.3.7 | A Fractional Perspective on Pectin | 109 |
| 4.4 | RHEOS - Open Source Rheology Software | 116 |
| 4.4.1 | Motivation | 116 |
| 4.4.2 | Deliverables | 117 |
| 4.4.3 | Architecture | 118 |
| 4.4.4 | Implementation Discussion | 123 |
| 4.4.5 | Future Development | 128 |
| 4.5 | Conclusion | 132 |
| 5 | Conclusions | 135 |
| 5.1 | Summary of Findings | 135 |
| 5.2 | Future Work | 137 |
| | References | 139 |
| | Appendix A RHEOS Features | 169 |
| A.1 | Fitting Rheological Models to Data and Making Predictions | 169 |
| A.2 | Arbitrary Loading Generation | 174 |
| A.3 | Resampling and Filtering | 176 |
| | Appendix B Summary of Fractional Viscoelastic Models | 179 |
| B.1 | Spring-pot | 179 |
| B.2 | Fractional Maxwell model | 181 |
| B.3 | Fractional Kelvin-Voigt model | 184 |
| B.4 | Fractional Zener model | 187 |
| B.5 | Fractional Poynting-Thomson model | 192 |
| | Appendix C Model Fits and Error Analysis | 195 |
| C.1 | Overview and Methodology | 195 |
| C.2 | Fits and Errors | 195 |
| C.3 | Tabulated Error Data | 206 |
| | Appendix D Summary of Statistics | 207 |
| D.1 | Overview and Methodology | 207 |
| D.2 | SLS2 Parameters | 207 |
| D.2.1 | DM33, DM41, DM50 and Mixtures | 207 |
| D.2.2 | DM40 Block and Random | 211 |
| D.2.3 | <i>Arabidopsis</i> Hypocotyl | 212 |

| | | |
|-------------------|--|------------|
| D.3 | Fractional SLS Parameters | 213 |
| D.3.1 | DM33, DM41, DM50 and Mixtures | 213 |
| D.3.2 | DM40 Block and Random | 214 |
| Appendix E | Singularity Error Analysis | 215 |
| Appendix F | Scientific Output Related to Thesis | 217 |

List of figures

| | | |
|------|--|----|
| 1.1 | Cheese Rheology Adapted from [1] | 2 |
| 2.1 | Elastic Force Deformation Schematics | 8 |
| 2.2 | Canonical Relaxation and Creep Tests | 10 |
| 2.3 | Elastic and Viscoelastic Linearity | 11 |
| 2.4 | Schematic for Derivation of the Hereditary Integral | 12 |
| 2.5 | DMA Testing in Time Domain and The Complex Modulus | 14 |
| 2.6 | Schematic Representation of Spring and Dashpot Viscoelastic Prototypes | 17 |
| 2.7 | Response of a Spring, Dashpot | 18 |
| 2.8 | Combination Rules for Stress, Strain in Series and Parallel | 18 |
| 2.9 | Various Spring and Dashpot Models | 19 |
| 2.10 | Stress and Strain Response of Some Viscoelastic Models | 21 |
| 2.11 | Storage and Loss Moduli of Some Viscoelastic Models | 22 |
| 2.12 | Two Plant Extensometers, Adapted From [2] and [3] | 24 |
| 2.13 | Two Shear Rheometers, Adapted From [4] and [5] | 25 |
| 2.14 | AFM Diagram and Force-Distance Curve, Adapted From [6] | 26 |
| 2.15 | Four Pedagogical Indentation Figures | 28 |
| 2.16 | Schematic of Hertz model for Spherical Indentation | 30 |
| 3.1 | Plant Cell Wall Diagram | 35 |
| 3.2 | Cellulose Orientation: Kerstens, Green | 37 |
| 3.3 | Low DM Homogalacturonan Depiction: Højgaard Christensen, Ventura | 38 |
| 3.4 | Schematic diagram of various pectin structures | 40 |
| 3.5 | The Middle Lamella: Bou Daher | 42 |
| 3.6 | Hypocotyl Wave of Growth from Bou Daher et al. | 44 |
| 3.7 | Hypocotyl Anisotropy: Peaucelle | 45 |
| 3.8 | Pectin data from Ström et al. and Ngouémazong et al. | 49 |
| 3.9 | Figures for Explanation of Fitting Procedure | 57 |

| | | |
|------|--|-----|
| 3.10 | Viscoelastic Models Used for Pectin | 59 |
| 3.11 | Schematic Explanation of ISS and E/V ratio | 61 |
| 3.12 | HG Force vs. Distance Plots | 62 |
| 3.13 | HG Linear Viscoelastic and Poroelastic Rescaling | 64 |
| 3.14 | Pectin Model Evaluation: SLS2 and Burgers | 66 |
| 3.15 | SLS2 Main Parameters - Varying DMs | 68 |
| 3.16 | SLS2 Time-scales - Varying DMs | 69 |
| 3.17 | SLS2 Main Parameters - Different DBs | 73 |
| 3.18 | SLS2 Time-scales - Different DBs | 74 |
| 3.19 | Schematic of Pectin Energy Dissipation Hypothesis | 75 |
| 3.20 | <i>Arabidopsis</i> hypocotyl AFM stiffness map | 77 |
| 3.21 | SLS2 Parameters - Axial and Transverse Hypocotyl Walls | 78 |
| 3.22 | Plateau Stiffness and Step Response - Axial and Transverse Hypocotyl Walls | 80 |
| 3.23 | Diagram of Plastic Deformation Experiment | 83 |
| 3.24 | Plastic Deformation of DM41 HG | 84 |
| 4.1 | Generalised Maxwell and Kelvin-Voigt Models | 90 |
| 4.2 | Power Law Response Fitted by Generalised Maxwell Models | 92 |
| 4.3 | Springpot element and its relation to the spring and dashpot. | 95 |
| 4.4 | Springpot Responses | 96 |
| 4.5 | Multi-Springpot Model Selection Heuristics | 101 |
| 4.6 | Fractional SLS Model Fitted to the MPL | 102 |
| 4.7 | Fractionl BK model for Epithelial Monolayers, Adapted From [7] | 104 |
| 4.8 | Re-analysing Existing Data using Fractional Viscoelastic Models | 107 |
| 4.9 | Fractional SLS Model Fitted to Pectin Relaxation Data | 111 |
| 4.10 | FSLs Model Fitted to Pectin of Various DM | 113 |
| 4.11 | FSLs Model Fitted to Pectin of Various DB | 114 |
| 4.12 | RHEOS Architecture Diagram | 119 |
| 4.13 | RHEOS Model Fit Example | 120 |
| 4.14 | Ramp Correction Factor Example, Adapted From Oyen [8] | 124 |
| A.1 | Test Data Used For Fitting | 169 |
| A.2 | Test Data Fitted Using Two Models | 171 |
| A.3 | Validation Data Compared With Model Predictions | 172 |
| A.4 | Validation Data Compared With Model Predictions | 173 |
| A.5 | Load Generation Example, Addition and Multiplication | 174 |
| A.6 | Load Generation Example, Repetition and Noise | 176 |

| | | |
|------|---|-----|
| A.7 | Downsampling Using RHEOS | 177 |
| A.8 | Resampling and Smoothing Using RHEOS | 178 |
| B.1 | Springpot Relaxation, Creep and Oscillatory Response. | 180 |
| B.2 | Fractional Maxwell (Spring) Relaxation, Creep and Oscillatory Response. . | 182 |
| B.3 | Fractional Maxwell (Dashpot) Relaxation, Creep and Oscillatory Response. | 183 |
| B.4 | Fractional Kelvin-Voigt (Spring) Relaxation, Creep and Oscillatory Response. | 185 |
| B.5 | Fractional Kelvin-Voigt (Dashpot) Relaxation, Creep and Oscillatory Response. | 186 |
| B.6 | Fractional SLS Relaxation, Creep and Oscillatory Response. | 188 |
| B.7 | Fractional Jeffrey's Relaxation, Creep and Oscillatory Response. | 189 |
| B.8 | Fractional BK Relaxation, Creep and Oscillatory Response. | 190 |
| C.1 | SLS2 DM33 Fits and Error Analysis | 196 |
| C.2 | SLS2 DM41 Fits and Error Analysis | 196 |
| C.3 | SLS2 DM50 Fits and Error Analysis | 197 |
| C.4 | SLS2 DM41(33/50) Fits and Error Analysis | 197 |
| C.5 | SLS2 DM50(41/60) Fits and Error Analysis | 198 |
| C.6 | SLS2 DM50(33/70) Fits and Error Analysis | 198 |
| C.7 | SLS2 DM40 (block) Fits and Error Analysis | 199 |
| C.8 | SLS2 DM40 (random) Fits and Error Analysis | 199 |
| C.9 | SLS2 <i>Arabidopsis</i> Transverse Wall Fits and Error Analysis | 200 |
| C.10 | SLS2 <i>Arabidopsis</i> Axial Wall Fits and Error Analysis | 200 |
| C.11 | FSLs DM33 Fits and Error Analysis | 201 |
| C.12 | FSLs DM41 Fits and Error Analysis | 201 |
| C.13 | FSLs DM50 Fits and Error Analysis | 202 |
| C.14 | FSLs DM41(33/50) Fits and Error Analysis | 202 |
| C.15 | FSLs DM50(41/60) Fits and Error Analysis | 203 |
| C.16 | FSLs DM50(33/70) Fits and Error Analysis | 203 |
| C.17 | FSLs DM40 (Block) Fits and Error Analysis | 204 |
| C.18 | FSLs DM40 (Random) Fits and Error Analysis | 204 |
| C.19 | FSLs <i>Arabidopsis</i> Transverse Wall Fits and Error Analysis | 205 |
| C.20 | FSLs <i>Arabidopsis</i> Axial Wall Fits and Error Analysis | 205 |
| E.1 | Error Analysis for Avoiding the Singularity | 215 |

List of tables

| | | |
|-----|--|-----|
| 3.1 | SLS2 model parameters for different DM pectins | 69 |
| 3.2 | SLS2 model parameters for different DB pectins | 74 |
| 4.1 | FSLs model parameters for different DM pectins | 113 |
| 4.2 | FSLs model parameters for different DM pectins | 115 |
| C.1 | Bulk Mean Squared Errors | 206 |
| D.1 | SLS2 Parameters: ISS Statistics, Gels Batch 1 | 207 |
| D.2 | SLS2 Parameters: E/V Statistics, Gels Batch 1 | 208 |
| D.3 | SLS2 Parameters: Dashpot 1 Statistics, Gels Batch 1 | 208 |
| D.4 | SLS2 Parameters: Dashpot 2 Statistics, Gels Batch 1 | 209 |
| D.5 | SLS2 Parameters: Time-scale 1 Statistics, Gels Batch 1 | 209 |
| D.6 | SLS2 Parameters: Time-scale 2 Statistics, Gels Batch 1 | 210 |
| D.7 | FSLs Parameters: ISS Statistics, Gels Batch 1 | 213 |
| D.8 | FSLs Parameters: ISS Statistics, Gels Batch 1 | 213 |

Nomenclature

Roman Symbols

| | |
|--------------------|--|
| E | Young's Modulus/Relaxation Modulus |
| $E_{\alpha,\beta}$ | 2 Parameter Mittag-Leffler Function |
| E_{α} | 1 Parameter Mittag-Leffler Function, Equivalent to $E_{\alpha,1}$ |
| E^* | Complex Modulus |
| E' | Storage Modulus |
| E'' | Loss Modulus |
| f | Force |
| G | Shear Modulus |
| G^* | Complex Shear Modulus |
| J | Creep / Creep Shear Compliance |
| R | Radius Of Indenter |
| \bar{R} | Stoichiometric Ratio Defined As $2[\text{Ca}^{2+}]/[\text{COO}^-]$ |
| \bar{R}_{eff} | Stoichiometric Ratio Defined As $2[\text{Ca}^{2+}]/[\text{COO}^-]_{eff}$ |

Greek Symbols

| | |
|---------------|----------------|
| δ | Displacement |
| ε | Strain |
| Γ | Gamma Function |

σ Stress

Acronyms / Abbreviations

AFM Atomic Force Microscopy

BK Bonfanti-Kabla (model)

DB Degree of Blockiness

DMA Dynamic Mechanical Analysis

DM Degree of Methyl-esterification

FSLS Fractional Standard Linear Solid

GM Generalised Maxwell

HG Homogalacturonan

HMP High Methoxyl Pectin

IM Indentation Modulus

ISS Instantaneous Shear Stiffness, Equal to $G(0)$

LMP Low Methoxyl Pectin

MPL Modified Power Law

PG Polygalacturonase

PME Pectin Methyl-esterase

PSS Plateau Shear Stiffness

RG-I Rhamnogalacturonan I

RG-II Rhamnogalacturonan II

SLS2 2 time-scale Standard Linear Solid

Chapter 1

Introduction

Cell and tissue, shell and bone, leaf and flower, are so many portions of matter, and it is in obedience to the laws of physics that their particles have been moved, moulded and conformed.

[9] *D. W. Thompson, 1945*
On Growth and Form

1.1 Rheology and Its Application to Biology

If one wants to evaluate the ripeness of an avocado how can this be achieved? Countless generations of human experience suggest that the most straightforward method is a gentle squeeze. It is worthwhile taking the time to apprehend this simple but effective squeeze test in scientific terms; our exemplar imposes a low force, usually via the forefinger and thumb, and through these articles senses the resultant deformation, which can be compared with a learned memory of squeeze/tastiness relations. Indeed, through this apparently ordinary test, we can identify some rather extraordinary phenomena, the most relevant being that the human body is capable of such fine grained force transduction and deformation sensing. In addition, we might presume that those early humans who tested fruit for ripeness using the squeeze test can claim the title of the first practitioners of rheology, a field of scientific inquiry which will be defined below.

Although the word ‘rheology’ is derived from the Greek word for ‘flow’, it is generally understood to refer to the science of both deformation and flow [10]. The name was

officially given by Bingham, who proposed the term after consultation with some classicists in 1928 [11]. By 1929 the constitution for the first rheological society had been written [11]. Indeed, whilst there is evidence that rheological investigation has preoccupied humanity since its inception [11] – it was only in the early 1900s that it emerged as a rigorous scientific discipline. The fruit-ripeness example above has an aspect of the whimsical, but in fact many scientists are interested in the rheology of food for the purposes of satiating their intellectual appetite in addition to their belly. For example, the 1937 study by Davis in which creep tests were conducted on various type of cheese, shown in Figure 1.1. Not all problems of flow come under the rheology umbrella; for example, fluid mechanics is usually referred to as a field in its own right – though it does indeed have significant crossover with the field of rheology, particularly in the Stokes regime where inertial effects are ignored. In general, the term rheology is used when it is not just the deformation and flow behaviours of a material being considered, but also their relation to its composition and architecture [12]. Indeed, the rheologist's desire to connect the phenomenological with the structural is a key aspect of the modelling paradigm discussed in more detail in Chapter 2. However, the interest in the structural aspect should not be misinterpreted. Rheological models are largely phenomenological and not mechanistic. Even at small length scales, they are firmly grounded in the framework of continuum mechanics.

Figure of creep tests on cheese removed for copyright reasons. Copyright holder is Proprietors of Journal of Dairy Research. Figure 14 in original source.

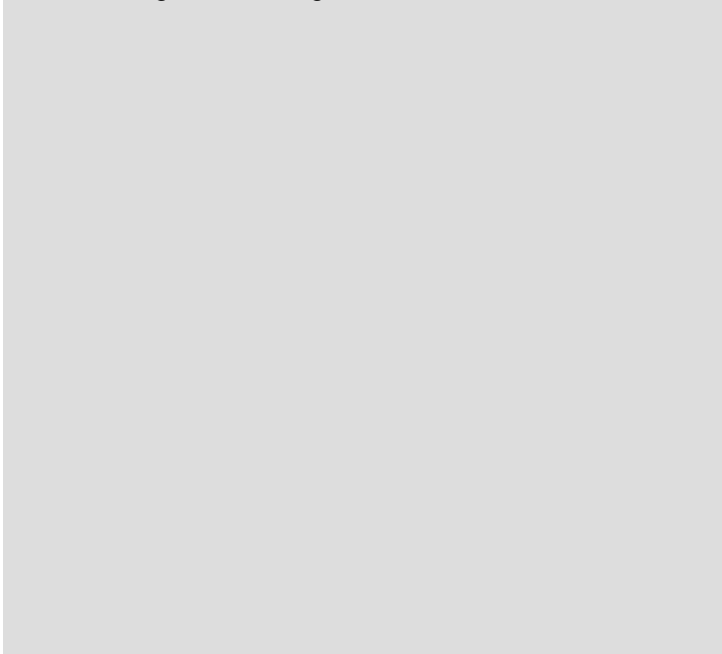


Fig. 1.1 Cyclical creep tests on Cheddar, Cheshire, Leicester and Lancashire cheese, from Davis [1].

Concurrent with the emergence of rheology as a discipline was a growing awareness of the role of mechanics in biological systems – as poetically articulated by D’Arcy Thompson in the above quote from his classic work ‘On Growth and Form’. There are now abundant examples of biological phenomena in which mechanical processes are known to play an essential role. More closely related to this thesis, there are also manifold examples of interplay between rheology and biology. For instance, the 2006 study by Engler et al. which found that when mesenchymal stem cells are placed on substrates with stiffnesses comparable to brain, muscle and bone tissue, they differentiate into brain, muscle and bone cells respectively [13]. Building on this, modifications of the viscous properties of the substrate, in addition to the elastic properties, have been shown to induce their own nuances on stem cell fate [14, 15]. Another example is the 2017 study by Laronda et al. [16], who 3D printed a bio-prosthetic mouse ovary which successfully restored ovarian function in sterilised mice: tuning of rheological properties was important in both ensuring bio-compatibility of the prosthetic ovary, and during the 3D printing process.

1.2 Purview and Structure of Thesis

The previous section introduced rheology and its utility in biology. This section provides a brief overview of the main subjects and unifying themes of this thesis, along with their placement in the overall structure of the text.

Rheology is a broad subject, and a great many textbooks are filled with exposition of its theoretical details, much of which is not directly relevant to the work in Chapters 3 and 4. For this reason, the thesis begins in Chapter 2 with enough theory for the complete dissertation to be relatively self-contained. To this end, it contains an overview of one-dimensional linear elasticity and viscoelasticity, linear modelling using springs and dashpots, contact models, and experimental methods.

Pectin is a hydrophilic polysaccharide gel which is produced in the Golgi of land plants and deposited at the cell wall [17]. As will be detailed in Chapter 3, it has many uses in food and biotechnology, and is known to play a key role in plant development – likely due to the diverse mechanical properties it can be imbued with depending on its precise formulation. As to its importance in food science, we can return to our initial question of fruit ripeness assessment for an example; pectin is known to play a crucial role in the ripening process and associated mechanical changes [18, 19]. During plant development, mechano-chemical pectin changes are known to underlie numerous morphological symmetry breaking events,

some of which will be detailed in Chapter 3. For the above reasons, tools for the mechanical characterisation of pectin *in vitro* and its putative effect on plant rheology are valuable. The advancement of such tools is the main aim of Chapter 3. It begins with a detailed discussion of pectin and its uses, with *in vivo* context provided by discussion of other plant cell wall components. Following this, the literature on mechanical testing of pectin and plants is reviewed. This leads in to the main body of experimental work, in which atomic force microscopy (AFM) force relaxation and creep protocols are established for pectin *in vitro* and the *Arabidopsis* hypocotyl, that part of a young seedling's stem which is above its roots but below its cotyledons (leaves). These methods are used to probe the relationship between pectin chemistry and mechanical properties *in vitro*, and viscoelastic properties which may contribute to symmetry breaking of the *Arabidopsis* hypocotyl *in vivo*.

Chapter 4 links together the previous work and builds on it by use of more advanced viscoelastic theory – fractional viscoelasticity. The centre piece of this theory, the springpot, is an idealised viscoelastic prototype which can be used to model power law behaviour, and can be combined with the aforementioned spring and dashpot units to capture more complex behaviour. Viscoelastic modelling is dominated by the idealised spring and dashpot prototypes which leads to models with a mathematical form depending on a number of exponential terms. Many complex and biological materials exhibit power law rheology, which a finite sum of exponential terms can only approximate. The use of springpots for capturing power law behaviour thus leads to viscoelastic models which use far less parameters than would be required using springs and dashpots, and which confers a number of advantages. In the chapter, a brief history of fractional viscoelasticity is given, followed by a technical overview. Its relevance to biorheology is demonstrated with numerous examples, presented in a format which lies somewhere in between a review and original scientific work. The pectin data from Chapter 3, which was found to exhibit power law behaviour, is re-evaluated with the benefit of the fractional viscoelastic concepts introduced previously. In the second half, a fractional viscoelastic open-source data analysis program is introduced (RHEOS). This is motivated by the potentially inaccessible complexity of fractional viscoelasticity, the interdisciplinary research groups who may find it useful, and the wider benefits of open-source scientific software, all of which are discussed in greater detail within the chapter. The architecture, main features, implementation details and planned future work of RHEOS are also discussed.

Although the main findings and future work of Chapters 3 and 4 are summarised at the end of each chapter respectively, the overall conclusions are summarised more holistically in

Chapter 5.

1.3 Main Aims of Thesis

The key aims of the thesis are listed below.

- Validate an AFM protocol for viscoelastic testing of pectin *in vitro*.
- Use the above methodology to improve understanding of pectin mechano-chemistry.
- Adapt the AFM protocol for relaxation and creep testing *in planta* and use this to investigate symmetry breaking in the *Arabidopsis* hypocotyl and its potential relation to pectin mechano-chemistry.
- Highlight the efficacy of the fractional viscoelastic framework for biological materials, and in particular, demonstrate its clear suitability for the modelling of pectin.
- Demonstrate the need for, and utility of, an open-source software package, RHEOS, for rheological data analysis.

Chapter 2

Mechanical Characterisation of Materials

The organization of our science is thus seen as a very recent development; indeed, its importance as a factor in human development is only now coming to be realized, but from time immemorial men must have been interested in the flow and deformation-properties of materials.

[11] G. W. Scott-Blair, 1949
*A Survey of General
and Applied Rheology*

2.1 Overview of Chapter

In this chapter, the main elements of one-dimensional linear elastic and viscoelastic theory are summarised, and several linear viscoelastic models are examined and discussed. This is followed by a brief discussion of the contact mechanics relevant to subsequent parts of the thesis. Lastly, a curated selection of biomaterials testing methods are discussed, with particular emphasis on Atomic Force Microscopy which has been used in Chapter 3.

2.2 Fundamentals of Rheology

2.2.1 Elastic Deformation

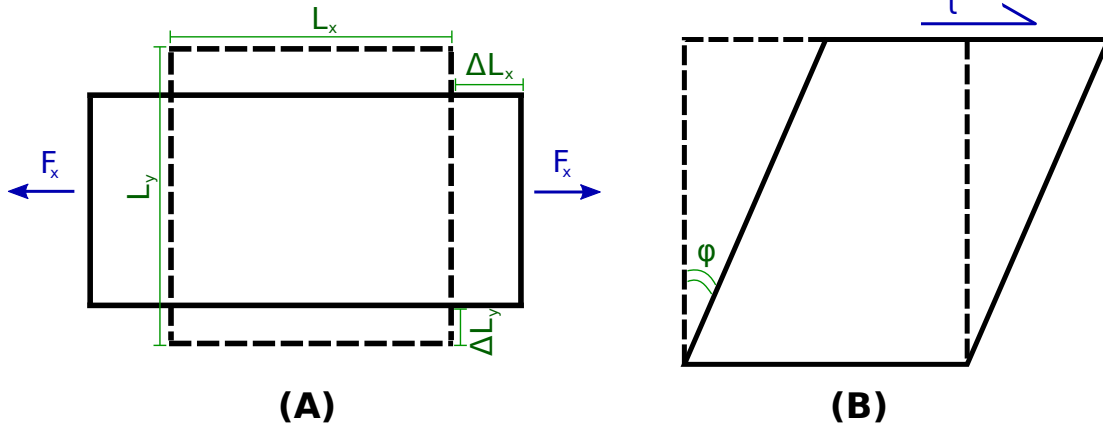


Fig. 2.1 A) Schematic of a square with a normal force F_x applied along the x axis. Solid line is deformed shape, dashed line is original shape. B) Schematic of a square under shear stress τ . ϕ is the shear strain. Solid line is deformed shape, dashed line is original shape.

It is convenient to begin theoretical discussion with the simplest type of rheology – reversible deformation without dependence on time. This is known as the elastic regime. In the one dimensional case that is most relevant to this thesis, there are three physical quantities that we are concerned with: force, deformation, and a physical constant which relates the two. With two or three dimensions, we rely on an additional constant for each dimension known as the Poisson's ratio which relates extension in one dimension to compression in another, and vice versa (if the material is isotropic the Poisson's ratio is the same for all three dimensions). Often the quantities are re-scaled. In the case of a normal force, as shown in Figure 2.1A, the force might be re-scaled by the square cross-sectional area to which it is applied. However, if we imagine the square in Figure 2.1A is isotropic and projects into the page with unit length, we can see that the area that the force is initially applied to reduces after the force is actually applied. *True stress* takes this updated surface area into account, so here it would be defined as $\sigma_{true} = F_x/A_1$, where A_1 is the surface area after the force has been applied. However, it is much more common to use *engineering stress* in which the original surface area is always used. For very small deformations, the difference between the two can be small. Regarding the deformation re-scaling, there is a similar duality. *True strain* is defined as $\epsilon_{true} = \ln(1 + \Delta L/L)$, whilst *engineering strain* is defined simply as $\epsilon_{eng} = \Delta L/L$; the two are approximately equal for small deformations, which can be seen by Taylor expanding the natural logarithm. In this thesis, stress and strain will always refer to engineering stress and engineering strain respectively, so stress $\sigma = \sigma_{eng}$

and strain $\epsilon = \epsilon_{eng}$. If the force acts parallel to the plane rather than normal to it, the *shear stress* and *shear strain* are used, for example as shown in Figure 2.1B. For convenience, in what follows below, normal stress and strain are always used except where noted otherwise.

In the general case, the constant which links the stress and the strain is known as an elastic modulus. For the case of a normal stress applied to a hypothetical one-dimensional bar, we have the following constitutive equation

$$\sigma = E\epsilon^\gamma, \quad (2.1)$$

where E is the elastic modulus and γ is an elastic index. If $\gamma < 1$ then the material is hypoelastic, if $\gamma = 1$ the material is linear elastic, and if $\gamma > 1$ the material is hyperelastic. Many materials under small amounts of tension or compression can be approximately described by the linear elastic theory, in which case $\gamma = 1$. In this linear case, the constant is known as the Young's Modulus. A key feature of this linear elastic regime was noted by Hooke in 1678, who visualised it as a spring and said that “the power of any spring is in the same proportion with the tension thereof” [20]. In concrete terms, applying twice the strain yields twice the stress and vice versa. This feature is depicted in Figure 2.3A.

2.2.2 Relaxation, Creep and Linear Viscoelasticity

Having introduced the quasi-static elastic theory, the ‘flow’ (time dependent) aspect of rheology can now be discussed. This is of interest as many materials exhibit time dependent behaviour. For an example of this, the reader is again directed to Figure 1.1 in Chapter 1, in which it can be seen that when a constant force is applied to various cheeses, they all deform over time. Although in that study by Davis [1], the load was increased at several intervals, the general idea is essentially the same as a *creep* test – in which a constant load is applied to a material and the deformation is observed. In contrast, a *relaxation* test is where a displacement is imposed and the load required to hold that displacement is observed. Relaxation and creep tests are the two canonical viscoelastic testing paradigms; they are shown graphically in Figure 2.2. The motivations for the choice of either one can depend on several factors including the experimental hardware used, and the physical modes of deformation under investigation. Of course, more complicated loading patterns are sometimes used that defy classification as either a creep or relaxation test, these will be discussed further in Section 2.2.3.

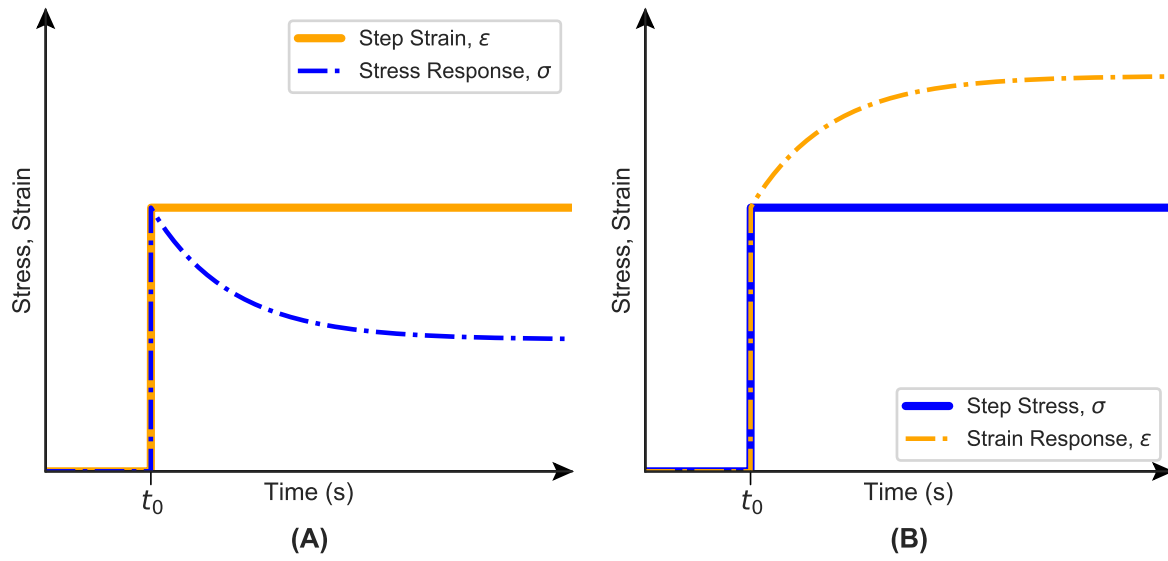


Fig. 2.2 A) Canonical stress relaxation test. Material is subjected to a step strain resulting in an instantaneous stress which then decreases monotonically over time. B) Canonical creep test. Material is subjected to a step stress resulting in an instantaneous strain which then increases monotonically over time.

So how are these behaviours modelled? In general, this is done through the use of either relaxation or creep moduli as appropriate. These moduli are time dependent functions that are analogues of stiffness and compliance – their output has the same physical units as those quantities respectively (Pa and Pa^{-1}). Indeed, the creep modulus is often referred to as the creep compliance. Further, the symbols used are the same respectively, but they are denoted as functions of time, i.e. $E(t)$ is the relaxation modulus and $J(t)$ is the creep compliance. To model a relaxation test, with a step in strain at time $t = t_0$ we can write the following

$$\sigma(t) = E(t - t_0)\epsilon_0 H(t - t_0), \quad (2.2)$$

where H is the Heaviside function and ϵ_0 is the magnitude of the step strain. This relaxation test is depicted in Figure 2.2A. For the special case in which $E(t)$ is equal to a constant, Equation 2.2 represents a linear elastic material. However, in the general viscoelastic case, $E(t)$ is a monotonically decreasing function of time. To model a creep test, with a step in stress at time $t = t_0$ we can write

$$\epsilon(t) = J(t - t_0)\sigma_0 H(t - t_0), \quad (2.3)$$

where σ_0 is the amplitude of the stress step at t_0 . The creep test is shown in Figure 2.2B. Unlike the elastic compliance, which is just the inverse of the stiffness, the process of inverting the linear viscoelastic modulus is more complicated as it involves passing into Laplace space – this is touched on in section 2.2.5.

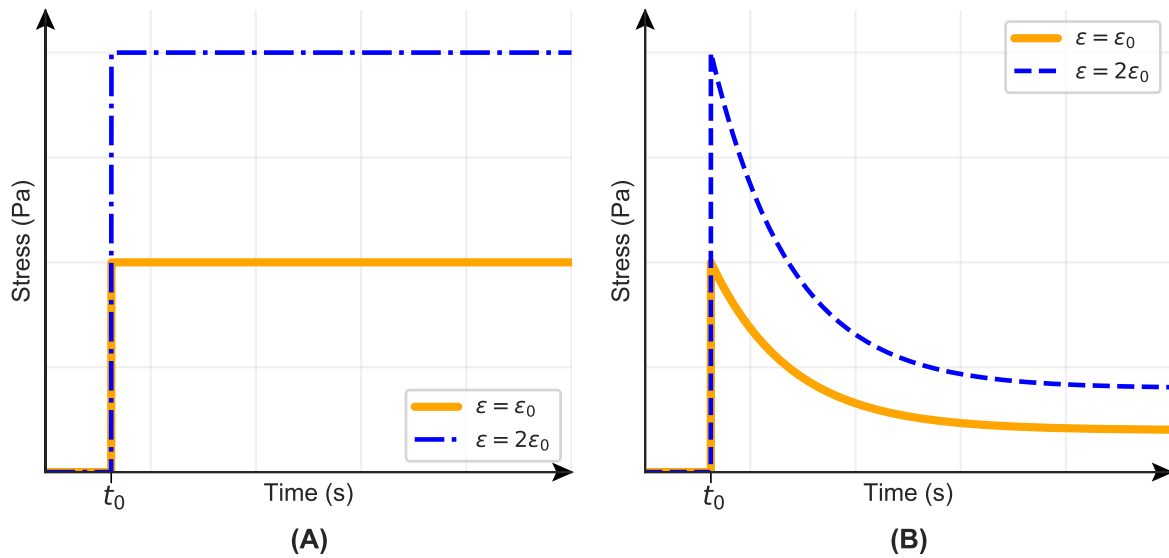


Fig. 2.3 A) Stress response of an elastic model to two different step strain loads both applied at time $t = t_0$, one twice the strain of the other. The doubled strain results in double the stress. B) The same two strains applied to a linear viscoelastic material. With twice the strain load applied, the stress is doubled for all time.

As with elasticity, there are both linear and non-linear variations of the theory. Although this thesis is largely concerned with linear viscoelasticity it worth mentioning briefly their differences. The moduli of the linear viscoelastic theory are functions of time only, whereas the moduli of non-linear viscoelasticity may also depend on the displacement/strain itself. A key consequence of viscoelastic linearity is that two step strains of different magnitude yield two stress relaxation curves which are proportional to each other for all time. A concrete example of this is depicted in Figure 2.3B; the upper curve is the resultant stress from a step strain of $2\epsilon_0$ and is always 2 times larger than the stress relaxation resulting from a step strain of ϵ_0 . A similar implication of linearity is also true in the case of creep.

2.2.3 Arbitrary Loading and the Hereditary Integral

There are a number of reasons why it might be important to consider arbitrary loading of stress/strain rather than be confined to canonical creep/relaxation tests. For example, in

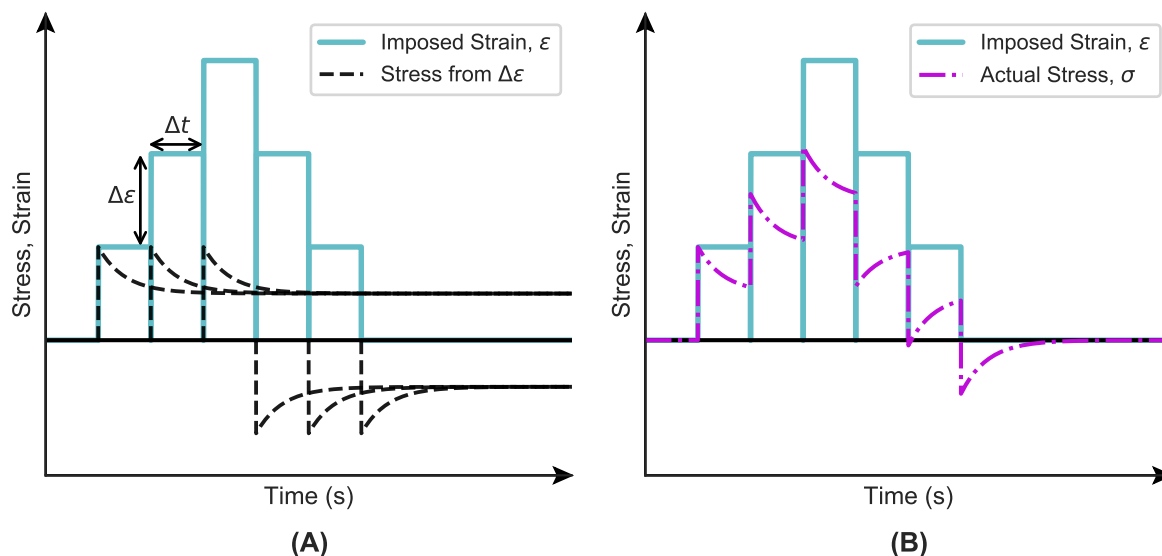


Fig. 2.4 A) Strain loading partitioned into a series of step-on and step-off blocks. The stress resulting from the change in strain at each block start is also shown. B) The same strain loading before, but now the total resultant stress is shown rather than just that for a change in strain.

practice, an instantaneous step strain or stress is not possible to achieve. Although many studies simply ramp as fast as possible and approximate their data fitting by assuming a step loading, this may not always be feasible – particularly if the very short time-scale behaviours are of interest. In other cases, more complex loading patterns might be preferred for any number of reasons, motivated by either scientific questions or hardware constraints.

When considering arbitrarily complex loading patterns, the entire loading history must be accounted for. Although we discussed the relaxation and creep moduli in the context of idealised relaxation and creep tests, they can still be used to capture arbitrary loading by use of the *hereditary integral*. Essentially, the hereditary integral captures the idea that arbitrary loading/deformation can be thought of as a series of increasingly small step loads/deformations, so the response is a summation of infinitesimally small creep/relaxation tests. In what follows, the viscoelastic hereditary integral is derived for the case of arbitrary strain loading. A similar process can be used to derive the arbitrary stress loading and this form will be summarised. The derivation is adapted from that given by Gutierrez-Lemini [21]. The first step in the derivation is to visualise some arbitrary strain deformation history and then discretize it into a number of individual steps as shown in Figure 2.4A. Due to linearity, each step change in strain can be considered independent of the others. This is one way of stating Boltzmann’s superposition principle. Thus, a single change in strain can first be

considered

$$\Delta\epsilon(t_k) = \epsilon(t_k) - \epsilon(t_{k-1}), \quad (2.4)$$

where t_k is the time of current step initiation and t_{k-1} is the time of previous step initiation. The value $\Delta\epsilon$ is depicted in Figure 2.4A. Next, the resultant stress due to this change in strain can be considered

$$\Delta\sigma(t_k) = E(t - t_k)\Delta\epsilon(t_k). \quad (2.5)$$

The relaxation modulus E is shifted to start at $t = t_k$ as we only need to consider the response to this single step change at present. This individual stress response is also plotted in Figure 2.4A. For each time point, we can now sum over the history of individual step loads yielding the following

$$\sigma(t = t_N) = \sum_{k=-\infty}^N E(t - t_k)\Delta\epsilon(t_k), \quad (2.6)$$

where it should be noted that $t_k \leq t_N$ and is thus valid for any time point t without the need for Heaviside functions. Multiplying and dividing the right hand side by Δt leads to

$$\sigma(t = t_N) = \sum_{k=-\infty}^N E(t - t_k) \frac{\Delta\epsilon(t_k)}{\Delta t_k} \Delta t_k. \quad (2.7)$$

Equation 2.7 is now amenable to be transformed into a continuous integral. Letting $\Delta t \rightarrow 0$ and replacing the discrete t_k with the continuous variable τ we attain the viscoelastic hereditary integral for arbitrary strain loading

$$\sigma(t) = \int_{-\infty}^t E(t - \tau) \frac{d\epsilon}{d\tau} d\tau. \quad (2.8)$$

An equivalent derivation can be pursued for arbitrary stress loading which leads to

$$\epsilon(t) = \int_{-\infty}^t J(t - \tau) \frac{d\sigma}{d\tau} d\tau. \quad (2.9)$$

In practical application, Equations 2.8 and 2.9 are of limited use. Computationally, the infinite lower limit causes difficulties. Physically, it seems unlikely that the entire load history of a material could ever be accounted for. For these reasons, it is commonly assumed that significant stress or strain loads only occur at the beginning of a specific experiment, and this moment is set to $t = 0$. For example in the case of the stress relaxation hereditary integral this leads to

$$\sigma(t) = \int_0^t E(t - \tau) \frac{d\epsilon}{d\tau} d\tau. \quad (2.10)$$

The behaviour when subject to a step loading at time $t = 0$ can be clarified by noting that

$$\int_{0^-}^{0^+} E(t - \tau) \frac{d\varepsilon}{d\tau} d\tau + \int_{0^+}^t E(t - \tau) \frac{d\varepsilon}{d\tau} d\tau = E(t) \varepsilon(0^+) + \int_{0^+}^t E(t - \tau) \frac{d\varepsilon}{d\tau} d\tau, \quad (2.11)$$

under the assumption that $\varepsilon(0^-) = 0$. In this thesis, when the lower limit of the hereditary integral is set to 0, it will be assumed that this refers to 0^- such that any instantaneous loading at time $t = 0$ is included. The task of computing the simplified viscoelastic hereditary integral has additional important subtleties which are discussed briefly in Chapter 3, where a Python/SciPy convolution algorithm was used for analysis, and in more detail in Chapter 4 with reference to a Julia-based open source implementation written as part of this PhD.

2.2.4 Dynamic Mechanical Analysis

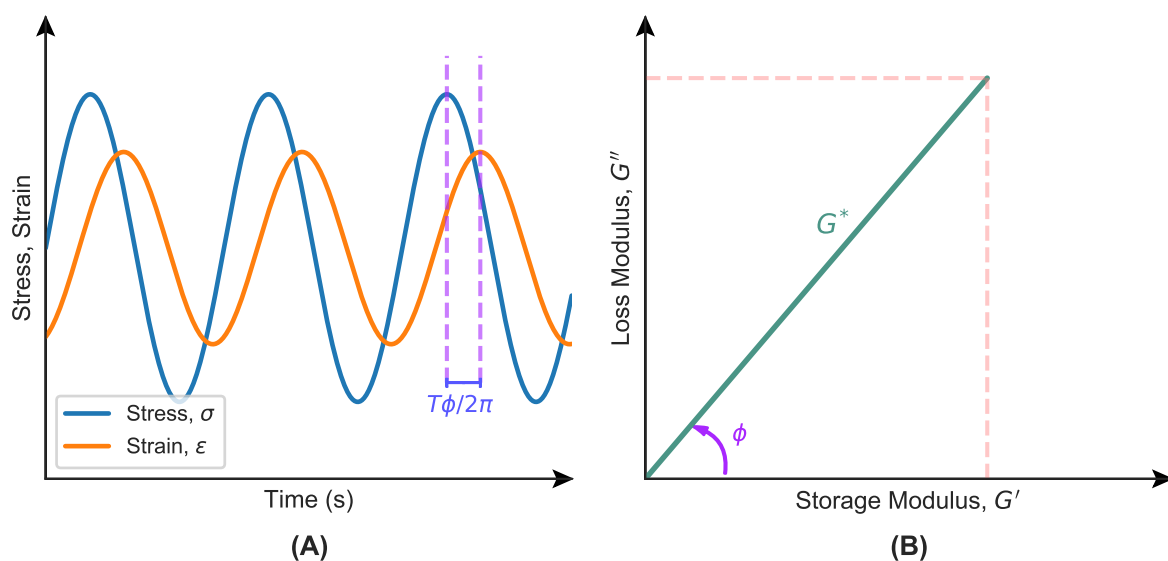


Fig. 2.5 A) Steady-state oscillatory stress loading and out-of-phase strain response. T is the time period of oscillation. B) Argand diagram representation of the complex modulus where the real axis represents the storage modulus and the imaginary axis represents the loss modulus.

In addition to creep and relaxation tests, a third common testing methodology is dynamic mechanical analysis (DMA) in which an oscillatory (normal or shear) load is applied to the material. In viscoelastic materials, a steady-state phase difference emerges between the stress and the strain once transients have faded, this steady-state is depicted in Figure 2.5A. For purely elastic materials the phase difference is 0° and for purely viscous materials the phase difference is 90° . For viscoelastic materials, the phase difference lies between these two

values. Once this phase difference is known, a modulus, usually denoted E^* , can be found. This modulus takes the form of a complex number with real and imaginary components of E' and E'' , often referred to as the storage and loss modulus respectively. Explicitly

$$E^*(\omega) = E'(\omega) + iE''(\omega), \quad (2.12)$$

where ω represents the frequency in radians. The moduli names come from the fact that energy is stored in an idealised elastic material but dissipated in a purely viscous material. An example complex modulus is shown represented on an Argand diagram in Figure 2.5B in which the significance of the phase angle ϕ can be seen; when the angle is 0° the complex modulus is entirely real and all the energy is stored, when the angle is 90° the complex modulus is entirely imaginary and all the energy is lost (dissipated). The tangent of this angle is simply the ratio of loss modulus to storage modulus, $\tan(\phi) = E''/E'$. With DMA, generally speaking, the time scale being investigated is the inverse of the testing frequency, $1/f$. For real materials and viscoelastic models, the complex modulus E^* varies with frequency so a spectral analysis over a range of relevant frequencies is normally carried out. Although often presented in the literature on their own, complex moduli can be fitted to models in much the same way as relaxation and creep test data, though no hereditary integral is required as the behaviour is steady-state. It is possible to explicitly convert a relaxation modulus to a complex modulus by the following relations [22]

$$E'(\omega) = E_e + \omega \int_0^\infty [E(\tau) - E_e] \sin(\omega\tau) d\tau, \quad (2.13)$$

$$E''(\omega) = \omega \int_0^\infty [E(\tau) - E_e] \cos(\omega\tau) d\tau, \quad (2.14)$$

where $E_e = \lim_{t \rightarrow \infty} E(t)$ is known as the equilibrium or plateau modulus. A complex compliance can also be used, but is much less common – it brings no particular benefits over the regular complex modulus.

2.2.5 Viscoelastic Models

Background

In the previous section, linear viscoelasticity was introduced, the viscoelastic hereditary integral was derived, and the complex modulus was presented. However, a key part of rheological modelling was left generic – the form of the creep, relaxation and complex moduli. Indeed, this is the ‘model’ part of viscoelastic modelling theory and is discussed in more detail in this section. Viscoelastic models are useful for a number of reasons. In a best

case scenario, parameters of the model can be related to mechanistic modes of a material's deformation. In other cases, the parameters can be related to intuitive or sensory criteria. Even if neither of the above are possible, models are often still informative, particularly with regards to dominant material time-scales and their qualitative manifestation. In any case, the identification of a suitable constitutive material model facilitates commensurability between different studies.

There are manifold different forms that viscoelastic moduli can take, with the only restriction on their form being adherence to the laws of thermodynamics. For this reason, and with the exception of a spring which is constant, creep moduli of passive viscoelastic materials are monotonically increasing whilst relaxation moduli are monotonically decreasing with time. The moduli may asymptotically approach a plateau or not, and this distinction is generally used to determine whether a material is a viscoelastic solid or viscoelastic fluid respectively. Generally speaking, there are two ways in which the specific mathematical form of the moduli is derived. The first will be referred to in this thesis as the 'empirical' method, and moduli derived by this method as 'empirical models'. The method consists of qualitative inspection of the creep, relaxation or DMA data by use of different scale plots and formulating a mathematical ansatz that captures the main qualitative features. The end result of this process is usually a single modulus of interest that may or may not be analytically converted into the other moduli. The second method, though still empirical in a sense, is more systematic than the first. It relies on viscoelastic units, each with their own constitutive differential equation, that can be combined in series or parallel, much like electrical components in a circuit model. There are numerous different viscoelastic units in the literature that can be used to model elastic, viscous, power law and plastic deformation [11, 20]. By far the most common of these are the Hookean spring and the Newtonian dashpot, and these will form the basis of discussion in the next section. An intermediate between the two, known as a springpot, is discussed in Chapter 4. Before discussion of springs and dashpots, it is worth briefly discussing the advantages of the systematic framework of viscoelastic units over the empirical moduli. Firstly, the viscoelastic units can be represented schematically and provide a helpful visual intuition for a model's behaviour. This also increases commensurability between studies as it is easy to compare models visually, regardless of the parameterisation used. Further, they necessarily yield a constitutive differential equation from which, as we will see later in this section, it is straightforward to derive relaxation, creep and complex moduli.

Springs and Dashpots

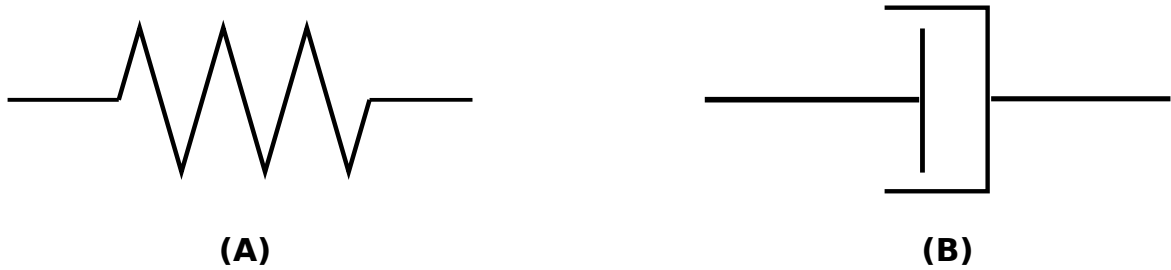


Fig. 2.6 A) Schematic representation of a Hookean spring unit. B) Schematic representation of a Newtonian dashpot unit.

The first viscoelastic unit discussed here is the Hookean spring, shown in Figure 2.6A. It is a linear elastic unit, thus its constitutive equation is the same as Equation 2.1, but its physical constant is often parameterised using k instead of E , to avoid confusion with the Young's modulus. Its constitutive equation is therefore

$$\sigma(t) = k\varepsilon(t). \quad (2.15)$$

The second fundamental unit is the Newtonian dashpot, its schematic representation is shown in Figure 2.6B. For this unit, the stress is directly proportional to the first derivative of the strain, i.e.

$$\sigma(t) = \eta \frac{d\varepsilon(t)}{dt}. \quad (2.16)$$

The responses of the spring and dashpot units to a step in stress are shown in Figure 2.7B. The responses to a step in strain are not shown at this stage – the behaviour of the spring would be qualitatively the same as in Figure 2.3A, but the dashpot is simply a singularity at the moment of step application – it will be discussed further in later sections.

Combinations of Springs and Dashpots

Now that the basic units are defined, we can investigate their combination. The main goal when deriving the constitutive differential equation of a combination model is to obtain a relationship between the total stress and total strain in the system. To achieve this, we need to know how the stresses and strains of the individual components can be combined. The two fundamental rules for combining viscoelastic units in series and parallel respectively are depicted in Figure 2.8. In the series case, the strain seen by the two units are simply summed to attain the total strain. The stress σ in all units is equal to the applied stress. In parallel

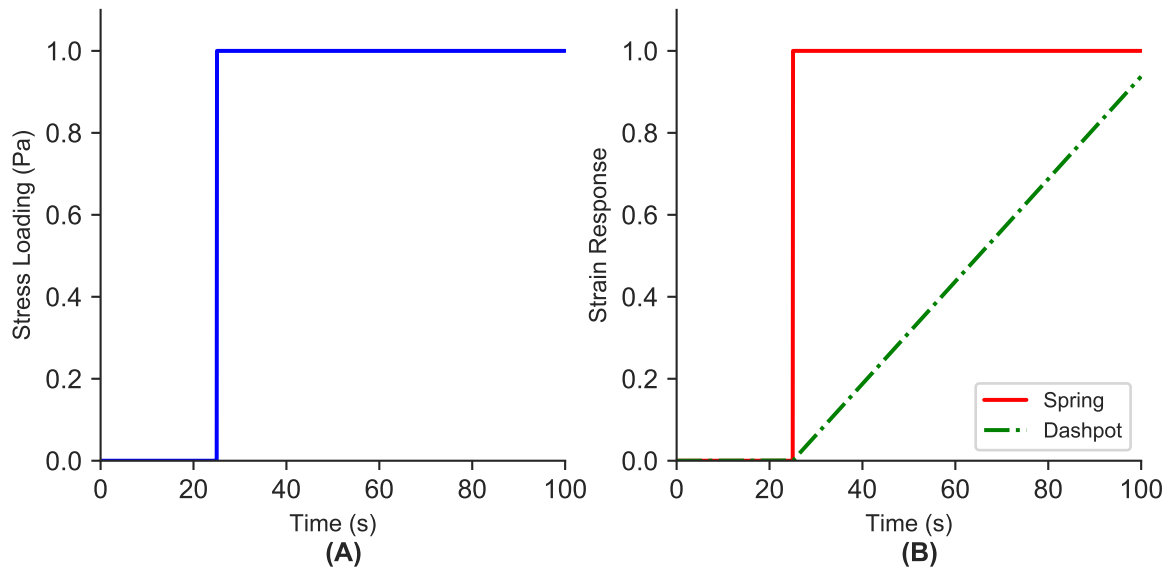


Fig. 2.7 A) Stress loading $\sigma_0 = 1$ Pa imposed at time $t = 25$ s. B) The strain response to the loading for the case of a spring and dashpot respectively, where $k = 1$ Pa and $\eta = 80$ Pa s.

however, the converse is true. The strain is the same for both viscoelastic units but the stress is distributed between the two units. Note that in the above, the term ‘unit’ can be thought of more generally than just a spring or dashpot – the unit could itself be a series/parallel combination of springs and dashpots.

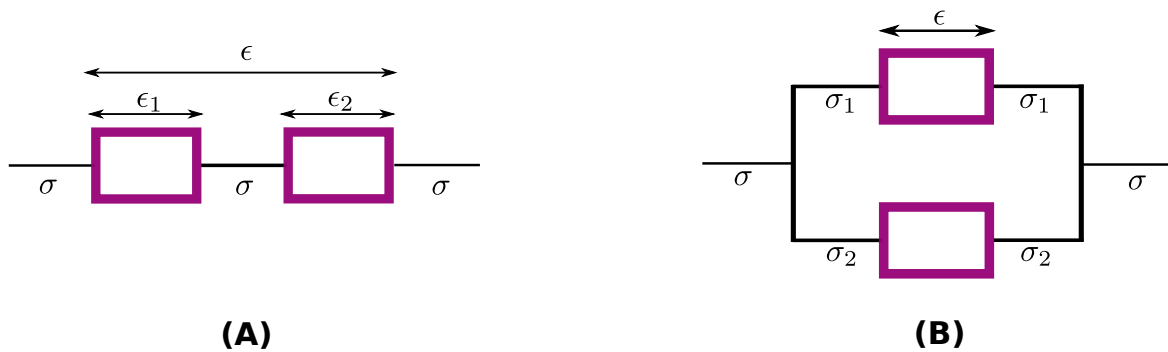


Fig. 2.8 A) Schematic showing stress and strain relationships when adding viscoelastic units in series. B) Schematic showing stress and strain relationships when adding viscoelastic units in parallel.

Three Canonical Models

There are two prototypical viscoelastic combinations, from which many more complex models are derived; they are known as the Maxwell model and the Kelvin-Voigt model, and

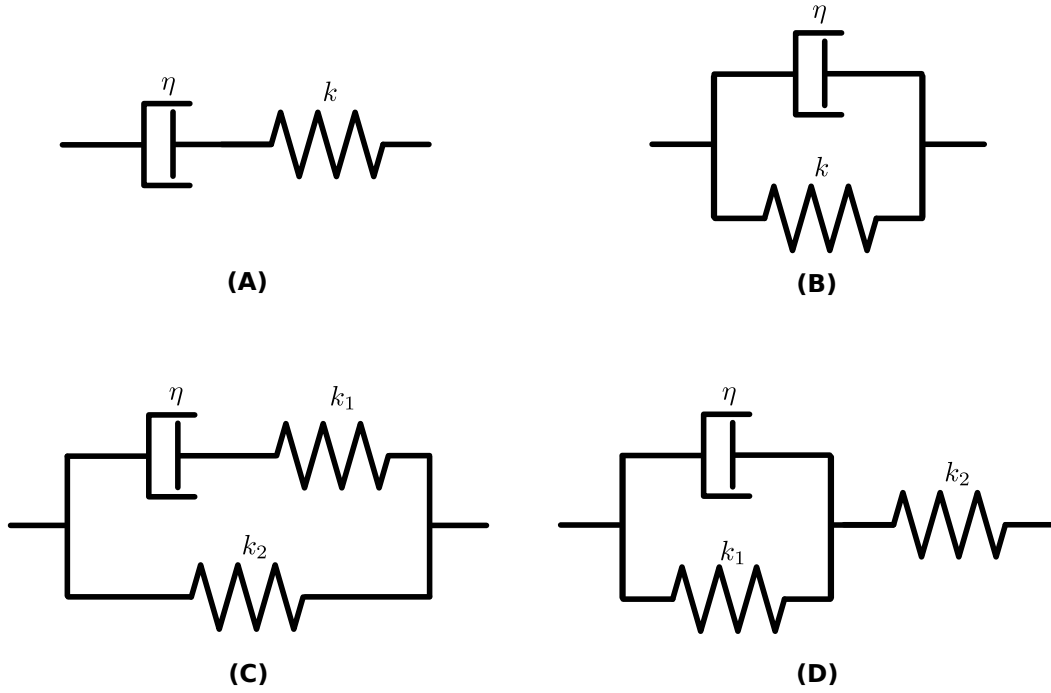


Fig. 2.9 A) Maxwell model spring/dashpot schematic. B) Kelvin-Voigt model spring/dashpot schematic. C) Standard Linear Solid (Maxwell form) spring/dashpot schematic. D) Standard Linear Solid (Kelvin-Voigt form) spring/dashpot schematic.

are shown in Figures 2.9A and 2.9B respectively. From these figures, it can be seen that the Maxwell model is a series combination of a spring and dashpot whilst the Kelvin-Voigt model is a parallel combination. The series and parallel stress/strain summation rules shown in Figure 2.8 can be applied to derive the two models' differential equations. The following is a brief derivation of the Maxwell model. First noting that in series the stress in each unit is equal to the other we can write

$$\sigma(t) = k\varepsilon_1(t) = \eta\dot{\varepsilon}_2(t), \quad (2.17)$$

where k is the spring constant, η is the dashpot constant, and ε_1 and ε_2 are the strain contributions from each element. We can then differentiate the constitutive equation for the spring leading to

$$\dot{\sigma}(t) = k\dot{\varepsilon}_1(t). \quad (2.18)$$

Noting the above mentioned rule, in series the total strain is the sum of the individual strains. This relationship can be differentiated leading to

$$\dot{\varepsilon}_1(t) + \dot{\varepsilon}_2(t) = \dot{\varepsilon}(t). \quad (2.19)$$

Lastly, we substitute a rearranged Equation 2.18 and the constitutive equation for the dashpot into the above and multiply through by η yielding

$$\sigma(t) + \frac{\eta}{k} \dot{\sigma}(t) = \eta \dot{\epsilon}(t), \quad (2.20)$$

which is the differential equation for the Maxwell model. A similar process to the above can be carried out to derive the constitutive differential equation of the Kelvin-Voigt model, which turns out to be

$$\sigma(t) = \eta \dot{\epsilon}(t) + k\epsilon(t), \quad (2.21)$$

where it should be noted that k and η now represent parameters of the Kelvin-Voigt model.

The last step of this Chapter's excursion into spring and dashpot models concerns the Standard Linear Solid (SLS) model. It is one of the most popular viscoelastic models in the literature and serves as a good example of a combination that is more complex than the standard Maxwell or Kelvin-Voigt models. First, its differential equation is derived, which is then used to obtain the model's creep, relaxation and complex moduli. The SLS model can be represented in two different ways, the spring/dashpot schematics of these are shown in Figure 2.9C and 2.9D. The first is known as the Maxwell representation as it can be viewed as a Maxwell model with an additional spring in parallel. The second is known as the Kelvin-Voigt representation as it can be viewed as a Kelvin-Voigt model with an additional spring in series. The parameters are different in the two models, but can be interconverted; apart from this difference, the choice of representation is arbitrary. For the sake of example, the Maxwell representation of the SLS is used herein. First, the upper arm should be considered as it is the more complex of the two. Noting that the upper arm stress σ_1 is equal in both units, we can differentiate the upper spring's constitutive equation and combine with the dashpot's constitutive equation to find the total strain derivative. Explicitly

$$\dot{\epsilon}(t) = \dot{\epsilon}_1(t) + \dot{\epsilon}_2(t) = \frac{1}{\eta} \sigma_1(t) + \frac{1}{k_1} \dot{\sigma}_1(t). \quad (2.22)$$

Now we need to find a way to sum stresses σ_1 and σ_2 to obtain the total stress in terms of the total strain. To do this, we turn to the constitutive equation for the lower arm and its rearranged, differentiated forms

$$\sigma_2(t) = k_2 \epsilon(t), \quad (2.23)$$

$$\frac{1}{\eta} \sigma_2(t) = \frac{k_2}{\eta} \epsilon(t), \quad \frac{1}{k_1} \dot{\sigma}_2(t) = \frac{k_2}{k_1} \dot{\epsilon}(t). \quad (2.24)$$

Adding the forms in Equation 2.24 to Equation 2.22 and multiplying through by η , and noting that $\sigma(t) = \sigma_1(t) + \sigma_2(t)$ and the same for its derivative leads to

$$\sigma(t) + \frac{\eta}{k_1} \dot{\sigma}(t) = k_2 \varepsilon(t) + \eta \left(1 + \frac{k_2}{k_1}\right) \dot{\varepsilon}(t), \quad (2.25)$$

which is the constitutive differential equation of the SLS model. From this we can derive the various moduli.

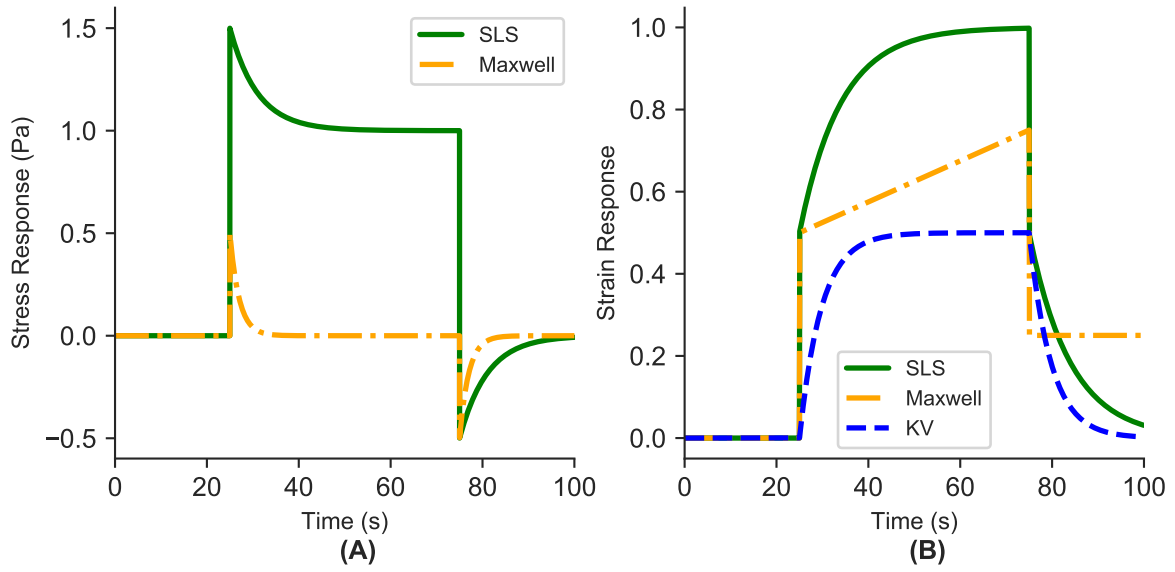


Fig. 2.10 A) Stress response to step load in strain at $t = 25$ s and removal at $t = 75$ s for the SLS and Maxwell models. Maxwell model: $\eta = 1$ Pa s, $k = 0.5$ Pa. SLS model (Maxwell form): $\eta = 3$ Pa s, $k_1 = 0.5$ Pa, $k_2 = 1$ Pa. B) Strain response to step load in stress at $t = 25$ s and removal at $t = 75$ s for the SLS, Maxwell and Kelvin-Voigt models. Maxwell model: $\eta = 200$ Pa s, $k = 2$ Pa. Kelvin-Voigt model: $\eta = 9.5$ Pa s, $k = 2$ Pa. SLS model (Kelvin-Voigt form): $J_0 = 1$ Pa, $J_1 = 0.5$ Pa, $\tau_r = 9$ s.

First, the relaxation and creep moduli can be derived. This is done by taking the Laplace transform of the differential equation shown in Equation 2.25. The process converts our differential equation into an algebraic one. Assuming initial conditions are equal to zero, the Laplace transform results in

$$\left(1 + \frac{\eta}{k_1} s\right) \bar{\sigma}(s) = \left(k_2 + \eta s \left(1 + \frac{k_2}{k_1}\right)\right) \bar{\varepsilon}(s), \quad (2.26)$$

where $\bar{\sigma}(s)$ and $\bar{\varepsilon}(s)$ are the Laplace transforms of stress and strain respectively. The derivation of a relaxation modulus assumes a step loading of strain, which in Laplace space means that $\bar{\varepsilon} = \bar{\varepsilon}_0 = 1$. All that is then left to do is rearrange 2.26 such that the stress is

written in terms of all the parameters on the RHS. Lastly, inverting the Laplace transform results in

$$G(t) = k_2 + k_1 e^{-t k_1 / \eta}. \quad (2.27)$$

Note that the parameters in the exponent, η/k_1 , form a time-scale which is known as the *relaxation* time-scale. A similar process can be carried, but with $\bar{\sigma} = \bar{\sigma}_0 = 1$ assuming a step load of stress, which leads to the creep modulus

$$J(t) = J_0 - J_1 e^{-t/\tau_r}, \quad (2.28)$$

where

$$J_0 = \frac{1}{k_2}, \quad J_1 = \frac{k_1}{k_2(k_1 + k_2)}, \quad \tau_r = \frac{\eta(k_1 + k_2)}{k_1 k_2}, \quad (2.29)$$

and τ_r is usually referred to as the *retardation* time-scale. It is interesting to note that the retardation time scale is scaled by a ratio that is similar in form to an arithmetic mean divided by a geometric mean of the spring constants. The relaxation and creep responses to a step-up and step-down loading of the SLS model, in addition to the Maxwell and Kelvin-Voigt models are shown in Figure 2.10. The Kelvin-Voigt relaxation response is not shown as its behaviour is singular at the step loading points.

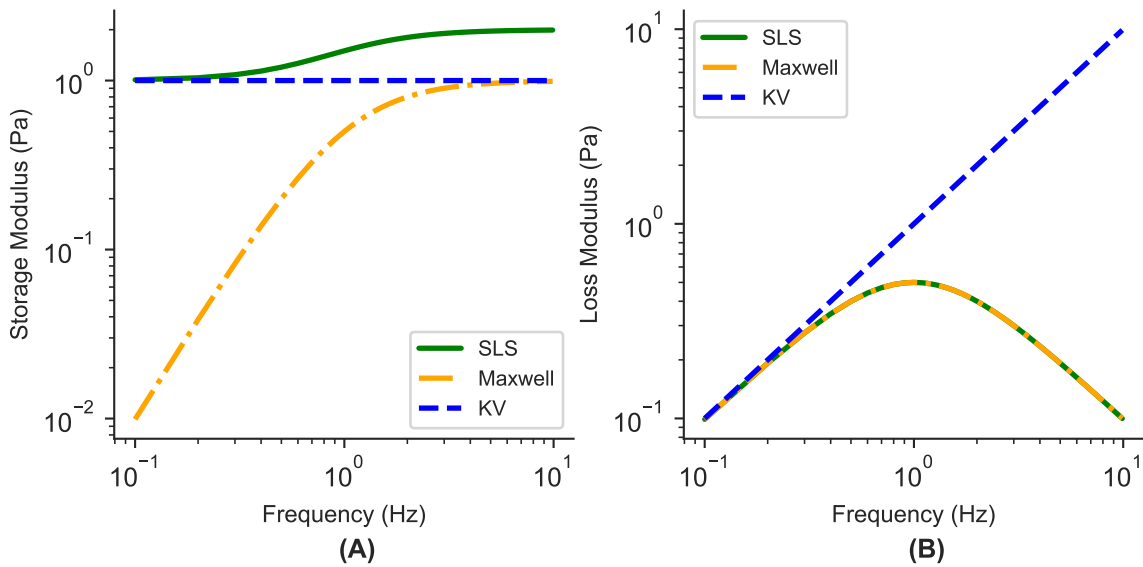


Fig. 2.11 A) Storage modulus behaviour over three frequency decades for the SLS, Kelvin-Voigt (KV) and Maxwell models. All model parameters set to unity. B) Loss modulus behaviour over three frequency decades for the SLS, Kelvin-Voigt (KV) and Maxwell models. All model parameters set to unity.

Lastly, the complex modulus of the SLS is derived. This is done by taking the Fourier transform of Equation 2.25 instead of the Laplace transform used previously. Also, unlike last time we do not need to transform back as we are specifically interested in the frequency response of the model. The Fourier transform of Equation 2.25 is

$$\left(1 + \frac{\eta}{k_1}(j\omega)\right) \hat{\sigma}(\omega) = \left(k_2 + \eta(j\omega) \left(1 + \frac{k_2}{k_1}\right)\right) \hat{\varepsilon}(\omega), \quad (2.30)$$

where $\hat{\sigma}(\omega)$ and $\hat{\varepsilon}(\omega)$ are the Fourier transforms of stress and strain respectively, $j = \sqrt{-1}$, and ω is frequency. The next step is to find the ratio $\hat{\sigma}(\omega)/\hat{\varepsilon}(\omega)$ in terms of the model parameters. After some algebra the following is obtained

$$\frac{\hat{\sigma}(\omega)}{\hat{\varepsilon}(\omega)} = \frac{k_1\eta^2\omega^2 + k_1^2\eta j\omega}{k_1^2 + \eta^2\omega^2} + k_2, \quad (2.31)$$

which is equal to the complex modulus $G^*(\omega)$. Separating the real and imaginary parts yields the storage and loss moduli

$$G'(\omega) = \frac{k_1\eta^2\omega^2}{k_1^2 + \eta^2\omega^2} + k_2, \quad (2.32)$$

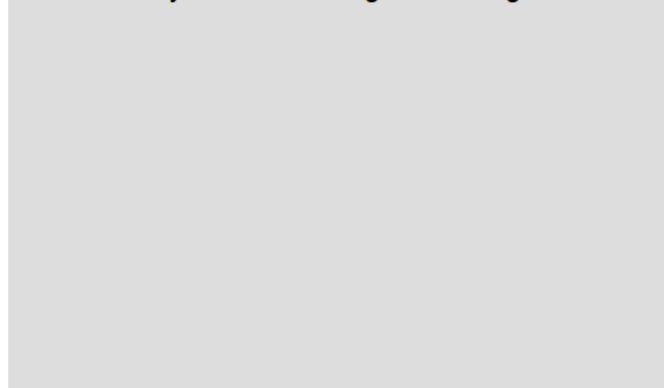
$$G''(\omega) = \frac{k_1^2\eta\omega}{k_1^2 + \eta^2\omega^2}. \quad (2.33)$$

The behaviour of the storage and loss moduli are plotted in Figure 2.11 along with that of the Maxwell and Kelvin-Voigt models for comparison.

2.3 Experimental Methods in Plants and Pectin

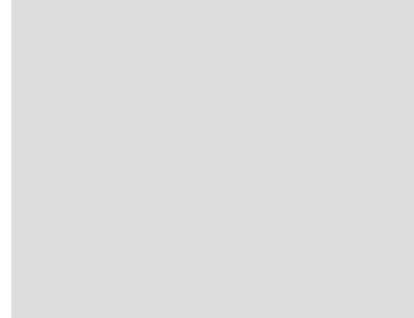
There are many different tools used for the viscoelastic testing of plants and pectin. In this section, their diversity will be highlighted through discussion of the main testing paradigms, along with a curated set of examples. Atomic Force Microscopy (AFM) will then be discussed in more detail as it was used for the experimental work in Chapter 3 of this thesis. Lastly, contact models which are utilised during indentation methods such as AFM are introduced.

Figure of extensometer apparatus removed for copyright reasons. Copyright holder is Wiley / The New York Academy of Sciences. Figure 2 in original source.



(A)

Figure of extensometer apparatus removed for copyright reasons. Copyright holder is American Society of Plant Biologists. Figures 1A and 1B in original source.



(B)

Fig. 2.12 A) Plant extensometer used to test *Avena* coleoptiles adapted from [2]. B) A more recently developed plant extensometer that can incorporate light microscopy, images adapted from [3].

2.3.1 Main Testing Paradigms

The first category of experimental methods can be described colloquially as stretchers and squishers. Their identifying characteristic is that they constrain a biomaterial and then either stretch it out or compress it. These types of tests have a considerable history in plants. Although many devices were intended to investigate ‘extensibility’ rather than viscoelasticity, the terms can often be used interchangeably in the context of plant biomechanical literature. (This is discussed further in Chapter 3.) Some of the earliest examples can be seen in the work of Heyn in the 1930s [23] but the idea has been refined and adapted many times since then. A 1967 example is the Instron-based extensometer used by Cleland to study *Avena* coleoptiles [2] – its schematic is shown in Figure 2.12A. A much more recent example can be seen in the 2017 work by Robinson et al. who developed an automated stress controlled extensometer combined with a confocal microscope which enabled visualisation of plant tissue architecture under load [3] – it can be seen in Figure 2.12B. Tissue stretching methods are not limited to plants, they are also used for animal tissues. For example, the recent study by Khaligaribi et al. who developed a system for tension experiments of epithelial monolayers [24]. Lastly, for two compressive examples, parallel plates were used for the microcompression of tomato mesocarp cells by Li et al. [25], and also for the testing of both ionic and covalently bonded alginate gels [26].

Another group of experimental methods can be classed as shear rheometry; as the name implies, its main feature is that it involves shearing the material of interest, as opposed to the

Figure of shear rheometer apparatus removed for copyright reasons. Copyright holder is John Wiley & Sons. Figure 1 in original source.

Figure of shear rheometer apparatus removed for copyright reasons. Copyright holder is Elsevier Science Ltd. Figure 1 in original source.

(A)

(B)

Fig. 2.13 A) Rotating shear rheometer developed for the study of pectin rheology [4]. B) Parallel plate shear rheometer developed for soft biomaterials [5].

previous class of tests which imposed normal forces. This is particularly useful if the material is difficult to constrain, for example many liquid-like materials, as they can be deposited in a cylinder and subjected to rotational shearing loads. An interesting early example of this is the pectin rheometer developed by Cheftel and Mocquard in 1947, shown in Figure 2.13A, which was one of the most advanced used for pectin testing at that time. It imposes a rotational shear load via a load-weighted pulley and measures the angular displacement over time. Another good example was that used by Arbogast et al. [5], in which the sample was placed between two plates that applied a normal pre-load, and then sheared in an oscillatory pattern allowing soft biomaterials to be tested over a range of frequencies. A schematic of the testing apparatus is shown in Figure 2.13B. A third type of apparatus used for numerous shear rheology investigations of biomaterials, e.g. the work of Gibbs et al. on hyaluronic acid [27], consists of two concentric cylinders within which the material of interest is sandwiched; angular oscillations of one of the cylinders is used to apply the shear loading.

A third class of testing methods can be considered – the ‘local’ methods. These are the various devices which can resolve the mechanical properties of biomaterials at high spatial resolution. One device that falls into this category is magnetic tweezers, which use magnets to manipulate particles embedded in the test sample to probe its rheological properties [28]. Another approach, which can be used to interrogate the forces generated by cells, is traction force microscopy [29]. The tool used for the experimental work of this thesis, Atomic Force Microscopy (AFM), also enables local mechanical testing and is discussed in more detail in the following section; first its general operating principles and function modes, then a short

overview of its use in biomaterials.

2.3.2 Atomic Force Microscopy

Figure of AFM apparatus and data removed for copyright reasons. Copyright holder is Marina Linardić. Figure 1.8 in original source.



Fig. 2.14 Both figures adapted from [6]. A) Operating schematic of the key AFM components. B) A standard indentation force-displacement curve obtained via AFM highlighting the region where the tip is in contact with the sample.

The main operating principle of the AFM is shown in Figure 2.14A. In short, a laser is directed at the indenting end of a cantilever which is then reflected back to a photo-detector that is very sensitive to changes in position of the received laser beam. The cantilever stiffness is usually approximated by a simple spring constant – knowing this spring constant and the deflection of the laser, the force applied to the sample can thus be calculated. There are many different types of cantilever available for use. The geometry of the cantilever tip, along with the relative presence of material adhesion, determines which contact model should be used. The geometry of the tip itself also determines the minimum lengthscale of features which can be resolved.

There are several different modes of operation in which an AFM can be used; some are used for building up a topographical map of the sample whilst other modes can be used to generate a rheological map of the sample; the latter are most relevant to this thesis. The simplest type of force spectroscopy is elastic testing in which the indenter is lowered (usually rapidly) into the sample up to a prescribed force and then withdrawn. An example resultant curve for this type of test is shown in Figure 2.14B. Although the approach and retract

motions happen in a finite time, they are generally assumed to occur fast enough such that the result can be modelled as an instantaneous, elastic procedure. It is for this reason that the indentation curves are generally plotted as force against indentation depth, with no reference to time, as can be seen in Figure 2.14B. In other words Figure 2.14B can be thought of as follows, the red line shows the decreasing height of the cantilever as it approaches the sample and when it makes contact the force rises as the cantilever deflects, the reverse occurs during cantilever retraction. Adhesion to the sample can be detected by analysis of any negative portions of the force during approach or retract – in Figure 2.14B a small amount of adhesion can be observed during the retraction phase. The effect of cantilever bending on the actual height of the cantilever tip is often corrected for in post-processing, this is the quantity referred to as ‘tip-sample separation’ in Figure 2.14B. Although the term ‘tip-sample separation’ may initially appear to be a misnomer, it is used by some AFM manufacturers in place of ‘indentation depth’ or ‘cantilever depth’ as a metric that should be considered positive when not in-contact with the sample and negative when in-contact with the sample. The simplest possible analysis fits a straight line to either the approach or retract curves and uses the slope as a metric for elastic strength. Generally however, an appropriate contact model will be applied to one of the curves to extract a Young’s Modulus. This approach is discussed further in Section 2.3.3.

For further intuition building, two prototypical AFM experiments are depicted in Figure 2.15. In Figure 2.15A, the dynamic time evolution of Force and Cantilever Depth are shown for a perfectly elastic material, whilst in Figure 2.15B, the phase-space representation (without reference to time) is shown. As discussed above, the assumption is often made that sample behaviour can be approximated as elastic and thus only the phase-space representation of data need be considered. The above force spectroscopy method can be extended for viscoelastic analysis by use of a holding period during which the force or depth of displacement is held constant. This is shown in the time-domain and phase-space in Figures 2.15C and D respectively. In Figure 2.15C we can also observe another interesting feature which is that, in the first region, the cantilever is not in contact with the sample. Detecting the point in time at which the indenter makes contact with the sample requires some consideration and is discussed further in the Methods section of Chapter 3. In the second region, the depth of the cantilever increases linearly (in our idealised sketch) whilst the force response evolves. The third section is when the depth is held by the AFM and force is allowed to relax. The cantilever is retracted in the fourth section and finally leaves the sample in the fifth section. The phase space representation of this idealised experiment can be seen in Figure 2.15D, the cantilever approaches and then follows the phase-space diagram

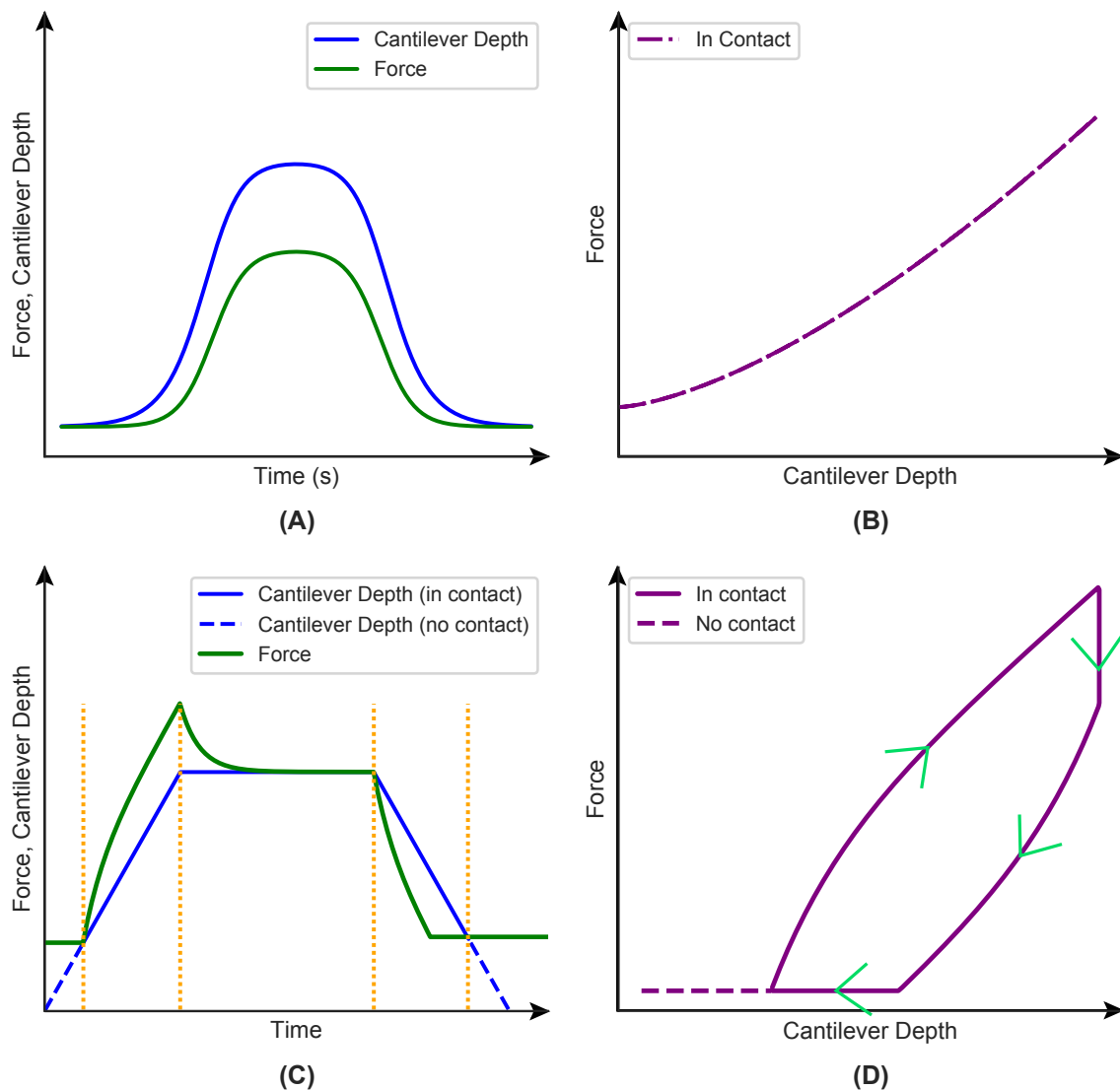


Fig. 2.15 A) Idealised sketch of elastic material indentation experiment, Force and Cantilever Depth against time for a spherical indenter. B) Phase-space representation (without reference to time) of the data sketched in Figure A. C) Idealised sketch of a viscoelastic AFM test, Force and Cantilever Depth against time, now also depicting the ‘pre-contact’ region. The five regions separated by vertical dashed lines represent pre-contact, approach, hold, retract and post-contact parts of the experiment. D) Phase-space representation of the viscoelastic idealised experiment in Figure C. Area of curve represents energy dissipated. Green arrows represent direction of time.

around the line in a clockwise fashion.

Another AFM method involves oscillation of the cantilever whilst in contact with the sample and then extracting the complex modulus. Likely due to hardware limitations, often only a small number of frequencies are investigated, though larger frequency ranges have been used in more recent studies [30]. The situation can be improved in some AFM setups by simultaneous excitation of the cantilever at its resonance modes; often only the first two are used (bimodal) but higher mode counts can be found in the literature [31]. Due to the low Reynolds number context of AFM indentation owing to the small length scales involved, and the fact that drag in the Stokes' regime increases with proximity to boundaries [32], hydrodynamic drag effects often need to be considered for oscillatory tests, but are less relevant for creep/relaxation tests which are relatively static after the initial indentation. A hydrodynamic correction protocol for oscillatory AFM tests was proposed by Alcaraz et al. [33].

AFM has emerged as a valuable tool for high spatial resolution mechanical testing of plants and other soft materials, though much of the work in plants has focused on the elastic response [34–36]. AFM viscoelastic testing of animal cells appears to be more common, with examples in lung, ovary, breast and epithelial cells [37–41]. The plant AFM viscoelastic examples found for this literature review investigated the *Arabidopsis* shoot apical meristem [42], *Arabidopsis* epidermal roots cells *in vivo* [43]. Further, a recent (2018) PhD thesis used bimodal oscillatory AFM testing to investigate the *Arabidopsis* hypocotyl [44]. Where relevant, some of the above studies are discussed in more detail in Chapter 3.

2.3.3 Contact Models

As mentioned above, the mechanical properties of a material at a relatively fine spatial resolution are often of interest. In other cases, there may be a desire to connect the bulk mechanical properties with those at a smaller scale. A commonly used tool to achieve the above is indentation methods, in which an indenter is pressed into the surface of a material. In regular normal and shear rheology tests, the relationship between the force and area of application is well defined. In contrast, the contact area between an indenter and the indented sample varies significantly during indentation. Contact models can be used to apprehend the often complicated and non-linear relationship between subjected force and sample displacement during indentation. There are many different types of indenter geometry used. In what follows, the relatively simple case of a spherical indenter is considered. Assuming the sample can be treated as an infinite elastic half space, that the indenter is

approximately rigid, and that friction and adhesion between the two is negligible, we can use the classic Hertz contact expression for a spherical indenter [45]

$$f = \frac{4\sqrt{R}}{3} \frac{E}{(1-\nu^2)} \delta^{3/2}, \quad (2.34)$$

where f is the force applied in the Z direction, R is the radius of the sphere indenter, E is the Young's modulus, ν is the Poisson's ratio of the sample, and δ is the Z axis displacement into the sample. The set up is depicted in Figure 2.16.

Figure of Hertz contact removed for copyright reasons. Copyright holder is Springer-Verlag Berlin Heidelberg. Figure 5.3 in original source.

Fig. 2.16 Diagram of the Hertz model for spherical indentation of an infinite elastic half space. Adapted from [46].

There are a number of more complicated elastic contact models which model additional physical phenomena such as the Johnson-Kendall-Roberts (JKR) model which accounts for adhesion outside of the contact zone [47], or the Derjaguin–Muller–Toporov (DMT) model which accounts for adhesion within the contact region [48]. The Hertz model above has, by use of an elastic-viscoelastic correspondence principle developed by Lee and Radok [49], been extended for viscoelastic testing. By assuming incompressibility of the sample ($\nu = 0.5$), and thus noting that the shear modulus $G = E/3$ and applying the elastic-viscoelastic correspondence principle the following relationship can be found for relaxation [50]

$$f(t) = \frac{8\sqrt{R}}{3} \int_0^t G(t-\tau) \frac{d\delta^{3/2}}{d\tau} d\tau, \quad (2.35)$$

and equivalently for creep [8]

$$\delta^{3/2}(t) = \frac{3}{8\sqrt{R}} \int_0^t J(t-\tau) \frac{df}{d\tau} d\tau. \quad (2.36)$$

It should be noted that the above are only valid for monotonically increasing contact area, though further extensions have been developed that allow decreasing contact area as well [51, 52]. A viscoelastic analogue of the JKR model has also been developed [47].

Chapter 3

Mechanical Properties of Pectin *In vitro* and *In vivo*

*Then to find out the reason of the
operation of Herbs, plants, &c., by the
Stars ... I consulted with my two
brothers, Dr. Reason and
Dr. Experience, and took a voyage to
visit my mother Nature, by whose advice,
together with the help of Dr. Diligence, I
at last obtained my desire*

[53] N. Culpeper, 1653
The Complete Herbal

3.1 Author Contributions

Thomas Torode (SLCU post-doctoral researcher) made all pectin gels and performed initial elastic tests on the DM50(41/60), DM50(33/70), DM40 (block) and DM40 (random) gels. Firas Bou Daher (SLCU/UCLA post-doctoral researcher) cultivated plant samples and performed plant viscoelastic testing experiments. Apart from the above, all experiments and analysis were performed by JLK.

3.2 Overview of Chapter

In this chapter, a protocol for viscoelastic micro-indentation using atomic force microscopy (AFM) is developed and applied to pectin *in vitro* and *in vivo*. After determining linear viscoelasticity as a suitable theoretical framework for *in vitro* pectin, two models are evaluated for their goodness of fit for pectin relaxation: the 2 time-scale standard linear solid, and the Burgers model, the former was found to provide a better fit. Further analyses were conducted with the 2 time-scale standard linear solid viscoelastic model. The results indicate a strong coupling between elastic and viscous properties over a range of degrees of methylesterification (DM). Both elasticity and viscosity were found to vary non-linearly with DM which had interesting consequences for pectin gels of mixed DM. In *Arabidopsis* cell walls, the 2 time-scale standard linear solid model was also found to fit the data well. In this *in vivo* composite material a weaker elastic-viscous coupling was exhibited and correlated with DM. The viscoelastic testing *in vivo* of rapidly elongating cell walls, rich in high DM pectin, displayed a longer viscous time-scale. The implications of the testing method and results are discussed in the context of mechanobiology, mechano-chemistry, and cell growth.

The chapter begins with an overview of pectin's usual habitat, the cell wall of land plants. The cell wall's major constituents are briefly discussed along with their putative mechanical roles. This is followed by an overview of pectin itself in more detail. Relevant literature on the mechanical testing of pectin and plants is then reviewed, followed by the experimental work.

3.3 Introduction

3.3.1 The Plant Cell Wall

In contrast to the cells of most other multicellular eukaryotic organisms, plant cells are encased in a cell wall which can take myriad forms across species, as well as a single plant's organs and developmental life-cycle. Rheological diversity of the plant cell wall has not always been appreciated. In the 1974 book 'An introduction to biorheology' [12], D. C. Spanner authored the single chapter on plant rheology and declared that "Compared with the animal world, the world of plants has relatively little to offer in the way of rheological interest; that is, if we exclude the phenomena associated with protoplasm itself" [54]. This is in stark contrast to the current field of plant rheology which has grown significantly since then, particularly with regards to that part of the plant cell which is exterior to the protoplasm – the cell wall – now acknowledged to be a critical arbiter of plant morphogenesis. It is

generally understood that the wall's role is performed via mechanochemical alterations of its constituent parts, thereby enabling selective yield to turgor pressure [55–57].

The following will largely focus on the primary cell walls of land plants with occasional comparisons made to functionally analogous cell wall components in algae and secondary cell walls of land plants. From a high level perspective the primary cell wall of land plants is traditionally viewed as a composite material in which rigid cellulose fibres are tethered together by flexible hemi-cellulose linkers and embedded in a pectin gel [58] – as depicted in Figure 3.1. Each of these three components comprises approximately one third of the biomass in the cell wall [59, 60], though of course this varies across species, cell type and developmental stage. Furthermore, these three components each in turn exhibit rich diversity in terms of architecture, chemical composition, and resultant mechanical properties; and all of these properties vary dynamically, across organs, tissues and even within single cell walls. In short, those studying the mechanochemical properties of cell walls and their relation to plant development have a tremendous amount of complexity to contend with.

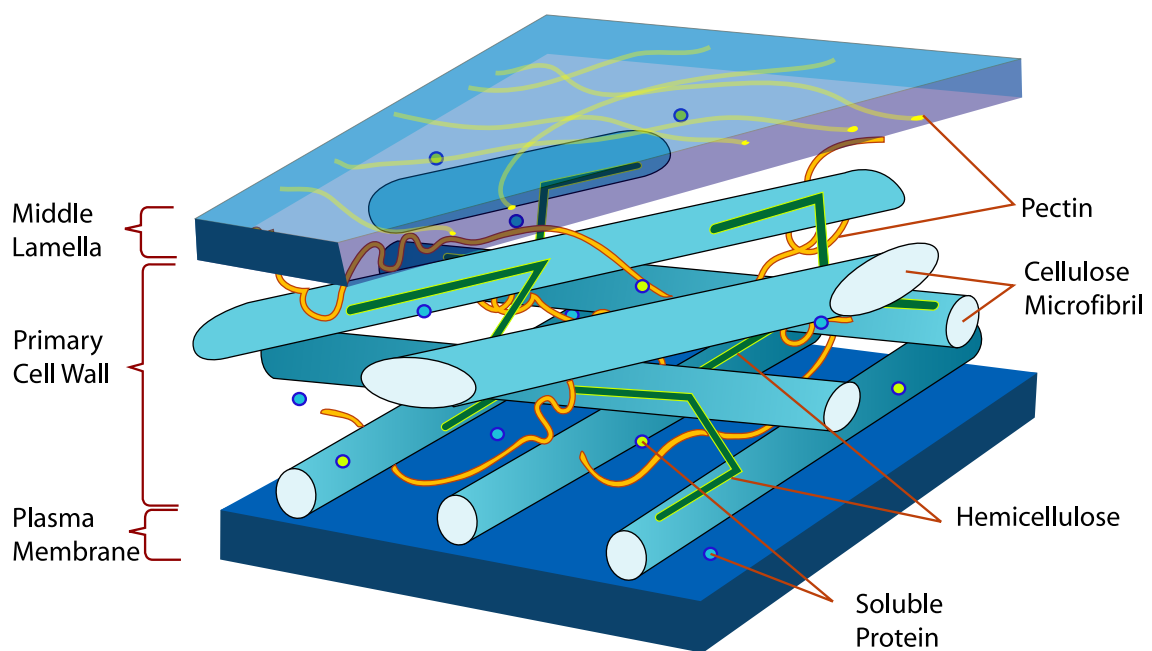


Fig. 3.1 Schematic diagram of the primary plant cell wall of land plants. Reproduced under Creative Commons License (LadyofHats)

Attempts to understand the relationship between endogenous biochemicals, cell wall mechanical properties and morphogenesis took place as early as 1931 by Heyn [23, 61]

who focused on the phytohormone auxin, and subsequently by many others [62, 2, 63]. It was not until later on that the role of specific cell wall components began to be articulated. The orientation of cellulose and lignin in secondary cell walls were studied as early as 1961 [64]. In the 1962 paper ‘Mechanism for Plant Cellular Morphogenesis’ [55], Paul Green described how the orientation of cellulose in the green alga *Nitella* and *Bryopsis* acted analogously to ‘hoops around a barrel’ and thusly facilitated the development of anisotropic form. Sketches from this paper are shown in Figure 3.2B, which illustrate bulk orientations of cellulose over sections of plant organ (not individual cells). Concurrently, a similar line of investigation was pursued by Provine and Perseus [65] who demonstrated creep anisotropy in *Nitella*, and hypothesised cellulose orientation as its cause. More recently, this hypothesis was tested in *Allium sativum* (onion) and *Kalanchoe blossfeldiana* using DMA [58]. The authors found that in onion, which had significant cellulose orientation anisotropy, the storage modulus was much higher parallel to the mean cellulose orientation than perpendicular to it. In *Kalanchoe* the near-isotropic cellulose orientation corresponded with an isotropic storage moduli. The resultant cell shapes of the two species matched well with Green’s ‘hoops round a barrel’ analogy; the onion cells showed distinctly anisotropic growth whilst the *Kalanchoe* cells exhibited isotropic growth (Figure 3.2A). (The undulations visible in the *Kalanchoe* cell wall perimeter are fairly common in plant pavement cells [66] and are generally believed to be caused by elastic buckling instabilities, though recent work suggests that specific mechanochemical heterogeneities in cell wall pectin play an important role [35].) In other cases, the applicability of Green’s hypothesis appears less clear due to mean cellulose orientation varying greatly over the multi-lamellar structure of primary walls and on the internal and external sides of epidermal cell walls [60, 67]. Further, in 2000 it was found that elongation of pea internodes, oat and rice coleoptiles, oat mesocotyls, soybean hypocotyls, dandelion peduncles, and the *Arabidopsis* hypocotyl takes place even though the mean cellulose orientation matches the axis of cell elongation [68, 69]. These studies clearly demonstrate that non-cellulosic cell wall components make significant contributions to growth anisotropy in many plant systems.

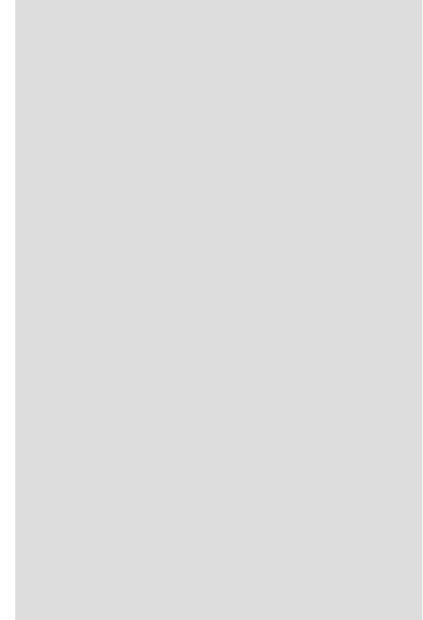
The hemicelluloses are a group of polysaccharides consisting of heteromannans, xyloglucan, heteroxylans, and mixed-linkage glucan [59]. Although the precise structure and connections of these hemicelluloses are still not fully understood, significant progress has been made in recent years [70]. The following will focus on xyloglucan as it is the most abundant hemicellulose in dicots [71] and thus *Arabidopsis*, which has been studied experimentally for this thesis. Xyloglucan was once thought to have a ubiquitous role in cell walls as a binder of cellulose microfibrils, but is now believed to act in a more localised manner at

Figure of cell microscopy removed for copyright reasons.
Copyright holder is American Society of Plant Biologists.
Figure 1 in original source.



(A)

Figure of cell schematic sketches removed for copyright reasons.
Copyright holder is Paul B. Green.
Figure 1 in original source.



(B)

Fig. 3.2 A) Confocal images of onion (upper two) and *Kalanchoe* (lower two) cells, from Kersten et al. [58]. B) Sketches by Green [55] depicting the cellulose-anisotropy model of morphogenesis. ‘Cellulose’ lines represent bulk orientation over organ sections.

so-called ‘biomechanical hot-spots’, which can be selectively removed by a group of proteins, known as expansins, in order to loosen the cell wall [56, 72, 73]. A computational model of the cell wall that incorporates these biomechanical hot-spots has indicated that they may give rise to a percolation limit which determines whether or not the wall will creep when subjected to a stress [74]. An intriguing 2016 study revealed significant heterogeneity unique to the cellulose architecture of the plant cell wall, and the presence of hydrophobic regions along cellulose microfibrils which facilitated the creation of these biomechanical hot-spots – presumably due to the conformation being energetically favourable [75]. Lastly, a number of papers over the last decade have identified significant bonding between pectins and cellulose suggesting that some of the functionality previously attributed to hemicelluloses may in fact be orchestrated by the pectic polysaccharides [76, 77].

3.3.2 Pectin *In vitro* and *In vivo*

Overview of Physical and Chemical Structure

Figure of pectin schematic removed for copyright reasons. Copyright holder is Elsevier Ltd.

(A)

Figure of pectin schematics at low and high calcium concentrations removed for copyright reasons. Copyright holder is Elsevier Ltd. Figure 4 in original source.

(B)

(C)

Fig. 3.3 A) Egg-box calcium bond structure of homogalacturonan, from [78]. B) Alternative schematic representation of egg-box bond junctions at low calcium concentrations, adapted from [79]. C) Schematic representation of egg-box bond junctions and calcium monocomplexes that form at high calcium concentrations, adapted from [79].

Pectin is a type of hydrogel. Hydrogels are defined as a network of hydrophilic polymer chains and are a critically important class of material in biology [80, 81]. The umbrella term ‘pectin’ generally refers to a variety of pectic polysaccharides which cohabit the cell wall including homogalacturonan (HG), rhamnogalacturonan I (RG-I), rhamnogalacturonan II (RG-II) and xylogalacturonan [17]. In dicots HG, α -(1-4)-D-galacturonic acid, is the largest component by a significant margin ($\sim 65\%$) and is the backbone onto which the other pectic polysaccharides are attached [17]. For this reason, HG will be the main focus of this work. A

key feature of HG is its initial state, which is highly methyl-esterified [82]. These methyl-ester groups can be selectively removed in a blockwise contiguous mode, a non-contiguous random mode, or somewhere in between as quantified by the degree of blockiness (DB) metric [83–86]. Similarly, the percentage of methyl-ester groups (as opposed to free carboxyl groups) is quantified by the degree of methyl-esterification (DM) metric [87–89], sometimes alternatively named the degree of esterification (DE) [90]. (In the literature, low DM gels are sometimes referred to as low methoxyl pectins, LMPs, and high DM pectins as high methoxyl pectins, HMPs, with the crossover DM being either DM45 or DM50 [91, 92]; in this thesis DM50 will be taken as the crossover point.) The DM and DB of HG largely depend on the method of de-esterification used. For example, in *Arabidopsis* there are sixty-six (66) pectin methyl-esterase (PME) enzymes [93], each of which is thought to yield specific patterns of methyl-esterification [88, 94]. Strong acid and alkali solutions are known to induce de-esterification with significantly lower DB than the enzymatic methods; acid de-esterification is sometimes preferred as the alkaline method tends to depolymerise the pectin chains [83, 95–97]. When a methyl-ester group is removed (i.e. de-esterification) a negative charge is left in its place and two negatively charged sugars can cross-link using Ca^{2+} ions [92]. Indeed, calcium cross-linking is the primary method of gelation for low DM gels and longer ‘blocks’ of de-esterified units form stronger bonds – provided there is sufficient free calcium available to do so [83]. Further, it has been found that a minimum number of consecutive calcium junctions, estimated to be between 6–20, are required for stable inter-chain bonding [98–100]. These type of ionic bonds in HG are often referred to as ‘egg-box’ bonds and were first identified by Grant et al. in 1973 [92, 101]. More recently, a 2012 study found evidence for more complex pectin-calcium gel structure when there was an abundance of calcium: at higher calcium concentrations the number of egg-box type bonds may decrease and be replaced by monocomplexes of single ionic bonds, leading to a reduced gel stiffness [79]. See Figure 3.3 for a graphical representation of these HG egg-box and monocomplex bonding structures. In the literature, the molar calcium concentration used to gelate pectin is sometimes defined in terms of a stoichiometric ratio \bar{R} (the over-bar has been added in this thesis to avoid confusion with the radius R symbol used elsewhere), defined as [102]

$$\bar{R} = \frac{2[\text{Ca}^{2+}]}{[\text{COO}^-]}, \quad (3.1)$$

which comes from the fact that every two free carboxyls require one calcium ion in order to bond. Sometimes an effective ratio, \bar{R}_{eff} , is defined that considers $[\text{COO}^-]_{eff}$, which represents only those carboxyl groups that are part of a contiguous chain longer than that required for stable egg-box bonding [103]. However, if monocomplexes do occur at high \bar{R}

then use of an \bar{R}_{eff} may not be helpful in high calcium scenarios. Lastly, it has been shown that low DM HG can gelate using divalent ions other than calcium [95, 104].

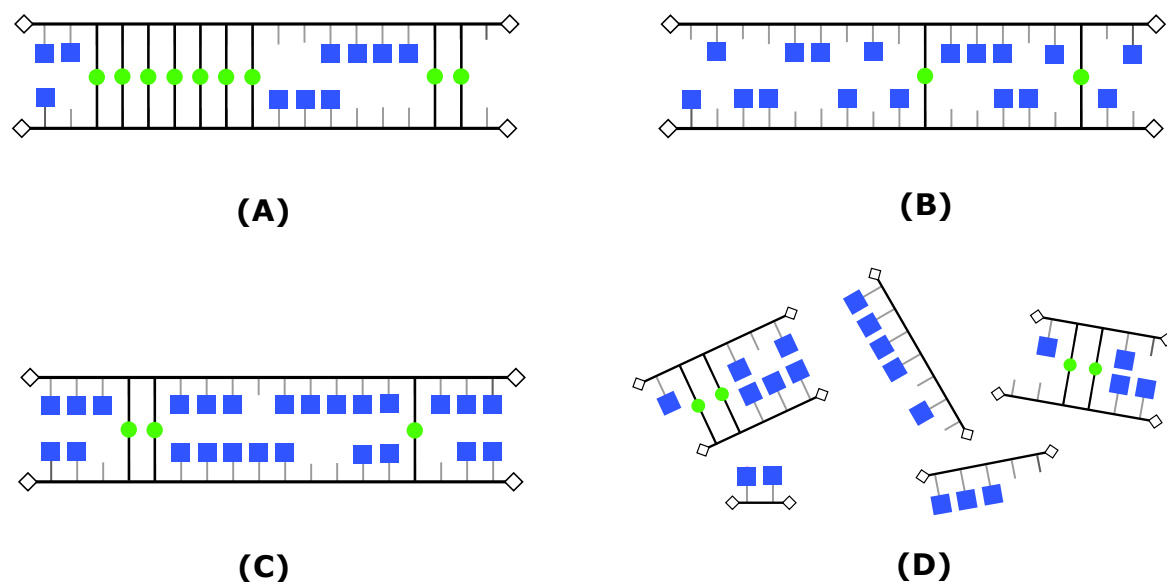


Fig. 3.4 Pectin schematic diagrams: blue squares are methyl groups, green circles are calcium bonds, sticks are de-esterified pectin sections that have not bonded and have a single negative ionisation. A) Low DM, high DB HG showing relatively long, contiguously de-esterified sections of pectin that have successfully bonded via calcium ions. B) Low DM, low DB HG with intermittently de-esterified sections of pectin resulting in a weaker bonding pattern than that seen in A. C) High DM HG with limited bonding sites available. D) Partially de-esterified pectin with chains that have been split apart through the action of pectinase enzymes.

In contrast to the above, high DM HG relies on hydrogen bonds and hydrophobic interactions for gelation [89, 100]. The hydrogen bonds are generally thought to be relatively weak, unless they exist closely and in large number [105, 106]. Hydrophobicity is localised at the methyl-esterified groups and the inter-chain bonding that arises from these parts is a natural consequence of the minimisation of free hydrophobic surface area, and thus total energy of the system. The importance of hydrophobic interactions versus hydrogen bonds can vary greatly depending on the presence of sugar solutes. A study of high DM pectin with all sucrose removed and substituted with ethanol, t-butanol or dioxane solutions estimated the contribution of hydrophobic interaction to the free energy of gelation to be approximately half of that from hydrogen bonds [91]. A more recent investigation found that a 30% sucrose solution increased the storage moduli of high DM pectin by 2-5 times, demonstrating that hydrophobic interactions may be more important than hydrogen bonding in some scenarios [84]. Further work has been done to elucidate the effects of different sugars on the gelation and

rheological properties of pectin [107–112].

The RG-I and RG-II pectin side-chains, which can be covalently linked to HG [113], are considerably more complex than HG and our understanding of their effects on bulk mechanical properties of pectin *in vivo* and *in vitro* is limited [114]. An *in vitro* 2016 study by Lin et al. [115] found evidence that pectic side-chains increased pectin bonding to cellulose by as much as 33%; this cellulose-pectin bonding increased the effective stiffness of the material, an effect which may or may not be replicated in plants as the cellulose-pectin composite materials in that study were constructed without any calcium present. RG-II is able to form boron cross-links in an analogous way to HG calcium cross-linking, but the precise plant physiological role of these boron cross-links has not yet been elucidated [116].

Industrial Uses of Pectin

Pectin isolate has manifold uses. In fact, even when pectin was first identified as a material in its own right in 1824 by both Payen and Braconnot separately, the latter author noted its potential for use in confectionery and pharmaceutical products [117, 118]. Circa 1909, Goldthwaite was reportedly the first to evaluate pectin's utility in jellies with scientific rigour, though it was likely used in a more *ad hoc* artisanal manner before this [119]. Pectin has now become a common food ingredient. With this knowledge, a clear motivation for understanding the effects of different sugars on pectin gelation and rheology emerges, with studies from as recently as 2017 [108–110, 120]. Perhaps given the dietary hazards associated with excess sugar consumption, flavour requirements or other economic concerns, there has long been prevalent use of low DM pectin with calcium as a substitute for high DM gels whilst attaining similar textural-rheological properties. Low DM pectins have been manufactured since the 1940s and research into their rheological properties either on their own, or in some high/low DM pectin mixture is still ongoing [84, 97]. The many studies of different pectin formulations' effect on a food's rheological properties sometimes cross over into the territory of psychorheology, a field which attempts to rigorously apprehend the nuanced relationship between the rheology of materials and the psychological perception of their texture [121–124]. In addition to jams and jellies, a non-exhaustive list of food products that sometimes have added pectin are bakers' glazes, malted-milk thickener, milk gels and puddings, barbecue sauce, salad dressings, and cheese [124, 125]. Pectin has numerous pharmaceutical uses. It is known to reduce the coagulation time of blood, whilst sulfated pectin increases the coagulation time [89, 126]. Pectins sourced from various fruits have been found to significantly reduce cholesterol levels *in vivo* [127]. In 2006 modified citrus

pectin was shown to increase the urinary excretion of various toxic substances and it was hypothesised that this was due to chelation by RG-II [128]. Lastly, products, or product prototypes containing pectin have been developed for nasal, oral, and ocular drug delivery, as well as gene delivery and tissue engineering [104, 129]. For overviews of the many other demonstrated pharmaceutical and other non-food use cases of pectin, see the reviews by Thakur et al. [89], Liu et al. [129], Munarin et al. [104], and the book chapter by Endress [130].

The Mechanical Roles of Pectin *In Vivo*

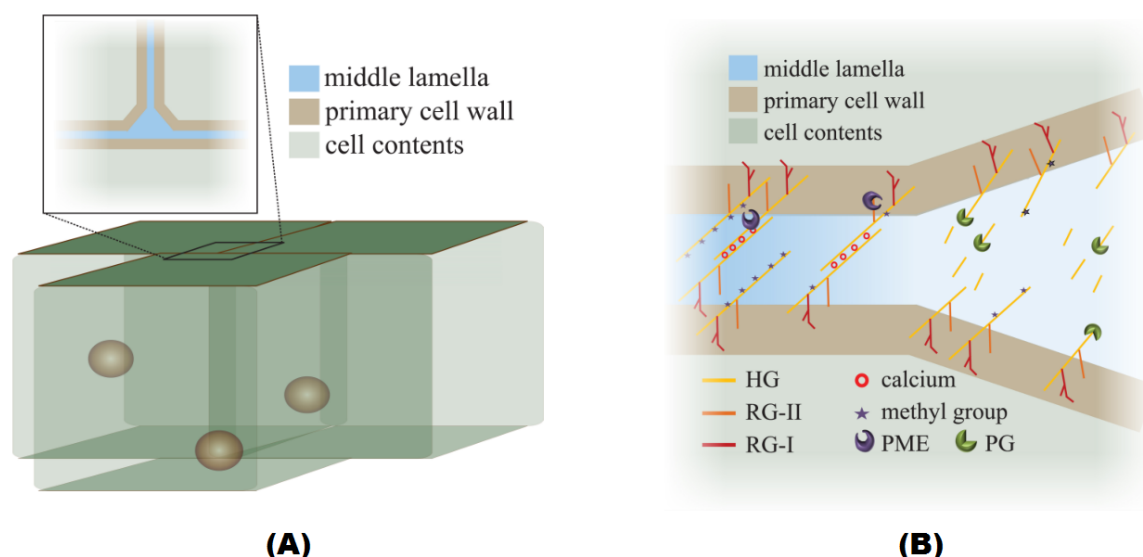


Fig. 3.5 A) Location of the Middle Lamella, from Bou Daher and Braybrook [131]. B) Composition of the Middle Lamella, from Bou Daher and Braybrook [131].

What are the known roles of pectin *in vivo*? To answer this question, it is convenient to begin with that part of the plant which consists of mostly pectin. The middle lamella is a narrow region between adjacent cell walls; it is significantly richer in pectin than the walls themselves [131]. Much of the time, its role is to adhere the adjacent cell walls, but at other times it is necessary for cells to separate. Two examples of developmental cell separation are dehiscence, the separation of cells to allow seed release [132], and abscission, the purposeful removal of plant parts (e.g. leaves dropping in autumn, or fruit dropping when ripe) [133]. For adhesion maintenance, evidence suggests that de-esterified, calcium cross-linked HG is key [131, 134, 135]. For separation, the polygalacturonase (PG) enzymes are critical [131, 136, 137]; they depolymerise the HG pectic backbone via hydrolysis with strong substrate preference for lower DM HG, thereby implicating the PME enzymes as

important precursors for PG-mediated separation [131, 138]. Interestingly, the pattern of de-esterification (or DB) appears to be significant, with more blockwise (higher DB) PME de-esterification being associated with adhesion and more random (lower DB) PME de-esterification being associated with regions of separation [88].

Additionally, in more structurally complex cell walls, the action of PGs has been found to play a role in the selective pectin weakening associated with cell growth [94, 139]. It's also possible that PG plays a role during the formation of the lobe patterns observed in many pavement cells; a 2017 study on *Arabidopsis* pavement cells found that the concave side cell wall of lobes was less stiff and had lower DM pectin relative to the convex side [35] (though this could also be due to spatial variation in calcium levels available for cross-linking). At the shoot apical meristem (the location of plant meristem cells above ground), a lower DM has been correlated with a decrease in stiffness [140, 42]. Again, PG is one possible culprit in this case, but a lack of available calcium would also have the same effect. Importantly, auxin is thought to be the first step in organ initiation but the intermediate steps between auxin delivery and actual formation of organ primordia are still in question. Acid growth theory provides a framework for understanding this auxin-mediated growth, but a limit on the spatial resolution of current pH testing methods places a major technical barrier in the way of its validation [56, 141]. Given that pectin's rheology is sensitive to pH [83, 108], it is plausible that pH changes at the shoot apical meristem contribute to the observed compliance. Similarly to the shoot apical meristem, de-esterification of pectin in leaf primordia of *Arabidopsis* is also negatively correlated with stiffness. Further, the de-esterification pattern displays strong abaxial/adaxial asymmetry which, in conjunction with computational modelling work by the authors, suggests pectin plays an important role in leaf asymmetry [142].

In contrast to the previous two examples, localised de-esterification of plant stomata (guard cells) pectin corresponds with an increased stiffness of the guard cell wall [144, 145] suggesting calcium cross-linking. Further, polygalacturonase appears to be important in regulating stomatal geometry and opening/closing dynamics [146]. The strongly directed, cylindrical growth of pollen tubes appears to be largely enabled by softening at the apical end via high DM HG, relative to the stiffer low DM HG around the stem of the tubes [114, 147, 148]. The hypocotyl is that part of a young seedling's stem which is above the root but below its cotyledons, it elongates rapidly for the first few days of growth, with very little cell division occurring (Figures 3.6 and 3.7). A 2007 study observed a correlation between DM and hypocotyl elongation and hypothesised calcium cross-linking of HG as a key elongation limiter [149]. A 2015 study by Peaucelle et al. [150] attributed the cause of hypocotyl growth

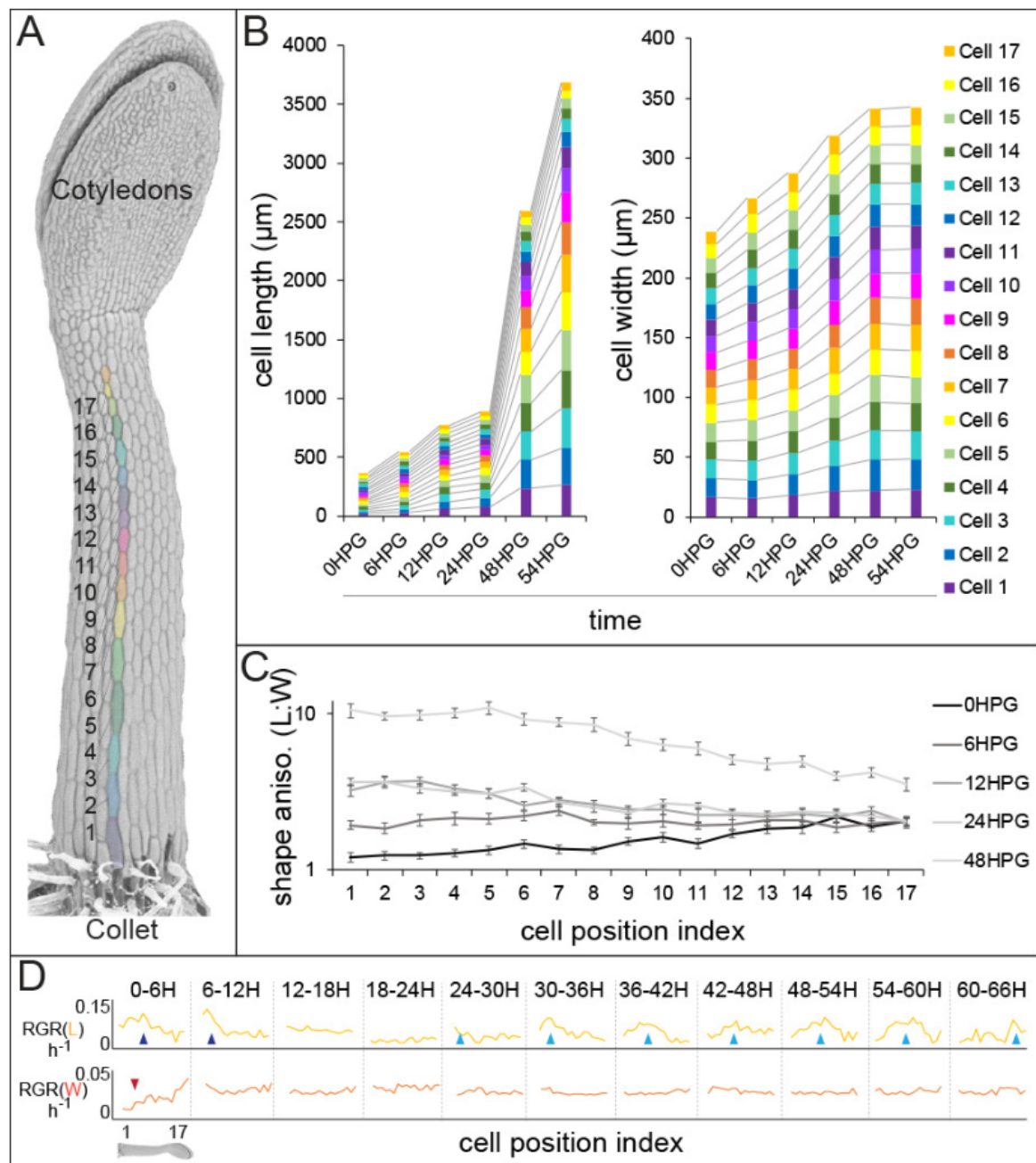


Fig. 3.6 Hypocotyl growth wave adapted from Bou Daher et al. [143]. A) Scanning electron micrograph of 24H after germination hypocotyl with indices of non-dividing cells highlighted. B) Cell length and width by cell position index. C) Cell shape anisotropy by cell index. D) Relative growth rates for length and width of cells by index.

anisotropy to be a higher stiffness in transverse (lateral) walls compared to longitudinal (axial, upward growing) walls. Confusingly, the authors correlated this stiffness with higher DM pectin in the transverse walls relative to the axial walls. In contrast, a 2018 study by Bou

Daher et al. noted the same mechanical difference in stiffness between the walls but observed via immunoassay that there was more de-esterified pectin in the transverse walls than the axial walls; this supports the data found by Derbyshire et al. [149] and suggests that calcium cross-linked HG is an important player in hypocotyl growth anisotropy.

Figure of hypocotyl microscopy removed for copyright reasons. Copyright holder is Elsevier Ltd. Figure 1A in original source.




Fig. 3.7 AFM stiffness maps showing the onset of anisotropic growth in an *Arabidopsis* hypocotyl from 9 to 32 hours after germination, adapted from Peaucelle et al. [150]. Scale bars 50 μm .

The above discussion, a curated selection of the most relevant known roles of pectin *in planta*, should be evidence enough that the rheological properties of pectin are carefully spatio-temporally regulated by plants throughout their life-cycle [57, 151]. What is particularly interesting is that most of the examples above can be loosely thought of as forms of fine-grained symmetry breaking, suggesting a developmental niche of pectin. For example, the breaking of radial symmetry in pavement cells, and the breaking of mirror symmetry in hypocotyl cell elongation. This is particularly interesting as pectin is not found configured in an architecturally directional manner, as is the case for cellulose, but achieves the symmetry breaking through highly localised changes in mechanical properties. This observation, combined with the other more macro putative roles of pectin [70], affirms pectin's central role in plant development. However, it is also clear that a number of questions remain. In the context of this thesis, we are particularly interested in those results based on elastic mechanical tests,

which may benefit from the added depth of insight that time dependent viscoelastic testing can bring.

3.3.3 Mechanical Testing of Pectin and the Plant Cell Wall

Historical Perspective of Pectin *In Vitro* Mechanical Testing

Due to its popularity as a gelling agent in foods, much of the early pectin isolate mechanical testing, in the first half of the 1900s, focused on high DM pectin-sugar gels and measured their viscosity and the so-called ‘jellying power’ of the pectins used; the latter metric was somewhat cumbersome and derived from the amount of a specific pectin required to form a gel under a specific set of preparation conditions, limiting commensurability between different gel preparations [117, 152, 153]. Furthermore, the ‘jellying power’ metric relied on a subjective interpretation of when a gel had been sufficiently formed.

Creep, Relaxation and Dynamic Mechanical Analysis of Pectin *In Vitro*

Although an elaborate analog rheology testing device for pectin was proposed as early as 1947 [4], it was not until the 1960s when evaluation of pectin using a more universally commensurable rheology framework, that incorporated viscoelasticity rather than just viscosity, began to develop. Harvey in 1960, and then Watson in 1966 appear to have been among the first to explicitly note pectin’s viscoelastic nature and use standard rheological testing methodologies [154]. In Watson’s paper, high DM sugar-gelled pectin was subjected to creep using a mechanical compression device. Sucrose, glucose and cerelese sugars were tested, no viscoelastic model was fitted to the data, and elastic or plastic behaviour was observed depending on the strain applied. In 1976, Kawabata and Sawayama used a parallel plate viscoelastometer to perform creep tests on a variety of high and low DM pectin gels [155]. Although the majority of the main text remains untranslated from the original Japanese, useful information can still be gleaned from the tables, equations and figures. The authors used a six element extended Burgers-type model: two Kelvin-Voigt units in series with a Maxwell unit. Interestingly, the low DM pectin gels appear to have been tested using milk, and then (separately) a water-based calcium chloride solution to provide the calcium required for gelation – suggesting that the precise molar calcium concentration may not have been controlled. A 1979 study by Plashchina et al. also used a parallel plate rheometer for creep tests of sugar-gelled DM60 pectin extracted from citrus [156], no viscoelastic models were fitted, the authors were focused on the effects of temperature and concentration on creep behaviour at particular time points. Plaschina et al. followed this

up in 1983 with a similar study, again testing pectin of approximately DM60, but with the addition of glycerol [157]. Comby et al. (1985) used an Instron machine for compressive stress relaxation of high DM (DM60) pectins at a range of pectin concentrations (1.4% - 1.8% w/w) and sucrose concentrations (60.3% - 72.3% w/w), they also varied the pH within the acidic range (2.4 - 3.2) [158]. For viscoelastic analysis they used a generalised Maxwell model with 2 time-scales – or equivalently, 2 Maxwell models in parallel. Elastic parameters were positively correlated with concentration, negatively correlated with pH, and positively correlated with sucrose concentration. The larger time-scale of the model also followed the elastic correlations, whilst the second time-scale parameter's behaviour was more ambiguous.

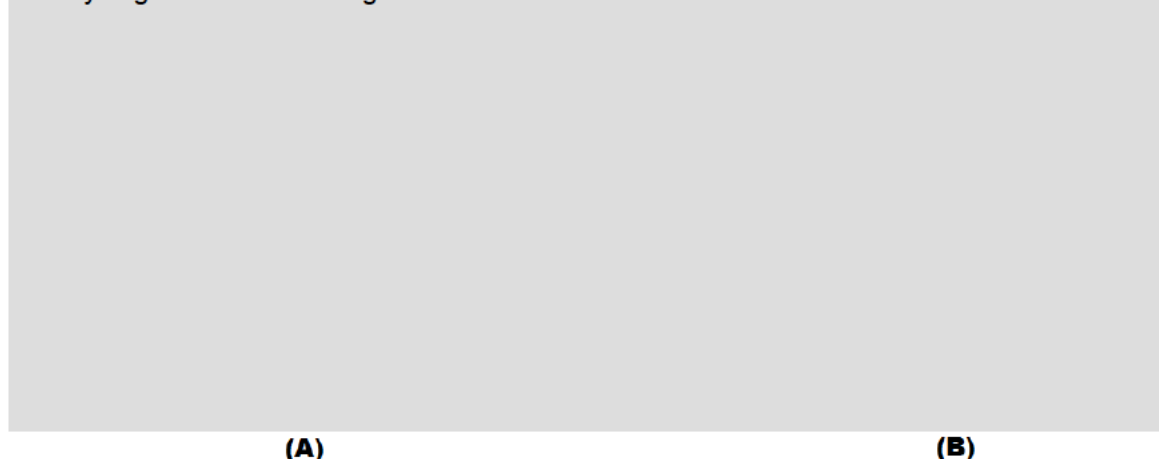
Over a similar time period, a number of low DM studies were conducted. A 1976 study by Mitchell and Blanshard tested very low DM4 pectin using parallel plate rheometry [159]. They fitted an unusually complex 8 parameter model to the creep data – an extended Burgers model consisting of three Kelvin-Voigt units and a Maxwell unit in series; a square root relationship between the concentration and inverted creep compliance was observed. Two years later, Kim et al. studied the relaxation behaviour of pectins of approximately DM30 - DM40, and amidated pectins de-esterified using an acid-ammonia protocol [87]. Sucrose was added to the gels, no rheological model was used, and the gels were compressed up to point of fracture. In 1980, Gross et al. performed creep and stress relaxation tests on low DM pectins, ranging from approximately DM25 to DM40, using an Instron Universal Testing Machine for relaxation tests and a custom designed compressive loader for creep tests [90]. They explored several mechanical models and in the end decided that a 2 time-scale generalised Maxwell model was best suited for fitting stress relaxation data, and that the Burgers model was better suited to creep data; psychorheological tests of firmness, coarseness and graininess were also conducted and some correlations between model parameters and the sensory metrics were identified. All elastic and viscous parameters of both models were found to have moderate negative correlation with DM, which might be expected due to the increased ionic bonding activity. However, a clearer negative correlation may have been inhibited by the fact that the gels were made in low pH and with 30% sucrose which would lessen dependence of calcium cross-linking. Furthermore, the calcium concentration was not adjusted for different DMs so optimum ionic bonding may not have been achieved.

Apart from the above discussed relaxation and creep studies, several of which fitted viscoelastic models to the data, almost all chronologically subsequent pectin rheology studies found for this literature review took a model-free, oscillatory approach by only finding experimental values of the complex modulus G^* . DMA studies on a single, low DM pectin type

have investigated their rheology with varying pectin concentration, formation temperature and stoichiometric ratio \bar{R} [160, 161]. Similar studies were conducted on sucrose-containing high DM pectins but also investigated their gel formation and ageing process [162–164]. Interestingly, Lopes da Silva et al., in their study of temperature effects on both high and low DM pectins, did use an empirical model for viscosity but chose not to model the viscoelasticity [162]. In fact, after the 1985 stress relaxation paper by Comby et al. [158], only a small number of exceptions to the oscillatory, model-free approach found for this literature review were found. Examples of note include a 2002 study by Alonso-Mougan et al. on amidated low DM pectin [165] and a 2009 study by Gigli et al. [166] on low DM pectin. The paper by Alonso-Mougan et al. fitted a power-law model to their DMA frequency spectrum data obtained from amidated low DM pectin testing and it fitted well over a fairly large range of frequencies. The Gigli et al. study investigated the effects of calcium concentration and curing temperatures on DM22.5 pectin rheology via DMA and creep testing; the data were fitted to a generalised Kelvin-Voigt model consisting of 5 Kelvin-Voigt units in series, a model with 10 parameters in total. For further evidence of the dominance of the model-free DMA approach in pectin rheology, see the numerous modern studies of added sugar effects on high DM pectins [107–112] and the rheological contribution of RG-I and RG-II side-chains [116, 167–170].

From the mechanochemical perspective, the work in this chapter is most closely related to the following three studies on pectin-calcium gels. In 2007, Ström et al. performed DMA tests on calcium-pectin gels that had been de-esterified by means of alkali and two different plant-derived enzymes [171]. The stoichiometric calcium ratio was $\bar{R} = 0.3$, which was chosen as it was found to be the minimum that enabled gelation of the alkali de-esterified pectin – the others were presumably able to gelate at lower calcium concentrations. For the three pectin types tested (one alkali and two enzyme de-esterified pectin types) it was found that G' positively correlated with the DB, and negatively correlated with DM – with the alkali de-esterified pectin storage modulus dropping off most sharply with increase in DM. The G' vs. DM correlation is shown in Figure 3.8A. For both DM and DB, the storage modulus changed over several orders of magnitude with respect to the correlative directions mentioned above. Unfortunately the loss modulus was only reported for a small subsection of the tested pectins, shown in Figure 3.8B. Fraeye et al. performed a related study in 2009 in which similar correlations were observed [86]; as before, the loss modulus was not reported in the main DM and DB plots, however a subset of the pectins tested were shown separately with loss modulus shown. The authors also investigated different pectin and calcium concentrations and found that storage and loss moduli were positively correlated with both up to a

Figures of pectin data removed for copyright reasons. Copyright holder is American Chemical Society. Figures 3 and 5 in original source.



Figures of pectin data removed for copyright reasons. Copyright holder is Elsevier Ltd. Figures 3B and 4B in original source.



Fig. 3.8 A) DM vs. G' from Ström et al. [171]. Triangles are alkali de-esterified, circles are papaya PME de-esterified, triangles are citrus PME de-esterified. $R = 0.3$. B) DM vs. G' , G'' from Ström et al. [171], with pectin de-esterified using papaya-derived PME (DM30) and orange-derived PME (other DMs). $R = 0.3$. C) DM vs. G' from Ngouémazong et al. [172] for pectins de-esterified with carrot-derived PME (squares) alkaline NaOH (triangles) fungus-derived PME (circles). D) As in (C) but with the absolute degree of blockiness in the horizontal axis.

point, with plateaus appearing to emerge at higher pectin and calcium concentrations in some pectins. Heat depolymerised pectin gels were also tested and both storage and loss moduli were found to decrease with increasing depolymerisation. A 2012 study by Ngouémazong et al. focused more on fine structure, but also tested pectin that had been de-esterified with a fungal PME [172]. Similar correlations as the above two studies were found for the storage modulus but, as in the above two studies, the loss modulus G'' was not reported. Results from this study are shown in Figures 3.8C and D. The correlations discussed above agree

with the intuition that a higher number of ionic bonds (lower DM) that are increasingly stable (higher DB) will result in stiffer gels, provided there is sufficient calcium and polymerisation of the HG chains.

Pectin Composites – *In Vitro* Cell Wall Analogues

In order to bridge the complexity between pure pectin gels and primary cell walls, some have investigated artificial composites containing only selected cell wall components. For relatively large compression of cellulose/pectin mixtures, the presence of pectin was found to increase resistance to compression, possibly due to reduced permeability [173]. Additional composites containing high or low DM pectin found that the viscoelastic properties and DM of the pectin used played a role in bulk properties [174]. A recent study investigating the viscoelastic properties of cellulose/pectin composites found that both the storage and loss modulus decreased approximately 5-fold from DM69 to DM33 [175] – possibly a consequence of insufficient free calcium as calcium is not mentioned in the paper. As a more general comment, the above composites are certainly interesting from an applied and industrial perspective, but some have questioned how much of this insight is transferable to plant developmental mechanics [114]. Furthermore, the cellulose used in the above studies was constructed by bacteria – it is not known whether it has similar heterogeneous properties recently observed in plant cellulose [75] or how important these properties are to plant cell walls' bulk rheology.

Viscoelastic Testing of Plants at High Spatial Resolution

Moving to plants, though a number of studies have used viscoelastic theory more formally, measures of 'extensibility' have often dominated the literature. The term is used in a number of ways, as summarised by Cosgrove [176]:

1. Strain/stress.
2. Strain rate/stress.
3. Strain at breaking point.
4. Stress at breaking point.
5. Δ Length after fixed time under fixed force.

Though not explicitly defined as such, items 1, 2 and 5 each have an equivalent in the viscoelastic modelling framework described in Chapter 2. Item 1 could be represented by a Hookean spring; item 2 could be represented by a Newtonian dashpot; item 5 would then simply represent the dashpot from item 2 as convolved with the force history. (Items 3 and 4 are part of plasticity theory and fracture mechanics and are of less interest to us here, where testing deformations are small.) For these reasons, employing the viscoelastic framework directly seems wise as it gives greater commensurability between studies, whilst losing no descriptive accuracy, in fact it gains accuracy by making no *a priori* assumptions about the elastic, viscous or viscoelastic nature of the material being tested. Though a number of viscoelastic studies have been conducted on plants using a variety of tools [63, 42, 177, 25, 43, 178], the AFM has emerged as the tool best suited for high spatial resolution mechanical testing *in vivo* [35, 34, 36]. However, possibly due to the difficulty of viscoelastic testing using AFM and the interdisciplinary nature of subject, viscoelastic studies of plants using AFM appears to have only been done a handful of times, with AFM studies generally only considering the elastic response of the plant specimens. The AFM viscoelastic examples found for this literature review did tests on the *Arabidopsis* shoot apical meristem [42] and on *Arabidopsis* epidermal roots cells *in vivo* [43]. This is in contrast to the more widespread use of AFM for viscoelastic tests of animal cells [37–41]. The papers most closely related to the work in this chapter are the elastic AFM studies by Peaucelle et al. [150] and Bou Daher et al. [143], both of whom conducted AFM elastic indentation tests to better understand the origins of *Arabidopsis* hypocotyl growth anisotropy – as discussed earlier in this chapter. The experimental work here attempts to expand rheological understanding of this growth anisotropy by use of AFM viscoelastic tests. (It should be noted that some time after the experimental and analysis work presented here was completed, a PhD thesis was released (2018, University of Oxford) [44] in which viscoelastic DMA data from *Arabidopsis* hypocotyls were presented.)

3.4 Overview of Experimental Work

We have seen from the above discussion that insight into pectin rheology is important in both applied and plant developmental contexts. In the following work, a protocol for the rheological testing of pectin gels using AFM was developed and used to test the viscoelastic properties of pectins of various DM (33, 41, 50) and DB (random and blocky). Due to the putative DM heterogeneity of pectin *in vivo*, mixed DM pectin was also tested. Although high/low DM mixtures have been tested in previous studies [84, 179], sucrose was included which would have increased the bonding of high DM chains. As there appears to be no evi-

dence of sucrose presence in *Arabidopsis* cell walls in quantities that would have significant effects on the mechanical strength of pectin, the previous sucrose-containing studies may not be developmentally relevant. We generated two mixed gels with an effective DM50, one using a combination of DM33 and DM70, and another using a combination of DM41 and DM60. We also generated one mixed gel with an effective DM41 using a combination of DM33 and DM50 pectin. Inspired by the early pectin rheology, but in contrast to the majority of studies over the last two decades, a model-based force relaxation approach was used in an attempt to make connections between model parameters and pectin mechanochemistry.

A number of investigations have been conducted to better understand the relationship between the fine-grained structure of pectin and its bulk mechanical properties [102, 179–186]. Rheological tests have generally been conducted at either the bulk scale, length-scales distinguishable by the human eye, or a much smaller scale, elastic tests of single pectic chains. There is certainly interest in understanding the architecture and mechanochemistry of pectin at intermediate length scales, and this has been attempted using particle tracking rheology [186]. Whilst AFM has been used in at least one pectin study to investigate elastic extension of single pectic chains [180], its potential for mesoscale viscoelastic pectin testing has not been explored. In addition to the above, the AFM viscoelastic testing methodology used in pectin was adapted for use on the *Arabidopsis* hypocotyl. Recent work [143], discussed above, showed that in the elongating dark-grown *Arabidopsis* hypocotyl, epidermal cells display an elastic asymmetry coincident with a difference in pectin DM; faster growing axial cell walls were more compliant and had a higher DM compared to slower growing transverse walls. The AFM viscoelastic testing methodology developed here was used to provide greater rheological insight into the differences between the transverse and axial walls. Short time-scale results mirrored previous elastic work closely but at longer time-scales the compliance of axial and transverse walls appeared to get closer, suggesting a possible coupling. In summary, it is expected that the work presented below will be of interest to both pectin and plant rheology investigators alike.

3.5 Materials and Methods

3.5.1 Preparation of HG Gels

The DM40 Block and DM40 Random pectin pre-gel mixtures were made in the laboratory of Prof. Bill Williams at the University of Massey, New Zealand. A highly methyl-esterified

pectin was the starting point for both block and random pectins. The DM40 Random pectin was de-esterified using alkali NaOH. The DM40 block was de-esterified with a processive Valencia orange peel PME from Sigma Aldrich (P5400). The DB of the block and random pectins was estimated to be 95% and 39% respectively. For further detail on the methods for the block and random pectins see the paper by Ström et al. [171]. The DM33, DM41, DM50, DM60 and DM70 HG pre-gel mixtures were from Herbstreith & Fox, UK. The Herbstreith & Fox HG Samples had the following galacturonic acid contents: DM33 - 84%, DM41 - 90%, DM50 - 86%, DM60 - 89%, DM70 - 83%); the samples were therefore mostly HG and assumed to have behaviour approximately equivalent to 100% HG. All the pectin gels (or gel blends) were dissolved in de-ionised water, neutralised with NaOH to pH6.5, and made up to 1.5% (w/v). Gels were set using the CaCO_3 /gluconolactone (GDL) method commonly used to set calcium cross-linked hydrogels [103], via addition of CaCO_3 (Cat. No. 21061, Sigma, UK) and GDL (Cat. No. G4750, Sigma, UK) into the pectin solution to facilitate the controlled, slow release of Ca^{2+} ions. The pectic/ CaCO_3 /GDL mixture was left on a microscope slide for 12 hours at room temperature to fully set prior to use in experiments. The ratio of calcium ions available to bind pairs of de-methylated galacturonan residues was kept at $\bar{R} = 1$ for all gels, where \bar{R} is defined in Equation 3.1. A stoichiometric ratio of GDL, $[\text{GDL}] = 2 \times [\text{Ca}^{2+}]$, was used to solubilise all CaCO_3 in the gel, without altering the pH via excessive proton release. Prior to AFM experiments, the homogalacturonan hydrogels were soaked for 30 minutes in CaCl_2 solutions of equal molarity of Ca^{2+} as within the hydrogels.

3.5.2 Preparation of Plant Material

Arabidopsis thaliana ecotype Col-0 seeds were surface sterilized with 70% ethanol for five minutes then rinsed with 100% ethanol for one minute and left to dry prior to plating them on half strength Murashige and Skoog (MS) media. Seeds were stratified for 2 days at 4 °C in the dark before transferring them to a growth chamber with 16/8-hours light/dark cycle at 20 °C for germination. Germinated seeds were transferred to half strength MS plates containing 87.6 mM sorbitol, sealed with aluminum foil and left to grow for 24 hours prior to AFM scanning.

3.5.3 AFM-based indentation tests

Gels: Elastic and Viscoelastic Tests

A 50 μm diameter silicon bead (Cat# C-SIO-50.0 from Microspheres-Nanospheres, Corpucular, Cold Spring, NY, USA) was mounted on a nominally rated 2.8 N m^{-1} tipless cantilever

(TL-FM-10, Windsor Scientific Co., UK) for DM50 gels and DM50 mixtures, and a nominally rated 48 N m^{-1} tipless cantilever (TL-NCL-10, Windsor Scientific Co., UK) for lower DM gels, using standard 2-component epoxy as in [36]. Before bead fixation, due to slight manufacturing differences in the cantilevers used, they were calibrated in the following way. Firstly, the AFM cantilever holder was sonicated to remove debris and then wiped down with lint-free microfiber tissue and ethanol. Sensitivity was then determined by indenting a glass cover-slip and measuring the nm V^{-1} slope. After this, the spring constant was measured using the thermal noise method as described in the JPK manual [187]. Indentation speed used was $50 \mu\text{m s}^{-1}$. After the gels had been left to swell for 30 minutes in CaCl_2 (of equal molarity of calcium ions as within the hydrogels) the slides were carefully placed on the stage of a Nano Wizard 3 AFM (JPK Instruments, DE) and covered with just enough CaCl_2 solution to cover the gels. For elastic tests, a new (previously unindented) point near the centre of the gel was then subjected to a range of elastic indentations over a force range that was found to contain the indentation depths of interest. At each point the up/down direction of force variation was alternated to ensure pre-stress was not affecting the results (no pre-stress effects were observed). For elastic tests, six gel samples were tested, at three points on each sample. For viscoelastic indentations, the same settings as for elastic were used apart from the introduction of a 15 second constant height hold. For viscoelastic tests, six samples at each DM were used. Depending on time available, 3 - 5 points at each sample were tested. However, as the AFM was not optimally isolated from external noise, not all samples could be used. To filter out excessively noisy samples in an automated way, those found to have a time-scale 10x greater than the median were removed from further analysis. Sample numbers for each DM are as follows: $N_{33} = 15$, $N_{41} = 20$, $N_{50} = 25$, $N_{(33/50)} = 19$, $N_{(41/60)} = 22$, $N_{(33/70)} = 27$, $N_{block} = 17$, $N_{random} = 21$.

Plants: Elastic and Viscoelastic Tests

24 hour old seedlings were gently stuck on a double sided tape placed on a glass slide, immediately covered with a solution of 600 mM mannitol and plasmolysed for 15 minutes prior to scanning. A Nano Wizard 3 AFM (JPK Instruments, DE) mounted with a 10 nm diameter pyramidal tip (Windsor Scientific, UK) on a 45 N m^{-1} stiffness cantilever was used for indentations. The cantilevers used were calibrated using the same methods as in the above section. For elasticity testing, an area of $100 \mu\text{m} \times 50 \mu\text{m}$ at the base of the hypocotyl was indented with a resolution of 64×32 points using 500 nN force. Indentation speed used was $100 \mu\text{m s}^{-1}$. In elastic analysis 19 transverse and 15 axial wall indentation points were used. (Transverse walls run across the stem perpendicular to main direction of growth, axial walls

run parallel to the main growth axis.) For viscoelastic testing, 10 points were chosen on the cell wall of a basal cell (5 on the transverse wall and 5 on the axial wall) with a 15 second indentation hold time on each point. Seven hypocotyls were used. Of the viscoelastic data collected, 19 transverse and 18 axial wall indentation points were analyzed from across these seven hypocotyls, with the remainder discarded due to excess noise.

Indentation Speed Discussion

All indentations, both elastic and viscoelastic, were done at a fast indentation rate of $50 \mu\text{m s}^{-1}$ (pectin gels) and $100 \mu\text{m s}^{-1}$ (plants). For elastic indentations, this speed was in line with previous studies [36, 188]. However, as it is known that both HG and plants are not solely elastic, it is probable that the speed of indentation does affect the apparent elastic measurements. Indeed, preliminary experiments on gels and plants (data not shown) did indicate a slight positive correlation between apparent stiffness and indentation speed. However, the main focus of the experiments in this chapter is viscoelastic behaviour, where indentation speed is not likely to be a significant source of spurious results. More specifically, indentation speed would be an issue if a step loading assumption was used, but the analysis in this Chapter and Chapter 4 made use of the full loading history, taking into account the full Boltzmann convolution integral, which means that an arbitrarily complex loading pattern could be used. This is discussed further in Sections 3.5.5 and 4.4.4.

3.5.4 Hertz Contact Model for A Spherical Indenter

The Hertz contact model for a rigid sphere indenting a flat elastic half-space modified appropriately for AFM indentation [189] is

$$f = \frac{4\sqrt{R}}{3} \frac{E}{(1-\nu^2)} (z - z_0)^{3/2} H(z - z_0) + \xi + \beta z, \quad (3.2)$$

where f is force applied, R is the radius of the indenting sphere, E is the Young's Modulus, ν is the Poisson ratio which is assumed to be 0.5 (implying incompressibility), z is the position of the indenter as represented internally by the AFM, z_0 is the reference contact point, H is the Heaviside step function, ξ and β are used to represent the offset and drift respectively that commonly occur during AFM indentation. The offset and drift terms are caused by either internal AFM noise or noise from the surrounding environment; they are the main differences between Equation 3.2 and Equation 2.34. The Heaviside function is necessary as the AFM only sees the movement of the cantilever base, regardless of whether it is in contact with a sample or not; if the function were not there, it would incorrectly appear in our analysis that,

before contact, the sample is being displaced with no force being applied. For elastic analysis, the offset and drift were found to be minuscule for the majority of files but in any case were subtracted from the data using the JPK (JPK Instruments, DE) data processing software provided by the AFM manufacturer. For viscoelastic analysis β was taken as 0 in order to not affect the constant deformation/force section of the data for relaxation/creep tests respectively.

Regarding the value of the Poisson ratio, an exact value is unknown but values of 0.3 - 0.5 have been suggested and used in the literature [35, 42, 140, 190]. (Note that ν may vary with a significant degree of spatiotemporal resolution *in vivo*.) In this study, the value of $\nu = 0.5$ was used, which implies that the material is assumed incompressible. By inspection of Equation 3.2 we can see that the lower the Poisson ratio, the higher our estimation of E will become (for a fixed ratio of force over displacement). As such, if the actual value of ν is lower than 0.5 then we would be underestimating E , whereas if ν is higher than 0.5 then we would be overestimating E .

The reference contact point z_0 is not known *a priori*. Various methods of identifying the contact point have been proposed [191, 192, 189]. In this study, the contact point was found using a qualitatively determined force threshold. A specific threshold was selected for each material tested by plotting the force/displacement curves for that material semi-logarithmically in the force axis and observing where the largest change in force took place – which corresponds to initial contact. After this the material displacement, δ , could be found using the relation $\delta = z - z_0$. An example of this ‘thresholding’ is shown in Figure 3.9A, where orange dashed line shows the force threshold intersecting the curve at a particular height, which is then taken as our point of contact. The main advantage of this method is its simplicity, both conceptually and practically. It’s key disadvantage is that it tends to overestimate the force at which the contact point is determined. However, as this is a minor systematic bias for all data, relative comparisons between fitted parameters are still valid.

3.5.5 Computation of Viscoelastic Response

As described in Section 2.3.3, in the case of viscoelastic testing the elastic-viscoelastic correspondence principle [50] can be used to derive the time-dependent analogue of Equation 3.2 for displacement controlled (relaxation) tests. Noting that $E = 3G$ for the incompressible case, where G is the shear modulus, the linear viscoelastic relaxation equation is repeated

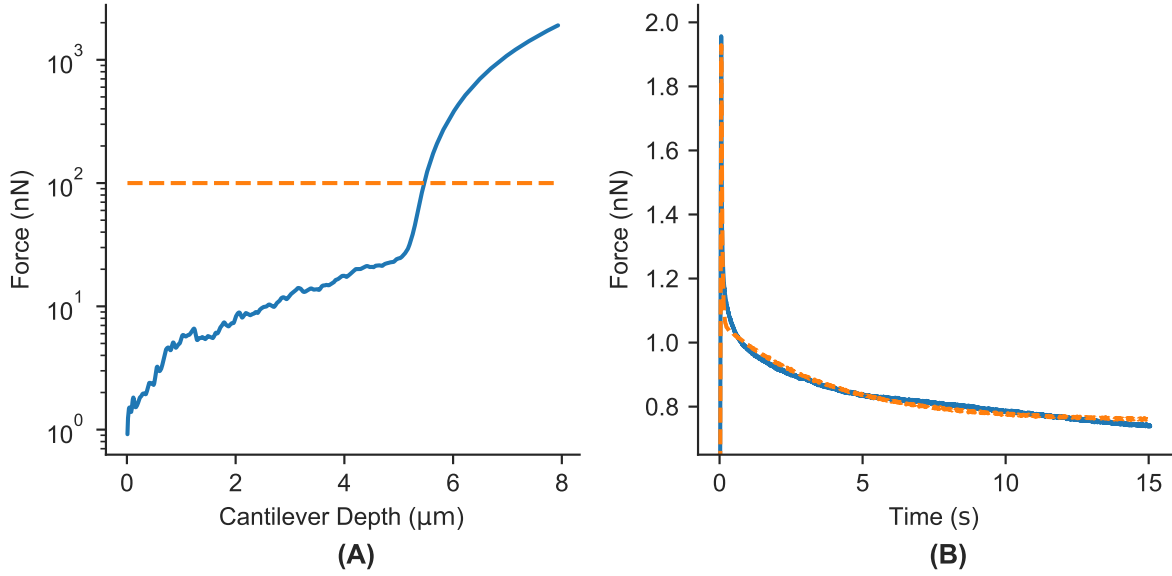


Fig. 3.9 A) Semi-logarithmic representative plot of force vs. depth for an ‘approach’ section of AFM curve, material is DM41 pectin. The orange dashed line shows the force threshold used to approximate the contact point. B) Representative plot of force vs. time showing the ‘approach’ and ‘hold’ sections of the AFM curve, with the predicted stress relaxation shown in the orange dashed line.

here for the reader’s convenience

$$f(t) = \frac{8\sqrt{R}}{3} \int_0^t G(t-\tau) \frac{d\delta^{3/2}(\tau)}{d\tau} d\tau, \quad (3.3)$$

where f , δ and G now represent dynamic functions and τ serves as an integration dummy variable. (Note this is the same as Equation 2.35.) A similar method can be followed [8] to derive the dynamic force-displacement relationship for stress controlled creep tests, this is already shown in Equation 2.36 but, as before, shown again here for the reader’s convenience

$$\delta^{3/2}(t) = \frac{3}{8\sqrt{R}} \int_0^t J(t-\tau) \frac{df(\tau)}{d\tau} d\tau, \quad (3.4)$$

where J is the material creep function and all other symbols have their previous meaning.

Now we have identified our contact point and offset, we can discard the data before contact (as the Heaviside function is not ‘switched on’ before that time), and the offset transform has already been applied. We also discard the ‘retract’ section where the AFM tip is leaving the sample as it is not accounted for in the elastic-viscoelastic correspondence principle. The key point regarding the above two equations is that we can use them ‘as-is’ without further modification (apart from discretisation, of course). Furthermore, the approach

used in the analysis here is far more flexible than other approaches used in the literature. For example, some authors have used assumptions of perfectly linear ramp and hold loading to simplify the above integral [8, 50]. However, the complex force/displacement feedback cycle used by the AFM meant it was not feasible to generate an accurate linear ramp. This motivated development of a more flexible method. To understand this more flexible method we first note that both equations can be solved using regular quadrature methods for arbitrary loading patterns, but this is usually prohibitively slow. Instead, we take advantage of the fact the both equations can in fact be viewed as convolutions, and there already exist highly optimised convolution algorithms available to us in Python. Therefore, to calculate the response to arbitrary force or displacement loading, a numerical convolution was performed using the NumPy Python package ('numpy.convolve'). This predicted response can then be subtracted from the actual response, and then squared, to form our squared-error cost function that is sent to the optimisation routine in order to find the most suitable set of parameters for a given model. The optimisation function used was 'scipy.optimize.least_squares', with the 'Trust Region Reflective algorithm' selected as, in trials, it was found to be the quickest to converge upon suitable solutions. A representative example fit is shown in Figure 3.9B. Computation of the viscoelastic response, and determination of model parameters from data, is discussed in significantly more detail in Chapter 4. In particular, Section 4.4.4.

3.5.6 Viscoelastic/Poroelastic Framework Evaluation

For a linear viscoelastic material, relaxation curves at different indentation depths will reduce to a single master curve when the following rescaling is applied

$$\frac{f(t) - f(t')}{f(0) - f(t')}, \quad (3.5)$$

where in our case $t = 0$ was recalibrated to be the moment that the AFM reached its force setpoint and t' was set to be 14 seconds after that, near the end of the relaxation hold. The poroelastic rescaling used was

$$\frac{f(t) - f(t^*)}{f(0) - f(t^*)}, \quad (3.6)$$

where $t^* = \alpha\delta$ as the tests did not generally reach a plateau within the time-frame of the experiment (see Moeendarbary et al. [193] and Strange et al. [194] for the more general case). The above curve is plotted against rescaled time $\bar{t} = t/\delta$. Also, as before, $t = 0$ was recalibrated to be the moment that the AFM reaches its force setpoint. δ was taken to be the average displacement occurring between 6 and 9 seconds into the experiment as a good approximation. The constant α was fixed for all curves and is arbitrary in the case of a

poroelastic material that reduces to a master curve – though it will introduce a ‘pinch-point’ where all the curves meet. This can be seen algebraically by converting t^* to rescaled time such that $\bar{t}^* = \alpha$ and noting that the numerator of Equation 3.6 will always be equal to 0 at this time point.

3.5.7 Viscoelastic Models

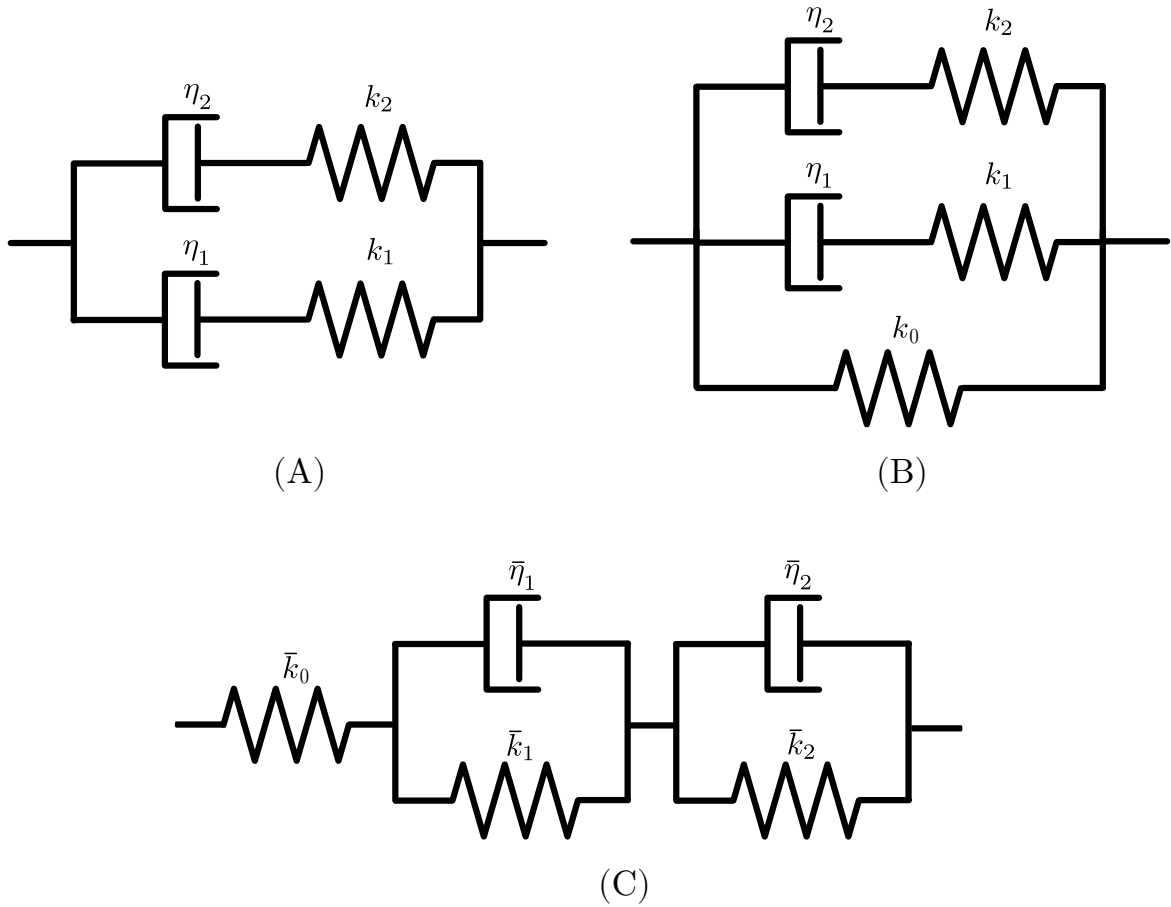


Fig. 3.10 A) 4 parameter Burgers model in relaxation form. B) 5 Parameter, 2 time-scale standard linear solid in relaxation form. C) 2 time-scale standard linear solid model as in previous, but in creep form. Alternate parameterisation is depicted by the bar over the glyphs.

The relaxation and creep moduli of the SLS2 model take the form of Prony series:

$$G(t) = G_0 + G_1 e^{-t/\tau_{r1}} + G_2 e^{-t/\tau_{r2}}, \quad (3.7)$$

$$J(t) = J_0 - J_1 e^{-t/\tau_{c1}} - J_2 e^{-t/\tau_{c2}}, \quad (3.8)$$

where τ_r and τ_c are relaxation and creep (retardation) time-scales respectively. Elastic/viscous ratios can be defined on the relaxation [50] and creep moduli in the following way:

$$(E/V)_G = G_{t \rightarrow \text{inf}}/G_{t=0} = \frac{G_0}{G_0 + G_1 + G_2}, \quad (3.9)$$

$$(E/V)_J = J_{t=0}/J_{t \rightarrow \text{inf}} = \frac{J_0 - J_1 - J_2}{J_0}. \quad (3.10)$$

In particular, the second ratio is acceptable due to the thermodynamic condition that there cannot be negative compliance so $J_0 > J_1 + J_2$. These ratios are depicted graphically in Figure 3.11. They are useful because they capture the ratio of static to dynamic behaviour in a material in a single number. Another shorthand value used in this chapter is the Instantaneous Shear Stiffness (ISS), which is equivalent to $G_{t=0} = G_0 + G_1 + G_2$ and $1/J_{t=0} = 1/(J_0 - J_1 - J_2)$. The ISS provides a convenient metric for comparison to studies which only reported elastic moduli or storage moduli.

For comparison with the canonical parameterisations of the spring-dashpot diagrams shown in Figures 3.10B and C, the following relationships are noted:

$$G_0 = k_0, \quad G_1 = k_1, \quad G_2 = k_2, \quad (3.11)$$

$$\tau_{r1} = \eta_1/k_1, \quad \tau_{r2} = \eta_2/k_2, \quad (3.12)$$

$$J_0 = 1/\bar{k}_0 + 1/\bar{k}_1 + 1/\bar{k}_2, \quad J_1 = 1/\bar{k}_1, \quad J_2 = 1/\bar{k}_2, \quad (3.13)$$

$$\tau_{c1} = \bar{\eta}_1/\bar{k}_1, \quad \tau_{c2} = \bar{\eta}_2/\bar{k}_2. \quad (3.14)$$

The parameters G and J are helpful as they are more in line with the literature and, in the case of G , explicitly remind us of the fact that they are dynamic shear moduli. The abstracted time-scale parameters are often useful parameters to associate with material deformation time-scales.

The Burgers model used here is the same as that given by Mainardi [195], and in its relaxation form is equivalent to two Maxwell units in parallel. Its relaxation modulus is written as:

$$G(t) = G_1 e^{-t/\tau_1} + G_2 e^{-t/\tau_2}, \quad (3.15)$$

which is similar to the SLS2 modulus in Equation 3.7 but does not have a plateau stiffness. This same model is sometimes referred to as a Generalised Maxwell model (truncated to two time-scales). Its spring-dashpot schematic can be seen in Figure 3.10A, and the following

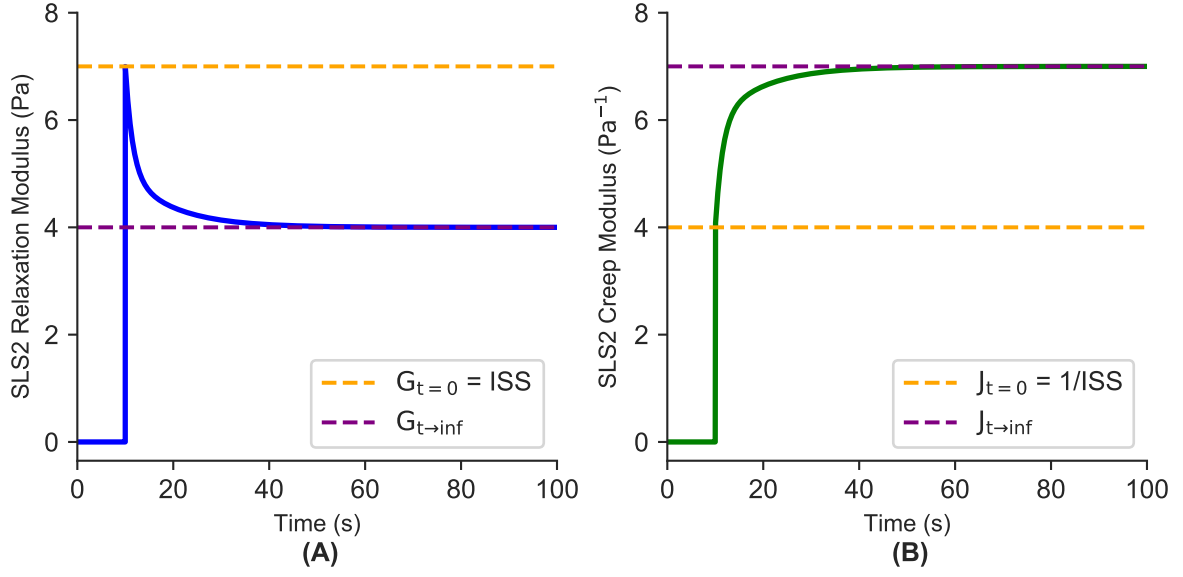


Fig. 3.11 A) SLS2 relaxation modulus response to a unit step at $t = 10$ s. $G_{t=0}$ and $G_{t \rightarrow \infty}$ are shown in dashed lines. Parameters used are $G_0 = 4$ Pa, $G_1 = 2$ Pa, $\eta_1 = 3$ Pa s, $G_2 = 1$ Pa, $\eta_2 = 10$ Pa s. B) SLS2 creep modulus response to a unit step at $t = 10$ s. $J_{t=0}$ and $J_{t \rightarrow \infty}$ are shown in dashed lines. Parameters used are $J_0 = 7$ Pa, $J_1 = 2$ Pa, $\eta_1 = 3$ Pa s, $J_2 = 1$ Pa, $\eta_2 = 10$ Pa s.

relationships with the canonical parameters are noted:

$$G_1 = k_1, \quad G_2 = k_2, \quad (3.16)$$

$$\tau_{r1} = \eta_1/k_1, \quad \tau_{r2} = \eta_2/k_2, \quad (3.17)$$

Lastly, an Instantaneous Shear Stiffness (ISS) metric can also be defined for the Burgers model. As above, it is defined as $G_{t=0}$.

3.6 Results and Discussion

3.6.1 Acquiring Force-Displacement Proxy Relationships

Due to the arbitrary nature of the AFM's displacement coordinate system and the absence of a closed loop control system on sample deformation, only a target force can be prescribed, not a target displacement. To ensure that tests across all gel types were done at comparable displacements in case of non-linearities, a number of forces were trialled on all the different HG gels until force ranges were found that covered between $1 \mu\text{m}$ and $4 \mu\text{m}$ displacement. Once the upper and lower limits of these ranges were identified, a higher resolution force-displacement mapping was obtained by finding several points on each gel and performing

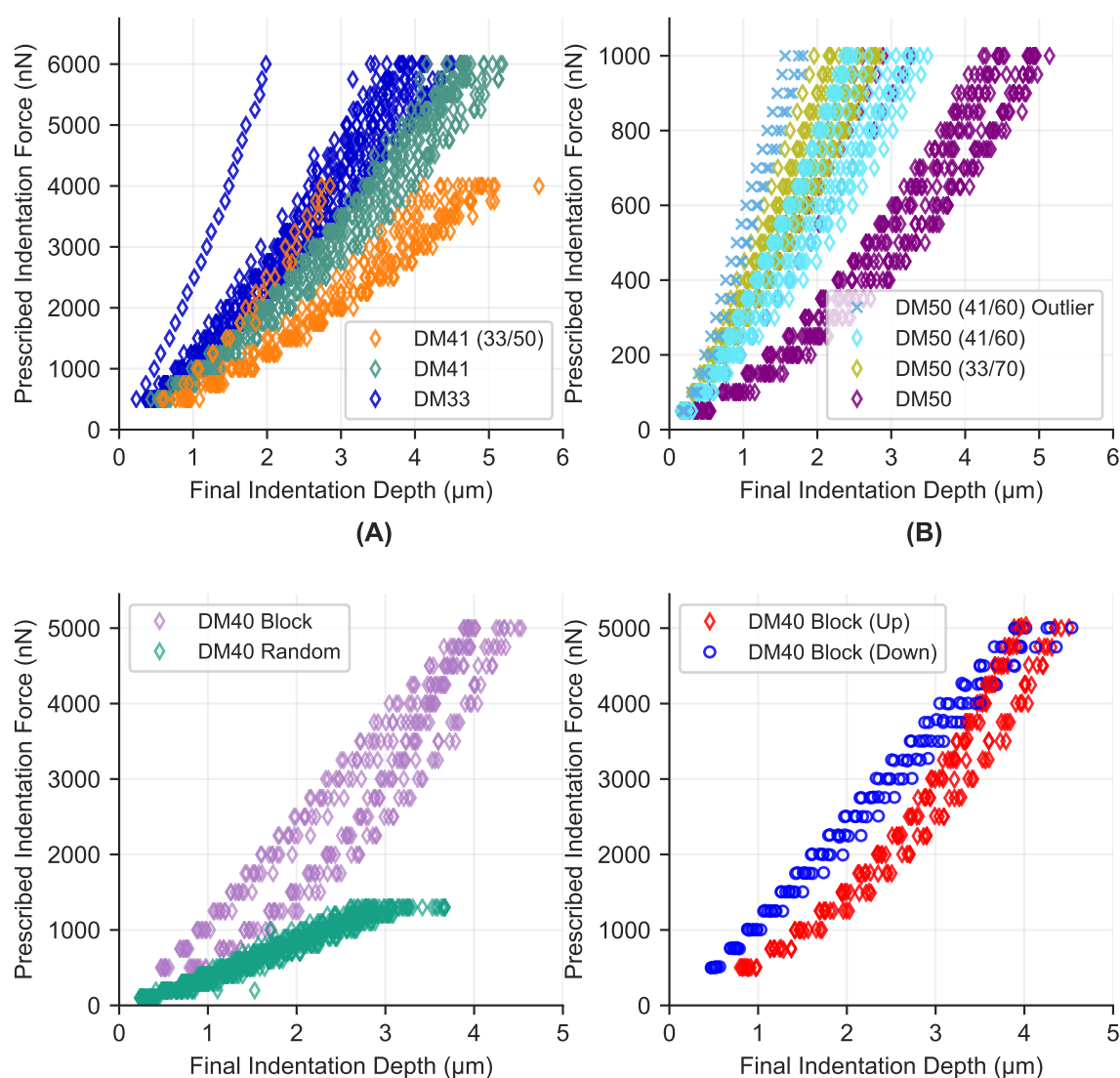


Fig. 3.12 A), B) and C) Plots of prescribed indentation forces against resultant indentation depth for the full variety of pectin gels tested. D) The prescribed indentation force versus the resultant indentation depth for the DM40 Block gel type, with markers coloured according to whether they were incrementing up or down the force range at a specific point on the gel.

repeated elastic indentations, alternately moving up or down the force range at each new point to investigate whether pre-stressing or plastic deformation was affecting the results significantly. Three (or more where time allowed) points were tested on six different gel samples, so there were a minimum of 18 points tested for each different gel type. The points shown in Figures 3.12A, B, C and D have been extracted from the final sample of the ‘approach’ phase of the AFM curves (see Figure 2.15 for reference). Note that brackets after a DM type indicates a mixture made up of the bracketed DM types with a resultant bulk DM

of that specified. For example, DM50 (41/60) is a pectin mixture with average DM50 but made up of DM41 and DM60 combined.

As stated above, the purpose of the experiment was to obtain force-displacement proxy relationships. However, some interesting observations were noted. Qualitatively, the general elastic strengths of all the gels agree well with the storage moduli presented by Fraeye et al. [86] and Ngouémazong et al. [172]. In Figure 3.12B, there is a stiffer grouping of three points in DM50 (41/60). The three outliers were found to all originate from the same gel sample. Although the gel sample thicknesses were on the order of millimetres it is likely that this particular sample was too thin and thereby increased the apparent stiffness, so it was duly noted to ensure adequate thickness of at least several millimetres in future samples. There is also one DM33 outlier and two DM41 (33/50) outliers, shown in Figure 3.12A, which were much stiffer than the other points, likely due to the testing point being too close to the edge of the sample where it was thinner so thereafter, more care was taken to test points closer to the centre of the sample.

In Figure 3.12C, a qualitatively bimodal behaviour was observed in the DM40 Block HG gels. Colorising the data points according to the direction of force traversal (up/down the range of test forces) identified the reason for this. The stresses at the higher end of the force range (5000 nN) stiffened the HG at subsequent lower forces. The pre-stressing effect appears to be caused only at the upper range of forces as both up and down directions overlap at the top of the range but not at the bottom of the range. Due to this behaviour, only the data going up the force range was used in subsequent analysis. It is plausible that the specific, highly blockwise configuration of the ionic cross-linking junctions in the DM40 block pectin becomes somehow further entangled by the higher stresses, giving rise to the apparent increase in stiffness at lower forces.

3.6.2 HG Is Linear Viscoelastic Under Micro-indentation

During indentation of HG gels, there may be several physical modes of deformation which occur simultaneously. These could include near-instantaneous extension and contraction of the pectin chain network, rearrangement of the network via breaking and reforming of ionic bonds, and flow of solution through the network. A number of *in vitro* pectin studies have found their samples to behave in accordance with linear viscoelasticity, and some others have assumed it [90, 171, 172, 196]. However, *in vitro* cellulose-pectin composites have been found to exhibit poroelasticity [173, 197] and it has been suggested that pectin acts a mediator of porosity *in vivo* [198]. Further, the dominant physical mechanisms observed may

depend not just on the pectin formulation, but also the length and time-scales of the testing method used [194, 26]. Thus, before a thorough comparison between different DM HG gels could be made, the appropriate theoretical framework to analyse the rheological data had to be identified.

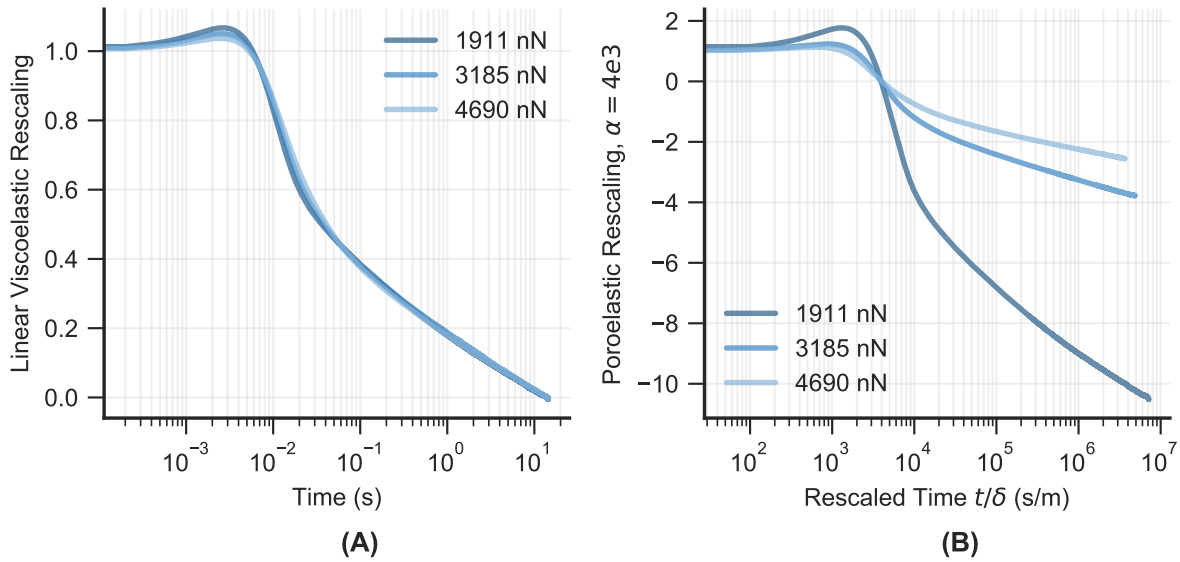


Fig. 3.13 A) Averaged relaxation data from DM41 HG at 2 μm , 3 μm and 4 μm rescaled according to the linear rescaling formula, x-axis is log scale. B) The same data rescaled according to the poroelastic rescaling formula, x-axis is log scale.

To achieve this, indentation depth data from the DM41 gel elastics tests were averaged and linear interpolation was used to estimate the forces that would yield the desired indentation depths. 15 second AFM force relaxation tests, in which deformation was held constant while force was monitored over a prescribed time, were performed on six DM41 gels at 2 μm , 3 μm and 4 μm indentation depths (corresponding to prescribed forces of 1911 nN, 3185 nN and 4690 nN respectively). These forces corresponded well to the indentation depths predicted by the first set of experiments. Every relaxation test on a specific gel sample was done at a unique point. Suitable rescalings were then applied to the data to assess the suitability of a poroelastic or viscoelastic theoretical framework (See Methods, Equations 3.5 and 3.6). The poroelastic scaling did not collapse to a master curve except at the start and a single pinch-point (Figure 3.13B); the pinch-point at $t/\delta = 4e3 \text{ s m}^{-1}$ is due to the selection of the rescaling parameter, α . If the gels were poroelastic, the curves would collapse to a master-curve regardless of the value of α . However, by further varying of α , this was definitively found not to be the case. Qualitatively, the linear viscoelastic rescaling resulted in a clear master-curve collapse (Figure 3.13A) suggesting it is the correct framework for subsequent

analysis. A possible explanation for this can be constructed using scaling arguments. The experimental length scale here is $L = \sqrt{R\delta} \sim 10^{-6}$ m. As L^3 is many orders of magnitude smaller than L^2 , the force required for the bulk displacement of water volume may be less significant than the direct pressure applied onto the material by the indenter's surface. Further, it may be that the permeability of the gel is high enough that there is negligible obstruction to fluid flow. A third explanation, similar to that proposed by Zhao et al. [26] for alginate relaxation with sufficient sample size, could be that the non-poroelastic behaviour is due to ionic cross-links reforming at a much faster rate than water migration. Unfortunately, average pore-size and permeability data for pectin of similar composition to that tested here could not be found in the literature. Having said this, it has been shown that sucrose-containing low DM pectin and pectin-alginate blends have relatively large pore sizes, in the order of 100 nm. If similar large pore sizes exist in the low DM gels tested here than that would go a long way to accounting for the absence of observable poroelastic behaviour.

In summary, these data indicate that HG gels behave as linear-elastic viscoelastic solids under micro-indentation. Subsequent tests on all gel types were conducted at $2\ \mu\text{m}$ to ensure data were in the linear viscoelastic range. Lastly, it should be noted that these results, and other similar tests from the literature, do not preclude *in vitro* pectin poroelasticity in all cases. Although very high pectin concentrations ($>30\%$ w/w, which would be comparable to the concentration in the plant cell wall) of high DM pectin have been found to be linear at small deformation [196], reducing the DM and raising the concentration of divalent ions may induce the gel closer to the syneresis-like phase sometimes alluded to in the literature [103] – in which permeability is likely to decrease significantly.

3.6.3 A Modelling Approach to *in vitro* Pectin Viscoelastic Analysis

As discussed earlier, much of the pectin testing literature has been done using a model-free DMA approach. Whilst informative, the fitting of viscoelastic models to data can yield greater insight into the material and improve commensurability across studies. In this section, inspiration is drawn from the early pectin investigations which used Generalised Maxwell and extended Burgers-type models to capture the creep and relaxation behaviours observed [90, 155, 158, 159]. The simplest two possible variants of the models tested in the above studies are a Generalised Maxwell model (two Maxwell units in parallel, depicted in Figure 3.10A) and a 2 time-scale Standard Linear Solid (SLS2, two Maxwell units in parallel, both in parallel with single spring which provides a relaxation stress plateau, shown in Figure 3.10B). The 2-unit Generalised Maxwell model is often referred to as the Burgers model and that is the term that is used in the remainder of this Chapter. Further, the Burgers

model can be considered a special case of the 2 time-scale Standard Linear Solid model where the spring $G_0 = 0$ Pa. See Equations 3.7 and 3.15 for comparison of their mathematical form. Figure 3.10A shows the spring-dashpot schematic of the Burgers model, whilst Figures 3.10B and C show the schematic of the SLS2 model in relaxation and creep form respectively. The distinction between having a stress relaxation plateau (e.g. the SLS2 model) and not having one (e.g. the Burgers model) is sometimes viewed as the defining characteristic of whether a material is a viscoelastic solid (with plateau) or a viscoelastic fluid (no plateau).

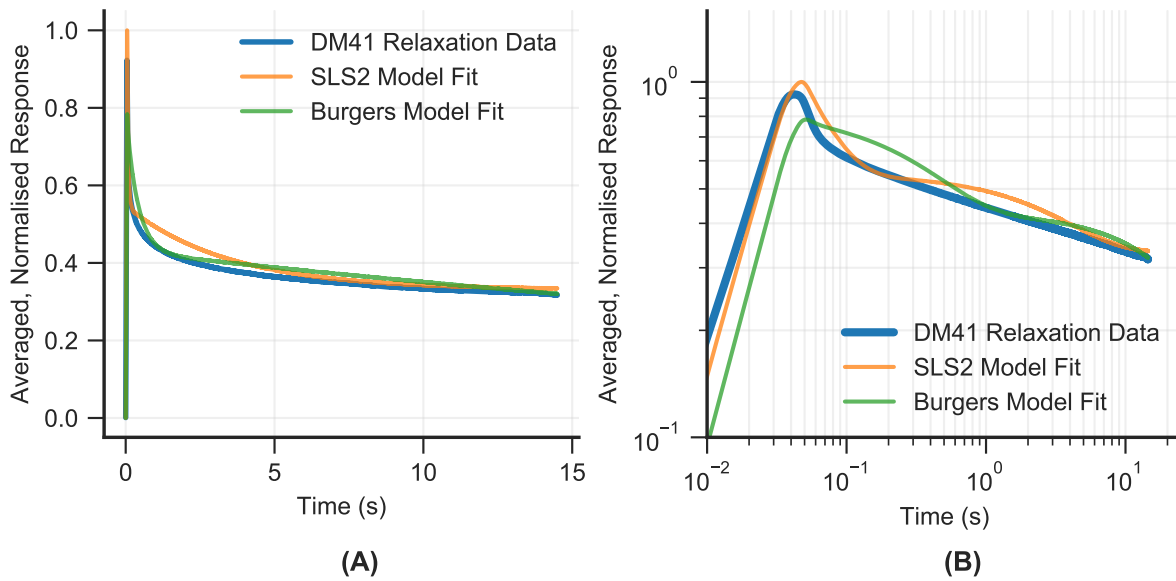


Fig. 3.14 A) Averaged relaxation data from all tests on DM41 HG at a depth of 2 μm , the averaged predicted relaxation response of the fitted Burgers model, and the averaged predicted relaxation response of the fitted SLS2 model. B) The same data as in A) but plotted in log-log scale.

The two models were fitted to all relaxation data samples from the DM41 gel at 2 μm indentation depth ($N = 20$ across 6 gel samples). The averaged data, along with the averaged responses of the two models is shown in Figure 3.14A. As can be seen from qualitative examination of the figure, the SLS2 model appears to fit better at very short and longer time-scales (although it does overshoot at the very beginning), whereas the Burgers model appears to fit better during the transition at approximately $t = 1$ s (and undershoots at the beginning). The averaged data was plotted in log-log scale for further analysis and from this (Figure 3.14B) it can be seen that the gel behaves as a power-law for much of time past $t = 0.5$ s. This is an important observation – it implies that our exponential-based models are only an approximation of the actual behaviour. Whilst two pectin studies have observed a power-law frequency dependence and fitted an empirical power-law model to the data with differing degrees of success [165, 199], the use of empirical models has its own set of

drawbacks. The power-law relaxation and its implications are further discussed in Chapter 4, in which the data is revisited with a more powerful modelling framework. Quantitatively, the averaged, normalised sum of squared residual error for the SLS2 model was 42.26 and the error for the Burgers model was 45.42. In the end it was decided to use the SLS2 model for subsequent investigations due its quantitatively better fit, and the fact that it was the more general model of the two – the fitting procedure could always find that the best fit plateau was 0.0 if appropriate. One drawback of the AFM method used here is that relaxation times longer than 15 seconds were found to be unfeasible due to the need for greater acoustic and vibration isolation, small amounts of piezo creep also appeared to occur during some of the longer indentations [200]. This meant that during the model fitting process, the models may have been implicitly extrapolating the plateau behaviour.

3.6.4 Elastic and Viscous SLS2 Parameters Are Inversely Correlated with DM

As discussed, the works of Ström et al., Fraeye et al. and Ngouémazong et al. investigated the effect of changing DM and DB on pectin-calcium gels using a model-free DMA approach. Whilst Ström et al. and Ngouémazong et al. only presented the storage modulus data, Fraeye et al. also presented the loss modulus G'' data but only for a subset of tested pectin gels [86, 171, 172]. For better characterisation of pectin rheology and potential insight into pectin's plant developmental role, it was decided to pursue a model-based approach to viscoelastic analysis. To assess the viscoelastic properties of the different pectin types available to us, 15 second AFM force relaxation tests were performed on HG gels with different DM but the same amount of available calcium ($\bar{R} = 1$, on the calcium saturation threshold). Tests on all gels were conducted at an indentation depth of 2 μm , where necessary forces to attain this depth were found by the previously discussed analysis of the elastic data. Resulting curves were analysed using the SLS2 model. The fitting results for testing gels of different DM are shown in Figures 3.15 and 3.16, and for testing gels of different DB in Figures 3.17 and 3.18. Mean parameters +/- standard error are also shown in tables 3.1 and 3.2. Parametric group-wise, and non-parametric pair-wise statistical analysis is summarised in Appendix D.

The first point of interest is a comparison of the absolute values of instantaneous shear stiffness (ISS) to the most closely related metric in other studies, the storage modulus, for the pure DMs tested (33, 41 and 50). The stoichiometric ratio \bar{R} used by Ström et al. [171] and Fraeye et al. [86] for comparable DM pectins was significantly lower (0.3 and 0.2

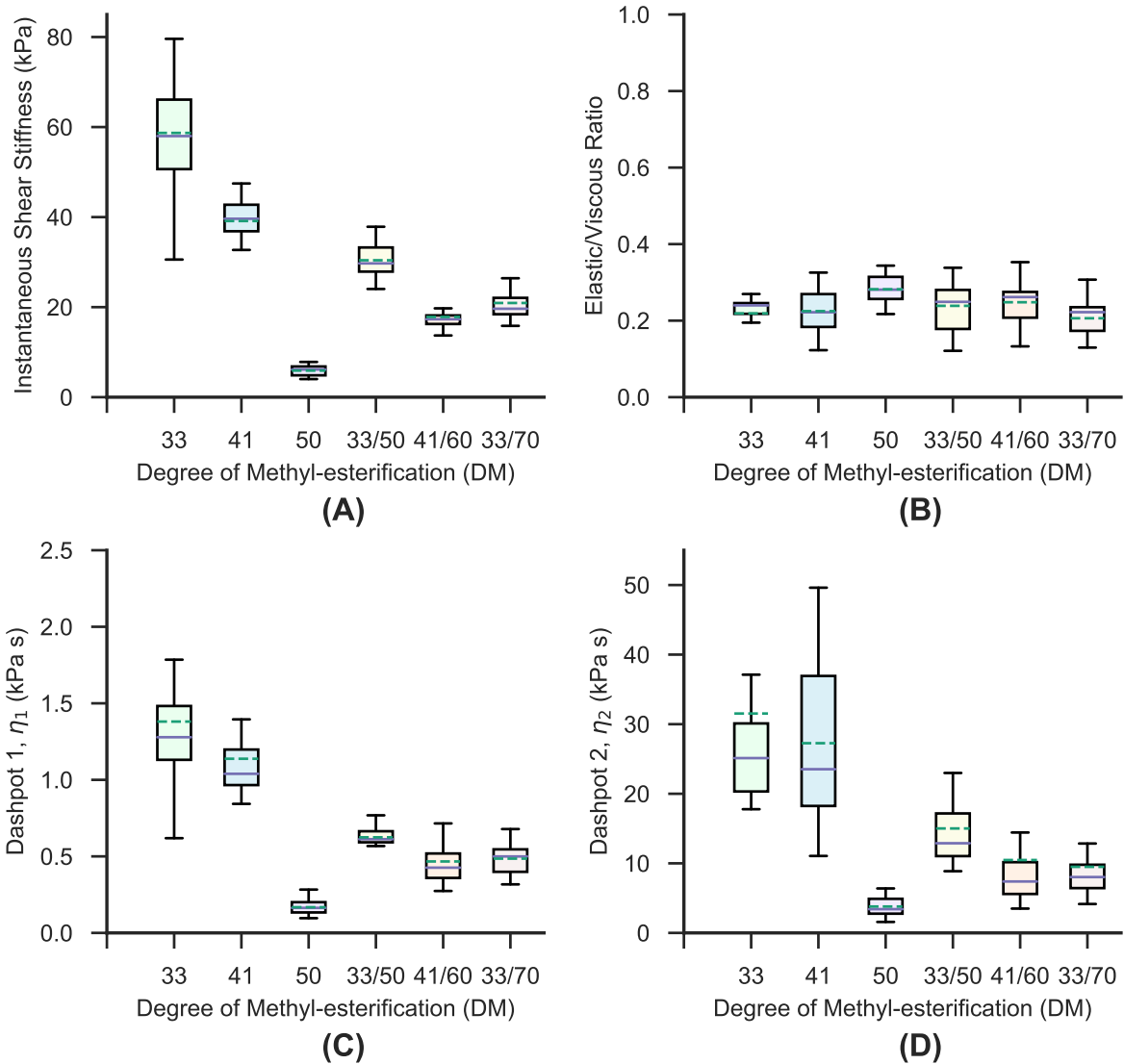


Fig. 3.15 SLS2 model parameters for the HG and HG mixtures tested. 33/50 represents the DM41 equivalent mixture, 41/60 and 33/70 represent the two DM50 equivalent mixtures. Continuous horizontal lines represent the median of the data, dashed lines represent the mean. Edges of the box represent the upper and lower quartiles and the whiskers represent the range of the observations.

respectively) which appears to have resulted in reported storage moduli of approximately an order of magnitude less than the ISS found here. However, Ngouémazong et al. [172] included data at $\bar{R} = 1$ and our results agree well at DM33 and DM41, though a slightly sharper decrease in ISS at DM50 was observed compared to their reported storage modulus. Indeed, the sharp drop in ISS observed is particularly dramatic. Whilst the mean ISS drops only 33% from DM33 to DM41, it drops 85% from DM41 to DM50. Looking at both dashpot values of the SLS2 model (Figures 3.15C and D), a similar qualitative pattern can

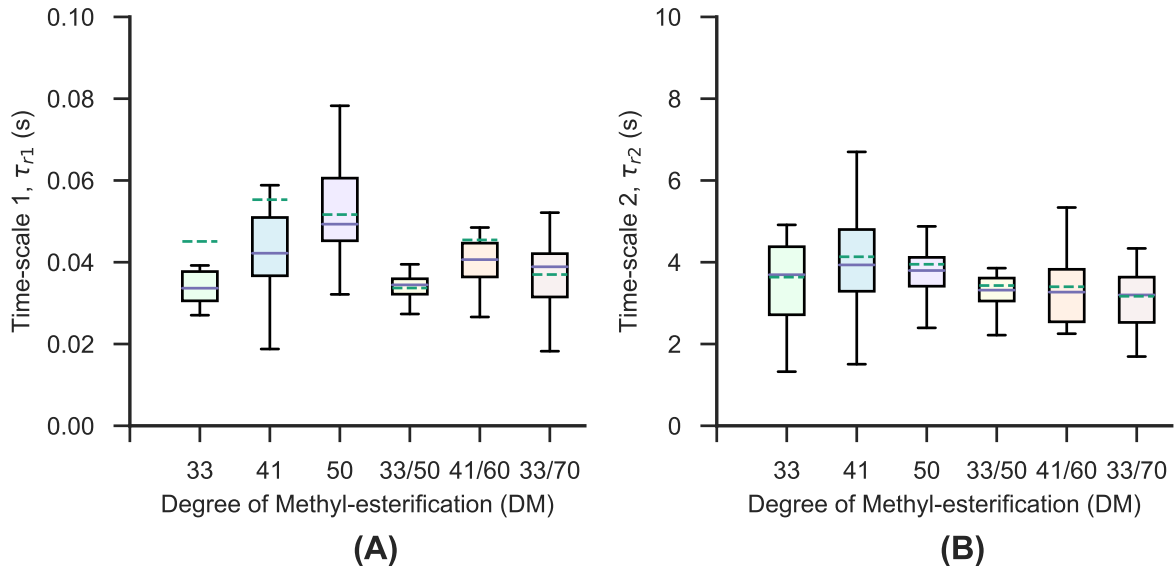


Fig. 3.16 SLS2 model relaxation time-scales for the HG and HG mixtures tested. 33/50 represents the DM41 equivalent mixture, 41/60 and 33/70 represent the two DM50 equivalent mixtures. Continuous horizontal lines represent the median of the data, dashed lines represent the mean. Edges of the box represent the upper and lower quartiles and the whiskers represent the range of the observations.

| HG DM | ISS (kPa) | η_1 (kPa s) | η_2 (kPa s) | τ_1 (s) | τ_2 (s) | E/V |
|-------|-----------------|------------------|------------------|-----------------|-----------------|-----------------|
| 33 | 58.7 ± 3.2 | 1.38 ± 0.15 | 31.5 ± 4.8 | 0.05 ± 0.01 | 3.64 ± 0.37 | 0.22 ± 0.01 |
| 41 | 39.1 ± 1.2 | 1.14 ± 0.09 | 27.3 ± 2.9 | 0.06 ± 0.01 | 4.13 ± 0.29 | 0.22 ± 0.01 |
| 50 | 5.90 ± 0.22 | 0.17 ± 0.00 | 3.79 ± 0.29 | 0.05 ± 0.00 | 3.95 ± 0.19 | 0.28 ± 0.00 |
| 33/50 | 30.4 ± 0.8 | 0.62 ± 0.03 | 15.0 ± 1.3 | 0.03 ± 0.00 | 3.43 ± 0.18 | 0.24 ± 0.01 |
| 41/60 | 17.8 ± 0.8 | 0.47 ± 0.04 | 10.5 ± 2.0 | 0.05 ± 0.00 | 3.40 ± 0.21 | 0.25 ± 0.01 |
| 33/70 | 20.9 ± 1.8 | 0.49 ± 0.02 | 9.50 ± 0.98 | 0.04 ± 0.00 | 3.17 ± 0.16 | 0.21 ± 0.00 |

Table 3.1 Mean SLS2 model derived parameters for all HG types +/- standard error. 'E/V' is Elastic/Viscous Ratio. '33/50' is the DM41 mixture. '41/60' and '33/70' are the two DM50 mixtures.

be seen. Furthermore, the elastic/viscous ratios shown in Figure 3.15B suggest that viscous effects varied approximately proportionally to elastic effects, an observation corroborated by the small subset of storage and loss moduli data presented by Ngouémazong et al. [172]. Although the variation of the elastic/viscous ratio means was fairly low, a groupwise ANOVA statistical test suggested a significant difference between the gel types tested ($p < 0.001$, see Appendix D for more details). Regarding the SLS2 time-scales, shown in Figures 3.16A and B, τ_1 appears somewhat correlated with DM whilst τ_2 is fairly constant for all three pure DMs. ANOVA tests of both τ_1 and τ_2 suggested that the differences observed across gel types may not be statistically significant ($p > 0.001$ for both time-scales); however, the binary nature of statistical significance tests can obscure subtle observations so the statistical tests

are interpreted here with caution. It is difficult to physically interpret a possible correlation between τ_1 and DM as the time-scales involved are very close to the approximate ramp time. The indentation speed used was $50 \mu\text{m s}^{-1}$ and the depth was approximately $2 \mu\text{m}$, so the time for indentation ramp was approximately 0.04 s. The fact that it was the force that was prescribed, not depth, complicates things further as there may be subtle interactions between force and displacement via the AFM's control system. Another reason for the difficulty of physical interpretation of SLS2 time-scales is the fact that we know from Figure 3.14B that HG displays power-law relaxation behaviour, so the two time-scales detected by the model are only approximations of the distribution of time-scales observed. This is discussed further in Chapter 4, in which a simpler yet more powerful model is fitted to the pectin data.

The tight coupling between elastic and viscous parameters has also been seen in previous studies where calcium and DMA frequency was varied as opposed to DM [86]. This coupling is suggestive of a single unified physical mechanism for both short-time deformation and longer-time relaxation/dissipation processes. The most parsimonious candidate for this mechanism is the breaking and reforming of ionic chains as it would successfully explain both the negative elastic and viscous correlations with DM, and the tight coupling of elastic and viscous properties themselves. Interestingly, this was the same conclusion reached by Zhao et al. [26] in their rheological study of pectin's algal equivalent, alginate, when the alginate was gelled ionically. Although speculative, it is a useful thought experiment to ask, assuming that the above hypothesis is true, what do the elastic and viscous parameters of our model represent physically? Perhaps the elastic, or approximately elastic, material response is determined by the presence of short but stable ionically bonded junctions whilst the longer time-scale processes are determined by the contiguously longer junctions. In this scenario it might be expected that HG with a more random pattern of de-esterification would appear more elastic due to the preponderance of shorter ionic junctions, whilst more blockwise de-esterified HG would appear more viscous due to the abundance of longer ionic junctions. This hypothesis would also suggest that in the above experiments, the concentration of short and long bonds changed proportionately across the different DMs. This physical hypothesis is discussed further in Section 3.6.6.

As noted above, a clear non-linear relationship between pectin DM and the coupled elastic and viscous parameters was observed. The rapid drop off in ISS and viscosity of both dashpots at approximately DM50 and above may be due to the minimum number of consecutive calcium bonds (approximately 6-20) required to form a stable inter-chain bond [98, 99, 96]; higher DM gels have a much lower probability of attaining the minimum

number of consecutive bonds required for consistent stable ionic junction formation. Initial tests were attempted on higher DM (60 and 70) gels but they were found to be so soft as to be incomparable to lower DM gels at similar indentation depths. This DM threshold may be analogous to a ‘percolation threshold’ which is a type of gel/solution transition point [201]. Intriguingly, the *Arabidopsis* hypocotyl study by Derbyshire et al. [149] found that a minimum DM of approximately 60% was required for hypocotyl elongation, suggesting the presence of a pectin-mediated percolation threshold *in vivo* that is remarkably close to that found in this *in vitro* study. The consequences of this non-linearity on mixed DM gels are investigated in Section 3.6.5.

3.6.5 Pectin Strength vs. DM is Non-Linear – Consequences For Mixed DM Gels

For the reasons discussed in Section 3.4, we wanted to build on the previous results in a more developmentally relevant direction. To this end, we generated two mixed gels with an effective DM50, one using a combination of DM33 and DM70, and another using a combination of DM41 and DM60. We also generated one mixed gel with an effective DM41 using a combination of DM33 and DM50 pectin. These were subjected to the same AFM force relaxation tests and SLS2 model fits as above to investigate whether their mechanical properties would be similar to the homogeneous DM pectin gels. The resulting data is summarised in Table 3.1 and Figures 3.15 and 3.16. Parametric group-wise, and non-parametric pair-wise statistical analysis is summarised in Appendix D.

As with the pure DMs, the elastic and viscous properties were found to be coupled across gel mixtures, as shown in Figure 3.15. Given the coupling between elastic and viscous parameters, we focus our discussion in this paragraph on the ISS metric for simplicity. The ISS of the gel mixtures were found to be significantly different to their effective homogeneous DM counterpart (pairwise ISS p-values between pure gels and mixtures were all $p < 0.001$). Comparing ISS: the effective DM41 was 22% more compliant than pure DM41, the effective DM50 (41/60 mix) was 202% stiffer than the pure DM50 gel, and the effective DM50 (33/70 mix) was 255% stiffer than the pure DM50 gel. These differences may be explained by the non-linear relationship between pectin DM and elastic/viscous properties discussed above. Given that pure DM50 ISS (mean 5.9 kPa) is roughly an order of magnitude less stiff than DM41 (mean 39.1 kPa) and DM33 (mean 58.7 kPa), and DM60 and DM70 have almost negligible stiffness in comparison to those two gels, it makes sense that a DM volume fraction

mix of the 41/60 or 33/70 would be significantly stronger than DM50 alone. (Indeed, the fact that the DM50 mixtures' mechanical integrity is dominated by the low DM contribution explains why the DM50 mixture based on DM33 was slightly stronger than the DM50 mixture based on DM41, as DM33 is slightly stronger than DM41.) The same phenomenon in reverse explains the relative weakness of the effective DM41 mixture. We can try and quantify this. Using the DM50 (41/60) mixture for example, the mass fraction, ϕ , of HGs used for the mixtures were found as follows

$$50 = 41\phi + (1 - \phi)60, \quad (3.18)$$

yielding 0.526 (3 d.p.). Multiplying this by the experimentally determined ISS for DM41 and assuming the DM60 ISS is negligible:

$$ISS_{41/60} = ISS_{41}\phi + (1 - \phi)ISS_{60} \approx 20.6 \text{ kPa}, \quad (3.19)$$

which is approximately 15% greater than the actual experimental mean value found for that mixture, which was 17.8 kPa. Repeating the same calculation for the other two mixtures estimates $ISS_{33/70} \approx 31.8 \text{ kPa}$ (experimental mean was 20.9 kPa) and $ISS_{33/50} \approx 33.8 \text{ kPa}$ (experimental mean was 30.4 kPa). Although the hierarchy of magnitudes of mixtures' ISS is correctly found by these rough calculations, $ISS_{41/60} < ISS_{33/70} < ISS_{33/50}$, they all overestimate to some extent and the DM mixture made of DMs of the largest difference is overestimated the most. Perhaps there is a physically manifested lack of ionic bonding synergy between two HGs with different DMs, and the bonding synergy reduces as the DM difference increases. This hypothesis certainly goes some way towards explaining the discrepancy between calculated and experimentally observed ISS values of mixtures.

3.6.6 Elasticity, Not Viscosity, Correlated with DB

In order to further validate the AFM viscoelastic testing methodology of *in vitro* pectin and explore the effects of different de-esterification patterns on the parameters of the SLS2 model, two DM40 pectins de-esterified by different means were tested. Although not found explicitly for this work, in a previous study by the same lab that made the pectin pre-mixtures, the pectin de-esterified by alkali was estimated to have a DB of 39% whilst the pectin de-esterified by highly processive PME derived from Valencia orange was estimated to have a DB of 95% [171]. As exact values were not found for this study, the two gels are referred to as 'random' (for alkali de-esterified) and 'block' (for PME de-esterified) herein. As before, 15 second AFM force relaxation tests at a depth of 2 μm were carried out on six samples of each

pectin type with at least 3 unique points tested on each gel sample, with necessary prescribed forces found via interpolation of the data in Figure 3.12C. The results of the SLS2 fitting are summarised in Table 3.2 and Figures 3.17 and 3.18. Parametric and non-parametric statistical analysis is summarised in Appendix D

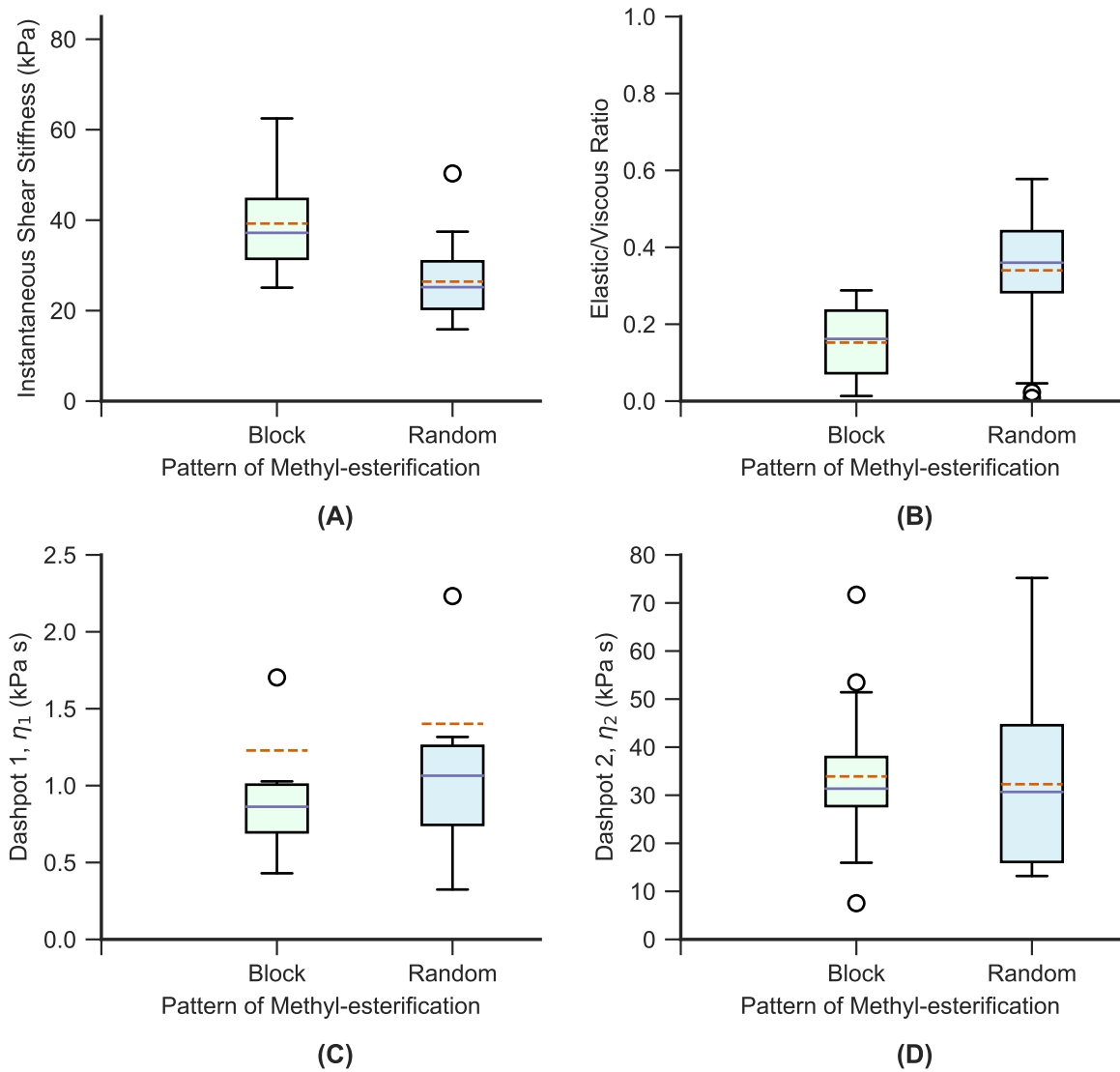


Fig. 3.17 SLS2 model parameters for the block and random de-esterified pectins tested. Continuous horizontal lines represent the median of the data, dashed lines represent the mean. Edges of the box represent the upper and lower quartiles and the whiskers represent the non-outlier range of the observations. Open circles are considered outliers as they are greater than $1.5 \times (\text{interquartile range})$ distance away from the upper or lower quartiles.

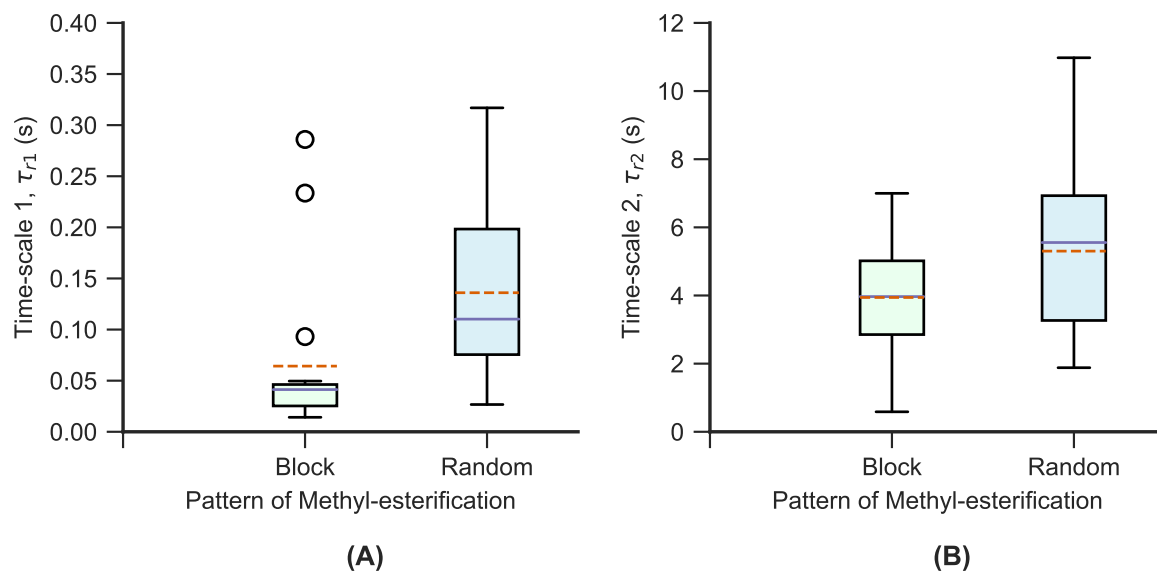


Fig. 3.18 SLS2 model relaxation time-scales for the block and random de-esterified pectins tested. Continuous horizontal lines represent the median of the data, dashed lines represent the mean. Edges of the box represent the upper and lower quartiles and the whiskers represent the non-outlier range of the observations. Open circles are considered outliers as they are greater than $1.5 \times$ (interquartile range) distance away from the upper or lower quartiles.

| HG DB | ISS (kPa) | η_1 (kPas) | η_2 (kPas) | τ_1 (s) | τ_2 (s) | E/V |
|--------|----------------|-----------------|-----------------|-----------------|-----------------|-----------------|
| Block | 39.3 ± 2.5 | 1.23 ± 0.26 | 33.9 ± 3.6 | 0.06 ± 0.01 | 3.94 ± 0.43 | 0.15 ± 0.00 |
| Random | 26.4 ± 1.7 | 1.40 ± 0.26 | 32.3 ± 3.5 | 0.14 ± 0.01 | 5.30 ± 0.53 | 0.34 ± 0.01 |

Table 3.2 Mean SLS2 model derived parameters for both pectin types \pm standard error. E/V is Elastic/Viscous Ratio.

As before, the absolute values of ISS agree well with the storage moduli previously reported in a study by Ngouémazong et al. [172], and are approximately an order of magnitude greater than that found by Ström et al. [171] who used a much lower calcium concentration. The key relative observation is that the block pectin was significantly stiffer than the random pectin (parametric $p < 0.001$, non-parametric $p = 0.0069$). This is likely due to the increased number of stronger, longer contiguous ionic junction zones. However, unlike the different DM mixtures tested, where the interquartile range of elastic/viscous ratios overlapped at least a small amount, the random elastic/viscous ratio was significantly higher than the block one (parametric and non-parametric $p < 0.001$), and both dashpot means and medians were similar for both gel types (parametric and non-parametric $p > 0.001$). Indeed, whereas the largest drop in mean elastic/viscous ratio in the previous test was 22% from DM50 to DM33, the difference in mean elastic/viscous ratio between the block and random pectins was found to be 55%. The reported ratios support the hypothesis discussed above whereby

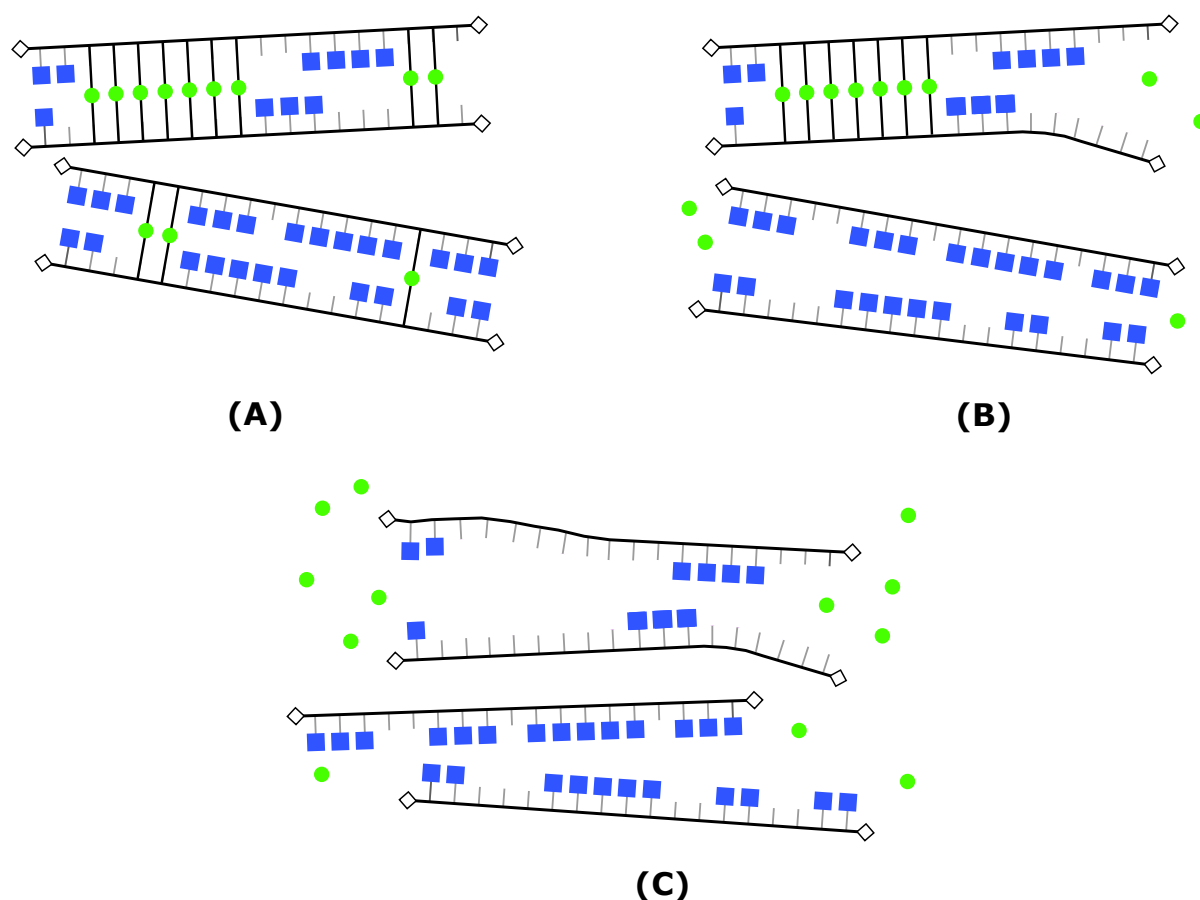


Fig. 3.19 Schematic diagrams of the proposed physical behaviour of pectin chains during indentation. Blue squares are methyl groups, green circles are calcium bonds, sticks are de-esterified pectin sections that have not bonded and have a single negative ionisation. De-esterified carboxyl groups repel each other due to their single positive charge. A) Two pairs of HG pectin chains before indentation, one has 1 strong linkage (7 ionic bonds) and 1 weak linkage, the other has two weak linkages. B) The same pectin chains at a short time-scale after indentation – the weak bonds have been broken. C) The same pectin chains after prolonged indentation, at longer time-scale. Stronger bond is now also broken.

a larger number of short bonds break and reform at very small time-scales and contribute to an apparent elasticity, whilst longer bonds break and reform over longer time-scales contributing to the observed relaxation. As predicted, the block pectin is more dominated by longer time behaviour (longer ionic junction zones) whereas the random pectin is more dominated by elastic short time behaviour (shorter ionic junction zones). Lastly, there were more outliers observed in the block and random pectin gels, marked on the plots by open circles, as compared to the previously tested HG gels where none were found. In the block pectin it is possible that these were caused by more, or less ‘blocky’ regions; in the random pectin it may be that there were regions of greater or less depolymerisation than the average. In short, whilst DM appears to determine both viscous and elastic properties in a coupled

fashion, the DB also determines elastic properties but correlations in the viscous parameters of the model are not present.

The physical hypothesis proposed here is shown schematically in Figure 3.19 and its justification is worthwhile discussing at greater length. We know that pectin of higher DB will have a greater concentration of longer ionically bonded junctions than pectin of lower DB. We also know that shorter chains of bonds are less strong than longer chains, so it seems reasonable to propose that these are the first to break upon indentation, as shown in Figure 3.19B. As the indentation force is held on the pectin, the longer bonds in the area surrounding indentation may either spontaneously break, or perhaps break when an opportunity arises to form a new bond with another pectin chain in a more suitable configuration with lower strain energy. Indeed, longer bonds may have to wait longer for a suitable pectin chain (with a similar number of free carboxyl groups) to arrive in close enough proximity to form a new, lower strain energy configuration. A longer time-scale schematic is shown in Figure 3.19C, after breaking of bonds but before potential reformation at lower strain energy configurations. In contradiction to the above, the block pectin has a higher ISS than the random pectin so longer pectin bond junctions must also contribute instantaneously but it is possible that this could be through an entanglement-like effect on the bulk short-time mechanical response, rather than their breaking apart in the short-time region after indentation.

3.6.7 The *Arabidopsis* Hypocotyl Cell Wall – From Elastic to Viscoelastic Analysis

As discussed in the literature review, it has recently been shown that the rapidly elongating axial cell walls of the dark-grown *Arabidopsis* hypocotyl epidermis displayed a reduced elastic modulus and increased amount of high DM pectin, when compared to more slowly growing walls in the same sample [143]. As the tests in that study were solely elastic, not viscoelastic, this system provided us with an ideal testing opportunity for our AFM-based rheology method *in planta*. It also allowed us to investigate whether our rheological results in gels translated to the *Arabidopsis* cell wall, which is more complex. The methodology used above with gels for the evaluation of poroelastic vs. viscoelastic dominance is much more difficult in the context of the primary cell wall. Although *in vitro* pectin has been found to be linear viscoelastic at concentrations similar to the cell wall ($\sim 30\%$) [196], there are a multitude of potential sources of non-linear mechanical behaviour in the plant cell wall. As pectin is the largest constituent of the primary cell wall in *Arabidopsis*, it was assumed

that the dominant behaviour would be linear viscoelastic, as in the HG gels. This assumption was in line with previous elastic studies which assumed linear elasticity based on the use of indentations of less than 10% of cell height [140]; further, the assumption greatly facilitated ease of comparison between *in vivo* and *in vitro* pectin results.

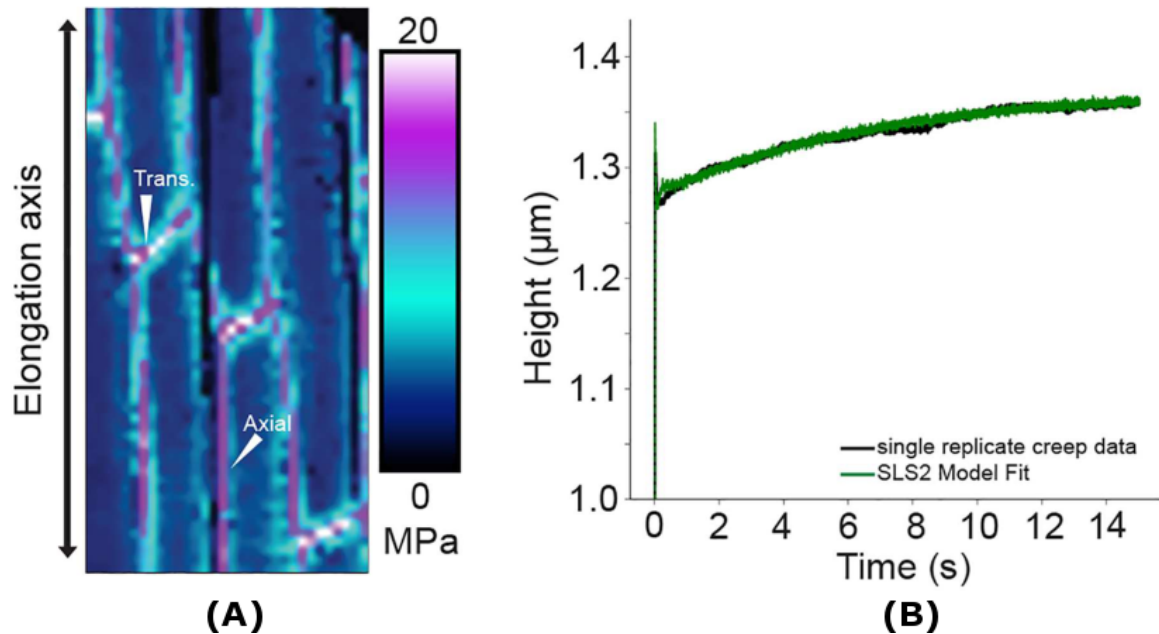


Fig. 3.20 A) Representative map of elastic indentation moduli over a section of *Arabidopsis* hypocotyl, wall marked as ‘Trans’ is a transverse wall perpendicular to elongation axis, other marked wall is an axial wall parallel to elongation axis. Width of figure represents 50 μm real-scale. B) Representative *Arabidopsis* hypocotyl viscoelastic creep data with SLS2 fit.

Before diving in to the data, the effect of AFM tip and model used to obtain the presented results should be discussed. In contrast to the spherical bead AFM tip used for the gels, a pyramidal indenter was used in the plant tests for greater localisation. The pyramid has a rounded point and it is the radius of this point (5 nm) that was provided by the manufacturer. Without knowing the precise geometry of the rounded point, the analysis in this chapter assumed that it was approximately hemi-spherical and thus the same Hertz model as for gels could be used. However, it is difficult to know how good of an approximation this is. There are several other models that may have been suitable if more information about the tip geometry was known. These include a higher-order spherical approximation and four-sided pyramid model [202]. Although the four-sided pyramid model seems perhaps the most plausible it is parameterized by a pyramidal angle which is not known in our case. In short, the difference in tip geometry between gel and plant experiments makes absolute comparisons of mechanical

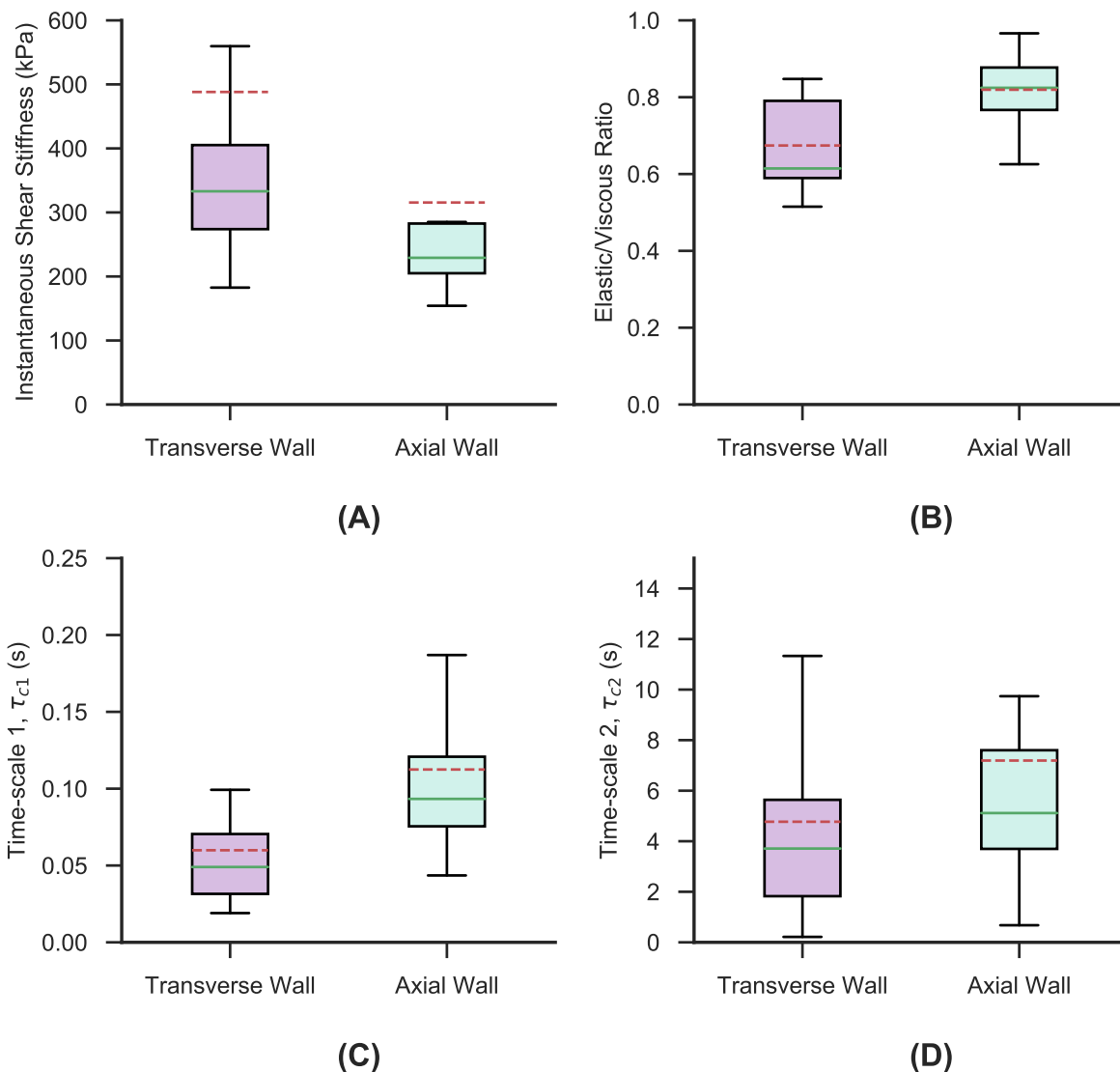


Fig. 3.21 Plant model fit results – continuous line represents median of data and dashed line represents mean of data. Edges of the box represent the upper and lower quartiles and the whiskers represent the range of the observations. A) ISS, or equivalent shear stiffness at time $t=0$, as found by the SLS2 model for both *Arabidopsis* wall types tested. B) Elastic/Viscous ratio as found by the SLS2 model for both *Arabidopsis* wall types tested. C) Retardation time scale 1 of the SLS2 model for fitted to both *Arabidopsis* wall types tested. D) Retardation time scale 2 of the SLS2 model for fitted to both *Arabidopsis* wall types tested.

parameters unfeasible. However, given the known difference in DM between axial and transverse walls in the *Arabidopsis* hypocotyl, a relative comparison to the *in vitro* data is valuable.

An elastic stiffness map was generated using the same AFM-based nanoindentation method utilized in the previous study [140, 143]. The basal, rapidly elongating, region of the

hypocotyl was exposed to rapid indentation. More precisely, the indentations were done in the same region as a previous study by Bou Daher et al. [143], approximately one third of the way up the hypocotyl; in Figure 3.6A, this approximately pertains to cell numbers 4 - 7. A Hertzian indentation model was used to generate a map of ‘indentation modulus’ (IM) 24 hours post-germination; Figure 3.20; indentation modulus is defined here as the Hertz-derived Young’s Modulus (E) for a plant cell where the cellular-solid nature of the material is non-standard for analysis of E . The IM map showed that the transverse walls were significantly stiffer than the axial walls (Transverse: 13.60 ± 1.82 MPa, Axial: 6.19 ± 0.60 MPa, $p < 0.001$), in good agreement with the previous work [143, 150]. The IM map was used to select points on each sample’s axial and transverse walls (5 points on each wall type per sample) at which creep tests were conducted of duration 15 s and force 500 nN. Creep tests were performed on the plants, instead of force relaxation used for HG testing, for two reasons: firstly, the AFM signal in plant viscoelastic testing was found to be far noisier and creep tests provided the best signal/noise ratio due to the force-feedback AFM controller. Secondly, the data would be more comparable to organ level extensometer data in the literature [3]. As exponential relaxation type models have been successfully used in various mechanical studies of plant cells, including those of the *Arabidopsis* hypocotyl [63, 42, 177, 25, 44], an SLS2 model was selected for the analysis of the plant viscoelastic data to facilitate commensurability with the HG data. A representative fit is shown in Figure 3.20B.

3.6.8 *In muro* DM Negatively Correlated With ISS and Rate of Creep – Predicted Plateau Shear Stiffness Appears To Be Coupled In Axial/Transverse Walls

Since we knew that transverse walls exhibited lower DM than axial walls [143], we could explore how DM was related to the SLS2 parameters in a more complex wall material. Figure 3.21A shows the ISS of the SLS2 model for both transverse and axial cell walls. As with the elastic force map, the ISS data demonstrate that at near-instantaneous time-scales the axial walls are significantly less stiff than the transverse walls (315 ± 46 kPa for axial walls compared to 488 ± 104 kPa for transverse walls, a 55% difference, non-parametric $p < 0.05$). This difference is in line with the elastic results found in this (Figure 3.20A), and earlier studies [150, 143]. When combined with our gel data above our results fit the hypothesis expounded by Bou Daher et al. [143] that lower DM pectin in the transverse hypocotyl cell wall results in an increased stiffness compared to the axial wall. However, it should be noted that the ISS values found by fitting the viscoelastic SLS2 model are approximately

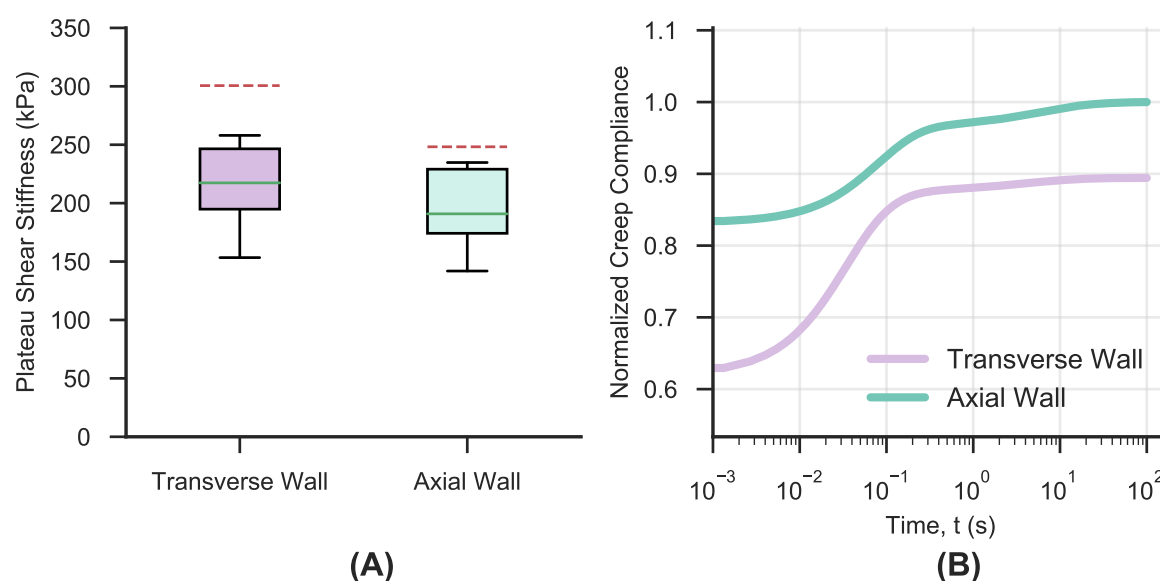


Fig. 3.22 A) PSS, or equivalent shear stiffness as time $t \rightarrow \infty$, as found by the SLS2 model for both *Arabidopsis* wall types tested – continuous line represents median of data and dashed line represents mean of data. Edges of the box represent the upper and lower quartiles and the whiskers represent the range of the observations. B) Simulated creep compliance for both wall types predicted by the fitted SLS2 model subject to a step load, line uses the mean parameters for that wall type, shaded area represents \pm one standard error of the parameters.

one order of magnitude smaller than the IM values at the same point, found using an elastic Hertz fit. This indicates that some of the deformation that the elastic analysis interpreted as stiffness may have been implicitly incorporated into the viscous elements of the viscoelastic model.

In the pectin gels examined earlier, the time for relaxation did not change with DM. In the primary cell wall, we found that increasing DM increased both time-scales τ_1 and τ_2 . Figures 3.21C and 3.21D show the time scales τ_1 and τ_2 as fitted by the SLS2 model. The mean values of both time-scales were higher in the axial walls (0.11 ± 0.02 s vs. 0.06 ± 0.01 s for τ_1 , and 7.2 ± 1.7 s vs 4.7 ± 0.9 s for τ_2 , axis and transverse walls respectively). However, only the difference in τ_1 was found to be statistically significant (non-parametric $p < 0.05$ for τ_1 compared to non-parametric $p \cong 0.39$ for τ_2). This difference was mirrored in the elastic/viscous ratio of the two wall types (Figure 3.21B); unlike the pure pectin gels tested earlier (Figure 3.15C), the plant cell walls exhibited different elastic/viscous ratios (0.82 ± 0.02 for axial walls and 0.67 ± 0.03 for transverse walls, non-parametric $p < 0.05$). So the viscoelastic response of the axial walls was dominated more by its small time-scale behaviour than the transverse walls. This could be due to any number of interactions between the pectin,

hemicelluloses and cellulose; or as we have seen from the tests in DM40 pectin gels of different DBs, the de-esterification pattern of the pectin itself may play a role.

Since our creep experiments on plant cell walls did not always reach plateaus during the maximum experimental time (15 s), we used our fitted SLS2 parameters to simulate the response of the creep moduli for axial and transverse walls to a step loading (Figure 3.22B; the solid lines represent response found using mean average parameters, shaded areas are responses using \pm standard error parameters). This simulation yielded a clear graphical explanation for the E/V ratio difference and provides insight into the difference in time-scales: the axial walls were less stiff instantaneously but plateaued at a similar time to the transverse walls. This would require a slower rate of creep and higher effective time-scale. Both axial and transverse wall compliance then plateaued at similar values, reflected in the overlap of their standard-error compliance in Figure 3.22B. Equivalently, these similar plateau compliances can be inverted and thought of as plateau shear stiffnesses (PSS), as plotted in Figure 3.22A. Compared to the 55% difference in ISS, there was only a 21% difference in the means of the two PSS values (PSS = 301 ± 53 kPa for transverse walls, PSS = 248 ± 31 kPa for axial walls); the PSS statistical significance was $p = 0.21$ (2 s.f.) reflecting greater overlap than the ISS. As this closeness in PSS was not observed across DMs in pure HG gels, it seems there must be a cell-wall-specific explanation. Given the small tip diameter (10 nm) the AFM results should be fairly localized. Therefore, one possibility is that other locally situated components of the cell wall play a role in setting the plateau shear stiffness of the axial and transverse walls, the mightily strong cellulose [203] being the most probable candidate. If longer range effects do come into play, it is possible that the axial and transverse walls are architecturally and geometrically coupled in such a way that is only mechanically realized at longer time-scales. For example, the cellulose fibres in the cell wall could be contiguous across cell faces which would provide such coupling.

3.7 Conclusion

In this study an AFM-based viscoelastic methodology has been developed and used to test the viscoelastic properties of pectin gels and *Arabidopsis* hypocotyl cells. For *in vitro* pectin, linear viscoelasticity was identified as a suitable theoretical framework with which to analyse the time-dependent mechanical data. Two possible constitutive models were fitted and analysed for their suitability: an SLS2 and a Burgers model. Although fairly close, quantitative evidence favoured the SLS2 model which was also more general. The choice of

model and its implications are discussed further in Chapter 4. Through use of the SLS2 model, it was observed that both elastic and viscous parameters changed in tandem with changes in DM; they were both negatively correlated with DM. From this, it was hypothesised that dynamic ionic bond reformation was the dominant mode of physical deformation during the force relaxation tests. The AFM viscoelastic methodology was further validated against two DM40 pectin gels with different patterns of de-esterification, one random and one blockwise, and only ISS was found to be correlated with DB. Explicit viscous parameters did not change significantly across the gel types, but the elastic/viscous ratio changed significantly, in line with the hypothesis that ionic bond reformation in random de-esterified pectin will be perceived as more elastic by the model, whereas block de-esterified relaxation behaviour will be more dominated by longer time-scale behaviours. The SLS2 model was then used to investigate several mixed DM HG gels. The non-linear relationship between gel ISS and DM was thought to explain the discrepancies between mixed and pure DM gels' ISS. Interestingly, the reports by Löfgren and Hermansson [179, 84] found that their calcium and sucrose containing high/low DM mixtures exhibited heterogeneous architecture, with clusters of low DM pectin forming.

In future work, it would be interesting to test these mixed gels with (and without) sucrose, using a more fine resolution AFM probe to better understand potential rheological heterogeneities, at what length scale they occur, and whether they can inform understanding on high/low DM pectin bonding synergies or lack thereof. Further, improving the speed of viscoelastic fitting could facilitate large-scale topographical maps of pectin viscoelastic properties. From a developmental perspective, further work could be done to investigate the conditions required for linearity. In particular, it would be interesting to evaluate poroelastic effects closer to syneresis. If poroelastic effects are found, the DM mixtures could also be retested under these conditions; although the high DM gels were found to have limited contributions to viscoelastic integrity, their presence may affect permeability when the bulk gel is close to syneresis. This would help inform our understanding of whether or not pectin regulates permeability *in muro*. Lastly, evaluation of plastic deformation using AFM is not straightforward. Near the end of this study, a novel way of evaluating plastic deformation was conceived and a preliminary test carried out. The method works as follows, a unique point is tested under creep conditions (4000 nN, 7.5 s and 15 s durations were tested), then at the moment of creep finish, a timer is started and after a fixed interval of time has passed, a rapid elastic indentation is carried out. From the contact point detected in this second, elastic indentation, the percentage indentation depth recovery can be calculated. A phase-space schematic of the experiment is shown in Figure 3.23. The results of this preliminary test are

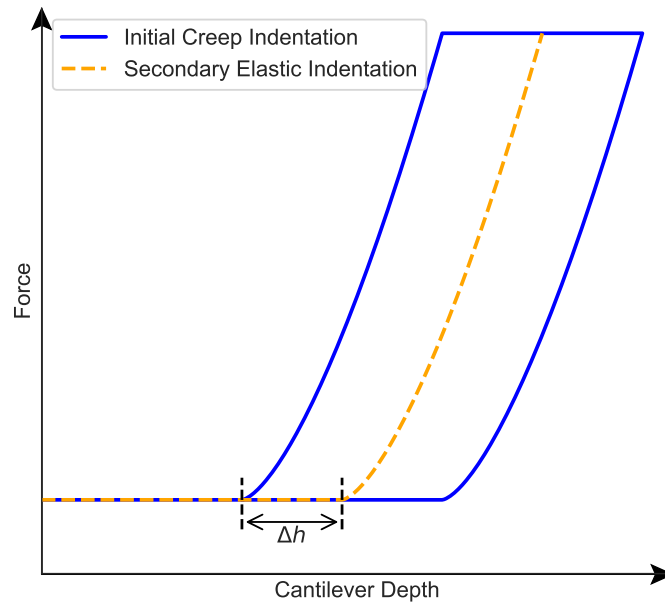


Fig. 3.23 Idealised phase-space schematic of the proposed plastic deformation experiment. In the first run (blue line), a creep test is performed. Time is in the direction of the blue line clockwise around the area it encloses. After this, some time is allowed to pass, and then an elastic indentation is conducted. From the difference in contact points between the two runs, the lasting deformation from the creep run, Δh , can be identified.

shown in Figure 3.24. As each test for different creep durations and recovery durations had to be done at a unique point, it is a time-consuming experiment. However, it does appear to yield a useful recovery curve which plateaus after approximately 30 s in the DM41 gel tested. This should be tested further as if the results are validated it would imply that a dashpot in series is required to be added to the model used to represent the plastic deformation.

The *in vivo* AFM creep protocol, already achieved in animal cells but adapted here for plant testing, appears to work well and complements the bimodal AFM viscoelastic method developed by Seifert [44] and the dissipation based method of Fernandes et al. [43]. The *in vivo* viscoelastic results built upon previous work on the elastic properties of *Arabidopsis* hypocotyl cell walls [143] and demonstrated that the SLS2 model provides a good fit to experimental creep data. The instantaneous shear stiffness was found to be in line with indentation moduli found in elastic indentation tests. Both data sets were congruent with HG gel mechanical data here and the hypothesis that pectin DM is significantly correlated with short time-scale mechanical compliance. The time for creep to plateau was found to be slower

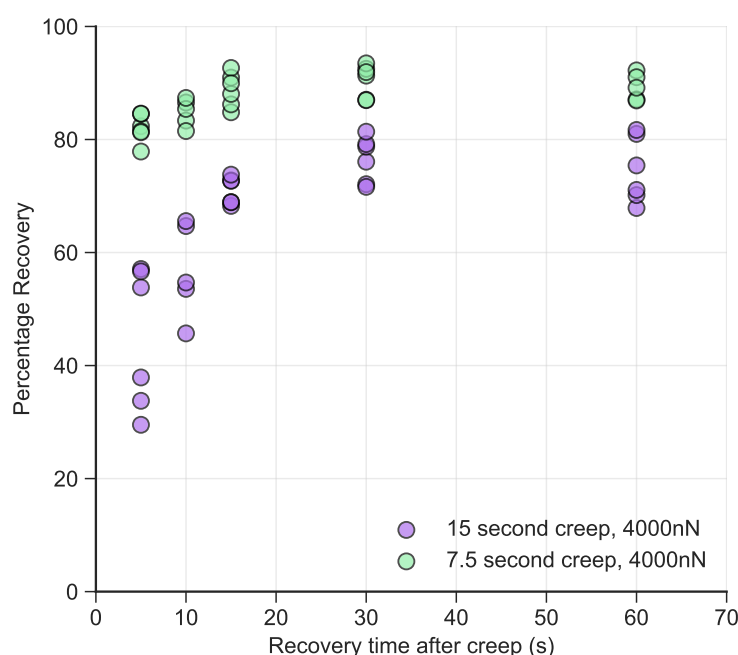


Fig. 3.24 Results of a preliminary investigation of a novel AFM protocol for detection of depth recovery dynamics and plastic deformation.

in axial walls than transverse walls, in contrast to the gels which displayed similar timescales over the range of DMs tested. Lastly, the mean plateau shear stiffness was far closer between wall types than the instantaneous shear stiffness indicating the possibility of a mechanical coupling between axial and transverse walls that is only realised at longer time-scales. As cell walls must have anisotropic mechanical properties to allow anisotropic growth, the differences in stiffness at short time-scale but similarities at longer time-scale suggest that short time-scale mechanical properties may be the arbiters of growth processes. This would partly explain why elastic moduli have been successfully used as developmental correlates and in plant growth modelling [56, 143]. This hypothesis is also supported by the fact that although there were differences between the elastic/viscous ratio of axial and transverse walls, they were both fairly elastic and thus their dynamics were concentrated more at shorter time-scales. However, given the fact that cell walls are clearly viscoelastic, the dynamic data presented here may be useful in development of more detailed growth models, computational or otherwise. Further work should be done to validate the SLS2 model as a constitutive phenomenological model for plant cell walls so that fitting and prediction can be done, and to establish it as a standard that can be used to compare chemically treated plants or genetic mutants. In addition, if the SLS2 is fully validated, the physical significance of the 2 time

scales should be established. Additional work could also explore longer time-scales, a finer spatial resolution, and probe the mechanisms that might be contributing to the apparent weak mechanical coupling between axial and transverse hypocotyl walls at longer time-scales.

Chapter 4

The Utility of Fractional Viscoelasticity and Its Software Implementation

Their problems of form are in the first instance mathematical problems... there is no branch of mathematics, however abstract, which may not some day be applied to phenomena of the real world.

[9] D. W. Thompson, 1945
On Growth and Form

4.1 Author Contributions

The first sections (up to the pectin re-analysis), and Appendix B, are based on a collaborative work with Alessandra Bonfanti (AB – post-doctoral researcher at CUED) and Alexandre Kabla (AK – supervisor at CUED) as part of a forthcoming paper/review. JLK wrote the majority of the code and documentation of the software package RHEOS; overall the software was a collaborative process involving discussion and testing feedback from AB and AK.

4.2 Overview of Chapter

This chapter can be considered as two halves. In the first, a brief history of fractional viscoelasticity is given, followed by an overview of its main technical elements, and comparisons with traditional spring and dashpot viscoelastic models. The pectin data from Chapter 3 is re-evaluated with the benefit of the fractional viscoelastic concepts introduced priorly. In the

second half, the motivation, architecture and features of a fractional viscoelastic open-source data analysis program is discussed (RHEOS).

4.3 Fractional Viscoelasticity

4.3.1 Introduction

In Chapter 2, the existence of power law rheology was briefly mentioned, whilst in Chapter 3, power law stress relaxation was observed in pectin *in vitro* and was approximated by a number of exponential terms arising from a spring and dashpot model. In what follows, the origins and uses of power law rheology are discussed in more detail. Power law rheology is also discussed with regards to its placement within the broader theoretical framework of fractional viscoelasticity. The power law model of viscoelasticity was first suggested by Nutting whilst studying pitch-like substances in 1921 [204]. The use of a power law model was continued by Scott Blair and others, who in the 1940s noted the fact that power law viscoelasticity arose naturally as the solution to a fractional differential equation [205, 206]. Although there had been intermittent theoretical progress of fractional calculus for several centuries before, Scott Blair and his colleagues appear to be the first to have used it in an applied context [207, 208]. Since that time, fractional viscoelasticity has found use in manifold different materials with the common attribute of complexity, wherein numerous mechanistic processes contribute simultaneously to the material's relaxation and creep processes such that a distribution of time-scales is observed. For instance, many examples can be found of fractional viscoelasticity applied to complex geological and construction materials such as bitumen (asphalt) [209, 210], concrete [211, 212], rock mass [213–218] and waxy crude oil [219, 220]. Numerous examples can also be found of fractional viscoelasticity applied to biological materials such as epithelial cells [7], breast tissue cells [221, 222], lung parenchyma [223], blood flow [224, 225] and others, as well as polymers more generally [226, 227].

From the above, it would be wrong to conclude that the use of fractional viscoelasticity is commonplace. Of popular rheology textbooks published in 1989 [20, 228], 2008 [229], 2009 [22] and 2013 [230], fractional viscoelasticity is only mentioned briefly in one of them [22]. This is in spite of the considerable rheological interest in materials that exhibit power law behaviour. In its place, a multitude of empirically derived moduli and approximations have been used. These include the empirical power law model [199], as well as more intricate models involving numerous power law terms [231] or products of power

law and exponential terms [232]. The approximation of power law behaviour by spring and dashpot models also appears to be fairly widespread, with one study using as many as ten parameters [166]. The topic of power law approximation via springs and dashpots is discussed in Section 4.3.2.

Before exploring some of the many interesting aspects of fractional viscoelasticity, it is worthwhile briefly placing the discussion that follows below within the wider context of power law material behaviour. As mentioned in Chapter 1, the work contained in this thesis is largely concerned with phenomenological viscoelastic models, sometimes described as ‘top-down’ models [233] because they attempt to accurately capture and predict the observed phenomena without explicitly accounting for its underlying causes. Although we may attempt to relate our model parameters to physical properties of a material, fractional viscoelasticity is still considered a phenomenological approach as it does not directly model the mechanistic causes of the behaviour. Other phenomenological approaches to modelling power law material behaviour used in the literature often involve some form of power law mathematical ansatz as mentioned in the above paragraph; in some cases these models can actually be shown to have direct fractional viscoelastic equivalents and this is discussed in Section 4.3.5. Alternatively, there also exist more mechanistic approaches to modelling power law behaviour such as soft glassy rheology (SGR) [234] and worm-like chain (WLC) models [235, 236]. WLC models have garnered interest from the biophysical community for their ability to model materials constructed of biofilaments [236, 235], though SGR models have also been used in a biological context [231]. In SGR theory, material elements are embedded in potential energy wells across a matrix, each well’s energy is defined according to a model-wide probability distribution [231, 234]. Indeed, the idea of distributions of physical quantities giving rise to power law behaviour appears to be a unifying theme. Some particular cases of SGR models have been shown to be exactly equivalent to fractional viscoelastic models in their resultant behaviour [237].

4.3.2 The Limitations of Spring and Dashpot Systems

A key tenet of this thesis is that a self-consistent, unified framework for viscoelastic modelling is better than an arbitrary, empirical method of moduli selection; this conviction is held by many others and motivated the development of the springpot. However, before discussion of the springpot itself, it is illuminating to first assess whether it is truly necessary by exploring the limitations of viscoelastic models based on the springpot’s spring and dashpot predecessors. More explicitly, to ask whether or not spring and dashpot models are capable of capturing power law viscoelasticity. Schiessel and Blumen [238] approached this question

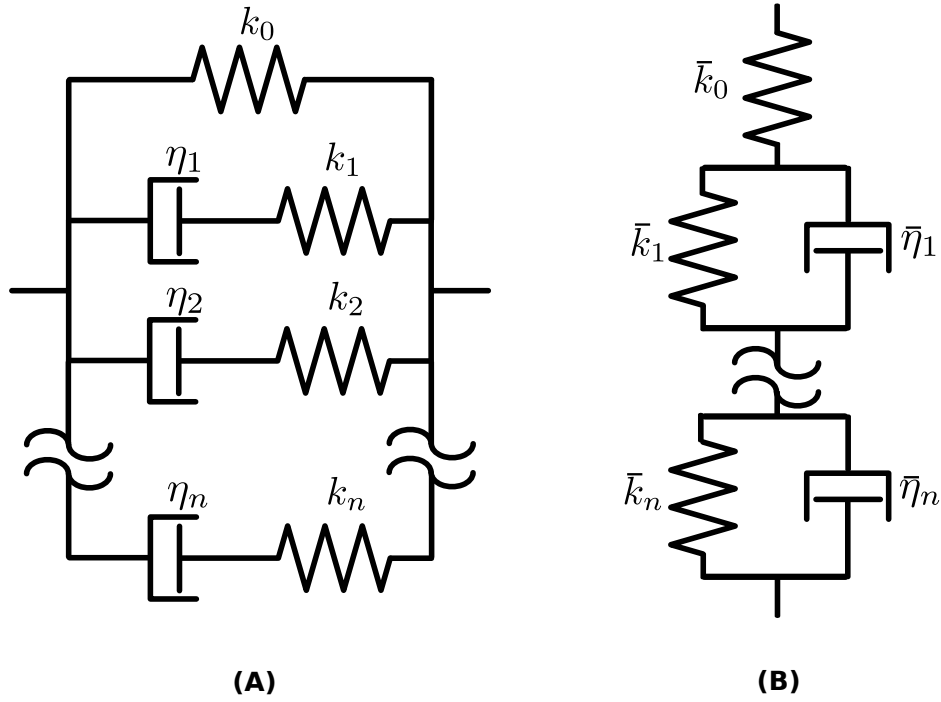


Fig. 4.1 A) Generalized Maxwell model with n Maxwell arms in parallel, each with its own time-scale, and an equilibrium (plateau) stiffness. B) Generalised Kelvin-Voigt model with n Kelvin-Voigt units in series, and a spring in series allowing instantaneous deformation. In both figures, double wave lines symbolise n repetitions of the Maxwell/Kelvin-Voigt units respectively. Overbars on parameter glyphs emphasise the fact that the parameters are not the same in both models, though they can be interconverted.

by use of self-similar ladder and fractal networks of springs and dashpots. Here however, the relaxation modulus of a generalised Maxwell (GM) model is used; the model consists of a number of Maxwell models in parallel and sometimes one spring in parallel which provides a relaxation plateau. Alternatively, one could explore the above question using a generalised Kelvin-Voigt model, which consists of a number of Kelvin-Voigt models, sometimes in series with a spring. (In fact, the pectin analysis in Chapter 3 utilised both of the above models, truncated to two time-scales.) The schematic diagrams of the two generalised models are shown in Figures 4.1A and B. From the fact that relaxation moduli are additive in parallel and creep moduli are additive in series, the relaxation modulus of the GM and the creep modulus of the generalised Kelvin-Voigt model can be deduced:

$$E(t) = k_0 + \sum_{i=1}^n k_i e^{-k_i t / \eta_i}, \quad (4.1)$$

$$J(t) = \sum_{i=0}^n \frac{1}{\bar{k}_i} - \sum_{i=1}^n \frac{1}{\bar{k}_i} e^{-\bar{k}_i t / \bar{\eta}_i}. \quad (4.2)$$

The key feature of both Equations 4.1 and 4.2 is that they consist of n summed exponential terms, each of which has its own time-scale. For the GM model these are relaxation time-scales, $\tau_i = \eta_i/k_i$, and for the generalised Kelvin-Voigt model they are retardation time-scales, $\bar{\tau}_i = \bar{\eta}_i/\bar{k}_i$. On first inspection, these well defined time-scales appear phenomenologically incompatible with scale-free power law behaviour. However, a sum of multiple well defined time-scales can be used to approximate scale-free power law behaviour, and this approximation process is useful to a number of fields beyond rheology. A method of optimal power law approximation by exponential terms has been suggested in the context of quantitative finance [239]. In a 2001 study on the distribution of genomic indel lengths, a complex signal exhibiting two power laws was fitted using 600 exponential terms [240]; however, inspection of the results found that just four terms contributed significantly, so the final empirical function was reduced to those four. If $n \rightarrow \infty$ then an exact power law can be recovered. For example, Winter and Chambon [241] derived, from physical considerations of a crosslinked polymer, a relaxation modulus that could be equivalently defined as either a power law or an infinite sum of exponential terms.

To get a better understanding of the GM model's ability to capture power law behaviour, three different truncations of the model were fitted to a true power law decay. The results of this are shown in Figure 4.2A. With only one Maxwell arm, a clear exponential curve is visible, as would be expected. With an increasing number of Maxwell arms the fit improves. Finally, with 6 Maxwell arms, a good fit is achieved over the full three decades of time. The increasing goodness of fit can be quantified, with the sum-of-squares error for 1, 2 and 6 time-scale truncations being 295.04, 60.97 and 3.45 respectively. From this, it may be tempting to conclude that spring and dashpot models are adequate, even for power law viscoelasticity. However, this is not the case due to three critical reasons. Firstly, increasing the number of parameters can lead to the problem of overfitting, defined by Hawkins as “the use of models or procedures that violate parsimony – that is, that include more terms than are necessary or use more complicated approaches than are necessary” [242]. To give a concrete example, if parsimony was ignored one could fit an elaborate polynomial to the above power law and claim it was an equally good model as any other. The second reason is that the rheologist is often interested in the physical interpretation of model parameters; a difficult task which becomes even more so when faced with an increasing number of parameters, some of which may be redundant. Thirdly, increasing the number of parameters greatly increases the computational burden of model fitting. The ideal modelling paradigm is one which fits the data well, enables accurate prediction, and where the qualitative features of the data are captured by a minimum number of parameters. The springpot brings us closer to

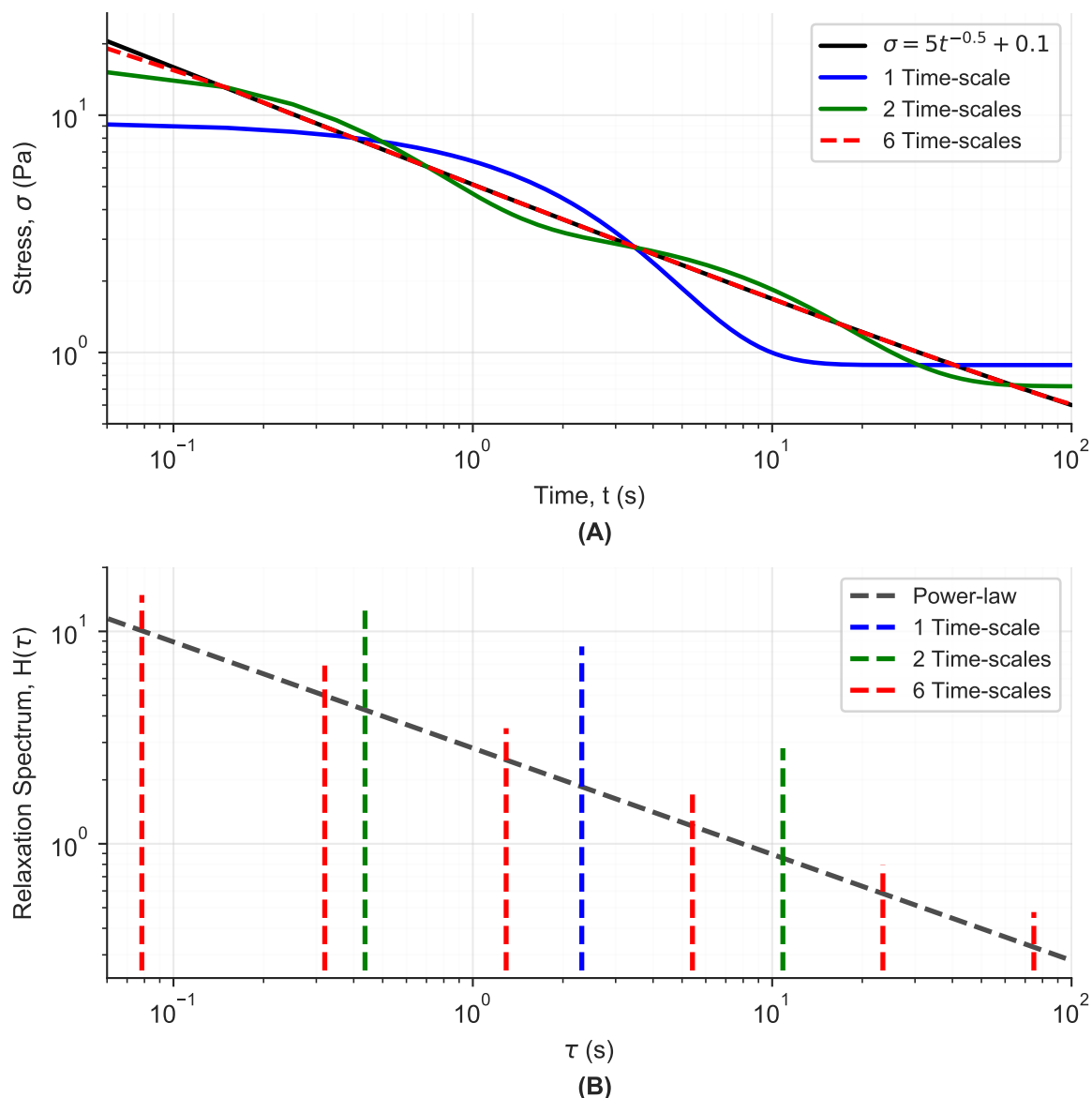


Fig. 4.2 A) Power law (with plateau) stress relaxation response fitted with generalised Maxwell models truncated at 1, 2 and 6 time-scales. Sum-of-squares errors are 295.04, 60.97 and 3.45 for each time-scale truncation respectively. B) Relaxation spectra of the power law response and generalised Maxwell models truncated at 1, 2, and 6 time-scales as fitted for in Figure A above. Note that the time-scales are approximately evenly spaced in logarithmic time.

this paradigm whereas a circumscription to springs and dashpots leads us astray.

It should also be noted that sometimes a continuous spectrum of time-scales, rather than a discrete infinite sum, is considered [243]:

$$E(t) - E_{\infty} = \int_0^{\infty} H(\tau) e^{-t/\tau} d\tau, \quad (4.3)$$

where E_{∞} is the relaxation plateau and $H(\tau)$ is known as the relaxation spectrum. The relaxation spectrum determines the relative dominance of particular time-scales. Simple relaxation spectra consisting of Dirac delta functions reduce Equation 4.3 to a regular GM model. This is shown qualitatively in Figure 4.2B which shows the relaxation spectra of the fitted GM models' spectra along with the power law spectrum. A number of more intricate spectra can be found in textbooks and papers [22]. A relaxation spectrum that yields an exact power law response could not be found for this thesis, but a closely related relationship was identified [244]

$$\frac{1}{\Gamma(\lambda)} \int_0^{\infty} x_0^{\lambda-1} e^{-tx_0} dx_0 = t^{-\lambda}, \quad (4.4)$$

where Γ is the gamma function, x_0 is a dummy integration variable, λ is the power law parameter and t is time. This can be seen by writing the LHS of 4.4 with the integral definition of the Γ function explicit

$$\frac{1}{\Gamma(\lambda)} \int_0^{\infty} x_0^{\lambda-1} e^{-tx_0} dx_0 = \frac{\int_0^{\infty} x_0^{\lambda-1} e^{-tx_0} dx_0}{\int_0^{\infty} x_1^{\lambda-1} e^{-x_1} dx_1}, \quad (4.5)$$

where x_1 is another dummy integration variable. Now, substituting $x_1 = tx_0$, so that $dx_1 = t dx_0$, we find

$$\frac{\int_0^{\infty} x_0^{\lambda-1} e^{-tx_0} dx_0}{\int_0^{\infty} x_1^{\lambda-1} e^{-x_1} dx_1} = \frac{\int_0^{\infty} x_0^{\lambda-1} e^{-tx_0} dx_0}{\int_0^{\infty} (tx_0)^{\lambda-1} e^{-tx_0} t dx_0} = \frac{\int_0^{\infty} x_0^{\lambda-1} e^{-tx_0} dx_0}{t^{\lambda} \int_0^{\infty} x_0^{\lambda-1} e^{-tx_0} dx_0} = t^{-\lambda}. \quad (4.6)$$

In the last simplification step, the integrals in the numerator and denominator cancelled each other out. Thus, the power law can be represented exactly in terms of a weighted average of exponential terms.

4.3.3 The Springpot

Power law viscoelasticity is observed in many materials, and we have seen in the previous section that spring and dashpot models are, in practice, inadequate tools for capturing power law behaviour. This leaves us with two options, an empirical power law formula can be

used, i.e. At^{-x} , or a proper viscoelastic element can be defined which is capable of capturing power law behaviour. The latter option is advantageous as it yields a constitutive differential equation which can be combined with springs and dashpots elements to capture more complex behaviours in a systematic manner. In this section, the constitutive differential equation of the springpot is derived and its response discussed. The first step in our semi-rigorous derivation of the springpot's constitutive equation is to integrate the strain, $\varepsilon(t)$, n times which results in

$$D^{-n}\varepsilon(t) = \int_0^t \int_0^{\tau_{n-1}} \dots \int_0^{\tau_1} \varepsilon(\tau_0) d\tau_0 \dots d\tau_{n-2} d\tau_{n-1}, \quad (4.7)$$

where τ_i are dummy variables of integration and D^i is the differintegral operator which represents differentiation for positive i and integration for negative i [245]. The above can be simplified using Cauchy's repeated integral formula [246], leading to

$$D^{-n}\varepsilon(t) = \frac{1}{(n-1)!} \int_0^t (t-\tau)^{n-1} \varepsilon(\tau) d\tau. \quad (4.8)$$

Next, we generalise the above function to real numbers by rewriting the factorial term using its real number generalisation, the Γ function, for consistency with later notation we also re-label $n = \alpha$. These changes lead to the following

$$D^{-\alpha}\varepsilon(t) = \frac{1}{\Gamma(\alpha)} \int_0^t (t-\tau)^{\alpha-1} \varepsilon(\tau) d\tau. \quad (4.9)$$

The substitution $\alpha = 1 - \beta$ is then made in equation 4.9, which leads to

$$D^{\beta-1}\varepsilon(t) = \frac{1}{\Gamma(1-\beta)} \int_0^t (t-\tau)^{-\beta} \varepsilon(\tau) d\tau. \quad (4.10)$$

Applying the single derivative differintegral operator D^1 to both sides, and noting that $D^a D^b = D^{a+b}$ and thus the operator is commutative [247], yields the definition of the Caputo fractional derivative of degree β [248]

$$D^\beta \varepsilon(t) = \frac{1}{\Gamma(1-\beta)} \int_0^t (t-\tau)^{-\beta} \frac{d\varepsilon}{d\tau} d\tau = \frac{d^\beta \varepsilon}{dt^\beta}. \quad (4.11)$$

Now, considering the most general power law viscoelastic relaxation form $E(t) = At^{-\beta}$ and substituting it into the viscoelastic hereditary integral derived in Chapter 2 yields

$$\sigma(t) = A \int_0^t (t-\tau)^{-\beta} \frac{d\varepsilon}{d\tau} d\tau, \quad (4.12)$$

which is essentially Equation 4.11 in disguise. Comparing the two, we find that in order to capture the full generality of the empirical power law in Equation 4.12, Equation 4.11 requires one more degree of freedom in the form of an additional parameter, henceforth called c_β . Putting it all together, we arrive at the constitutive differential equation for the springpot element

$$\sigma(t) = c_\beta \frac{d^\beta \varepsilon}{dt^\beta}. \quad (4.13)$$

The differential constitutive equation of the springpot could also have been derived via the Laplace transform of the empirical modulus. However, the above derivation highlights the remarkable congruence between the Caputo fractional derivative (Equation 4.11) and the viscoelastic hereditary integral with a power law kernel (Equation 4.12). Further, it has recently been found that the relaxation moduli of more complicated combinations of springs, dashpots and springpots are coincident with other definitions of the fractional derivative, e.g. that given by Baleanu and Fernandez [249]; this is the topic of an ongoing research collaboration. It should also be noted that differential equations involving fractional differintegrals are sometimes referred to as extraordinary differential equations [208].

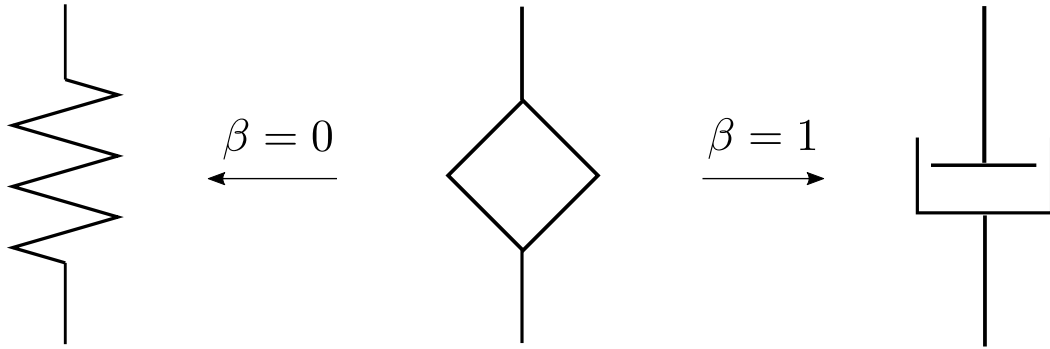


Fig. 4.3 The springpot (at centre) and its relation to the spring and dashpot elements via its β parameter. When $\beta = 0$ the springpot is equal to a spring, when $\beta = 1$ the springpot is equal to a dashpot.

An advantage of the springpot, as opposed to an empirical power law formulae, is its well defined fractional differential equation which reveals that power law viscoelasticity is in fact the interpolating behaviour between a spring and a dashpot. This can be seen from Equation 4.13 by letting $\beta \rightarrow 0$ and relabeling $c_\beta = k$ thus reducing it to the constitutive equation of the Hookean spring shown in Chapter 2; letting $\beta \rightarrow 1$ and relabelling $c_\beta = \eta$ leads to the constitutive equation for the Newtonian dashpot shown in Chapter 2. In application, the constraint $0 < \beta < 1$ is adhered to. The springpot's visual symbol, and its parametric relationship to the spring and dashpot are shown in Figure 4.3.

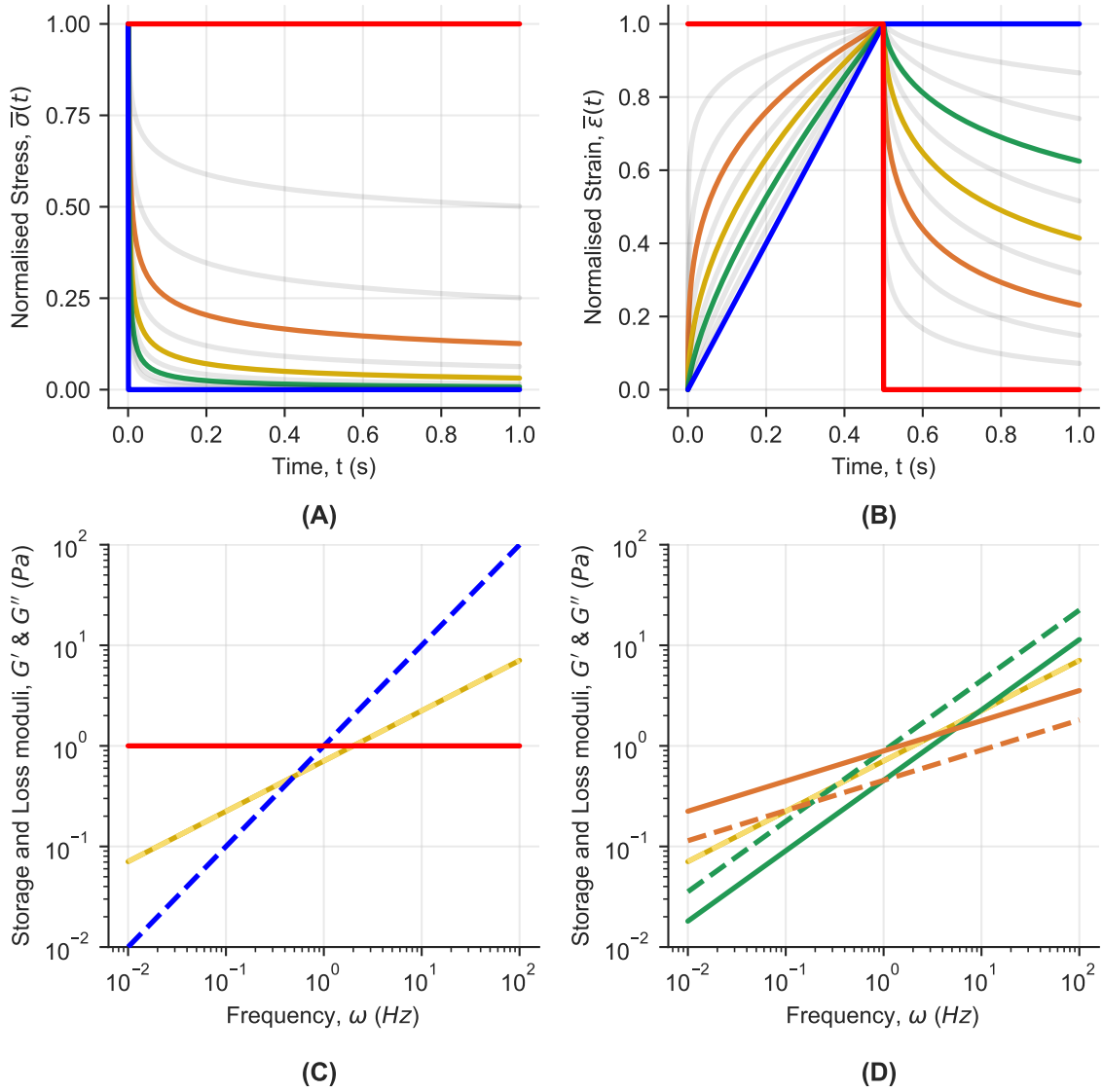


Fig. 4.4 A) Normalised relaxation response of a springpot when subject to a step strain load for β varying from 0 (red) to 1 (blue) in increments of 0.1. B) Normalised creep response of a springpot when subject to a step stress at $t = 0.0$ which is removed at $t = 0.5$. The same values of β and colours apply. C) Springpot storage modulus G' in solid line, and loss modulus G'' in dashed line, for $\beta = 0, 0.5, 1$ in red, yellow and blue respectively. D) As in previous figure but $\beta = 0, 1$ replaced by $\beta = 0.3, 0.7$ in orange and green respectively.

For qualitative insight, it is beneficial to see the response of the springpot firsthand. To this end, the relaxation modulus, creep modulus and complex modulus are written below and their responses with varying coefficient of dissipation β shown in Figure 4.4. The moduli are derived in exactly the same way as shown in Chapter 2: via Laplace transform for the creep

and relaxation moduli, and assuming oscillatory loading for the complex modulus.

$$E(t) = \frac{c_\beta}{\Gamma(1-\beta)} t^{-\beta}, \quad J(t) = \frac{1}{c_\beta \Gamma(1+\beta)} t^\beta, \quad (4.14)$$

$$G' = c_\beta \omega^\beta \cos\left(\frac{\pi}{2}\beta\right), \quad G'' = c_\beta \omega^\beta \sin\left(\frac{\pi}{2}\beta\right). \quad (4.15)$$

The plots in Figure 4.4 demonstrate the behavioural diversity that a single springpot is capable of. In particular, it can be seen from Figure 4.4 that the springpot qualitatively interpolates between springs and dashpots, regardless of which modulus is considered.

Due to the fact that fractional physical dimensions lie beyond the grasp of ordinary intuition, a difficulty associated with springpots, and fractional calculus more generally, is their physical interpretation (although this also applies to the empirical power law model). The springpot pioneer Scott Blair also contributed greatly to the field of psychorheology, introduced in Chapter 3; after carrying out investigations into the (admittedly subjective) perception of power law materials with colleague Flora Coppen, the term ‘firmness’ was decided appropriate for the parameter c_β , which has the admittedly inscrutable physical units of $\text{Pa s}^{-\beta}$. By similar methods, the dimensionless parameter β was named the ‘coefficient of dissipation’ [250, 251], alluding to the fact that Hookean springs ($\beta = 0$) store all energy, Newtonian dashpots ($\beta = 1$) dissipate all energy, and springpots interpolate between the two behaviours.

4.3.4 Multi-element Fractional Models

Deriving a Simple Fractional Model

Springpots can be combined with springs and dashpots in any series/parallel configuration desired. In this section, a simple combination of two springpots in series is derived. Note that the differential equations, moduli and graphic responses are shown for a number of general fractional models in Appendix B. First, we remind ourselves (from Chapter 2) that in series, the stress is equal and opposite at every junction in the system such that

$$\sigma = \sigma_\alpha = \sigma_\beta, \quad (4.16)$$

where σ is the applied stress, σ_α is the stress in the first springpot and σ_β is the stress in the second springpot. Then we can consider the differential equations of the two springpots

separately

$$\sigma = c_\alpha D^\alpha \varepsilon_\alpha, \quad (4.17)$$

$$\sigma = c_\beta D^\beta \varepsilon_\beta, \quad (4.18)$$

where D^i is the differintegral operator as before, and ε_α and ε_β are the strain contributions of the first and second springpot respectively. Reminding ourselves that strain is additive in series, the following relationship can be found

$$\varepsilon = \varepsilon_\alpha + \varepsilon_\beta, \quad (4.19)$$

where ε is the total strain. Differentiating Equation 4.19 using the operator D^α leads to

$$D^\alpha \varepsilon = D^\alpha \varepsilon_\alpha + D^\alpha \varepsilon_\beta. \quad (4.20)$$

For the first term on the RHS, we can simply rearrange Equation 4.17 to get $D^\alpha \varepsilon_\alpha = \sigma/c_\alpha$. For the second term on the RHS we can rearrange Equation 4.18 yielding $D^{\alpha-\beta} \sigma/c_\beta$. Substituting these into Equation 4.20, multiplying through by c_α and flipping the sides of the equation round we find that

$$\sigma + \frac{c_\alpha}{c_\beta} D^{\alpha-\beta} \sigma = c_\alpha D^\alpha \varepsilon, \quad (4.21)$$

which can be written in the more traditional differential notation as

$$\sigma(t) + \frac{c_\alpha}{c_\beta} \frac{d^{\alpha-\beta} \sigma(t)}{dt^{\alpha-\beta}} = c_\alpha \frac{d^\alpha \varepsilon(t)}{dt^\alpha}. \quad (4.22)$$

The above equation constitutes the governing extraordinary differential equation for the fractional Maxwell model consisting of two springpots in series. For adherence to the laws of thermodynamics it is required that the highest derivative in stress is lower than, or equal to, the lowest derivative in strain [252, 253]. This is satisfied for the springpot parameters $0 \leq \alpha \leq 1$ and $0 \leq \beta \leq 1$. However, due to mathematical properties of the Mittag-Leffler function, which arises in the moduli of this model, it required that $\alpha \geq \beta$. So the final bounds on the parameters are $0 \leq \beta \leq \alpha \leq 1$. A strong advantage of deriving the above model in its most generic form of two springpots allows them to be specialised. By appropriately setting springpot coefficients to 0 or 1, a total of four different models are attainable. In particular, by setting $\beta = 0$ and $\alpha = 1$, the tradition spring and dashpot Maxwell model is recovered. The full range of possible models for the above and other springpot combinations are enumerated in Appendix B along with plots of their qualitative response. By the process outlined in Chapter 2, Laplace and Fourier transforms of the fractional Maxwell differential

equation can be taken to find the creep, relaxation and complex moduli. These are written out in full in Appendix B.

There is one caveat to the above mentioned model specialisation process. For some models, it is essential that the springpot parameters are specialised before the moduli are derived from the differential equation. For example, the relaxation modulus of the fractional Kelvin-Voigt model (2 springpots in parallel) is the following

$$E(t) = \frac{c\alpha}{\Gamma(1-\alpha)}t^{-\alpha} + \frac{c\beta}{\Gamma(1-\beta)}t^{-\beta}. \quad (4.23)$$

To attempt to reduce this to a standard Kelvin-Voigt model, the second (β) springpot could be simplified to a spring without problem, but reducing the first (α) springpot to a dashpot yields undefined behaviour. This is due to the fact that $\lim_{\alpha \rightarrow 1} \Gamma(1-\alpha)$ tends to infinity, whilst $\lim_{t \rightarrow 0} t^\alpha$ tends to 0. So for $\alpha = 1$, the first springpot term is 0 everywhere apart from at $t = 0$ s where it's behaviour is undefined. By simplifying parameters before deriving the modulus, this can be clarified and reveals that the term reduces to a Dirac delta function. This is in agreement with the relaxation modulus for a traditional Kelvin-Voigt model [228].

The Mittag-Leffler Function

The moduli of many models constructed using springpots contain the Mittag-Leffler function. As this function arises frequently in the study of fractional viscoelasticity and fractional calculus more generally it is worthwhile introducing it properly – it can appear intractable at first, but there are some general qualitative observations about its behavior that can provide insight. There are one, two and three parameter versions of the Mittag-Leffler function [254], only the first two are discussed as they are most relevant. The function has a series definition and an integral definition [255], the former is more amenable to intuition so will be used here. The one parameter series representation is

$$E_\alpha(z) = \sum_{k=0}^{\infty} \frac{z^k}{\Gamma(1+\alpha k)}, \quad \alpha \geq 0, z \in \mathbb{C}. \quad (4.24)$$

The first special case of note is $E_0(z) = 1/(1-z)$, which can be confirmed by Taylor expanding the fraction about $z = 0$ and comparing with the series definition in Equation 4.24, noting that $\Gamma(1) = 1$. The second special case of note is $E_1(z) = e^z$, which can be seen by comparing Equation 4.24 to the series definition of the exponential function and noting that $\Gamma(k+1) = k!$ for $k \in \mathbb{N}^0$. These two special cases illuminate the fact that the Mittag-Leffler

function is capable of interpolating between power law and exponential behaviour. For values of $0 < \alpha < 1$ the behaviour is more complicated but asymptotic analysis has been done by others and is discussed in subsequent sections. The one parameter Mittag-Leffler function is in fact a special case of the two parameter function, $E_{\alpha,1} = E_{\alpha}$. The series representation of the two parameter Mittag-Leffler function is

$$E_{\alpha,\beta}(z) = \sum_{k=0}^{\infty} \frac{z^k}{\Gamma(\beta + \alpha k)}, \quad \alpha > 0, \beta \in \mathbb{R}, z \in \mathbb{C}. \quad (4.25)$$

As might be expected, the two parameter Mittag-Leffler function is capable of even greater behavioural diversity than the one parameter version. Although the manifold behaviours are not summarised here in their entirety as they lie beyond the scope of this thesis, one important property is noted: if $0 \leq \alpha = \beta \leq 1$ then the Mittag-Leffler function behaves as a power law for small time scales and a power law at large time-scales, with a significant exponential transition region between the two. This was exploited in the recent work by Bonfanti et al. [7] which is discussed in more detail in Section 4.3.5.

Model Selection

Fractional viscoelastic models can appear dauntingly complex at first. This is significant because – as will be evidenced in later sections – they are of great utility in interdisciplinary fields such as geomechanics and biomechanics. Therefore, it is important that non-specialists in those fields are able to assess whether or not fractional viscoelastic models are appropriate for their line of inquiry, and if so, to identify the most appropriate fractional model with which to analyse the data. In fact, the process of identifying an appropriate viscoelastic model, fractional or otherwise, is not as complex as their mathematical form might suggest. Plotting the data in semi-logarithmic scale on the y-axis can quickly reveal whether, and where the viscoelastic behaviour behaves exponentially as it will appear as a straight line. Plotting the data in logarithmic scale on both axes can reveal whether, and where the viscoelastic behaviour behaves as a power law. In the case of multiple springpots, multiple different power laws, dominating at different times, are visible. A model selection heuristic which captures the above is shown in Figure 4.5. The red and blue lines represent the contributions of the α and β springpot respectively, and the intersection of those two lines is the point at which both power laws contribute equally to the response. From the figure, it can also be seen that for a spring to result in a plateau as time $t \rightarrow \infty$ the spring must be in parallel, otherwise it only contributes to the instantaneous response. In the case of specialising to dashpots, the situation becomes a little more complex. A qualitative heuristic for this case

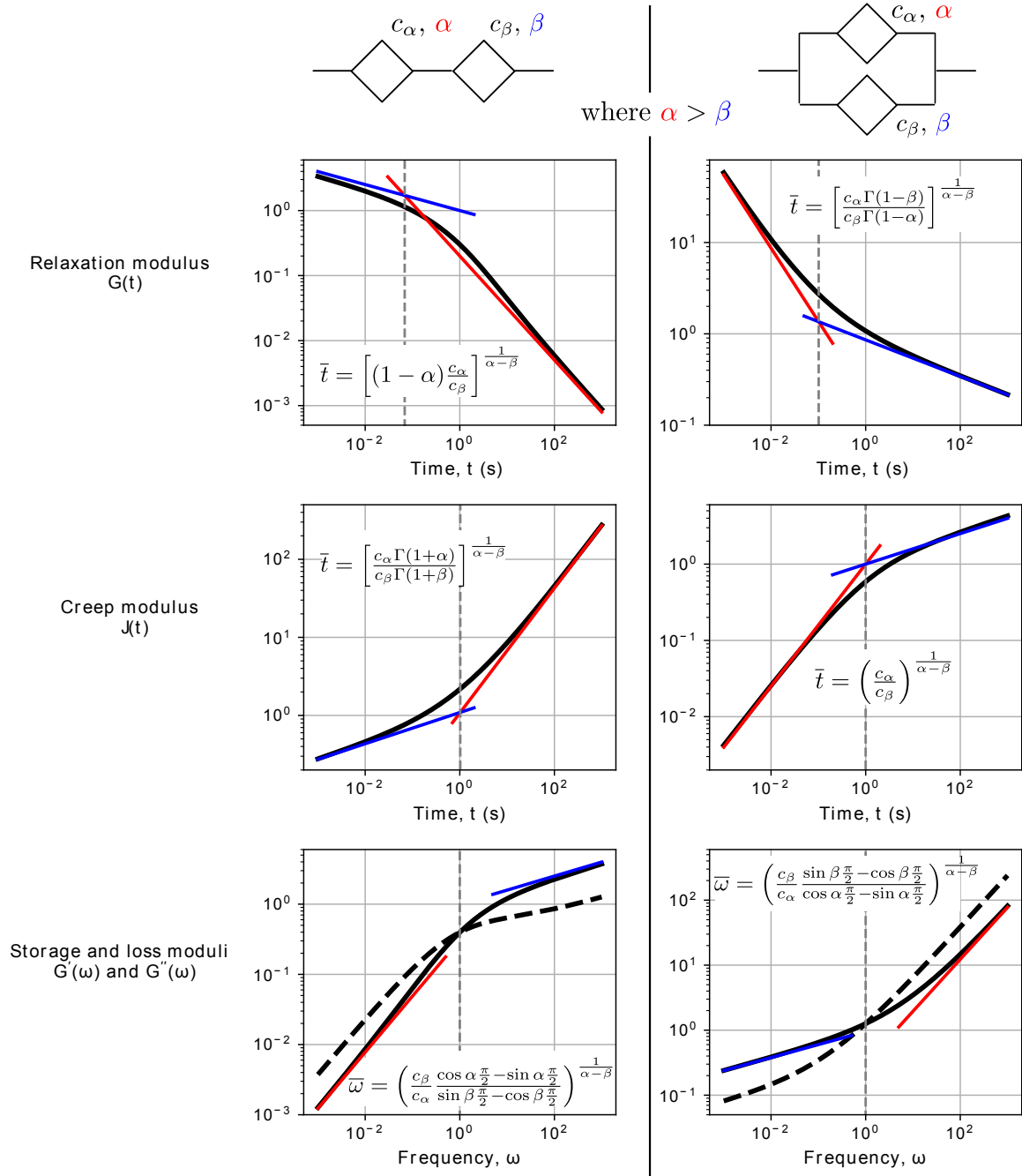


Fig. 4.5 Model selection heuristic showing the qualitative behaviour of two springpots in series and parallel. When two springpots are placed in series, the short time scale response is dominated by the springpot with lower dissipation coefficient, while the long time-scale response is dominated by the springpot with higher dissipation coefficient. The contrary is true for two springpots in parallel. Parameters of the models used are $c_\alpha = 1 \text{ Pa s}^{-\alpha}$, $\alpha = 0.8$, $c_\beta = 1 \text{ Pa s}^{-\beta}$, $\beta = 0.2$. \bar{t} and $\bar{\omega}$ are the intersections of the two springpot contributions in time or frequency respectively.

can be seen in Figure 4.7, adapted from the study by Bonfanti et al. [7], and is discussed subsequently.

4.3.5 Comparison with Empirical Moduli

Studies using standard empirical power law models of viscoelasticity are too numerous to mention individually. However, an important general observation about these papers is that, in using power law viscoelasticity, they are making use of fractional viscoelasticity but often without either knowledge, or acknowledgement of the fact. A smaller number of studies have used more complicated empirical models which involve power law terms. This section compares some of these complex empirical models with their closest possible equivalent derived using fractional viscoelasticity proper.

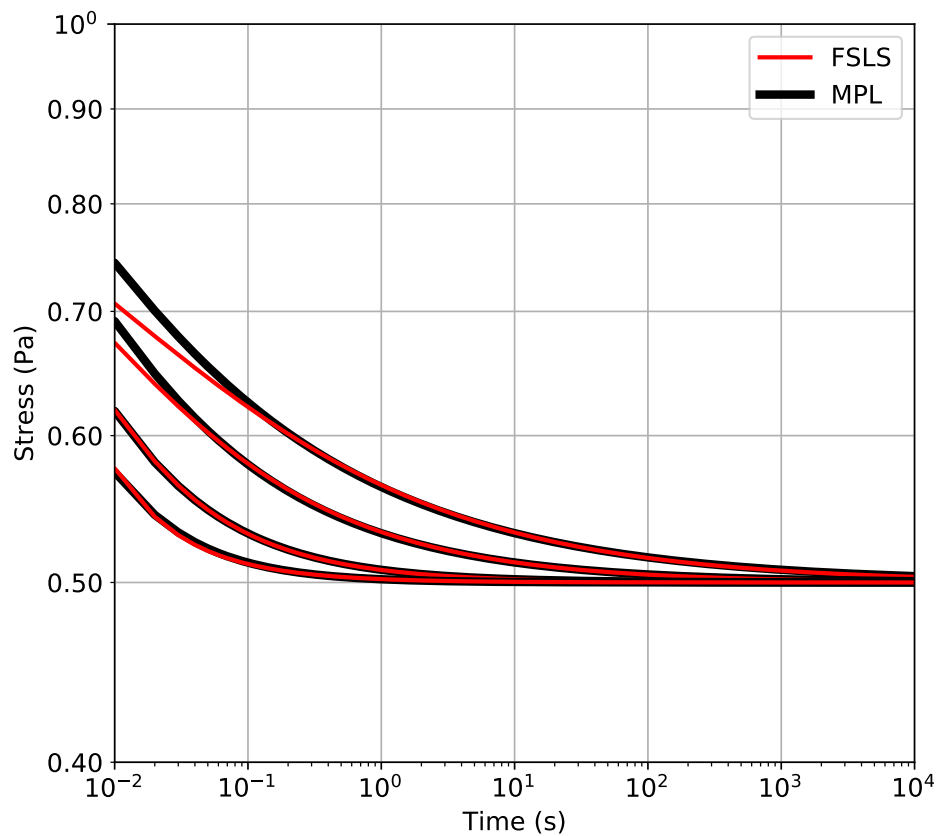


Fig. 4.6 Modified power law empirical model fitted with the fractional standard linear solid (FSLs) model. Parameters for MPL are: $E_0 = 0.5$, $E_\infty = 0.5$, $t' = 1e-3$ and α' takes values of 0.3, 0.4, 0.6 and 0.8 for each line from the highest to the lowest respectively. Respective errors are: 2.59e-01, 9.57e-03, 3.17e-05, 6.30e-05.

Modified Power Law and Fractional SLS Models

The first empirical model considered here is known as a modified power law (MPL). It is a convenient place to start as its form is only slightly different from a standard empirical power law relaxation modulus. It can be written as

$$E(t) = E_{\infty} + \frac{E_0 - E_{\infty}}{(1 + \frac{t}{t'})^{\alpha'}}, \quad (4.26)$$

where E_0 is the instantaneous or ‘glassy’ modulus, E_{∞} is the plateau or ‘rubbery’ modulus, t' is a time scaling, and α' determines the power law gradient of relaxation. In contrast to a regular power law modulus, the MPL has the convenient property of being well defined at $t = 0$ s. For $t \gg t'$, the MPL behaves as a scaled power law, with scaling determined by the parameter t' . As $t \rightarrow \infty$ the MPL approaches a plateau E_{∞} . The MPL has been used in several asphalt and asphalt-concrete studies [256–258], and more recently for the viscoelastic analysis of various benign and malignant cell lines [40]. As far as this model can be considered as a power law transition between two well defined points, its behaviour is notably similar to a fractional standard linear solid (FSLs) model, which is equivalent to a fractional Zener model with two springpots specialised to springs i.e. $\beta = \gamma = 0$. Its schematic diagram can be seen in Appendix B. The relaxation modulus of the FSLs model is

$$E(t) = k_{\beta} E_{\alpha,1} \left(-\frac{k_{\beta}}{c_{\alpha}} t^{\alpha} \right) + k_{\gamma}, \quad (4.27)$$

where k_{β} and k_{γ} are the two spring constants, c_{α} and α are the springpot parameters, and E is the Mittag-Leffler function. (See Appendix B for the more generic differential form.) The similarity between the two models was also discussed by Bagley [259], who made comparisons between their relaxation spectra. Here we show their similarity by directly matching their boundary condition parameters at $t = 0$ and $t \rightarrow \infty$ and fitting the FSLs parameters c_{α} and α to the MPL (Figure 4.6). The fractional model fits the MPL well, especially at longer time scales where both the Mittag-Leffler function and the MPL asymptotically approach a simple power law – though it tends to undershoot as $t \rightarrow 0$ where the Mittag-Leffler function has an infinitely negative derivative [260]. In this model comparison, the number of parameters in each is the same. However, the FSLs has the advantages of differential and dynamic representations, as well as a graphical spring/springpot schematic to aid intuition. Furthermore, the FSLs is able to express a wider variety of near-exponential decay behaviours as opposed to just power law decay.

Friedrich-Heymann and Fractional BK Models

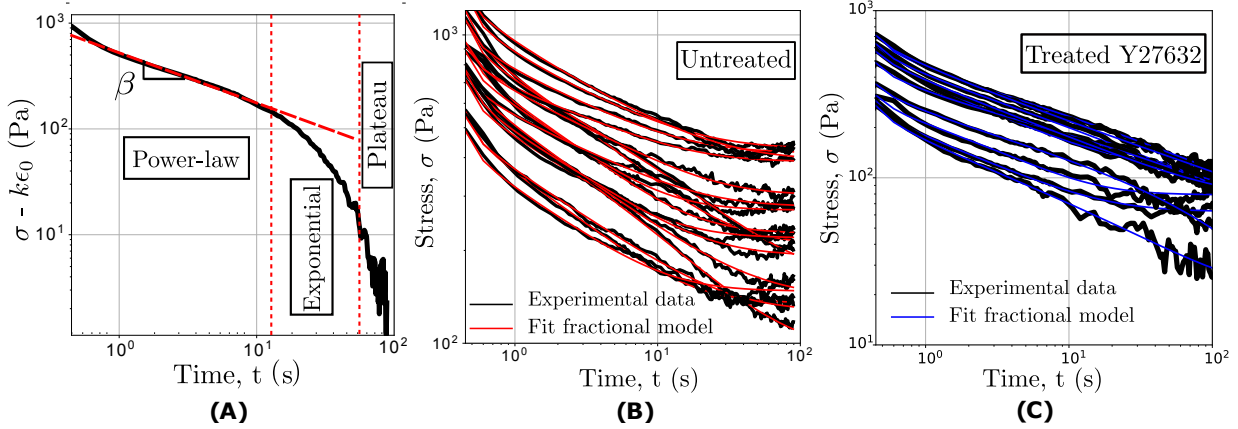


Fig. 4.7 Figures adapted from Bonfanti et al. [7]. A) Log-log plot of epithelial cell monolayer relaxation data to demonstrate the model selection heuristic. B) Fractional BK model fitted to several untreated epithelial monolayer relaxation tests. C) Fractional BK model fitted to several chemically treated epithelial monolayer relaxation tests.

Another power law based model – inspired by the work of Winter and Chambon [241] on the crosslinking polymer polydimethylsiloxane at its gel point – was given by Friedrich and Heymann [232] who added exponential behaviour and a plateau to the relaxation modulus, allowing a larger range of the gel data to be captured. Its form is the following

$$E(t) = At^{-\alpha}e^{-t/\tau} + B, \quad (4.28)$$

where A , α , τ and β are the four parameters of the model. This model has also been used to capture the rheological behaviour of alginate-based gels [261–264]. More recently, the model was independently constructed by Khalilgharibi et al. [24], who used it to analyse the viscoelasticity of epithelial monolayers. Although the connection between the fluid form of Equation 4.28 (i.e. without the plateau, B) and fractional viscoelasticity was noted by Friedrich in a follow-up paper [265], it was not until much more recently that its full (solid) fractional viscoelastic sibling was identified and utilised to its full potential. The study, by Bonfanti et al. [7], builds on the work of Khalilgaribi et al. [24] by reanalysing viscoelastic data of epithelial monolayers and individual epithelial cells using a fractional model consisting of a dashpot and springpot in series, both in parallel with a single spring. (For a schematic diagram of the model, see Appendix B.) The model is henceforth referred to as the fractional BK (Bonfanti-Kabla) model. The log-log scale plot heuristic used in the paper to deduce this model is shown in Figure 4.7A. This is an extension of the heuristic shown in Figure 4.5; by first ignoring the plateau, it is clear that the initial behaviour is power

law and requires a springpot, whilst subsequent behaviour is the limiting case where the coefficient of dissipation approaches unity thereby leading to exponential relaxation. If the behaviour was first exponential and then power law, a springpot in parallel with a dashpot would have been necessary. Finally, considering the plateau, this is essentially a stiffness (or the limiting case when the coefficient of dissipation approaches 0) which occurs at the largest timescales recorded, and must necessarily be placed in parallel. The mathematical form of the fractional BK's relaxation modulus is the following

$$E(t) = c_\beta t^{-\beta} E_{1-\beta, 1-\beta} \left(-\frac{c_\beta}{\eta} t^{1-\beta} \right) + k, \quad (4.29)$$

where c_β , β , η and k are model parameters, and E is the two parameter Mittag-Leffler function. As in the previous case study, an advantage of the fractional model is increased generality by virtue of the Mittag-Leffler function, which can represent an exponential function as a special case. Furthermore, the real power of this model is evidenced by its ability to accurately predict the response of epithelial monolayers to loads different to those that the parameters were trained on. The authors use this fit-predict model testing paradigm to make a strong case for the fractional BK model as a constitutive model for epithelial monolayers. The model is also tested on viscoelastic data from other studies on HeLa Kyoto cells and articular zonal chondrocytes with much success, suggesting that the fractional BK model may be a powerful, unifying tool for the mechanical investigation of many biological materials.

Fractional Kelvin-Voigt, Dual Power Law and Hysteretic Damping Models

The fractional Kelvin-Voigt model mentioned in the previous section, consisting of two springpots in parallel, has been used in some studies without knowledge or explicit acknowledgement of its fractional viscoelastic nature. In this aspect, an empirically derived model exactly matches one derived via the more rigorous fractional viscoelastic framework. Its springpot schematic diagram, differential equation and moduli are shown in Appendix B. However, for the reader's convenience its complex modulus is repeated below

$$G^*(\omega) = c_\alpha (i\omega)^\alpha + c_\beta (i\omega)^\beta, \quad (4.30)$$

where c_α , α , c_β , β are the parameters of the first and second springpot. DMA studies of bovine trachea muscle cells [266] and ATP-depleted epithelial cells [267] used the following

empirical complex modulus

$$G^*(\omega) = A(i\omega)^\alpha + B(i\omega)^\beta, \quad (4.31)$$

which is the same as the fractional Kelvin-Voigt complex modulus, only with differing parameter names. (Note that the paper by Hoffman et al. [267] used a slightly different parameterisation, however it still amounts to the same model.) The comparisons between fractional and empirical can be continued further by specialising one of the springpots of the model into a dashpot, i.e. letting $\alpha = 1$. Further modifying the parameterisation as follows: $c_\alpha = \mu$, $c_\beta = G_0/\omega_0^\beta$, $\bar{\eta} = \tan(\beta \frac{\pi}{2})$, after some algebra yields

$$G^*(\omega) = \mu(i\omega) + G_0 \left(\frac{\omega}{\omega_0} \right)^\beta (1 + \bar{\eta}i) \cos\left(\beta \frac{\pi}{2}\right). \quad (4.32)$$

This is in fact the exact form of an empirically derived model known as the structural (or hysteretic) damping model. It has been used in numerous biomechanics studies on different cell types including epithelial, mouse fibroblast and embryonic carcinoma lines amongst others [231, 268–273].

4.3.6 Fractional Models for Biological Materials

In this section, the data from several rheological studies of biological materials are re-analysed using fractional viscoelastic models and, where possible, comparison is made to the non-fractional models used in the original studies. The first study, by Darling et al. [274], investigates the rheological properties of zonal articular chondrocytes by use of AFM. As the Hertz model was used, the force and displacement data could be transformed into an effective stress and strain and the models fitted via a similar process as in Chapter 3. An SLS model was used in the original paper so this was first fitted to the data, followed by fractional models with the same or less parameters. The fractional Kelvin-Voigt model with one springpot specialised to a spring was found to be the best-fit fractional model. As this fractional model has the same number of parameters as the SLS model, and no physical interpretation of the SLS parameters is offered in the paper, the goodness of fit is the best metric with which to decide the most appropriate model. The qualitative difference between the two fits can be seen in Figure 4.8A, the fractional model is clearly the better fit. The SLS model appears to undershoot at small time scales, this can also be seen in the original paper. Quantitatively, the sum of squared residual errors for the SLS and fractional model were 2.41×10^{-2} and 1.04×10^{-2} respectively, therefore the error from the fractional model was

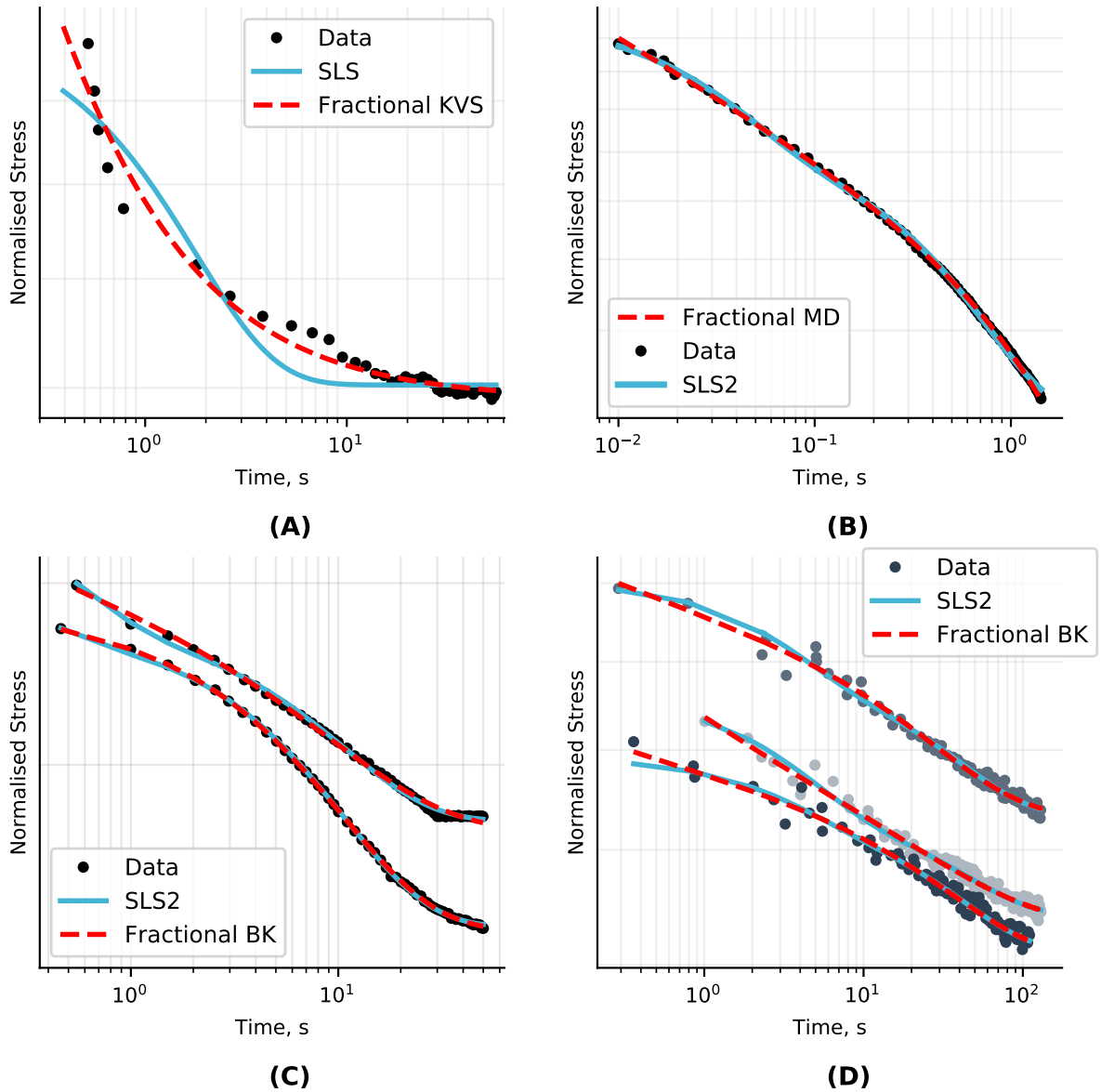


Fig. 4.8 A) Relaxation data from zonal articular chondrocytes [274] fitted with an SLS model and fractional Kelvin-Voigt specialised by one spring. B) Relaxation data from tomato mesocarp cells [25] fitted with an SLS2 model and a fractional Maxwell model specialized by one dash-pot. C) Relaxation data from PCL/bio-active glass [275] fitted with an SLS2 model a fractional BK model. D) Relaxation data from collagen fibrils [276] fitted with an SLS2 model and a fractional BK model. Quantified goodness of fits are discussed in text.

79% lower than the SLS model. The second study revisited using fractional models tested tomato mesocarp cells under high speed microcompression [25]. In the original paper, an SLS2 model was used – the same as was used for pectin gels and *Arabidopsis* hypocotyl tissue in Chapter 3. On qualitative inspection of the data, no plateau was observed, so no

spring in parallel was required; yet there appeared to be a short initial power law region followed by exponential relaxation. For these reasons, a fractional Maxwell model with one springpot specialised to a dashpot was used. It contains three parameters versus five for the traditional SLS2 model. From Figure 4.8 it can be seen that the fractional model provides a similarly good fit as the SLS2. Quantitatively, the sum of squared residual errors for the traditional and the fractional model was 1.70×10^{-3} and 1.42×10^{-3} respectively. Thus, the fractional model yielded 18% less error whilst using two less parameters than the SLS2. Combined with the fact that the SLS2 parameters do not appear to correspond directly to any physical mechanisms of relaxation, the case for using the fractional model appears strong.

The third and fourth examples come from rheological studies of polycaprolactone bioactive glass [275] and isolated collagen fibrils [276] respectively. In both original papers, the SLS2 model was fitted to the data; and for both sets of data, the fractional BK model was found to be the best fitting. The fractional BK model has one less parameter than the SLS2 model. However, it can be seen from Figures 4.8C and 4.8D that the fractional model is still able to obtain a qualitatively comparable goodness of fit as the SLS2 model. Regarding the two relaxation curves extracted from the work of Shahin-Shamsabadi et al. [275], the SLS2 sum of squared errors were 4.53×10^{-5} and 1.40×10^{-4} compared to the fractional BK which yielded errors of 2.28×10^{-5} and 2.16×10^{-4} . So the fractional model had 66% lower error than the SLS2 for the first relaxation curve, but a 43% higher error than the SLS2 for the second relaxation curve. The second curve is the only one of these examples in which the fractional model yielded a higher error than the traditional. However, given that the error of both models is so small in absolute terms, and that the fractional model has one less parameter, there is still a good case for the fractional viscoelastic model. Regarding the three relaxation curves extracted from the work of Shen et al. [276], the SLS2 sum of squared errors were 5.08×10^{-3} , 3.86×10^{-3} and 4.43×10^{-3} , compared to the fractional BK sum of squared errors of 4.33×10^{-3} , 3.55×10^{-3} and 4.07×10^{-3} respectively. Equivalently, the fractional BK model yielded an error that was 16%, 8% and 8% lower for each relaxation curve respectively. Again, a strong case for the advantages of the fractional model. Lastly, it should be noted that the first two examples are special cases of the fractional BK model, the first example takes the dashpot constant to be 0, the second takes the spring constant to be 0. This further consolidates the fractional BK model as a unifying phenomenological model across a diverse array of materials.

Lastly, it is briefly worth discussing the examples in Figure 4.8 with respect to the model selection guidelines outlined in Section 4.3.4 and Figure 4.5. In Figure 4.8A, the response

is convex in shape. From this, we know that the early time response must decay faster than the later time response, suggestive of two springpots in parallel as shown in Figure 4.5. As the response appears to plateau eventually, this suggests that one of those springpots may be specialised to a spring. In contrast, Figures 4.8B, C and D exhibit a concave relaxation response which is strongly suggestive of two springpots in parallel. In case B, the later time response developed into a more rapid exponential decay which led to the specialisation of one the springpots into a dashpot. In cases C and D, the same applied but with the inclusion of a spring in parallel to capture the plateau behaviour.

4.3.7 A Fractional Perspective on Pectin

Background

In the above sections, the limitations of spring and dashpot viscoelastic models and the utility of fractional viscoelastic modelling have been demonstrated. Armed with this insight, the pectin data presented in Chapter 3 can be revisited; some relevant background literature is first discussed. As outlined in Chapter 3, not many pectin studies take a modelling approach to analysing their viscoelastic data but rather assess the dynamic complex modulus in its raw form. The few studies that do take a modelling approach use models with a relatively large number of parameters. For example, Mitchell and Blanshard [159] fitted pectin creep data using a generalised Kelvin-Voigt model with three time-scales and an additional dashpot in series, amounting to eight model parameters in total. Or Kawabata and Sawayama [155], who fitted the same model less one time-scale for their viscoelastic study of pectin. A 2009 pectin viscoelastic study by Gigli et al. used a generalised Kelvin Voigt with five time-scales, implying a total of ten model parameters [166]! It seems likely that the reason for the apparent success of these models lies in the discussion above – that a large number of exponential modelling terms can be used to capture power law behaviour; but for the same reasons as discussed above, their use is fraught with several disadvantages. During the literature review for this thesis, only two pectin papers could be found that explicitly noted the power law nature of the response, both of these fitted a single empirical power law model to the data and did not acknowledge the fractional viscoelastic nature of the power law. The first, a 2002 paper by Alonso-Mougán et al. [165], studied the behaviour of amidated pectin using DMA – the storage and loss modulus were fairly well fitted by an empirical power law from approximately 0.01 Hz - 100 Hz. The second, a 2018 study by Zhang et al., performed DMA on pectin extracted from black cherry tomato waste; the viscosity was well fitted by an empirical power law up to approximately 10 Hz, above which it plateaued.

For further insight into potential modelling pathways, we can look beyond pectin. Alginate is brown algae's analogue of pectin, and can be extracted from its cell wall [277]; the two materials are similar enough that well blended mixtures are able to gelate successfully [89]. From the literature, it appears that there is greater recognition of alginate's power law viscoelastic nature than in pectin. For example, the numerous studies using a power law model [278, 279], and others using the extended model mentioned above which features an exponential power law product (Equation 4.28) [261–264]. Another polysaccharide hydrogel of interest is agarose. It is derived from red algae and has been blended with pectin in previous biomedical studies [280, 281]. In the 2004 study by Chen et al. on the viscoelastic properties of agarose, a single springpot captured the oscillatory behaviour well over two decades of frequency [227]. This appears to be the only example of explicit fractional viscoelasticity as applied to pectin or its algal siblings.

Looking beyond pectin and its algal analogues, there are plenty of examples of fractional viscoelastic modelling applied to a diverse array of gels and polymers. One of the early examples is the aforementioned work of Winter and Chambon [241] who derived a springpot-like modulus for crosslinking polymers at their gelation point, which was subsequently used for analysis of polydimethylsiloxane gel data; as well as the aforementioned empirical extension by Friedrich et al. [232], shown in Equation 4.28. Both colloidal [282] and carbopol [283] gel rheology data have been successfully analysed using a fractional Maxwell-type model consisting of a spring in series with a springpot – though the latter authors did not make their use of fractional viscoelasticity explicit. Two gelatin-based gel rheology studies [284, 285], a potato starch gel study [286], and a simulated three-dimensional particulate gel investigation [287] have all made use of the fractional Kelvin-Voigt model (a spring and springpot in parallel). Alcoutlabi and Martinez-Vega modelled the glassy amorphous polymer polymethyl-methacrylate [226] using a fractional Zener model.

Pectin Model Review

The pectin samples tested in Chapter 3 exhibited rapid initial relaxation, quickly followed by a power law region which dominated for the rest of the relaxation holds. In light of the above discussion on the limitations of spring and dashpot systems, it appears that although the data were fairly well fitted by the SLS2 model, it is not the most parsimonious choice as it merely approximates the power law region by virtue of its excess parameters. To remedy this, the simplest possible fractional model was identified that featured a power law transition but still had well defined boundaries – the FLS model. (See Appendix B, Zener section

for the schematic and full constitutive equations, and Equation 4.27 above for the relaxation modulus.) Furthermore, although the very short time behaviour (shown in Figure 4.9) was difficult to decipher qualitatively, it does appear to decay at faster rate than power law. The early time rapid exponential of the FSLS model was thus seen as a convenient approximation to this otherwise intractable region of behaviour. Another benefit of the FSLS model is that it is arguably the closest fractional analogue of a generalised Maxwell model truncated with one time scale, also known as a standard linear solid model; this enables exploration of any congruence or disharmony between the two models' results. Lastly, it is worth noting that in addition to the polymer study by Alcoutlabi and Martinez-Vega [226], other studies that also used the FSLS model include the viscoelastic analysis of arteries [224, 225], breast tissue cells [222] and lung parenchyma [223]. Indeed, in a similar vein to this section's analysis, the study by Dai et al. made comparisons between a one, and two timescale GM model and the FSLS model before concluding the FSLS was most appropriate for lung parenchyma. Carmichael et al. also made comparisons between a one timescale GM model (a.k.a the standard linear solid) and an FSLS model, and concluded that the fractional model was more suitable for breast tissue.

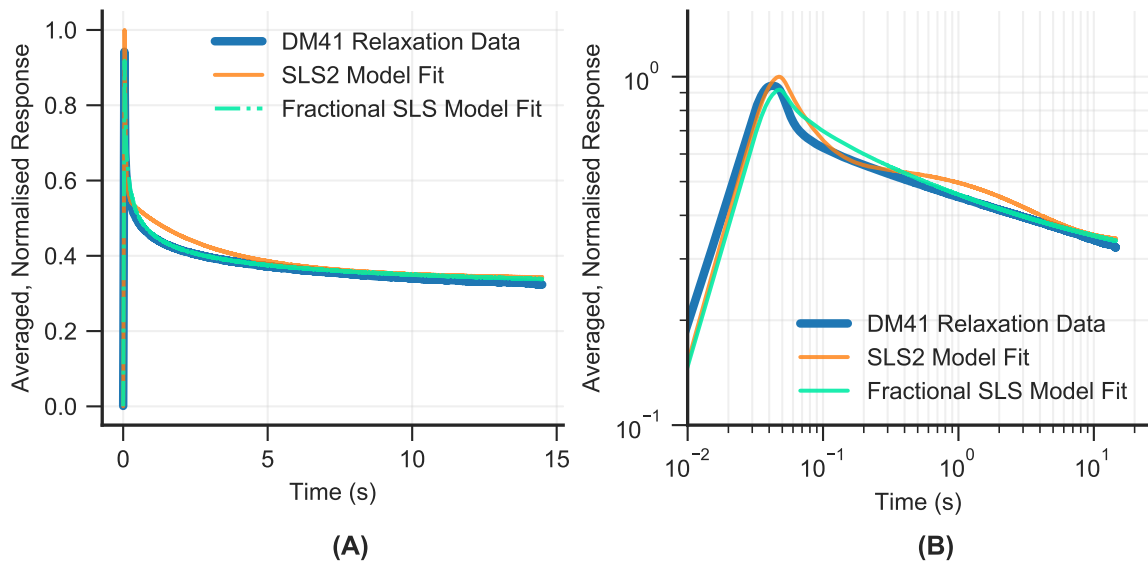


Fig. 4.9 A) Averaged relaxation data from all tests on DM41 HG at a depth of 2 μm, the averaged predicted relaxation response of the fitted FSLS model, and the averaged predicted relaxation response of the fitted SLS2 model. B) The same data as in A) but plotted in log-log scale.

Using the same methods of Chapter 2 the data were fitted to two models, the SLS2 and the FSLS model. (See Equation 4.27 for the relaxation modulus of the FSLS model.) Figure 4.9A shows the averaged data and relaxation responses of the SLS2 and FSLS models.

From the regular scale plot, it is clear that at shorter time-scales, the FSLs model yields a better fit than the SLS2 model. The log-log scale plot in Figure 4.9B confirms this, though we can see that even the FSLs model does not completely capture the early time behaviour for $t < 1$ s. The slight wavering in the SLS2 prediction that can be observed in Figure 4.9B is reminiscent of the almost oscillatory behaviour exhibited in Figure 4.2. Quantitatively, the SLS2 model did have lower bulk mean-squared-errors than the FSLs models for the gels tested (see Appendix C for full info), though the errors were all in the same order of magnitude. Perhaps more importantly, all the mean-squared-errors for both SLS2 fits and FSLs fits were many orders of magnitude lower than the data values themselves so relatively speaking, both can claim to fit the data well. These results are encouraging, especially given that the FSLs model has one less parameter than the SLS2 model, thus the short time-scale improvement is unlikely to be an artefact of overfitting. To further justify analysis using a fractional viscoelastic model, it is worthwhile revisiting the physical significance of the power law relaxation in more depth than Chapter 3. At the scale of individual sugar chains, there is a distribution of ionic egg-box junction lengths; which may give rise to a distribution of time-scales that result in power law viscoelasticity. A 2014 study by Basak and Bandyopadhyay [288] found that low DM pectin gelled via calcium crosslinking consisted of polydisperse flocs bonded to each other, and as the calcium concentration increased significantly higher than that required for concentration the size of flocs did not increase significantly but their interlinking did; interestingly they observed a power law increase in storage modulus with calcium concentration. Although it is possible that the pectin flocs have spatial self-similar properties which contribute to the power law behaviour [289–291], this cannot be taken for granted as a recent study found that a fractal microstructure does not necessarily lead to fractional viscoelasticity at the macroscale [292].

Revisiting Pectin *In Vitro* and *In Vivo*

Armed with the fractional viscoelastic model, the pectin relaxation data across different DMs and DBs was re-evaluated using a similar fitting process as in Chapter 3. The results of this are summarised in Figures 4.10 and 4.11, and Tables 4.1 and 4.2. The ISS derived parameter and the springpot parameter α are shown to maximise commensurability between the results of the two chapters.

For different DMs, the relative differences in ISS between gel types follow a similar qualitative trend for both SLS2 and FSLs models. Both showed a slight decrease in ISS in DM 41 pectin compared to DM 33, and a significant decrease in ISS at DM 50. In the

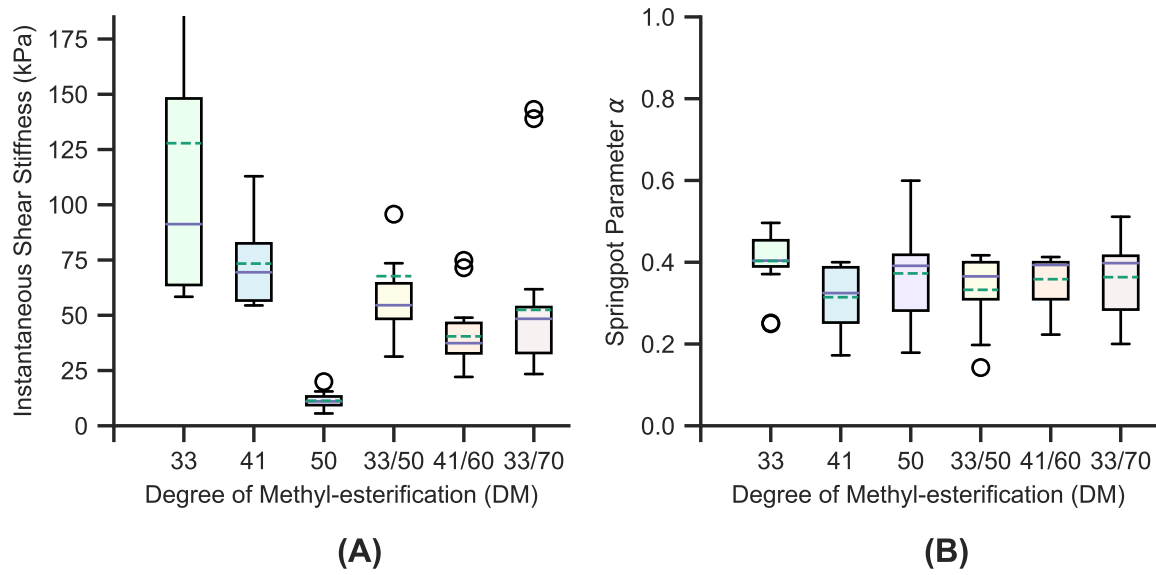


Fig. 4.10 FLS model parameters for the HG and HG mixtures tested. 33/50 represents the DM41 equivalent mixture, 41/60 and 33/70 represent the two DM50 equivalent mixtures. Continuous horizontal lines represent the median of the data, dashed lines represent the mean. Edges of the box represent the upper and lower quartiles and the whiskers represent the range of the observations. Open circles are considered outliers as they are greater than $1.5 \times (\text{interquartile range})$ distance away from the upper or lower quartiles.

| HG DM | ISS (kPa) | Springpot Parameter α |
|-------|------------------|------------------------------|
| 33 | 128.9 ± 23.7 | 0.40 ± 0.02 |
| 41 | 73.4 ± 5.9 | 0.31 ± 0.02 |
| 50 | 11.4 ± 0.8 | 0.37 ± 0.02 |
| 33/50 | 67.7 ± 1.2 | 0.33 ± 0.02 |
| 41/60 | 40.5 ± 2.8 | 0.36 ± 0.01 |
| 33/70 | 52.4 ± 6.5 | 0.36 ± 0.02 |

Table 4.1 Mean FLS model derived parameters for all HG types \pm standard error. 'E/V' is Elastic/Viscous Ratio. '33/70' is the DM41 mixture. '41/60' and '33/70' are the two DM50 mixtures.

same way that the elastic/viscous ratios of the SLS2 model (shown in Figure 3.15B) were fairly consistent over the full range of DMs tested, the spring parameter α of the FLS model (Figure 4.10B) also remained fairly consistent between gels tested (ANOVA $p=0.094$ including DM33, $p=0.35$ without DM33, pairwise p -values also suggest similarities) – in line with the proposed hypothesis that the elastic and viscous properties are coupled, and both are determined by DM; except for the relatively large, 25% difference between α values for DM33 and DM41. In contrast, the largest difference in E/V found by the SLS2 model was between DM33 and DM50 (24% difference). There was a large difference in the absolute values of instantaneous shear stiffness (ISS) between the two models. Compared to the SLS2

model, the FSLs ISS was 75%, 61% and 64% higher on average for DM 33, 41 and 50 respectively. This suggests that the FSLs model attributed more of its mechanical resistance to its instantaneous elastic elements whilst the SLS2 model attributed more of its mechanical resistance to its viscous elements (dashpots).

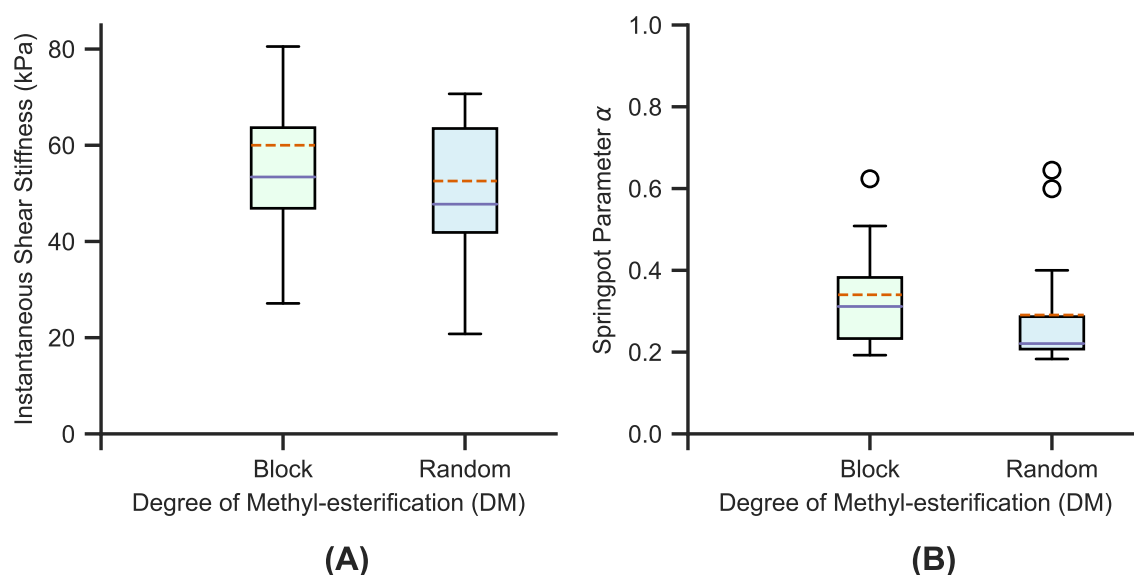


Fig. 4.11 FSLs model parameters for the block and random de-esterified pectins tested. Continuous horizontal lines represent the median of the data, dashed lines represent the mean. Edges of the box represent the upper and lower quartiles and the whiskers represent the range of the observations. Open circles are considered outliers as they are greater than $1.5 \times (\text{interquartile range})$ distance away from the upper or lower quartiles.

Considering the results from the pectin of different DBs, again the general trend is the same for both models, with the blockwise de-esterified pectin exhibiting an ISS 13% higher than the random de-esterified pectin. However, both parametric and non-parametric p-values were greater than 0.1 suggesting questionable statistical difference. Interestingly, this is considerably smaller than the 40% difference in ISS found using the SLS2 model. The springpot parameter α was 16% higher for the block pectin (though again, parametric and non-parametric $p > 0.1$). As this was the only non-spring element this suggests that the random pectin was more elastic than the block pectin. Reassuringly, this is in agreement with the SLS2 findings although the difference was much more pronounced in the SLS2 model parameters. The SLS2 E/V ratio was 78% higher in the random de-esterified pectin than the block. Both models agree that the randomly de-esterified DM40 pectin is the most elastic of all the samples tested. In contrast, the FSLs model suggests that the DM33 pectin is the most viscous, whilst the SLS2 model suggests that blockwise de-esterified DM40 pectin is

| HG DB | ISS (kPa) | Springpot Parameter α |
|--------|----------------|------------------------------|
| Block | 60.0 ± 7.8 | 0.34 ± 0.04 |
| Random | 52.6 ± 5.5 | 0.29 ± 0.04 |

Table 4.2 Mean FSLs model derived parameters for all HG types +/- standard error. 'E/V' is Elastic/Viscous Ratio. '33/70' is the DM41 mixture. '41/60' and '33/70' are the two DM50 mixtures.

the most viscous. As the exact de-esterification process used to make the DM33 pectin is not known, it is difficult to ascertain the significance of this incongruity. As the two parameters do not convey the same metric but are only analogous, the difference in the results is perhaps not too concerning. Though the physical interpretation of the above results discussed in Chapter 3 is not repeated here, it is noted that the FSLs model does not appear to be in conflict with it. Indeed, this raises the question of what advantages the FSLs model provides. The first is that, given the comparable fit accuracy whilst using one less parameter than the SLS2, it is plausible that the parameters yielded provide a better foundation upon which to build physically meaningful hypotheses. Secondly, it brings us a step closer to having a constitutive model for pectin that is able to make rheological predictions without testing all possible different compositions and loading patterns. This would certainly be useful in industrial application. More work should be done in future to test the FSLs model's ability to correctly predict gel response, and for the limits of the model's capability to be ascertained (it may not be suitable for very different pectin formulations and very large deformations).

Given the success of the FSLs model in gels, and the fractional MD model in tomato mesocarp cells (Figure 4.8B, refitted digitised data from [25]), the utility of fractional models for the *Arabidopsis* hypocotyl was of great interest – particularly as they appear to be little explored for plant systems. Only one paper could be found in the literature that made use of fractional viscoelastic modelling for plant material – Belović et al. performed DMA on tomato pomace and successfully fitted the data to a fractional Kelvin-Voigt-type model consisting of a spring and a springpot in series [293]. However, this model selection does not necessarily apply to the *Arabidopsis* hypocotyl as tomato pomace is considerably more fibrous and less pectinaceous than *Arabidopsis* hypocotyl cells. Yamamoto et al. [63] used a three time-scale GM model with a plateau (7 parameters in total) applied to stress relaxation data from *Avena* coleoptile and green pea stem under various auxin treatments; the authors noted that this was an approximation of the observed exponential and logarithmic decay signatures. Moving to the experimental results obtained for this thesis from the *Arabidopsis* hypocotyl system discussed in Chapter 3, the qualitative behaviour of the plant data creep curves were far more heterogeneous than the pectin and there was not a consistent pattern of power law or exponential behaviour amongst the collected data. The creep data was fitted

to the FSLs model. It was found that the springpot parameter of the FSLs model, α , was equal to 0.9958 ± 0.0031 and 0.99991 ± 0.00001 for axial and transverse walls respectively. This implied that the fractional springpot element essentially behaved as a standard dashpot. This suggests that any power law growth in compliance was negligible. This fits with the experience others have had using one and two time-scale SLS models in *Arabidopsis* seedlings [42, 177, 44]. Further, the FSLs model appeared to qualitatively struggle to fit some of the plant data (see Appendix C) and quantitative error was higher than the SLS2. For the above reasons, the use of fractional models for *Arabidopsis* hypocotyl rheology was not pursued further.

4.4 RHEOS - Open Source Rheology Software

4.4.1 Motivation

The second part of this Chapter details the motivation, architecture and features of an open source rheology data analysis software package – RHEOS [294]. In the above sections, the utility of fractional viscoelasticity has been demonstrated. Further, it has been shown that the conceptual process for fractional model selection is not excessively complicated; this last point is important given its demonstrable utility in interdisciplinary fields where non-experts may be interested in analysing rheological data. However, what has also been evidenced is the inherent mathematical complexity of fractional viscoelasticity, which also translates into difficulty of computational implementation, thus potentially rendering it beyond the reach of many interdisciplinary research groups. Indeed, this may be a key reason why its use has not become more commonplace. Thus, the main aim of RHEOS is to make the process of fitting fractional viscoelastic models to data as straightforward as possible.

There are also more general motivations worth discussing. The popularity of open source scientific software has grown massively over the last few decades, and this growth shows no sign of slowing [295]. It allows researchers to make more effective use of their time and budget, whilst also facilitating reproducibility of data analysis. Prominent examples of open source scientific software packages are NumPy, SciPy and Bioconductor [296], which have facilitated countless scientific investigations. Open-source utility software such as the LaTeX package ecosystem and the Zotero reference manager are also of great importance to the scientific community – and more personally, both were used extensively in producing this thesis! Furthermore, numerous recent scientific scandals have raised awareness of the importance of scrutinising scientific software and methodology [297]. In turn, this has led to

calls for making software review as important a part of paper publication as the review of the results themselves [298, 299].

4.4.2 Deliverables

The main aims of RHEOS are to provide the following:

- A library of standard and fractional linear viscoelastic models, with the facility to add user-defined models.
- Stress/strain/time data fitting to linear viscoelastic models.
- G'/G'' /frequency data fitting to linear viscoelastic models.
- Predict response given arbitrary time or frequency domain loading and a linear viscoelastic model.
- Efficient generation of artificial loading for intuition development.
- All of the above functionality must be achievable with minimal programming experience.

It is the authors conviction that RHEOS has met all these deliverables. Furthermore, RHEOS has been peer-reviewed and published in a journal for open-source scientific software [300] (Journal of Open-Source Software). The fulfilment of the first deliverable is demonstrated by the fact that all the models in Appendix B, including their specialised forms, are implemented in RHEOS. This model library is a comprehensive and useful tool for the research community, and the models are also included in the Annex of a review written by the same authors as RHEOS that has been accepted to a peer-reviewed journal, with a preprint already released [301], both of which will broaden their visibility. For the other deliverables, their fulfilment is demonstrated in subsequent sections by use of workflow examples. Where appropriate, code samples are included to demonstrate the simplicity of the syntax. Code used for plotting is not included for brevity. The sections are largely based on the RHEOS documentation. For a full list of functions and data structures, please see the API section of the documentation which is available online at the link in reference [302]. To demonstrate that RHEOS has met the above deliverables, there are detailed code examples and discussion, along with plotted results in Appendix A.

For further evidence that RHEOS has met the above aims, it should be noted where it has been used already. RHEOS has recently been used by Messaoud et al. [303] to investigate

the rheological properties of novel lipid lamellar hydrogels they developed. In their paper, they explore the fractional Kelvin-Voigt, fractional Maxwell, and fractional Zener models; and found that the fractional Zener model fitted the hydrogel data particularly well. RHEOS was used to perform all the analysis in the paper discussed above by Bonfanti et al. [233] which focused on the rheological response of epithelial cells. The researchers found that the fractional BK model was able to both fit and predict the behaviour of the cells with a high degree of accuracy. Furthermore, RHEOS was used for all the analysis in this Chapter apart from the pectin section, and is being used for the analysis of multiple forthcoming publications. It was presented at the Julia programming language conference in 2018 [304]. With regards to other software with similar functionality, other labs must have generated software with some overlapping functionality, but only one could be found that was published online as open-source software: ForceMetric written by Jacob Seifert as part of his PhD thesis [44, 305]. However, the package is specifically designed for analysis of AFM data files from one specific manufacturer and does not feature any fractional viscoelastic models.

It is important to note that RHEOS is not an optimisation package. It builds on another optimisation package, NLOpt [306], by adding a large number of abstractions and functionality specific to the exploration of viscoelastic data. The optimisation routine used by RHEOS is discussed in Section 4.4.3.

4.4.3 Architecture

High-level Overview

To get a better sense of how RHEOS fits together, and how its design facilitates its aims, it is helpful to have a top-down overview of the main data objects which RHEOS uses, and how they interact with each other. RHEOS is built around four main data types, *RheoTimeData*, *RheoFreqData*, *RheoModelClass* and *RheoModel*. Each will be discussed in more detail but briefly: *RheoTimeData* and *RheoFreqData* contain data information either generated or obtained experimentally, *RheoModelClass* and *RheoModel* contain modelling data where the parameters are either not known, or known respectively. These data structures enable the typical rheology data analysis workflows which are discussed in the following section.

Typical Workflows

RHEOS can fit and predict both time and frequency data, and the workflow for doing so is very similar. As such, in this section a very brief description of the workflow for fitting time data only is provided, as it maps very closely to the frequency domain case. A schematic

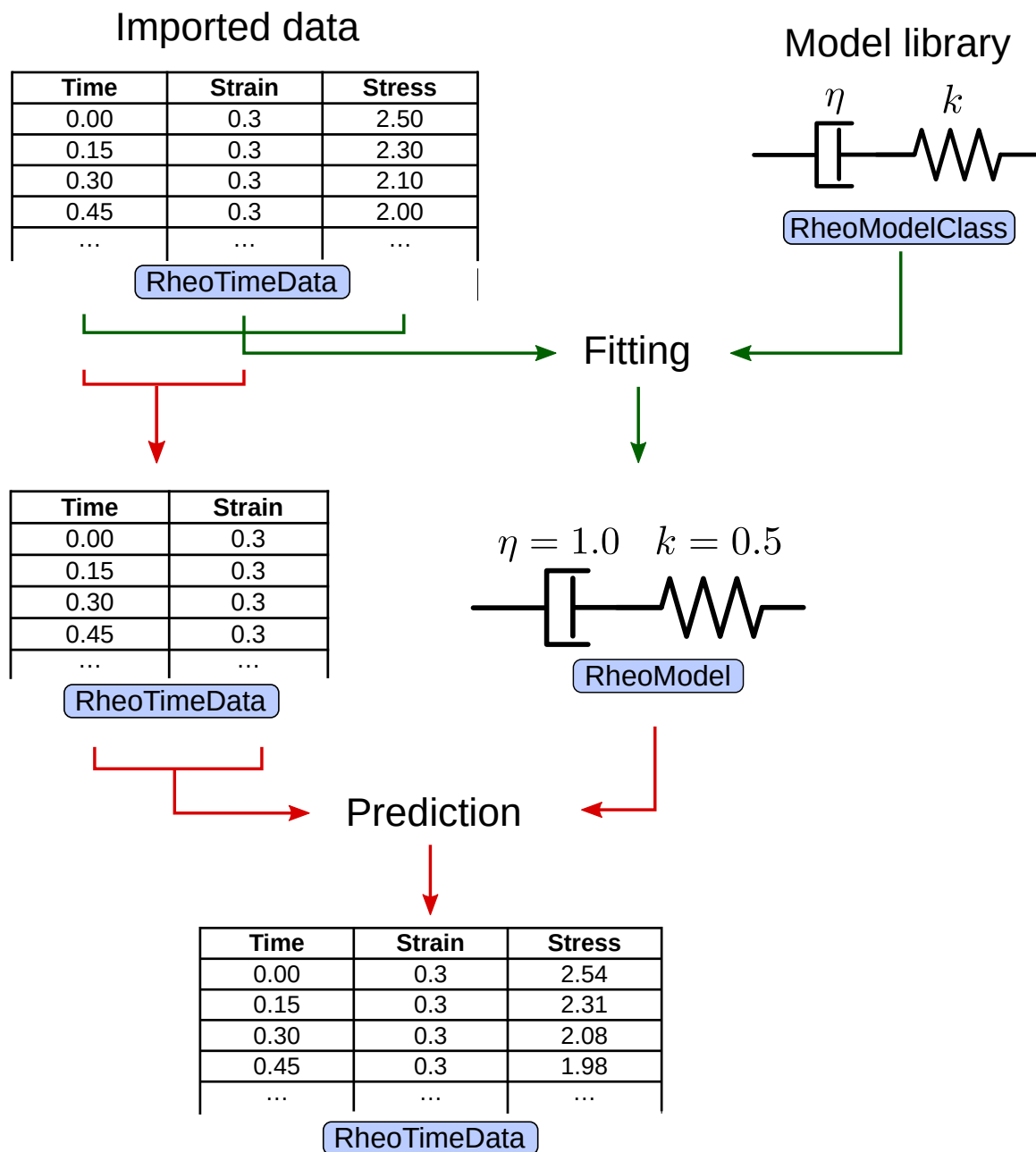


Fig. 4.12 Diagram showing the main objects used by RHEOS and how they relate to each other in a typical workflow case of fitting time-domain data to a viscoelastic model and evaluating its goodness of fit.

diagram of this workflow is shown in Figure 4.12. First, the data can be imported from three column CSV files into a *RheoTimeData* type using a convenience function provided by RHEOS. This data is then fitted to a *RheoModelClass*, which embeds expressions for key characteristics of the model (relaxation function, creep response, complex modulus) involving

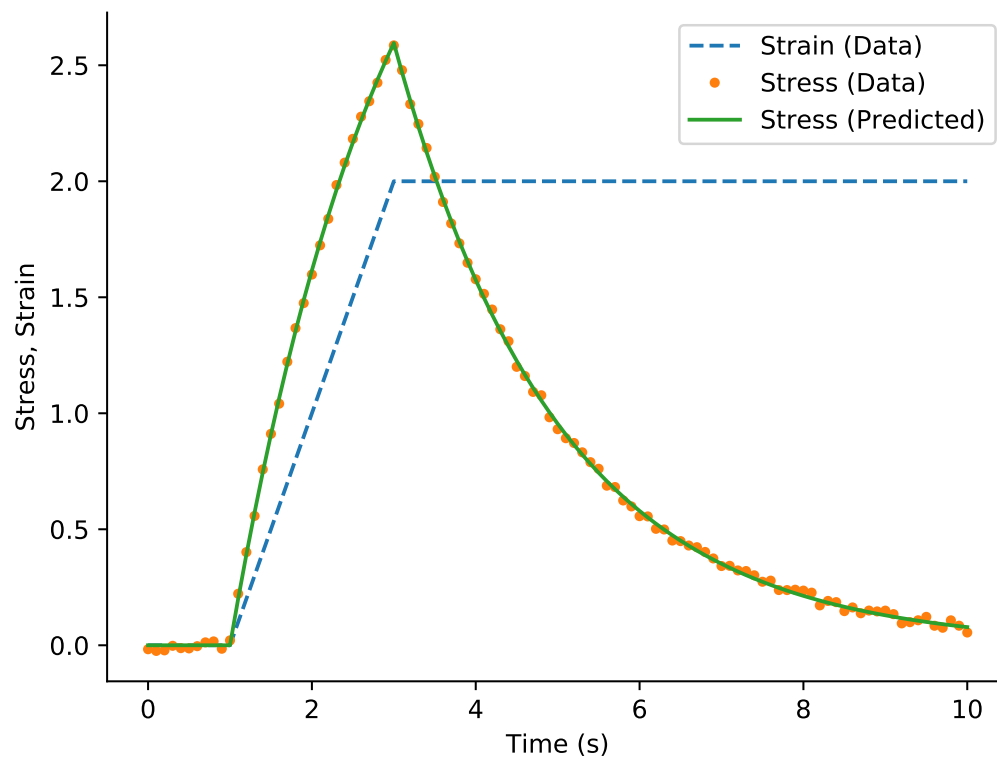


Fig. 4.13 Qualitative assessment of the model fitted and predicted using RHEOS. Sum-of-squares error of fit: $2.23\text{e-}02$ as reported by RHEOS.

symbolic parameters. This fitting process results in a fitted *RheoModel* where the previously symbolic parameters in the *RheoModel* are now substituted with the best-fit parameters found during the fitting process. In the prediction step, the fitted *RheoModel* is combined with partial data (here only time and strain) to simulate the stress values expected from the model. The original data and model can then be compared graphically and numerically. (RHEOS reports the squared-error of the model at the end of the fitting process.) Although the particular example shown in Figure 4.12 shows predicting against the same data used for fitting in order to evaluate the fit, one could also predict against new data not seen by RHEOS during the fitting stage to evaluate how well the model can extrapolate beyond data that it has been fitted against. Lastly, a more concrete demonstration of the above is provided by a figure of the resultant plot from a RHEOS fitting process, Figure 4.13. It is important to note that this was achieved using only three lines of RHEOS code: one for importing the data from a CSV file, one for fitting and one for predicting. Also, it should be noted that the data

for this particular example has been generated computationally by RHEOS for the purpose of this workflow example.

Discussion of Main Data Structures

In this section, the four main data structures of RHEOS are described in more detail. *RheoTimeData* contains the time, strain and stress data as vectors of floating point numbers. It is not necessary for all three to be filled, often only time and strain or time and stress will be filled, such as when predicting data. (For example, you only need time and stress combined with a model to predict a resultant strain.) *RheoTimeData* also contains a log. The log contains information of any processing that has been done to the data (the exact RHEOS functions used and the parameters provided in those function calls). This could include, for example, resampling or smoothing operations. A log can be extracted from one *RheoTimeData* object and applied to another *RheoTimeData* object so that it is processed in exactly the same way. In this way, the log feature can aid reproducibility of analysis. The only difference between *RheoTimeData* and *RheoFreqData* is that *RheoFreqData* contains frequency, storage and loss moduli fields (specific values at all frequencies) as opposed to time, stress and strain fields.

The *RheoModelClass* object contains a number of fields. It contains all of the model's moduli (creep, relaxation, complex). It also stores information on any constraints (such as those on combinations of springpots shown in Appendix B) and these are checked against the initial conditions provided for the fit to make sure they are not violated. The name of the model and an ASCII art schematic representation of it can also be included (and are included for all the models built-in to RHEOS). The symbolic names of the model parameters (e.g. η and k for a Maxwell model) are stored for specialisation purposes after the fitting process. As for the *RheoModelClass* object, the *RheoModel* object stores all the moduli of the model but now they are specialised to the parameters provided (either by the fitting process or the user directly). This means that the moduli embedded in a *RheoModel* object are only functions of time, not time and parameters as would be the case for a *RheoModelClass* object.

Optimisation

In the case of time-domain data, the functions that RHEOS optimises for are essentially rearrangements of the viscoelastic Boltzmann hereditary integrals derived in Chapter 2. Note that for any loading (stress or strain) that is more complex than a perfect step, it is not straightforward to compute the viscoelastic Boltzmann hereditary integral and this

computation is discussed in more detail in Section 4.4.4. Each predicted value is subtracted from the known data value, and this difference is squared. The sum of all these squared differences is the number that is sent to the specialised optimisation routine (not contained within RHEOS) to try and minimise. Written explicitly, the minimisation function if fitting via the relaxation modulus E is the following:

$$\min_{\mathbf{P} \in \mathbb{R}^n} \left(\sum_{t_i}^T \left(\int_0^{t_i} E(t_i - \tau, \mathbf{P}) \dot{\epsilon}(\tau) d\tau - data(t_i) \right)^2 \right), \quad (4.33)$$

where \mathbf{P} is a vector of length n containing the parameters to be fitted, t_i is a specific time sample, T is the final time sample, τ is a dummy integration variable, $\dot{\epsilon}$ is the first derivative of strain, and $data(t_i)$ is the i th data sample of the known force data. Note that the integral in Equation 4.33 must be considered as a discrete integral for computational purposes but the exact method of computing it has been left generic as it is discussed in detail in Section 4.4.4. For fitting against the creep modulus J , we have the following:

$$\min_{\mathbf{P} \in \mathbb{R}^n} \left(\sum_{t_i}^T \left(\int_0^{t_i} J(t_i - \tau, \mathbf{P}) \dot{\sigma}(\tau) d\tau - data(t_i) \right)^2 \right), \quad (4.34)$$

where $\dot{\sigma}$ is the first derivative of stress, and all other symbols have the same meaning as previously, except $data(t_i)$ now represents the i th data sample of the known strain data.

Fitting frequency data is slightly more straightforward as it does not require computation of the viscoelastic Boltzmann hereditary integral. It's minimisation objective is written:

$$\min_{\mathbf{P} \in \mathbb{R}^n} \left(\sum_{\omega_i}^{\Omega} (E'(\omega_i, \mathbf{P}) - dataE'(\omega_i))^2 + (E''(\omega_i, \mathbf{P}) - dataE''(\omega_i))^2 \right), \quad (4.35)$$

where E' and E'' are the storage and loss moduli, ω_i is the i th frequency sample, Ω is the highest frequency, $dataE'(\omega_i)$ is the i th data sample of the known storage modulus data and $dataE''(\omega_i)$ is the i th data sample of the known loss modulus data. Equation 4.35 involves the summation of two squared difference which can sometimes present difficulties to the optimisation algorithm used, especially if $dataE'(\omega_i)$ and $dataE''(\omega_i)$ occupy very different orders of magnitude. Techniques used by RHEOS to alleviate this problem are discussed in Section 4.4.4.

Internally, RHEOS sends the above cost functions to the NLOpt library [306], which itself uses a local optimisation algorithm known as the subplex algorithm, originally developed by in a doctoral thesis [307].

4.4.4 Implementation Discussion

Computation of the Hereditary Integral

A central part of almost any rheology analysis of time domain data involves computation of the hereditary integral derived in Chapter 2. For the reader's convenience, its stress relaxation and creep forms are written below

$$\sigma(t) = \int_0^t E(t - \tau) \dot{\varepsilon}(\tau) d\tau, \quad (4.36)$$

$$\varepsilon(t) = \int_0^t J(t - \tau) \dot{\sigma}(\tau) d\tau, \quad (4.37)$$

where ($\dot{}$) represents the first time derivative. For brevity, the subsequent discussions will just use the relaxation form for examples, though all discussion applies equally to both moduli. There are several ways to approach the computation of the above integrals. A simple method that is extensively used in the literature is to assume a step loading. Mathematically, this is equivalent to assuming that $\dot{\varepsilon}(t) = \varepsilon_0 \delta(t)$, where ε_0 is the constant step amplitude and $\delta(t)$ is the Dirac delta function. Substituting this into Equation 4.36 leads to

$$\sigma(t) = \int_0^t E(t - \tau) \varepsilon_0 \delta(\tau) d\tau, \quad (4.38)$$

and due to the sifting property of the Dirac delta function this can be simplified to

$$\sigma(t) = \varepsilon_0 E(t), \quad t \geq 0. \quad (4.39)$$

From this, the appeal of the step approximation is immediately clear – it enables the modulus to be used directly which vastly reduces the computational burden. It is the fastest approximation as it only requires a multiplication of the array of modulus values. For this reason, RHEOS includes functions to fit and predict using the step approximation. However, depending on the type of test and the hardware used, the step approximation may not be accurate enough. This is particularly important if the short time behaviour, close to the ramp up in stress or strain, is of interest. Or if the stress or strain is not held constant for any reason.

Figures of creep loading data removed for copyright reasons. Copyright holder is Materials Research Society. Figure 1 in original source.



Fig. 4.14 Figures adapted from Oyen [8]. A) Plot showing ramp and hold loading, with t_r as the total ramp time. B) Plot showing multiple ramp and holds.

One approximation for linear ramp and hold loading patterns, expounded by Oyen (creep), and Mattice et al. (relaxation) [8, 50], makes use of a so-called ramp correction factor. The idea behind this is to separate the load into two parts, the ramp and the hold sections. These two sections can be seen in Figure 4.14A. This method was independently developed by Di Paola et al. [308] who also showed that the fitted parameters of a springpot are very sensitive to the ramp presence. Mathematically, the loading is represented as

$$\varepsilon(t) = \begin{cases} \varepsilon_0 t/t_r & 0 \leq t < t_r \\ \varepsilon_0 & t \geq t_r \end{cases}, \quad (4.40)$$

where t_r is the total ramp time, shown on Figure 4.14A. This allows the hereditary integral to be simplified as follows

$$\sigma(t) = \begin{cases} \frac{\varepsilon_0}{t_r} \int_0^t E(t-\tau) d\tau, & 0 \leq t < t_r \\ \frac{\varepsilon_0}{t_r} \int_0^{t_r} E(t-\tau) d\tau, & t \geq t_r \end{cases}, \quad (4.41)$$

both of which are generally analytically tractable as they only require integration of the modulus itself. Although integration may not always be possible for more complex models, the above method has been used successfully with a fractional Kelvin-Voigt model with one springpot simplified to a spring [285]. This method can be extended for multiple linear

ramps, for example the loading shown in Figure 4.14B. The main limitation of this method is that any ramp sections in the loading must be well approximated as linear ramps.

For more complex loading, the entire load history must be taken into account. There are numerous ways of doing this. The most conspicuous method of computation would be to note that it is an integral equation, so regular quadrature methods can be used to compute the value of stress/strain at each time point. However, the computational complexity of this is $\mathcal{O}(n^2)$, where n is the length of the time array. This means that the speed of computation rapidly decreases as the number of time samples increase – this is particularly critical if the modulus depends on the Mittag-Leffler function, which is itself slow to compute. For exponential kernels, which qualifies all non-fractional models but precludes fractional models, the integral's computation can be quickened by splitting up the exponential terms and using the algorithm of Perdikaris and Karniadakis [224]. The key part of this is noting the following

$$I_{t+\Delta t} = \int_0^{t+\Delta t} e^{-\frac{(t+\Delta t-\tau)}{\tau_i}} \dot{\epsilon}(\tau) d\tau = e^{-\frac{\Delta t}{\tau_i}} I_t + \int_t^{t+\Delta t} e^{-\frac{(t+\Delta t-\tau)}{\tau_i}} \dot{\epsilon}(\tau) d\tau, \quad (4.42)$$

in which the i th exponential term has been considered and τ_i is its respective time-scale. In the second form of the RHS, the first term is essentially a memory term. Clearly the above method does not work with power law or Mittag-Leffler kernels, so for fractional models we need to look further. Singh and Chatterjee [309] have developed a method of local Galerkin approximation for some types of fractional viscoelastic kernels, whilst Diethelm and Freed [310] have suggested a highly optimised quadrature algorithm.

A useful property of Equations 4.36 and 4.37 is that they are essentially convolutions, and convolution is just multiplication in frequency space. For this reason, RHEOS takes advantage of the fast FFT based convolution algorithms already implemented in Julia [311] to compute viscoelastic hereditary integrals. Using this method, the algorithmic complexity of the convolution itself is $\mathcal{O}(n \log n)$. More importantly however, the viscoelastic kernel can be precomputed so that the number of calls to the expensive Mittag-Leffler function is minimised at $\mathcal{O}(n)$. In this way, RHEOS is able to compute the viscoelastic hereditary integral with excellent speed performance and for arbitrary loading patterns. A limitation of this method is that it cannot presently be used for variable sample rates, so in the variable case the full quadrature integration is used. However, there are several options to explore for improving this which are discussed in the Future Development section.

Normalisation Procedures for Complex Modulus Fitting

The storage and loss moduli can sometimes occupy different orders of magnitude, see Figure A.4 for an example of this. This can cause problems during fitting as the optimisation routine will weight errors at the higher orders of magnitude more strongly than those at the lower orders of magnitude. This is a more general problem often faced during multi-objective optimisation problems [312]. The main two approaches to solving this issue are careful choice of global optimisation routine, or rescaling. Regarding the former, extensive fittings tests of complex moduli were conducted using RHEOS and local optimisation routines were found to be superior in terms of both computational efficiency and goodness of fit. Regarding the latter, rescaling was found to be increasingly important as the storage and loss modulus diverged in magnitude. For this reason, RHEOS offers four rescaling options. The two that have worked most successfully so far are the local and logarithmic scaling options. The local option rescales the cost at every point by each value of the data point itself, i.e.

$$\min_{\mathbf{P} \in \mathbb{R}^n} \left(\sum_{\omega_i}^{\Omega} \frac{(E'(\omega_i, \mathbf{P}) - dataE'(\omega_i))^2}{dataE'(\omega_i)} + \frac{(E''(\omega_i, \mathbf{P}) - dataE''(\omega_i))^2}{dataE''(\omega_i)} \right), \quad (4.43)$$

where all symbols have the same meaning as described for Equation 4.35. The logarithmic approach simply re-scales all the storage and loss moduli and their predicted values logarithmically before finding the error between them, explicitly:

$$\min_{\mathbf{P} \in \mathbb{R}^n} \left(\sum_{\omega_i}^{\Omega} (\log(E'(\omega_i, \mathbf{P})/dataE'(\omega_i)))^2 + (\log(E''(\omega_i, \mathbf{P})/dataE''(\omega_i)))^2 \right), \quad (4.44)$$

where \log is the natural logarithm and the subtraction has been simplified using standard logarithm manipulation. In both cases, the benefit arises from the fact that the optimisation weighting is rebalanced in favour of smaller values. The logarithmic rescaling method seems to work particularly well but runs into problems if logarithm input is exactly 0 at any frequency, this is due to the negative singularity of the logarithmic function for the 0 argument. A third option in RHEOS divides the cost at each point by the mean value of the storage and loss modulus known data respectively, explicitly:

$$\min_{\mathbf{P} \in \mathbb{R}^n} \left(\sum_{\omega_i}^{\Omega} \frac{(E'(\omega_i, \mathbf{P}) - dataE'(\omega_i))^2}{mean(dataE')} + \frac{(E''(\omega_i, \mathbf{P}) - dataE''(\omega_i))^2}{mean(dataE'')} \right), \quad (4.45)$$

where $mean(dataE')$ and $mean(dataE'')$ are the mean averages of the known storage and loss moduli values respectively, and they are no longer functions of ω_i . This can work well

but performance is hindered if the storage or loss moduli individually vary over many orders of magnitude. The fourth option offered by RHEOS is simply manual weightings provided by the user for each modulus. Explicitly:

$$\min_{\mathbf{P} \in \mathbb{R}^n} \left(\sum_{\omega_i}^{\Omega} \phi_0 (E'(\omega_i, \mathbf{P}) - dataE'(\omega_i))^2 + \phi_1 (E''(\omega_i, \mathbf{P}) - dataE''(\omega_i))^2 \right), \quad (4.46)$$

where ϕ_0 and ϕ_1 are the user-supplied weighting constants. Although this method does not always work well, it is included to provide more flexibility to users.

Choice of Programming Language

The choice of programming language in which RHEOS is written should be briefly discussed. RHEOS is written in Julia [313]. It is a fairly new programming language – the first major version was only released in August 2018, though it has been growing in popularity since at least 2012 [314, 315]. Given the language’s novelty, it might at first seem a strange choice for scientific software that is intended to be as approachable as possible. In fact, it is an ideal choice. Julia provides just-in-time compilation, multiple dispatch and a powerful type system which enables it to achieve C/Fortran levels of computational speed, whilst using syntax that is very straightforward and heavily influenced by Python and MATLAB. Just-in-time compilation ensures that functions are compiled down to optimised machine code, whilst multiple dispatch essentially uses the type system in order to run the correct method with minimal overhead. The computational speed was found to be very important for the more complicated fractional viscoelastic models. The syntax’s similarities to Python and MATLAB are no coincidence, this was an important part of the design of Julia. Python and MATLAB are two of the most popular languages for scientific programming so the syntactic similarity facilitates an easy transition to Julia for the many scientific users of those languages. Lastly, Julia’s design, with multiple dispatch at its core, encourages the so-called ‘generic’ programming paradigm, wherein data structures and algorithms can be defined in a generic way that accomplishes multiple programming tasks simultaneously and facilitates inter-linking of different scientific software packages [316]. This may help RHEOS become integrated into other related projects.

Software Engineering Best Practice

Scientific software has a reputation for being structured in ways that increase the risk of pernicious errors, and reduce readability and maintainability [317]. As such, there is growing

awareness of the need for properly tested and documented scientific software [318]. Throughout the development of RHEOS, effort has been made to follow software engineering best practice as far as possible. The ways in which this has been achieved are briefly discussed in the following. First, from the ground up the code has been written to be as readable as possible so that it can quickly be understood by more advanced users who may desire to understand exactly what RHEOS is doing, and to facilitate peer review of the code. Secondly, RHEOS is fully documented using Julia's documentation package which allows online documentation to be easily updated, promoting long term maintenance. All the user-exposed functions have a doc string attached so that their call signatures and description can be accessed locally in a convenient manner. In terms of tooling, GIT has been used throughout RHEOS' development to facilitate collaboration with other members of the group. It is hoped that this will also encourage collaboration from other users in the future. Further, the Julia testing suite has been used, though complete testing coverage is still under development. The testing has been setup to work with the continuous integration services Travis CI [319] and AppVeyor [320] which run the tests on servers running Linux and Windows, thus promoting cross platform compatibility. Lastly, RHEOS has been licensed under the MIT open-source license which is extremely permissive and will hopefully encourage participation from the open-source scientific community.

4.4.5 Future Development

Functionality Extensions

There are plans to add a number of additional features to RHEOS – some of these are mentioned here. Regarding frequency based data, a convenience function will be added to transform $|G^*|$ and complex phase angle into G' and G'' data which can then be fitted in RHEOS. Regarding the hereditary integral, the most pressing requirement is an improvement to the computational speed of variable sample-rate datasets, and also those fractional viscoelastic kernels that contain the Mittag-Leffler function. Regarding the former, non-uniform fast Fourier transform convolutions will be investigated, aswell as the algorithms by Singh and Chatterjee [309], and Diethelm and Freed [310]. Regarding the latter, a similar method to Perdikaris and Karniadakis [224] will be tested as it enabled the computation of the hereditary integral in the Laplace domain in such a way as to avoid computing the Mittag-Leffler function in the time domain entirely. Another approach which could potentially benefit both issues is computing the model fitting process via the differential equation itself rather than the creep or relaxation moduli; preliminary testing of this approach has already proved promising.

Two further benefits of this approach are that it is entirely creep/relaxation agnostic so no choice of modulus would be required by the user, and it provides a good way of handling moduli singularities. (The latter point is discussed in more detail in the next section.) Lastly, the biggest current limitation of RHEOS is the fact that it only handles linear viscoelasticity. Work will be undertaken to implement non-linear viscoelasticity.

Singularities Within the Hereditary Integral

Although RHEOS has a fairly good method of approximating fractional viscoelastic models with singularities, several other approaches for handling these singularities are still under investigation. To be clear, this section is mostly concerned with singularities within the fractional viscoelastic moduli and not the Dirac delta function used to simulate step loading in stress or strain. The Dirac delta function is more amenable to approximation by a simple hat function, so long as it is ensured that integrating across it yields a Heaviside function then it will behave as required for our needs. It appears that the MPL model discussed above, and other empirical models such as the logarithmic Kuhn/Becker model [22, 321], were formulated specifically to get around the issue of the singular moduli. Indeed, this provides us with the simplest way to remove the issue, just add a spring in series or otherwise modify the moduli such that the singularity is removed. However, this approach would result in RHEOS no longer fitting into the self-consistent fractional viscoelastic framework of springs, springpots and dashpots, and the models provided would just be a collection of moduli with *ad-hoc* singularity removals. In fact, for the singularities encountered in Appendix B, the removal of the singularity should not be necessary because although the singular moduli yield hereditary integrals that are stated improperly, they are convergent. To see this we can consider a twice differentiable loading ε , which numerical experimental data always will be, and the springpot relaxation modulus. Integrating by parts, and noting that $z\Gamma(z) = \Gamma(z+1)$, we find

$$\begin{aligned}
 \sigma(t) &= \frac{1}{\Gamma(1-\beta)} \int_0^t (t-\tau)^{-\beta} \dot{\varepsilon}(\tau) d\tau \\
 &= \frac{-(t-\tau)^{1-\beta} \dot{\varepsilon}(\tau)}{\Gamma(2-\beta)} \Big|_0^t - \int_0^t \frac{-(t-\tau)^{1-\beta} \ddot{\varepsilon}(\tau)}{\Gamma(2-\beta)} d\tau \\
 &= \frac{t^{1-\beta} \dot{\varepsilon}(0)}{\Gamma(2-\beta)} + \int_0^t \frac{(t-\tau)^{1-\beta} \ddot{\varepsilon}(\tau)}{\Gamma(2-\beta)} d\tau
 \end{aligned} \tag{4.47}$$

which is now stated in proper form so the convergence of the integral is immediately clear. From this, we know that there is a convergent answer which can be calculated, but the best

way to achieve this numerically is still not obvious. At present RHEOS approximates the singularity by a method known as ‘avoiding the singularity’ [310, 322]. In concrete terms, this is done by not actually including the singular point but approximating it by taking a small offset distance from it, set to $\Delta t/10$ where Δt is the sample period. This works well but can introduce a small error that is difficult to quantify exactly as its value depends upon the loading imposed. (A representative example is shown in Appendix E.) For this reason, other approaches will be considered in future versions of RHEOS.

One approach that will be investigated is the same method used to attain Equation 4.47, i.e. integration by parts, which yields an equation that is immediately amenable to quadrature or FFT convolutional methods without modification as there are no singularities in the kernel. Another nice feature of this method is its ability to handle a step at time $t = 0$; as long as the step is approximated by a hat function as discussed above and we allocate the apex of the hat function to be the first element of the strain derivative array $\dot{\epsilon}$. Two possible drawbacks of this approach are the accumulation of error when using finite difference on noisy experimental error to calculate the second derivative, and the requirement that the integral of all singular moduli need to be stored in RHEOS which is slightly inelegant.

Another option is to keep the Laplace transform of the modulus stored in RHEOS and use it to calculate the convolution in the complex domain. This is similar to the method used by Perdikaris and Karniadakis [224] but the model used in that study was a fractional SLS that does not have any singularities, the authors used it to avoid approximation of the Mittag-Leffler function in the time domain. The numerical stability with time-domain singular models requires further exploration. A third possibility is to always use creep moduli when fitting as these never contain singularities. However, without testing it is not clear whether this works in all cases of arbitrary data.

Lastly, a fourth approach which at present appears the most promising. It avoids creep and relaxation moduli completely and just uses the differential equation of the model. For this reason it is currently only suitable for fitting, though if the method could be achieved using spectral differentiation then it could also be extended for predicting responses as well as fitting duties. Clearly it is also limited to models for which the differential equation is known, which may preclude some empirical models. The true strength of this method can be seen by considering the relaxation modulus of the dashpot, and noting that it is equal to its differential form

$$\sigma(t) = \eta \int_0^t \delta(t - \tau) \dot{\epsilon}(\tau) d\tau = \eta \dot{\epsilon}. \quad (4.48)$$

The intermediate representation is numerically intractable, whilst the differential representation is well defined and easy to compute. From this it can be seen that because the assumption of an unphysical step is a necessary part of the derivation of creep/relaxation moduli, the creep/relaxation moduli paradigm leads to numerical issues which can be effortlessly avoided by use of the constitutive differential equations of the models. (This is another strong benefit of the viscoelastic models derived through a framework of well defined viscoelastic units as they naturally yield a constitutive differential equation.) For a more complicated example, consider the differential equation of the fractional Kelvin-Voigt model from Appendix B

$$\sigma(t) = c_\alpha \frac{d^\alpha \varepsilon(t)}{dt^\alpha} + c_\beta \frac{d^\beta \varepsilon(t)}{dt^\beta} \quad (4.49)$$

which can easily be rearranged to form an objective function for minimisation routines. Explicitly:

$$\min_{c_\alpha, \alpha, c_\beta, \beta \in \mathbb{R}} \left(\sum_{t_i}^T \left(c_\alpha \frac{d^\alpha \varepsilon(t_i)}{dt^\alpha} + c_\beta \frac{d^\beta \varepsilon(t_i)}{dt^\beta} - \sigma(t_i) \right)^2 \right), \quad (4.50)$$

where $\varepsilon(t_i)$ and $\sigma(t_i)$ are known data samples of the strain and stress respectively. The relaxation function of this model has singularities, whilst the creep form depends on the Mittag-Leffler function. By using the differential equation form, we have avoided all singularity issues, avoided computation of the expensive Mittag-Leffler function, and we have made the entire fitting process completely creep/relaxation agnostic. This last point can be exploited to make the RHEOS user interface simpler, as a modulus would not even have to be chosen by the user. To calculate the fractional derivatives in Equation 4.49, the integration by parts method shown in Equation 4.47 could be used, followed by convolution, or one of the many numerical Caputo derivative algorithms presented in the literature [207, 323–327] – spectral methods are of particular interest for the reason discussed above that they may also allow the differential equation form to be used for prediction as well as fitting.

Future RHEOS Extension With Contact Models

There are also plans to build additional rheology software packages on top of RHEOS. For one, a project which already has some preliminary work done is a package that contains additional functions and data structures designed for experiments whose data can be mapped to an effective stress and effective strain. This could enable those doing indentation or magnetic tweezer experiments to easily make use of RHEOS' functionality. Consider for example the Hertz model used in Chapter 3, apart from raising the displacement to the power 3/2 element-wise and multiplying by a prefactor, all of the other operations that might

be required for fitting and predicting viscoelastic behaviour are the same. Concretely, the hereditary integral with a Hertz indentation model can be written

$$f(t) = \frac{8\sqrt{R}}{3} \int_0^t G(t-\tau) \frac{d}{d\tau} \delta^{3/2}(\tau) d\tau, \quad (4.51)$$

letting $\sigma_{eff} = f(t)$, and $\varepsilon_{eff} = (8\sqrt{R}/3)\delta^{3/2}$ results in

$$\sigma_{eff}(t) = \int_0^t G(t-\tau) \frac{d}{d\tau} \varepsilon_{eff}(\tau) d\tau, \quad (4.52)$$

which can be treated as a regular hereditary integral by RHEOS. Although the physical units are not the same, they are conceptually comparable. The Julia programming language, particularly the fields and properties feature added in version 1.0, will greatly facilitate integration of this extension package with RHEOS. Of course, it must be noted that not all contact models are amenable to the above type of transform and additional work will be required to implement those models.

4.5 Conclusion

In this chapter, fractional viscoelasticity has been introduced, and its utility demonstrated. Fractional viscoelastic counterparts to a number of empirical models from the literature have been discussed, and a number of studies on biomaterials have been re-analysed using fractional viscoelastic models with comparison made to the traditional models used in the original studies. It was shown that the fractional viscoelastic models were able to better characterise the biomaterials using the same or fewer parameters. The pectin data from Chapter 3 was re-evaluated using a fractional SLS model which was found to provide a similarly good fit whilst using one less parameter. The results across different pectin gel types were then discussed in light of the fractional viscoelastic results; a phenomenological interpretation of the fractional model's parameters was consistent with that found previously using the SLS2 model.

A software implementation of fractional viscoelastic models and their fitting and predicting functionality was then discussed. The motivation was outlined, followed by the main deliverables of the software, which were claimed to have already been fulfilled. (To further demonstrate the meeting of the main goals of RHEOS, the main features were demonstrated with the aid of code examples and plots where appropriate in Appendix A.) This was followed

by more detailed discussion of the technical implementation of RHEOS. Finally, plans for the future development of RHEOS and associated packages was detailed.

Chapter 5

Conclusions

*We shall not cease from exploration
And the end of all our exploring
Will be to arrive where we started
And know the place for the first time.*

*T. S. Eliot, 1942
Little Gidding*

5.1 Summary of Findings

In this thesis, methods for the viscoelastic analysis of pectin *in vitro* and *Arabidopsis* seedlings using the AFM have been developed and used to further understanding of their viscoelastic character. Whilst AFM does not appear to have been used previously for viscoelastic testing of pectin *in vitro*, it has been used in viscoelastic tests on *Arabidopsis*. The creep methodology presented in this thesis complements the bimodal AFM analysis developed by Seifert [44], and the dissipation based methods developed by Fernandes et al. [43]. For both material types, an SLS2 model was used for the majority of the discussion as it was found to provide a good fit. A fractional SLS model was found to provide a similarly good fit for pectin *in vitro* whilst using one less model parameter. Fitting the fractional model to the *Arabidopsis* hypocotyls data yielded a near exponential springpot component which suggested that a fractional modelling approach was not appropriate *in vivo*. This is perhaps surprising given that pectin is the largest constituent of the hypocotyl cell wall by volume; although the stiff elastic cellulose microfibrils in the wall, perhaps in conjunction with the hemicelluloses, likely account for the discrepancy, their precise role could not be pinned down by the methods used in this study. Regarding *in vitro* pectin, physical insights from

both the traditional and fractional models were in agreement. Where possible, comparisons were made with bulk DMA rheology data from the literature which was in good general agreement with the findings from both models. Having said this, it is the authors conviction that the relaxation test and model based approach presented here contribute a greater physical insight into pectin gels behaviour than the model-free DMA approach. It was observed that both elastic and viscous parameters were negatively correlated with DM. In DM40 pectin gels with different patterns of de-esterification, one random and one blockwise, the ISS was found to be correlated with DB and inversely correlated with elastic/viscous ratio. This is in accordance with the hypothesis that ionic bond reformation of random de-esterified pectin is perceived as more elastic by the models, whereas block de-esterified relaxation behaviour is dominated by longer time-scale behaviours. Mixed DM gels were also investigated and the non-linear relationship between gel ISS and DM was found to explain the discrepancies between mixed and pure DM gels' mechanical integrity. With regards to the *Arabidopsis* hypocotyl testing, the relative ISS was found to be in agreement with previous elastic studies, i.e. significantly higher in transverse walls than axial walls. The time for creep to plateau was found to be slower in axial walls than transverse walls, in contrast to the gels which displayed similar timescales over the range of DMs tested. The mean plateau shear stiffness was closer between wall types than the instantaneous shear stiffness indicating the possibility of mechanical coupling between axial and transverse walls at longer time-scales.

Fractional viscoelasticity was explored through use of existing data in the literature and was found to provide an improved goodness of fit using the same or less parameters for the studies examined. This observation, in addition to the aforementioned suitability of a fractional model for pectin *in vitro*, and the mathematical complexity of fractional viscoelasticity, led to the development of an open-source software package for rheology analysis, RHEOS. The deliverables of the software were enumerated. The features and implementation specifics were also outlined.

In summary, the main contributions of this thesis are the following.

- Development and validation of an AFM protocol for viscoelastic testing of pectin *in vitro*.
- Use of the above to improve understanding of pectin mechano-chemistry.
- Adaptation of the AFM methodology for testing *in planta*, used to investigate symmetry breaking in the *Arabidopsis* hypocotyl.

- Demonstration of fractional viscoelastic models' capacity to improve fitting quality and/or model parsimony for several studies in the literature, and *in vitro* pectin data.
- Development of an open-source software package, RHEOS, for rheological data analysis with an emphasis on increasing the usability of fractional viscoelastic models.

5.2 Future Work

The work presented in this thesis generates a number of scientific questions and pathways for further development. Regarding the experimental work in pectin, the AFM viscoelastic protocol will enable fine spatial resolution mechanical studies which may provide valuable insight into the relationship between pectin fine structure and observed mechanical properties. This could be combined with a larger variety of pectin formulations, perhaps including constituents which are relevant to industrial application such as sucrose. For developmental considerations, further work could be done to investigate the conditions required for linearity, particularly closer to syneresis. Further testing should be done to develop the plastic deformation assessment protocol suggested at the end of Chapter 3. Preliminary tests indicate that there may be plastic deformation occurring; this should be further investigated and, if confirmed, should inform an updated choice of model that incorporates a dashpot in series. Chemical perturbations may be useful in determining the physical mechanisms which underpin the elastic, viscous and plastic modes of deformation. More work should be done to identify limitations of the proposed fractional model for different formulations of pectin *in vitro*, for example at the extremes of low/high concentration, DB, DM or calcium concentration. Given the difficulty of disentangling the mechanical contribution of the various components of the plant cell wall, it would be fascinating to bring together the remarkable array of *in vitro* cellulose/pectin/hemicelluloses composites generated by authors in recent years with the generic modelling power of the fractional viscoelastic framework. With this combination, the interplay between model parameters, composite components and physical modes of deformation could be thoroughly investigated. In practice, having an effective modelling framework with which to predict the mechanical properties of pectin and pectin composites will be useful in food and biotechnology fields as it will allow pectin formulations to be reverse engineered based on their desired rheological properties, thereby significantly reducing product development time.

In *Arabidopsis*, there are several ways in which the work presented here could be developed further. In the first instance, viscoelastic tests could be carried out at a higher spatial resolution, and topographic rheological maps could be generated for the various

model parameters. (RHEOS would facilitate analysis by virtue of its fast computational speed.) This would help disentangle the various cell wall components which contribute to the observed mechanical properties. Most particularly with regard to the potential coupling of rheology observed at longer time-scales, and potential geometric effects. Further, it would be interesting to test the methodology used here in other *Arabidopsis* tissue at different developmental stages. The data from these tests could also be fitted to the SLS2 model and combined with existing knowledge of the cell wall architecture to develop a clearer picture of the contribution of specific cell wall components to the magnitude of the model parameters. It would also provide a good test of whether or not the SLS2 model itself can successfully be applied to *Arabidopsis* tissue beyond the hypocotyl. With the methodology and model further validated in other tissues, more complex studies could be undertaken. Of particular interest to the author is the mechanical contribution to morphogenesis. To investigate this, genetic alterations could be made to various cell-wall related genes via agrobacteria, but only to individual cells. The viscoelastic properties of the infected cell and surrounding cells could then be tested to investigate how adjacent cells compensate for stronger/weaker cells. More generally, the data presented here, and future data generated using the presented methodology could be used to inform the computational and mathematical models of *Arabidopsis* morphogenesis, many of which previously relied on elastic stiffness as a proxy material parameter.

Regarding fractional viscoelasticity more generally, there is plenty of work to be done in simply spreading word of its utility. RHEOS will hopefully help with this process by lowering barriers to entry. Regarding RHEOS itself, there are many options for expanding its functionality. These improvements, which are detailed in Chapter 4, can be summarised as improved data processing convenience functions, and improvements to the efficiency and accuracy of the fitting/predicting process. The planned extension for contact model compatible data types should widen the appeal of RHEOS, particularly as indentation methods are popular for biomaterials which, as demonstrated in Chapter 4, are often well suited to fractional viscoelastic models. The contact model extension will also aid the suggested future work in pectin and *Arabidopsis* on fine spatial resolution as it will enable large indented rheological mapping data to be processed with RHEOS, which provides excellent computational efficiency.

References

- [1] Davis JG. 162. The Rheology of Cheese, Butter and Other Milk Products. (The Measurement of “Body” and “Texture”). *Journal of Dairy Research*. 1937 Jun;8(2):245–264. Available from: <https://doi.org/10.1017/S0022029900002090>.
- [2] Cleland R. Auxin and the Mechanical Properties of the Cell Wall*. *Annals of the New York Academy of Sciences*. 1967;144(1):3–18. Available from: <https://nyaspubs.onlinelibrary.wiley.com/doi/abs/10.1111/j.1749-6632.1967.tb33997.x>.
- [3] Robinson S, Huflejt M, de Reuille PB, Braybrook SA, Schorderet M, Reinhardt D, et al. An Automated Confocal Micro-Extensometer Enables *in Vivo* Quantification of Mechanical Properties with Cellular Resolution. *The Plant Cell*. 2017 Dec;29(12):2959–2973. Available from: <http://www.plantcell.org/content/29/12/2959>.
- [4] Cheftel H, Mocquard J. Contribution to the Study of the Rheological Properties of Pectin Jellies. *Journal of the Society of Chemical Industry*. 1947 Sep;66(9):297–299. Available from: <http://doi.wiley.com/10.1002/jctb.5000660901>.
- [5] Arbogast KB, Thibault KL, Scott Pinheiro B, Winey KI, Margulies SS. A High-Frequency Shear Device for Testing Soft Biological Tissues. *Journal of Biomechanics*. 1997 Jul;30(7):757–759. Available from: <http://www.sciencedirect.com/science/article/pii/S0021929097000237>.
- [6] Linardić M. The Role of Brown Algal Cell Walls in Morphogenesis and Development. University of Cambridge. Cambridge; 2018.
- [7] Bonfanti A, Fouchard J, Khalilgharibi N, Charras G, Kabla A. A Unified Rheological Model for Cells and Cellularised Materials. *bioRxiv*. 2019 Feb;p. 543330. Available from: <https://www.biorxiv.org/content/10.1101/543330v1>.
- [8] Oyen ML. Spherical Indentation Creep Following Ramp Loading. *Journal of Materials Research*. 2005 Aug;20(08):2094–2100. Available from: http://www.journals.cambridge.org/abstract_S0884291400089536.
- [9] Thompson DW. *On Growth and Form*. 2nd ed. Cambridge University Press; 1945.
- [10] Scott Blair GW. Rheology in Food Research. In: Mrak EM, Stewart GF, editors. *Advances in Food Research*. vol. 8. Academic Press; 1958. p. 1–61. Available from: <http://www.sciencedirect.com/science/article/pii/S0065262808600178>.
- [11] Scott Blair GW. *A SURVEY OF GENERAL AND APPLIED RHEOLOGY*. 2nd ed. London: Sir Isaac Pitman & Sons, LTD; 1949.

- [12] Scott Blair GW. AN INTRODUCTION TO BIORHEOLOGY. Amsterdam: Elsevier Scientific Publishing Company; 1974.
- [13] Engler AJ, Sen S, Sweeney HL, Discher DE. Matrix Elasticity Directs Stem Cell Lineage Specification. *Cell*. 2006 Aug;126(4):677–689. Available from: <http://linkinghub.elsevier.com/retrieve/pii/S0092867406009615>.
- [14] Chaudhuri O, Gu L, Klumpers D, Darnell M, Bencherif SA, Weaver JC, et al. Hydrogels with Tunable Stress Relaxation Regulate Stem Cell Fate and Activity. *Nature Materials*. 2016 Mar;15(3):326–334. Available from: <http://www.nature.com/articles/nmat4489>.
- [15] Charrier EE, Pogoda K, Wells RG, Janmey PA. Control of Cell Morphology and Differentiation by Substrates with Independently Tunable Elasticity and Viscous Dissipation. *Nature Communications*. 2018 Jan;9(1):449. Available from: <https://www.nature.com/articles/s41467-018-02906-9>.
- [16] Laronda MM, Rutz AL, Xiao S, Whelan KA, Duncan FE, Roth EW, et al. A Bio-prosthetic Ovary Created Using 3D Printed Microporous Scaffolds Restores Ovarian Function in Sterilized Mice. *Nature Communications*. 2017 May;8:15261. Available from: <https://www.nature.com/articles/ncomms15261>.
- [17] Mohnen D. Pectin Structure and Biosynthesis. *Current Opinion in Plant Biology*. 2008;11:266–277. Available from: <https://doi.org/10.1016/j.pbi.2008.03.006>.
- [18] Tieman DM, Handa AK. Reduction in Pectin Methylesterase Activity Modifies Tissue Integrity and Cation Levels in Ripening Tomato (*Lycopersicon Esculentum* Mill.) Fruits. *Plant Physiology*. 1994 Oct;106(2):429–436. Available from: <http://www.plantphysiol.org/lookup/doi/10.1104/pp.106.2.429>.
- [19] Ali ZM, Chin LH, Lazan H. A Comparative Study on Wall Degrading Enzymes, Pectin Modifications and Softening during Ripening of Selected Tropical Fruits. *Plant Science*. 2004 Aug;167(2):317–327. Available from: <http://www.sciencedirect.com/science/article/pii/S0168945204001530>.
- [20] Barnes HA, Hutton JF, Walters K. An Introduction to Rheology. Amsterdam, The Netherlands: Elsevier; 1989.
- [21] Gutierrez-Lemini D. In: Constitutive Equations in Hereditary Integral Form. Boston, MA: Springer US; 2014. p. 23–52. Available from: http://link.springer.com/10.1007/978-1-4614-8139-3_2.
- [22] Lakes R. Viscoelastic Materials. Cambridge: Cambridge University Press; 2009. Available from: <http://ebooks.cambridge.org/ref/id/CBO9780511626722>.
- [23] Heyn ANJ. Der Mechanismus Der Zellstreckung. Amsterdam: De Bussy; 1931.
- [24] Khalilgharibi N, Fouchard J, Asadipour N, Yonis A, Harris A, Mosaffa P, et al. Stress Relaxation in Epithelial Monolayers Is Controlled by Actomyosin. *bioRxiv*. 2018 Apr;p. 302158. Available from: <https://www.biorxiv.org/content/10.1101/302158v1>.

- [25] Li Z, Zhang Z, Thomas C. Viscoelastic-Plastic Behavior of Single Tomato Mesocarp Cells in High Speed Compression-Holding Tests. *Innovative Food Science & Emerging Technologies*. 2016 Apr;34:44–50. Available from: <http://linkinghub.elsevier.com/retrieve/pii/S1466856416000175>.
- [26] Zhao X, Huebsch N, Mooney DJ, Suo Z. Stress-Relaxation Behavior in Gels with Ionic and Covalent Crosslinks. *Journal of Applied Physics*. 2010 Mar;107(6):063509. Available from: <http://aip.scitation.org/doi/10.1063/1.3343265>.
- [27] Gibbs DA, Merrill EW, Smith KA, Balazs EA. Rheology of Hyaluronic Acid. *Biopolymers*. 1968 Jun;6(6):777–791. Available from: <http://doi.wiley.com/10.1002/bip.1968.360060603>.
- [28] Basoli F, Giannitelli SM, Gori M, Mozetic P, Bonfanti A, Trombetta M, et al. Biomechanical Characterization at the Cell Scale: Present and Prospects. *Frontiers in Physiology*. 2018 Nov;9. Available from: <https://www.frontiersin.org/article/10.3389/fphys.2018.01449/full>.
- [29] Colin-York H, Fritzsche M. The Future of Traction Force Microscopy. *Current Opinion in Biomedical Engineering*. 2018 Mar;5:1–5. Available from: <http://www.sciencedirect.com/science/article/pii/S2468451117300727>.
- [30] Schächtele M, Hänel E, Schäffer TE. Resonance Compensating Chirp Mode for Mapping the Rheology of Live Cells by High-Speed Atomic Force Microscopy. *Applied Physics Letters*. 2018 Aug;113(9):093701. Available from: <http://aip.scitation.org/doi/10.1063/1.5039911>.
- [31] Solares SD, An S, Long CJ. Multi-Frequency Tapping-Mode Atomic Force Microscopy beyond Three Eigenmodes in Ambient Air. *Beilstein Journal of Nanotechnology*. 2014 Sep;5(1):1637–1648. Available from: <https://www.beilstein-journals.org/bjnano/articles/5/175>.
- [32] Niedermayer T, Eckhardt B, Lenz P. Synchronization, Phase Locking, and Metachronal Wave Formation in Ciliary Chains. *Chaos*. 2008;18.
- [33] Alcaraz J, Buscemi L, Pui-de-Morales M, Colchero J, Baró A, Navajas D. Correction of Microrheological Measurements of Soft Samples with Atomic Force Microscopy for the Hydrodynamic Drag on the Cantilever. *Langmuir*. 2002;18:716–721. Available from: <http://dx.doi.org/10.1021/la0110850>.
- [34] Milani P, Braybrook SA, Boudaoud A. Shrinking the Hammer: Micromechanical Approaches to Morphogenesis. *Journal of Experimental Botany*. 2013;64(15):4651–62. Available from: <https://doi.org/10.1093/jxb/ert169>.
- [35] Majda M, Grones P, Sintorn IM, Vain T, Milani P, Krupinski P, et al. Mechanochemical Polarization of Contiguous Cell Walls Shapes Plant Pavement Cells. *Developmental Cell*. 2017 Nov;43(3):290–304.e4. Available from: <https://linkinghub.elsevier.com/retrieve/pii/S1534580717308304>.
- [36] Braybrook SA. Measuring the Elasticity of Plant Cells with Atomic Force Microscopy. In: Paluch E, editor. *Biophysical Methods in Cell Biology*. vol. 125. Cambridge, Massachusetts: Academic Press; 2015. p. 237–254.

- [37] Alcaraz J, Buscemi L, Grabulosa M, Trepas X, Fabry B, Farré R, et al. Microrheology of Human Lung Epithelial Cells Measured by Atomic Force Microscopy. *Biophysical Journal*. 2003;84:2071–2079. Available from: [http://dx.doi.org/10.1016/S0006-3495\(03\)75014-0](http://dx.doi.org/10.1016/S0006-3495(03)75014-0).
- [38] Ketene AN, Schmelz EM, Roberts PC, Agah M. The Effects of Cancer Progression on the Viscoelasticity of Ovarian Cell Cytoskeleton Structures. *Nanomedicine: Nanotechnology, Biology and Medicine*. 2012 Jan;8(1):93–102. Available from: <http://linkinghub.elsevier.com/retrieve/pii/S1549963411001845>.
- [39] Moreno-Flores S, Benitez R, dM Vivanco M, Toca-Herrera JL. Stress Relaxation and Creep on Living Cells with the Atomic Force Microscope: A Means to Calculate Elastic Moduli and Viscosities of Cell Components. *Nanotechnology*. 2010 Nov;21(44):445101. Available from: <http://stacks.iop.org/0957-4484/21/i=44/a=445101?key=crossref.d2cf510398a1237607dc9356a038e678>.
- [40] Efremov YM, Wang WH, Hardy SD, Geahlen RL, Raman A. Measuring Nanoscale Viscoelastic Parameters of Cells Directly from AFM Force-Displacement Curves. *Scientific Reports*. 2017 May;7(1):1541. Available from: <https://doi.org/10.1038/s41598-017-01784-3>.
- [41] Wang B, Wang W, Wang Y, Liu B, Liu L. Dynamical Modeling and Analysis of Viscoelastic Properties of Single Cells. *Micromachines*. 2017 Jun;8(6):171. Available from: <http://www.mdpi.com/2072-666X/8/6/171>.
- [42] Peaucelle A, Braybrook SA, Le Guillou L, Bron E, Kuhlemeier C, Höfte H. Pectin-Induced Changes in Cell Wall Mechanics Underlie Organ Initiation in *Arabidopsis*. *Current Biology*. 2011;21:1720–1726. Available from: <https://doi.org/10.1016/j.cub.2011.08.057>.
- [43] Fernandes AN, Chen X, Scotchford CA, Walker J, Wells DM, Roberts CJ, et al. Mechanical Properties of Epidermal Cells of Whole Living Roots of *Arabidopsis Thaliana*: An Atomic Force Microscopy Study. *Physical Review E*. 2012 Feb;85(2). Available from: <https://link.aps.org/doi/10.1103/PhysRevE.85.021916>.
- [44] Seifert J. *In Vivo* Dynamic AFM Mapping of Viscoelastic Properties of the Primary Plant Cell Wall. University of Oxford; 2018.
- [45] Johnson KL. *Contact Mechanics*. Cambridge University Press; 1987.
- [46] Popov VL. *Contact Mechanics and Friction: Physical Principles and Applications*. Springer Science & Business Media; 2010.
- [47] Lin YY, Hui CY, Baney JM. Viscoelastic Contract, Work of Adhesion and the JKR Technique. *Journal of Physics D: Applied Physics*. 1999 Sep;32(17):2250–2260. Available from: <http://stacks.iop.org/0022-3727/32/i=17/a=316?key=crossref.a88aa43b095013f179a4c565b50910e8>.
- [48] Barthel E. Adhesive Elastic Contacts: JKR and More. *Journal of Physics D: Applied Physics*. 2008 Aug;41(16):163001. Available from: <http://stacks.iop.org/0022-3727/41/i=16/a=163001?key=crossref.29f23ff178c2c68a59f2067d84f6dd5d>.

- [49] Lee EH, Radok JRM. The Contact Problem for Viscoelastic Bodies. *Journal of Applied Mechanics*. 1960 Sep;27(3):438–444. Available from: <http://dx.doi.org/10.1115/1.3644020>.
- [50] Mattice JM, Lau AG, Oyen ML, Kent RW. Spherical Indentation Load-Relaxation of Soft Biological Tissues. *Journal of Materials Research*. 2006 Aug;21(08):2003–2010. Available from: http://www.journals.cambridge.org/abstract_S0884291400083771.
- [51] Hunter SC. THE HERTZ PROBLEM FOR A RIGID SPHERICAL INDENTER AND A VISCOELASTIC HALF-SPACE. *Journal of the Mechanics and Physics of Solids*. 1960;p. 16. Available from: [https://doi.org/10.1016/0022-5096\(60\)90028-4](https://doi.org/10.1016/0022-5096(60)90028-4).
- [52] Ting TCT. The Contact Stresses Between a Rigid Indenter and a Viscoelastic Half-Space. *Journal of Applied Mechanics*. 1966;33(4):845. Available from: <http://AppliedMechanics.asmedigitalcollection.asme.org/article.aspx?articleid=1397955>.
- [53] Culpeper N. *The Complete Herbal*. London: Thomas Kelly; 1653.
- [54] Spanner DC. In: *Botanical Aspects of Biorheology*. Amsterdam: Elsevier Scientific Publishing Company; 1974. .
- [55] Green P. Mechanism for Plant Cellular Morphogenesis. *Science*. 1962;138(3548):1404–1405. Available from: <https://doi.org/10.1126/science.138.3548.1404>.
- [56] Braybrook SA, Jönsson H. Shifting Foundations: The Mechanical Cell Wall and Development. *Current Opinion in Plant Biology*. 2016;29:115–120. Available from: <https://doi.org/10.1016/j.pbi.2015.12.009>.
- [57] Levesque-Tremblay G, Pelloux J, Braybrook SA, Müller K. Tuning of Pectin Methylesterification: Consequences for Cell Wall Biomechanics and Development. *Planta*. 2015;242:791–811. Available from: <https://dx.doi.org/10.1007/s00425-015-2358-5>.
- [58] Kerstens S, Decraemer WF, Verbelen JP. Cell Walls at the Plant Surface Behave Mechanically Like Fiber-Reinforced Composite Materials. *Plant Physiology*. 2001;127(2):381–385.
- [59] Pauly M, Gille S, Liu L, Mansoori N, de Souza A, Schultink A, et al. Hemicellulose Biosynthesis. *Planta*. 2013 Oct;238(4):627–642. Available from: <http://link.springer.com/10.1007/s00425-013-1921-1>.
- [60] Roelofsen PA. Ultrastructure of the Wall in Growing Cells and Its Relation to the Direction of the Growth. In: *Advances in Botanical Research*. vol. 2. Elsevier; 1966. p. 69–149. Available from: <http://linkinghub.elsevier.com/retrieve/pii/S0065229608602505>.
- [61] Heyn ANJ. The Physiology of Cell Elongation. *The Botanical Review*. 1940 Oct;6(10):515–574. Available from: <http://link.springer.com/10.1007/BF02879296>.
- [62] Cleland R. A Separation of Auxin-Induced Cell Wall Loosening into Its Plastic and Elastic Components. *Physiologia Plantarum*. 1958 Jul;11(3):599–609. Available from: <http://doi.wiley.com/10.1111/j.1399-3054.1958.tb08255.x>.

- [63] Yamamoto R, Shinozaki K, Masuda Y. Stress-Relaxation Properties of Plant Cell Walls with Special Reference to Auxin Action. *Plant and Cell Physiology*. 1970 Dec;11(6):947–956. Available from: <https://academic.oup.com/pcp/article/1819261/Stress-relaxation>.
- [64] Hengartner H. Die Fluoreszenzpolarisation der verholzten Zellwand. *Holz als Roh- und Werkstoff*. 1961 Aug;19(8):303–309. Available from: <http://link.springer.com/10.1007/BF02609689>.
- [65] Probst MC, Preston RD. Cell Growth and the Structure and Mechanical Properties of the Wall in Internodal Cells of *Nitella Opaca*: II. MECHANICAL PROPERTIES OF THE WALLS. *Journal of Experimental Botany*. 1962 Feb;13(1):111–127. Available from: <https://academic.oup.com/jxb/article/13/1/111/463989>.
- [66] Vőfély RV, Gallagher J, Pisano GD, Bartlett M, Braybrook SA. Of Puzzles and Pavements: A Quantitative Exploration of Leaf Epidermal Cell Shape. *New Phytologist*. 2019;221(1):540–552. Available from: <https://nph.onlinelibrary.wiley.com/doi/abs/10.1111/nph.15461>.
- [67] Iwata K, Hogetsu T. Orientation of Wall Microfibrils in *Avena* Coleoptiles and Mesocotyls and in *Pisum* Epicotyls. *Plant and Cell Physiology*. 1989 Jul; Available from: <https://academic.oup.com/pcp/article-lookup/doi/10.1093/oxfordjournals.pcp.a077801>.
- [68] Paolillo DJ. Axis Elongation Can Occur with Net Longitudinal Orientation of Wall Microfibrils. *New Phytologist*. 2000;145(3):449–455. Available from: <https://nph.onlinelibrary.wiley.com/doi/abs/10.1046/j.1469-8137.2000.00601.x>.
- [69] Verbelen JP, Kerstens S. Polarization Confocal Microscopy and Congo Red Fluorescence: A Simple and Rapid Method to Determine the Mean Cellulose Fibril Orientation in Plants. *Journal of Microscopy*. 2000 May;198(2):101–107. Available from: <http://doi.wiley.com/10.1046/j.1365-2818.2000.00691.x>.
- [70] Cosgrove DJ. Nanoscale Structure, Mechanics and Growth of Epidermal Cell Walls. *Current Opinion in Plant Biology*. 2018 Dec;46:77–86. Available from: <http://www.sciencedirect.com/science/article/pii/S1369526617301991>.
- [71] Scheller HV, Ulvskov P. Hemicelluloses. *Annual Review of Plant Biology*. 2010 Jun;61(1):263–289. Available from: <http://www.annualreviews.org/doi/10.1146/annurev-arplant-042809-112315>.
- [72] Park YB, Cosgrove DJ. Xyloglucan and Its Interactions with Other Components of the Growing Cell Wall. *Plant & Cell Physiology*. 2015;56(2):180–194. Available from: <https://doi.org/10.1093/pcp/pcu204>.
- [73] Park YB, Cosgrove DJ. A Revised Architecture of Primary Cell Walls Based on Biomechanical Changes Induced by Substrate-Specific Endoglucanases. *Plant Physiology*. 2012 Apr;158(4):1933–1943. Available from: <http://www.plantphysiol.org/content/158/4/1933>.

- [74] Nili A, Yi H, Crespi VH, Puri VM. Examination of Biological Hotspot Hypothesis of Primary Cell Wall Using a Computational Cell Wall Network Model. *Cellulose*. 2015 Apr;22(2):1027–1038. Available from: <http://link.springer.com/10.1007/s10570-015-0568-4>.
- [75] Wang T, Yang H, Kubicki JD, Hong M. Cellulose Structural Polymorphism in Plant Primary Cell Walls Investigated by High-Field 2D Solid-State NMR Spectroscopy and Density Functional Theory Calculations. *Biomacromolecules*. 2016 Jun;17(6):2210–2222. Available from: <http://pubs.acs.org/doi/10.1021/acs.biomac.6b00441>.
- [76] Phyto P, Wang T, Xiao C, Anderson CT, Hong M. Effects of Pectin Molecular Weight Changes on the Structure, Dynamics, and Polysaccharide Interactions of Primary Cell Walls of *Arabidopsis Thaliana* : Insights from Solid-State NMR. *Biomacromolecules*. 2017 Sep;18(9):2937–2950. Available from: <http://pubs.acs.org/doi/10.1021/acs.biomac.7b00888>.
- [77] Dick-Perez M, Wang T, Salazar A, Zabolina OA, Hong M. Multidimensional Solid-State NMR Studies of the Structure and Dynamics of Pectic Polysaccharides in Uniformly ¹³C-Labeled Arabidopsis Primary Cell Walls. *Magnetic Resonance in Chemistry*. 2012;50(8):539–550. Available from: <https://onlinelibrary.wiley.com/doi/abs/10.1002/mrc.3836>.
- [78] Højgaard Christensen S. Pectins. In: Glicksman M, editor. *Food Hydrocolloids*. vol. 3. Boca Raton, Florida: CRC Press; 1986. .
- [79] Ventura I, Jammal J, Bianco-Peled H. Insights into the Nanostructure of Low-Methoxyl Pectin–Calcium Gels. *Carbohydrate Polymers*. 2013 Sep;97(2):650–658. Available from: <http://www.sciencedirect.com/science/article/pii/S0144861713005304>.
- [80] Oyen ML. Mechanical Characterisation of Hydrogel Materials. *International Materials Reviews*. 2014;59:44–59. Available from: <https://doi.org/10.1179/1743280413Y.0000000022>.
- [81] Pollack GH. Is the Cell a Gel - and Why Does It Matter? *Japanese Journal of Physiology*. 2001;51:649–660. Available from: <https://doi.org/10.2170/jjphysiol.51.649>.
- [82] Sterling JD, Quigley HF, Orellana A, Mohnen D. The Catalytic Site of the Pectin Biosynthetic Enzyme α -1,4-Galacturonosyltransferase Is Located in the Lumen of the Golgi. *Plant Physiology*. 2001 Sep;127(1):360–371. Available from: <http://www.plantphysiol.org/content/127/1/360>.
- [83] Löfgren C, Guillotin S, Evenbratt H, Schols H, Hermansson AM. Effects of Calcium, pH, and Blockiness on Kinetic Rheological Behavior and Microstructure of HM Pectin Gels. *Biomacromolecules*. 2005;6:646–652. Available from: <https://dx.doi.org/10.1021/bm049619+>.
- [84] Löfgren C, Hermansson AM. Synergistic Rheological Behaviour of Mixed HM/LM Pectin Gels. *Food Hydrocolloids*. 2007 May;21(3):480–486. Available from: <http://www.sciencedirect.com/science/article/pii/S0268005X06001494>.

- [85] Ström A, Schuster E, Goh SM. Rheological Characterization of Acid Pectin Samples in the Absence and Presence of Monovalent Ions. *Carbohydrate Polymers*. 2014 Nov;113:336–343. Available from: <http://www.sciencedirect.com/science/article/pii/S0144861714006894>.
- [86] Fraeye I, Doungra E, Duvetter T, Moldenaers P, Van Loey A, Hendrickx M. Influence of Intrinsic and Extrinsic Factors on Rheology of Pectin–Calcium Gels. *Food Hydrocolloids*. 2009 Dec;23(8):2069–2077. Available from: <http://www.sciencedirect.com/science/article/pii/S0268005X09000769>.
- [87] Kim WJ, Rao VNM, Smit CJB. EFFECT OF CHEMICAL COMPOSITION ON COMPRESSIVE MECHANICAL PROPERTIES OF LOW ESTER PECTIN GELS. *Journal of Food Science*. 1978 Mar;43(2):572–575. Available from: <http://doi.wiley.com/10.1111/j.1365-2621.1978.tb02357.x>.
- [88] Willats WGT, Orfila C, Limberg G, Buchholt HC, van Alebeek GWM, Voragen AGJ, et al. Modulation of the Degree and Pattern of Methyl-Esterification of Pectic Homogalacturonan in Plant Cell Walls. *The Journal of Biological Chemistry*. 2001;276:19404–19413. Available from: <https://doi.org/10.1074/jbc.M011242200>.
- [89] Thakur BR, Singh RK, Handa AK, Rao MA. Chemistry and Uses of Pectin — A Review. *Critical Reviews in Food Science and Nutrition*. 1997 Feb;37(1):47–73. Available from: <http://www.tandfonline.com/doi/abs/10.1080/10408399709527767>.
- [90] Gross MO, Rao VNM, Smit CJB. RHEOLOGICAL CHARACTERIZATION OF LOW-METHOXYL PECTIN GEL BY NORMAL CREEP AND RELAXATION. *Journal of Texture Studies*. 1980 Sep;11(3):271–290. Available from: <http://doi.wiley.com/10.1111/j.1745-4603.1980.tb00326.x>.
- [91] Oakenfull D, Scott A. Hydrophobic Interaction in the Gelation of High Methoxyl Pectins. *Journal of Food Science*. 1984 Jul;49(4):1093–1098. Available from: <http://doi.wiley.com/10.1111/j.1365-2621.1984.tb10401.x>.
- [92] Axelos MAV, Thibault JF. CHAPTER 6 - The Chemistry of Low-Methoxyl Pectin Gelation. In: Walter RH, editor. *The Chemistry and Technology of Pectin*. Food Science and Technology. San Diego: Academic Press; 1991. p. 109–118. Available from: <http://www.sciencedirect.com/science/article/pii/B978008092644550011X>.
- [93] Wang M, Yuan D, Gao W, Li Y, Tan J, Zhang X. A Comparative Genome Analysis of PME and PMEI Families Reveals the Evolution of Pectin Metabolism in Plant Cell Walls. *PLoS ONE*. 2013 Aug;8(8):e72082. Available from: <http://dx.plos.org/10.1371/journal.pone.0072082>.
- [94] Pelloux J, Rustérucci C, Mellerowicz EJ. New Insights into Pectin Methyltransferase Structure and Function. *Trends in Plant Science*. 2007;12(6):1360–1385. Available from: <https://doi.org/10.1016/j.tplants.2007.04.001>.
- [95] Thibault JF, Rinaudo M. Interactions of Mono- and Divalent Counterions with Alkali- and Enzyme-Deesterified Pectins in Salt-Free Solutions. *Biopolymers*. 1985 Nov;24(11):2131–2143. Available from: <https://onlinelibrary.wiley.com/doi/abs/10.1002/bip.360241109>.

- [96] Ralet MC, Dronnet V, Buchholt HC, Thibault JF. Enzymatically and Chemically De-Esterified Lime Pectins: Characterisation, Polyelectrolyte Behaviour and Calcium Binding Properties. *Carbohydrate Research*. 2001 Nov;336(2):117–125. Available from: <http://www.sciencedirect.com/science/article/pii/S0008621501002488>.
- [97] Taylor AJ. Intramolecular Distribution of Carboxyl Groups in Low Methoxyl Pectins — A Review. *Carbohydrate Polymers*. 1982 Jan;2(1):9–17. Available from: <http://www.sciencedirect.com/science/article/pii/0144861782900418>.
- [98] Powell DA, Morris ER, Gidley MJ, Rees DA. Conformations and Interactions of Pectins: II. Influence of Residue Sequence on Chain Association in Calcium Pectate Gels. *Journal of Molecular Biology*. 1982 Mar;155(4):517–531. Available from: <http://www.sciencedirect.com/science/article/pii/0022283682904855>.
- [99] Braccini I, Pérez S. Molecular Basis of Ca^{2+} -Induced Gelation in Alginates and Pectins: The Egg-Box Model Revisited. *Biomacromolecules*. 2001 Dec;2(4):1089–1096. Available from: <http://pubs.acs.org/doi/abs/10.1021/bm010008g>.
- [100] Chan SY, Choo WS, Young DJ, Loh XJ. Pectin as a Rheology Modifier: Origin, Structure, Commercial Production and Rheology. *Carbohydrate Polymers*. 2017;161:118–139. Available from: <https://doi.org/10.1016/j.carbpol.2016.12.033>.
- [101] Grant GT, Morris ER, Rees DA, Smith PJC, Thom D. Biological Interactions between Polysaccharides and Divalent Cations: The Egg-Box Model. *FEBS Letters*. 1973 May;32(1):195–198. Available from: <http://www.sciencedirect.com/science/article/pii/0014579373807707>.
- [102] Ström A, Lundin L, Morris E, Williams MAK. Relation between Rheological Properties of Pectin Gels and Pectin Fine Structure. *Annual Transactions of the Nordic Rheology Society*. 2012;20.
- [103] Vincent RR, Williams MAK. Microrheological Investigations Give Insights into the Microstructure and Functionality of Pectin Gels. *Carbohydrate Research*. 2009 Sep;344(14):1863–1871. Available from: <http://linkinghub.elsevier.com/retrieve/pii/S0008621508005600>.
- [104] Munarin F, Tanzi MC, Petrini P. Advances in Biomedical Applications of Pectin Gels. *International Journal of Biological Macromolecules*. 2012 Nov;51(4):681–689. Available from: <http://www.sciencedirect.com/science/article/pii/S0141813012002759>.
- [105] Van Buren JP. CHAPTER 1 - Function of Pectin in Plant Tissue Structure and Firmness. In: Walter RH, editor. *The Chemistry and Technology of Pectin*. Food Science and Technology. San Diego: Academic Press; 1991. p. 1–22. Available from: <http://www.sciencedirect.com/science/article/pii/B9780080926445500066>.
- [106] Oakenfull DG. CHAPTER 5 - The Chemistry of High-Methoxyl Pectins. In: Walter RH, editor. *The Chemistry and Technology of Pectin*. Food Science and Technology. San Diego: Academic Press; 1991. p. 87–108. Available from: <http://www.sciencedirect.com/science/article/pii/B9780080926445500108>.

- [107] Rao MA, Cooley HJ. Influence of Glucose and Fructose on High-Methoxyl Pectin Gel Strength and Structure Development. *Journal of Food Quality*. 1994 Mar;17(1):21–31. Available from: <https://onlinelibrary.wiley.com/doi/abs/10.1111/j.1745-4557.1994.tb00128.x>.
- [108] Evageliou V, Richardson RK, Morris ER. Effect of pH, Sugar Type and Thermal Annealing on High-Methoxy Pectin Gels. *Carbohydrate Polymers*. 2000 Jul;42(3):245–259. Available from: <http://www.sciencedirect.com/science/article/pii/S0144861799001915>.
- [109] Yoo B, Yoo D, Kim YR, Lim ST. Effect of Sugar Type on Rheological Properties of High-methoxyl Pectin Gels. *Food Science and Biotechnology*. 2003 Jun;12(3):316–319. Available from: <http://www.dbpia.co.kr/Article/NODE01793864>.
- [110] Tsoga A, Richardson RK, Morris ER. Role of Cosolutes in Gelation of High-Methoxy Pectin. Part 2. Anomalous Behaviour of Fructose: Calorimetric Evidence of Site-Binding. *Food Hydrocolloids*. 2004 Nov;18(6):921–932. Available from: <http://linkinghub.elsevier.com/retrieve/pii/S0268005X04000293>.
- [111] Tsoga A, Richardson RK, Morris ER. Role of Cosolutes in Gelation of High-Methoxy Pectin. Part 1. Comparison of Sugars and Polyols. *Food Hydrocolloids*. 2004 Nov;18(6):907–919. Available from: <http://linkinghub.elsevier.com/retrieve/pii/S0268005X04000281>.
- [112] do Nascimento GE, Simas-Tosin FF, Iacomini M, Gorin PAJ, Cordeiro LMC. Rheological Behavior of High Methoxyl Pectin from the Pulp of Tamarillo Fruit (*Solanum Betaceum*). *Carbohydrate Polymers*. 2016 Mar;139:125–130. Available from: <http://linkinghub.elsevier.com/retrieve/pii/S0144861715011571>.
- [113] Ridley BL, O'Neill MA, Mohnen D. Pectins: Structure, Biosynthesis, and Oligogalacturonide-Related Signaling. *Phytochemistry*. 2001 Jul;57(6):929–967. Available from: <http://www.sciencedirect.com/science/article/pii/S0031942201001133>.
- [114] Bidhendi AJ, Geitmann A. Relating the Mechanics of the Primary Plant Cell Wall to Morphogenesis. *Journal of Experimental Botany*. 2016 Jan;67(2):449–461. Available from: <https://doi.org/10.1093/jxb/erv535>.
- [115] Lin D, Lopez-Sanchez P, Gidley MJ. Interactions of Pectins with Cellulose during Its Synthesis in the Absence of Calcium. *Food Hydrocolloids*. 2016 Jan;52:57–68. Available from: <http://www.sciencedirect.com/science/article/pii/S0268005X1500260X>.
- [116] Funakawa H, Miwa K. Synthesis of Borate Cross-Linked Rhamnogalacturonan II. *Frontiers in Plant Science*. 2015;6. Available from: <https://www.frontiersin.org/articles/10.3389/fpls.2015.00223/full>.
- [117] Bonner J. The Chemistry and Physiology of the Pectins. *The Botanical Review*. 1936 Oct;2(10):475–497. Available from: <http://link.springer.com/10.1007/BF02869919>.

- [118] Lawrance HW. A STUDY OF METHODS FOR THE PRODUCTION OF LOW-SUGAR PECTINATES FROM B. C. APPLES. The University of British Columbia. Canada; 1946. Available from: <https://open.library.ubc.ca/cIRcle/collections/ubctheses/831/items/1.0105717>.
- [119] Pilgrim GW, Walter RH, Oakenfull DG. CHAPTER 2 - Jams, Jellies, and Preserves. In: Walter RH, editor. The Chemistry and Technology of Pectin. Food Science and Technology. San Diego: Academic Press; 1991. p. 23–50. Available from: <http://www.sciencedirect.com/science/article/pii/B9780080926445500078>.
- [120] Kastner H, Einhorn-Stoll U, Drusch S. Structure Formation in Sugar Containing Pectin Gels - Influence of Gel Composition and Cooling Rate on the Gelation of Non-Amidated and Amidated Low-Methoxylated Pectin. Food Hydrocolloids. 2017 Dec;73:13–20. Available from: <http://www.sciencedirect.com/science/article/pii/S0268005X16311043>.
- [121] Scott Blair GW. PSYCHORHEOLOGY: LINKS BETWEEN THE PAST AND THE PRESENT. Journal of Texture Studies. 1974 Apr;5(1):3–12. Available from: <http://doi.wiley.com/10.1111/j.1745-4603.1974.tb01083.x>.
- [122] Beach P, Davis E, Ikkala P, Lundbye M. Characterization of Pectins. In: Fishman ML, Jen JJ, editors. Chemistry and Function of Pectins. vol. 310. Washington, DC: American Chemical Society; 1986. p. 103–116. Available from: <http://pubs.acs.org/doi/abs/10.1021/bk-1986-0310.ch009>.
- [123] Angalet SA. EVALUATION OF THE VOLAND-STEVEN'S LFRA TEXTURE ANALYZER FOR MEASURING THE STRENGTH OF PECTIN SUGAR JELLIES. Journal of Texture Studies. 1986 Mar;17(1):87–96. Available from: <http://doi.wiley.com/10.1111/j.1745-4603.1986.tb00716.x>.
- [124] Korish M, Abd Elhamid AM. Improving the Textural Properties of Egyptian Kariesh Cheese by Addition of Hydrocolloids. International Journal of Dairy Technology. 2012 May;65(2):237–242. Available from: <http://doi.wiley.com/10.1111/j.1471-0307.2011.00818.x>.
- [125] Hoefler AC. CHAPTER 3 - Other Pectin Food Products. In: Walter RH, editor. The Chemistry and Technology of Pectin. Food Science and Technology. San Diego: Academic Press; 1991. p. 51–66. Available from: <http://www.sciencedirect.com/science/article/pii/B978008092644550008X>.
- [126] Vityazev FV, Golovchenko VV, Patova OA, Drozd NN, Makarov VA, Shashkov AS, et al. Synthesis of Sulfated Pectins and Their Anticoagulant Activity. Biochemistry (Moscow). 2010 Jun;75(6):759–768. Available from: <https://doi.org/10.1134/S0006297910060118>.
- [127] Brouns F, Theuvsen E, Adam A, Bell M, Berger A, Mensink RP. Cholesterol-Lowering Properties of Different Pectin Types in Mildly Hyper-Cholesterolemic Men and Women. European Journal of Clinical Nutrition. 2012 May;66(5):591–599. Available from: <https://www.nature.com/articles/ejcn2011208>.

- [128] Eliaz I, Hotchkiss AT, Fishman ML, Rode D. The Effect of Modified Citrus Pectin on Urinary Excretion of Toxic Elements. *Phytotherapy Research*. 2006;20(10):859–864. Available from: <https://onlinelibrary.wiley.com/doi/abs/10.1002/ptr.1953>.
- [129] Liu L, Fishman ML, Hicks KB. Pectin in Controlled Drug Delivery – a Review. *Cellulose*. 2006 Dec;14(1):15–24. Available from: <http://link.springer.com/10.1007/s10570-006-9095-7>.
- [130] Endress HU. CHAPTER 12 - Nonfood Uses of Pectin. In: Walter RH, editor. *The Chemistry and Technology of Pectin*. Food Science and Technology. San Diego: Academic Press; 1991. p. 251–268. Available from: <http://www.sciencedirect.com/science/article/pii/B9780080926445500170>.
- [131] Bou Daher F, Braybrook SA. How to Let Go: Pectin and Plant Cell Adhesion. *Front Plant Sci*. 2015;6:523. Available from: <https://doi.org/10.3389/fpls.2015.00523>.
- [132] Ferrandiz C. Regulation of Fruit Dehiscence in Arabidopsis. *Journal of Experimental Botany*. 2002 Oct;53(377):2031–2038. Available from: <https://academic.oup.com/jxb/article-lookup/doi/10.1093/jxb/erf082>.
- [133] Sexton R, Roberts JA. Cell Biology of Abscission. *Annual Review of Plant Physiology*. 1982;33(1):133–162. Available from: <https://doi.org/10.1146/annurev.pp.33.060182.001025>.
- [134] Leboeuf E, Guillon F, Thoirion S, Lahaye M. Biochemical and Immunohistochemical Analysis of Pectic Polysaccharides in the Cell Walls of *Arabidopsis* Mutant QUASIMODO 1 Suspension-Cultured Cells: Implications for Cell Adhesion. *Journal of Experimental Botany*. 2005;56:3171–3182. Available from: <https://dx.doi.org/10.1093/jxb/eri314>.
- [135] Orfila C, Sørensen SO, Harholt J, Geshi N, Crombie H, Truong HN, et al. QUASIMODO1 Is Expressed in Vascular Tissue of Arabidopsis Thaliana Inflorescence Stems, and Affects Homogalacturonan and Xylan Biosynthesis. *Planta*. 2005 Nov;222(4):613–622. Available from: <https://doi.org/10.1007/s00425-005-0008-z>.
- [136] Francis KE, Lam SY, Copenhaver GP. Separation of Arabidopsis Pollen Tetrads Is Regulated by QUARTET1, a Pectin Methylesterase Gene. *Plant Physiology*. 2006 Nov;142(3):1004–1013. Available from: <http://www.plantphysiol.org/content/142/3/1004>.
- [137] González-Carranza ZH, Elliott KA, Roberts JA. Expression of Polygalacturonases and Evidence to Support Their Role during Cell Separation Processes in Arabidopsis Thaliana. *Journal of Experimental Botany*. 2007 Oct;58(13):3719–3730. Available from: <https://academic.oup.com/jxb/article/58/13/3719/496078>.
- [138] Burns JK. CHAPTER 9 - The Polygalacturonases and Lyases. In: Walter RH, editor. *The Chemistry and Technology of Pectin*. Food Science and Technology. San Diego: Academic Press; 1991. p. 165–188. Available from: <http://www.sciencedirect.com/science/article/pii/B9780080926445500145>.

- [139] Xiao C, Somerville C, Anderson CT. POLYGALACTURONASE INVOLVED IN EXPANSION1 Functions in Cell Elongation and Flower Development in *Arabidopsis*. *The Plant Cell*. 2014 Mar;26(3):1018–1035. Available from: <http://www.plantcell.org/lookup/doi/10.1105/tpc.114.123968>.
- [140] Braybrook SA, Peaucelle A. Mechano-Chemical Aspects of Organ Formation in *Arabidopsis Thaliana*: The Relationship between Auxin and Pectin. *PLOS ONE*. 2013;8(3). Available from: <https://doi.org/10.1371/journal.pone.0057813>.
- [141] Arsuffi G, Braybrook SA. Acid Growth: An Ongoing Trip. *Journal of Experimental Botany*. 2018 Jan;69(2):137–146. Available from: <https://academic.oup.com/jxb/article/69/2/137/4683755>.
- [142] Qi J, Wu B, Feng S, Lü S, Guan C, Zhang X, et al. Mechanical Regulation of Organ Asymmetry in Leaves. *Nature Plants*. 2017 Sep;3(9):724. Available from: <https://www.nature.com/articles/s41477-017-0008-6>.
- [143] Bou Daher F, Chen Y, Bozorg B, Clough JH, Jönsson H, Braybrook SA. Anisotropic Growth Is Achieved through the Additive Mechanical Effect of Material Anisotropy and Elastic Asymmetry. *eLife*. 2018 May; Available from: <http://doi.org/10.7554/eLife.38161>.
- [144] Carter R, Woolfenden H, Baillie A, Amsbury S, Carroll S, Healicon E, et al. Stomatal Opening Involves Polar, Not Radial, Stiffening Of Guard Cells. *Current Biology*. 2017 Oct;27(19):2974–2983.e2. Available from: <http://www.sciencedirect.com/science/article/pii/S0960982217310151>.
- [145] Amsbury S, Hunt L, Elhaddad N, Baillie A, Lundgren M, Verhertbruggen Y, et al. Stomatal Function Requires Pectin De-Methyl-Esterification of the Guard Cell Wall. *Current Biology*. 2016 Nov;26(21):2899–2906. Available from: <http://www.sciencedirect.com/science/article/pii/S0960982216309332>.
- [146] Rui Y, Xiao C, Yi H, Kandemir B, Wang JZ, Puri VM, et al. POLYGALACTURONASE INVOLVED IN EXPANSION3 Functions in Seedling Development, Rosette Growth, and Stomatal Dynamics in *Arabidopsis Thaliana*. *The Plant Cell*. 2017 Oct;29(10):2413–2432. Available from: <http://www.plantcell.org/content/29/10/2413>.
- [147] Parre E, Geitmann A. Pectin and the Role of the Physical Properties of the Cell Wall in Pollen Tube Growth of *Solanum Chacoense*. *Planta*. 2005 Feb;220(4):582–592. Available from: <http://link.springer.com/10.1007/s00425-004-1368-5>.
- [148] Zerzour R, Kroeger J, Geitmann A. Polar Growth in Pollen Tubes Is Associated with Spatially Confined Dynamic Changes in Cell Mechanical Properties. *Developmental Biology*. 2009 Oct;334(2):437–446. Available from: <http://www.sciencedirect.com/science/article/pii/S0012160609011099>.
- [149] Derbyshire P, McCann MC, Roberts K. Restricted Cell Elongation in *Arabidopsis* Hypocotyls Is Associated with a Reduced Average Pectin Esterification Level. *BMC Plant Biology*. 2007;7(1):31. Available from: <http://bmcplantbiol.biomedcentral.com/articles/10.1186/1471-2229-7-31>.

- [150] Peaucelle A, Wightman R, Höfte H. The Control of Growth Symmetry Breaking in the *Arabidopsis* Hypocotyl. *Current Biology*. 2015 Jun;25(13):1746–1752. Available from: <https://linkinghub.elsevier.com/retrieve/pii/S0960982215005965>.
- [151] Knox JP, Linstead PJ, King J, Cooper C, Roberts K. Pectin Esterification Is Spatially Regulated Both within Cell Walls and between Developing Tissues of Root Apices. *Planta*. 1990 Jul;181(4):512–521. Available from: <https://doi.org/10.1007/BF00193004>.
- [152] Johnstin R, Denton MC. The Relation of Alcohol Precipitate to Jellying Power of Citrus Pectin Extracts. *Industrial & Engineering Chemistry*. 1923 Aug;15(8):778–780. Available from: <http://pubs.acs.org/doi/abs/10.1021/ie50164a003>.
- [153] Baker GL. High-Polymer Pectins and Their Deesterification. In: Mrak EM, Stewart GF, editors. *Advances in Food Research*. vol. 1. Academic Press; 1948. p. 395–427. Available from: <http://www.sciencedirect.com/science/article/pii/S006526280860213X>.
- [154] Watson EL. Stress-Strain and Creep Relationships of Pectin Gels. *Journal of Food Science*. 1966 May;31(3):373–380. Available from: <http://doi.wiley.com/10.1111/j.1365-2621.1966.tb00508.x>.
- [155] KAWABATA A, SAWAYAMA S. Viscoelasticity of the Pectin Gel. *Nippon Nōgeikagaku Kaishi*. 1976;50(11):555–562. Available from: https://doi.org/10.1271/nogeikagaku1924.50.11_555.
- [156] Plashchina IG, Fomina OA, Braudo EE, Tolstoguzov VB. Creep Study of High-Esterified Pectin Gels. I. The Creep of Saccharose-Containing Gels. *Colloid and Polymer Science*. 1979;p. 8.
- [157] Plashchina IG, Gotlieb AM, Braudo EE, Tolstoguzov VB. Creep Study of High-Esterified Pectin Gels. 2. The Creep of Glycerol-Containing Gels. *Colloid and Polymer Science*. 1983;p. 5.
- [158] Comby S, Doublier JL, Lefebvre J. STRESS-RELAXATION STUDY OF HIGH-METHOXYL PECTIN GELS. In: *Gums and Stabilisers for the Food Industry*. vol. 3. Wrexham, Wales; 1985. p. 203–212.
- [159] Mitchell JR, Blanshard JMV. RHEOLOGICAL PROPERTIES OF PECTATE GELS. *Journal of Texture Studies*. 1976 Dec;7(3):341–351. Available from: <http://doi.wiley.com/10.1111/j.1745-4603.1976.tb01141.x>.
- [160] Durand D, Bertrand C, Clark AH, Lips A. Calcium-Induced Gelation of Low Methoxy Pectin Solutions — Thermodynamic and Rheological Considerations. *International Journal of Biological Macromolecules*. 1990 Feb;12(1):14–18. Available from: <http://www.sciencedirect.com/science/article/pii/014181309090076M>.
- [161] Garnier C, Axelos MAV, Thibault JF. Dynamic Viscoelasticity and Thermal Behaviour of Pectin—Calcium Gels. *Food Hydrocolloids*. 1991 May;5(1):105–108. Available from: <http://www.sciencedirect.com/science/article/pii/S0268005X09802932>.

- [162] Lopes da Silva JA, Gonçalves MP. Rheological Study into the Ageing Process of High Methoxyl Pectin/Sucrose Aqueous Gels. *Carbohydrate Polymers*. 1994 Jan;24(4):235–245. Available from: <http://www.sciencedirect.com/science/article/pii/014486179490068X>.
- [163] Lopes da Silva JA, Gonçalves MP, Rao MA. Influence of Temperature on the Dynamic and Steady-Shear Rheology of Pectin Dispersions. *Carbohydrate Polymers*. 1994 Jan;23(2):77–87. Available from: <http://linkinghub.elsevier.com/retrieve/pii/0144861794900310>.
- [164] Lopes da Silva JA, Gonçalves MP, Rao MA. Kinetics and Thermal Behaviour of the Structure Formation Process in HMP/Sucrose Gelation. *International Journal of Biological Macromolecules*. 1995 Jan;17(1):25–32. Available from: <http://www.sciencedirect.com/science/article/pii/014181309593514X>.
- [165] Alonso-Mougan M, Meijide F, Jover A, Rodriguez-Nunez E, Vázquez-Tato J. Rheological Behaviour of an Amide Pectin. *Journal of Food Engineering*. 2002 Nov;55(2):123–129. Available from: <http://www.sciencedirect.com/science/article/pii/S0260877402000262>.
- [166] Gigli J, Garnier C, Piazza L. Rheological Behaviour of Low-Methoxyl Pectin Gels over an Extended Frequency Window. *Food Hydrocolloids*. 2009 Jul;23(5):1406–1412. Available from: <http://linkinghub.elsevier.com/retrieve/pii/S0268005X08002427>.
- [167] Axelos MAV, Thibault JF. Influence of the Substituents of the Carboxyl Groups and of the Rhamnose Content on the Solution Properties and Flexibility of Pectins. *International Journal of Biological Macromolecules*. 1991 Apr;13(2):77–82. Available from: <http://www.sciencedirect.com/science/article/pii/014181309190052V>.
- [168] Hwang J, Kokini JL. Contribution of the Side Branches to Rheological Properties of Pectins. *Carbohydrate Polymers*. 1992 Jan;19(1):41–50. Available from: <http://linkinghub.elsevier.com/retrieve/pii/014486179290053S>.
- [169] Sousa AG, Nielsen HL, Armagan I, Larsen J, Sørensen SO. The Impact of Rhamnogalacturonan-I Side Chain Monosaccharides on the Rheological Properties of Citrus Pectin. *Food Hydrocolloids*. 2015 May;47:130–139. Available from: <http://linkinghub.elsevier.com/retrieve/pii/S0268005X15000296>.
- [170] Mikshina PV, Petrova AA, Faizullin DA, Zuev YF, Gorshkova TA. Tissue-Specific Rhamnogalacturonan I Forms the Gel with Hyperelastic Properties. *Biochemistry (Moscow)*. 2015 Jul;80(7):915–924. Available from: <http://link.springer.com/10.1134/S000629791507010X>.
- [171] Ström A, Ribelles P, Lundin L, Norton I, Morris ER, Williams MAK. Influence of Pectin Fine Structure on the Mechanical Properties of Calcium-Pectin and Acid-Pectin Gels. *Biomacromolecules*. 2007 Sep;8(9):2668–2674. Available from: <http://pubs.acs.org/doi/abs/10.1021/bm070192r>.
- [172] Ngouémazong DE, Jolie RP, Cardinaels R, Fraeye I, Van Loey A, Moldenaers P, et al. Stiffness of Ca²⁺-Pectin Gels: Combined Effects of Degree and Pattern of Methylesterification for Various Ca²⁺ Concentrations. *Carbohydrate Research*. 2012

- Feb;348:69–76. Available from: <http://www.sciencedirect.com/science/article/pii/S0008621511005581>.
- [173] Lopez-Sanchez P, Martinez-Sanz M, Bonilla MR, Wang D, Walsh CT, Gilbert EP, et al. Pectin Impacts Cellulose Fibre Architecture and Hydrogel Mechanics in the Absence of Calcium. *Carbohydrate Polymers*. 2016 Nov;153:236–245. Available from: <http://www.sciencedirect.com/science/article/pii/S0144861716309110>.
- [174] Lopez-Sanchez P, Martinez-Sanz M, Bonilla MR, Wang D, Gilbert EP, Stokes JR, et al. Cellulose-Pectin Composite Hydrogels: Intermolecular Interactions and Material Properties Depend on Order of Assembly. *Carbohydrate Polymers*. 2017 Apr;162:71–81. Available from: <http://www.sciencedirect.com/science/article/pii/S0144861717300607>.
- [175] Lin D, Lopez-Sanchez P, Selway N, Gidley MJ. Viscoelastic Properties of Pectin/Cellulose Composites Studied by QCM-D and Oscillatory Shear Rheology. *Food Hydrocolloids*. 2018;79:13–19. Available from: <https://doi.org/10.1016/j.foodhyd.2017.12.019>.
- [176] Cosgrove DJ. Wall Extensibility: Its Nature, Measurement and Relationship to Plant Cell Growth. *New Phytologist*. 1993;124(1). Available from: <https://doi.org/10.1111/j.1469-8137.1993.tb03795.x>.
- [177] Hayot CM, Forouzesh E, Goel A, Avramova Z, Turner JA. Viscoelastic Properties of Cell Walls of Single Living Plant Cells Determined by Dynamic Nanoindentation. *Journal of Experimental Botany*. 2012;63(7):2525–2540. Available from: <https://doi.org/10.1093/jxb/err428>.
- [178] Elsayad K, Werner S, Gallemí M, Kong J, Guajardo ERS, Zhang L, et al. Mapping the Subcellular Mechanical Properties of Live Cells in Tissues with Fluorescence Emission–Brillouin Imaging. *Sci Signal*. 2016 Jul;9(435):rs5–rs5. Available from: <http://stke.sciencemag.org/content/9/435/rs5>.
- [179] Löfgren C, Walkenström P, Hermansson AM. Microstructure and Rheological Behavior of Pure and Mixed Pectin Gels. *Biomacromolecules*. 2002;3:1144–1153. Available from: <https://dx.doi.org/10.1021/bm020044v>.
- [180] Williams MAK, Marshall AT, Anjukandi P, Haverkamp RG. Investigation of the Effects of Fine Structure on the Nanomechanical Properties of Pectin. *Physical Review E*. 2007 Aug;76(2). Available from: <https://link.aps.org/doi/10.1103/PhysRevE.76.021927>.
- [181] Schuster E, Lundin L, Williams MAK. Investigating the Relationship between Network Mechanics and Single-Chain Extension Using Biomimetic Polysaccharide Gels. *Macromolecules*. 2012 Jun;45(11):4863–4869. Available from: <http://pubs.acs.org/doi/10.1021/ma300724n>.
- [182] Kastner H, Einhorn-Stoll U, Senge B. Structure Formation in Sugar Containing Pectin Gels – Influence of Ca²⁺ on the Gelation of Low-Methoxylated Pectin at Acidic pH. *Food Hydrocolloids*. 2012 May;27(1):42–49. Available from: <http://www.sciencedirect.com/science/article/pii/S0268005X11002578>.

- [183] Mansel BW, Chu CY, Leis A, Hemar Y, Chen HL, Lundin L, et al. Zooming in: Structural Investigations of Rheologically Characterized Hydrogen-Bonded Low-Methoxyl Pectin Networks. *Biomacromolecules*. 2015 Oct;16(10):3209–3216. Available from: <http://pubs.acs.org/doi/10.1021/acs.biomac.5b00870>.
- [184] Ngouémazong DE, Nkemamin NF, Cardinaels R, Jolie RP, Fraeye I, Van Loey AM, et al. Rheological Properties of Ca²⁺-Gels of Partially Methylesterified Polygalacturonic Acid: Effect of “Mixed” Patterns of Methylesterification. *Carbohydrate Polymers*. 2012 Mar;88(1):37–45. Available from: <http://www.sciencedirect.com/science/article/pii/S0144861711010447>.
- [185] Ngouémazong DE, Tengweh FF, Fraeye I, Duvetter T, Cardinaels R, Van Loey A, et al. Effect of De-Methylesterification on Network Development and Nature of Ca²⁺-Pectin Gels: Towards Understanding Structure–Function Relations of Pectin. *Food Hydrocolloids*. 2012 Jan;26(1):89–98. Available from: <http://www.sciencedirect.com/science/article/pii/S0268005X11001147>.
- [186] Vincent RRR, Mansel BW, Kramer A, Kroy K, Williams MAK. Micro-Rheological Behaviour and Nonlinear Rheology of Networks Assembled from Polysaccharides from the Plant Cell Wall. *New Journal of Physics*. 2013 Mar;15(3):035002. Available from: <http://stacks.iop.org/1367-2630/15/i=3/a=035002?key=crossref.e6989d93080c6c493cc8652c637ffdb7>.
- [187] JPK. NanoWizard 3 User Manual; 2012. Available from: <https://www.nanophys.kth.se/nanolab/afm/jpk/manuf-manuals/usermanual.4.2.pdf>.
- [188] Braybrook SA, Höfte H, Peaucelle A. Probing the Mechanical Contributions of the Pectin Matrix. *Plant Signaling & Behavior*. 2012;7:8:1037–1041. Available from: <https://doi.org/10.4161/psb.20768>.
- [189] Spagnoli C, Beyder A, Besch S, Sachs F. Atomic Force Microscopy Analysis of Cell Volume Regulation. *Physical Review E*. 2008 Sep;78(3). Available from: <https://link.aps.org/doi/10.1103/PhysRevE.78.031916>.
- [190] Sampathkumar A, Krupinski P, Wightman R, Milani P, Berquand A, Boudaoud A, et al. Subcellular and Supracellular Mechanical Stress Prescribes Cytoskeleton Behavior in *Arabidopsis* Cotyledon Pavement Cells. *eLife*. 2014 Apr;3. Available from: <https://elifesciences.org/articles/01967>.
- [191] Lin DC, Dimitriadis EK, Horkay F. Robust Strategies for Automated AFM Force Curve Analysis—I. Non-Adhesive Indentation of Soft, Inhomogeneous Materials. *Journal of Biomechanical Engineering*. 2006 Nov;129(3):430–440. Available from: <http://dx.doi.org/10.1115/1.2720924>.
- [192] Gavara N. Combined Strategies for Optimal Detection of the Contact Point in AFM Force-Indentation Curves Obtained on Thin Samples and Adherent Cells. *Scientific Reports*. 2016 Aug;6(1). Available from: <http://www.nature.com/articles/srep21267>.
- [193] Moeendarbary E, Valon L, Fritzche M, Harris AR, Moulding DA, Thrasher AJ, et al. The Cytoplasm of Living Cells Behaves as a Poroelastic Material. *Nature Materials*. 2013;12:253–261. Available from: <http://dx.doi.org/10.1038/NMAT3517>.

- [194] Strange DGT, Fletcher TL, Tonsomboon K, Brawn H, Zhao X, Oyen ML. Separating Poroviscoelastic Deformation Mechanisms in Hydrogels. *Applied Physics Letters*. 2013 Jan;102(3):031913. Available from: <http://aip.scitation.org/doi/10.1063/1.4789368>.
- [195] Mainardi F, Spada G. Creep, Relaxation and Viscosity Properties for Basic Fractional Models in Rheology. *The European Physical Journal Special Topics*. 2011 Mar;193(1):133–160. Available from: <http://arxiv.org/abs/1110.3400>.
- [196] Zsivanovits G, MacDougall AJ, Smith AC, Ring SG. Material Properties of Concentrated Pectin Networks. *Carbohydrate Research*. 2004 May;339(7):1317–1322. Available from: <http://www.sciencedirect.com/science/article/pii/S0008621504001077>.
- [197] Dolan GK, Yakubov GE, Bonilla MR, Lopez-Sanchez P. Friction, Lubrication, and in Situ Mechanics of Poroelastic Cellulose Hydrogels. *Soft Matter*. 2017;13(19):3592–3601. Available from: <http://dx.doi.org/10.1039/C6SM02709A>.
- [198] Baron-Epel O, Gharyal PK, Schindler M. Pectins as Mediators of Wall Porosity in Soybean Cells. *Planta*. 1988 Sep;175(3):389–395. Available from: <http://link.springer.com/10.1007/BF00396345>.
- [199] Zhang W, Xie F, Lan X, Gong S, Wang Z. Characteristics of Pectin from Black Cherry Tomato Waste Modified by Dynamic High-Pressure Microfluidization. *Journal of Food Engineering*. 2018 Jan;216:90–97. Available from: <http://www.sciencedirect.com/science/article/pii/S0260877417303308>.
- [200] Croft D, Shed G, Devasia S. Creep, Hysteresis, and Vibration Compensation for Piezoactuators: Atomic Force Microscopy Application. *Journal of Dynamic Systems, Measurement, and Control*. 2001;123(1):35. Available from: <http://DynamicSystems.asmedigitalcollection.asme.org/article.aspx?articleid=1478036>.
- [201] Jones RAL. *Soft Condensed Matter*. Oxford University Press; 2002.
- [202] JPK. *Determining the Elastic Modulus of Biological Samples Using Atomic Force Microscopy*; 2012.
- [203] Vincent J. *Structural Biomaterials*. 3rd ed. New Jersey: Princeton University Press; 2012.
- [204] Nutting PG. A NEW GENERAL LAW OF DEFORMATION. *Journal of the Franklin Institute*. 1921;191(5):7. Available from: [https://doi.org/10.1016/S0016-0032\(21\)90171-6](https://doi.org/10.1016/S0016-0032(21)90171-6).
- [205] Scott Blair GW, Veinoglou BC, Caffyn JE. Limitations of the Newtonian Time Scale in Relation to Non-Equilibrium Rheological States and a Theory of Quasi-Properties. *Proceedings of the Royal Society A: Mathematical, Physical and Engineering Sciences*. 1947 Mar;189(1016):69–87. Available from: <http://rspa.royalsocietypublishing.org/cgi/doi/10.1098/rspa.1947.0029>.
- [206] Scott Blair GW. The Role of Psychophysics in Rheology. *Journal of Colloid Science*. 1947 Feb;2(1):21–32. Available from: <http://www.sciencedirect.com/science/article/pii/009585224790007X>.

- [207] Podlubny I. *Fractional Differential Equations: An Introduction to Fractional Derivatives, Fractional Differential Equations, to Methods of Their Solution and Some of Their Applications*. Elsevier; 1998.
- [208] Oldham KB, Spanier J. *The Fractional Calculus*. vol. 111 of *Mathematics in Science and Engineering*. San Diego: Academic Press; 1974.
- [209] Scott Blair GW, Veinoglou BC. A Study of the Firmness of Soft Materials Based on Nutting's Equation. *Journal of Scientific Instruments*. 1944 Sep;21(9):149–154. Available from: <http://stacks.iop.org/0950-7671/21/i=9/a=301?key=crossref.1e5a00657d13a720da6e98f8fb7fb907>.
- [210] Di Mino G, Airey G, Di Paola M, Pinnola FP, D'Angelo G, Lo Presti D. LINEAR AND NONLINEAR FRACTIONAL HEREDITARY CONSTITUTIVE LAWS OF ASPHALT MIXTURES. *JOURNAL OF CIVIL ENGINEERING AND MANAGEMENT*. 2016 Jul;22(7):882–889. Available from: <http://journals.vgtu.lt/index.php/JCEM/article/view/1884>.
- [211] Barpi F, Valente S. Creep and Fracture in Concrete: A Fractional Order Rate Approach. *Engineering Fracture Mechanics*. 2002 Mar;70(5):611–623. Available from: <http://www.sciencedirect.com/science/article/pii/S0013794402000413>.
- [212] Bouras Y, Zorica D, Atanacković TM, Vrcelj Z. A Non-Linear Thermo-Viscoelastic Rheological Model Based on Fractional Derivatives for High Temperature Creep in Concrete. *Applied Mathematical Modelling*. 2018 Mar;55:551–568. Available from: <http://www.sciencedirect.com/science/article/pii/S0307904X17307199>.
- [213] Zhou HW, Wang CP, Han BB, Duan ZQ. A Creep Constitutive Model for Salt Rock Based on Fractional Derivatives. *International Journal of Rock Mechanics and Mining Sciences*. 2011 Jan;48(1):116–121. Available from: <https://linkinghub.elsevier.com/retrieve/pii/S1365160910002066>.
- [214] Wu F, Liu JF, Wang J. An Improved Maxwell Creep Model for Rock Based on Variable-Order Fractional Derivatives. *Environmental Earth Sciences*. 2015 Jun;73(11):6965–6971. Available from: <http://link.springer.com/10.1007/s12665-015-4137-9>.
- [215] Ding X, Zhang G, Zhao B, Wang Y. Unexpected Viscoelastic Deformation of Tight Sandstone: Insights and Predictions from the Fractional Maxwell Model. *Scientific Reports*. 2017 Sep;7(1):11336. Available from: <https://www.nature.com/articles/s41598-017-11618-x>.
- [216] Liao M, Lai Y, Liu E, Wan X. A Fractional Order Creep Constitutive Model of Warm Frozen Silt. *Acta Geotechnica*. 2017 Apr;12(2):377–389. Available from: <http://link.springer.com/10.1007/s11440-016-0466-4>.
- [217] Zhang CC, Zhu HH, Shi B, Fatahi B. A Long Term Evaluation of Circular Mat Foundations on Clay Deposits Using Fractional Derivatives. *Computers and Geotechnics*. 2018 Feb;94:72–82. Available from: <http://www.sciencedirect.com/science/article/pii/S0266352X17302343>.

- [218] Ma C, Zhan Hb, Yao Wm, Li Hz. A New Shear Rheological Model for a Soft Interlayer with Varying Water Content. *Water Science and Engineering*. 2018 Apr;11(2):131–138. Available from: <http://www.sciencedirect.com/science/article/pii/S167423701830053X>.
- [219] Zhang Z, Hou L, Chen X, Zhou Y, Liu M, Zhou W. A Rheological Model to Quantify Strain of Waxy Crude Oil Loaded by Linear Increased Stress. *Journal of Dispersion Science and Technology*. 2016 Mar;37(3):326–332. Available from: <http://www.tandfonline.com/doi/full/10.1080/01932691.2015.1007378>.
- [220] Hou L, Song C, Yan W, Zhang Z. A New Approach to Model Strain Change of Gelled Waxy Crude Oil under Constant Stress. *Rheologica Acta*. 2014 Apr;53(4):349–356. Available from: <http://link.springer.com/10.1007/s00397-014-0762-6>.
- [221] Coussot C, Kalyanam S, Yapp R, Insana MF. Fractional Derivative Models for Ultrasonic Characterization of Polymer and Breast Tissue Viscoelasticity. *IEEE Transactions on Ultrasonics, Ferroelectrics, and Frequency Control*. 2009 Apr;56(4):715–726. Available from: <https://dx.doi.org/10.1109/TUFFC.2009.1094>.
- [222] Carmichael B, Babahosseini H, Mahmoodi SN, Agah M. The Fractional Viscoelastic Response of Human Breast Tissue Cells. *Physical Biology*. 2015 May;12(4):046001. Available from: <http://stacks.iop.org/1478-3975/12/i=4/a=046001?key=crossref.b3248fd95161eea20bbe87811f3ad0b3>.
- [223] Dai Z, Peng Y, Mansy HA, Sandler RH, Royston TJ. A Model of Lung Parenchyma Stress Relaxation Using Fractional Viscoelasticity. *Medical Engineering & Physics*. 2015 Aug;37(8):752–758. Available from: <https://linkinghub.elsevier.com/retrieve/pii/S1350453315001216>.
- [224] Perdikaris P, Karniadakis GE. Fractional-Order Viscoelasticity in One-Dimensional Blood Flow Models. *Annals of Biomedical Engineering*. 2014 May;42(5):1012–1023. Available from: <http://link.springer.com/10.1007/s10439-014-0970-3>.
- [225] Yu Y, Perdikaris P, Karniadakis GE. Fractional Modeling of Viscoelasticity in 3D Cerebral Arteries and Aneurysms. *Journal of Computational Physics*. 2016 Oct;323:219–242. Available from: <https://linkinghub.elsevier.com/retrieve/pii/S0021999116302637>.
- [226] Alcoutlabi M, Martinez-Vega JJ. Application of Fractional Calculus to Viscoelastic Behaviour Modelling and to the Physical Ageing Phenomenon in Glassy Amorphous Polymers. *Polymer*. 1998 Dec;39(25):6269–6277. Available from: <http://www.sciencedirect.com/science/article/pii/S0032386198001682>.
- [227] Chen Q, Suki B, An KN. Dynamic Mechanical Properties of Agarose Gels Modeled by a Fractional Derivative Model. *Journal of Biomechanical Engineering*. 2004;126(5):666. Available from: <http://Biomechanical.asmedigitalcollection.asme.org/article.aspx?articleid=1412556>.
- [228] Findley WN, Lai JS, Onaran K. Creep and Relaxation of Nonlinear Viscoelastic Materials: With an Introduction to Linear Viscoelasticity. 2nd ed. Dover Books on Engineering. New York: Dover; 1989. Original work published 1976.

- [229] Brinson HF, Brinson LC. *Polymer Engineering Science and Viscoelasticity: An Introduction*. New York: Springer; 2008.
- [230] Ward IM, Sweeney J. *Mechanical Properties of Solid Polymers*. Third edition ed. Chichester, West Sussex, United Kingdom: Wiley; 2013.
- [231] Fabry B, Maksym GN, Butler JP, Glogauer M, Navajas D, Fredberg JJ. Scaling the Microrheology of Living Cells. *Physical Review Letters*. 2001 Sep;87(14). Available from: <https://link.aps.org/doi/10.1103/PhysRevLett.87.148102>.
- [232] Friedrich C, Heymann L. Extension of a Model for Crosslinking Polymer at the Gel Point. *Journal of Rheology*. 1988 Apr;32(3):235–241. Available from: <http://sor.scitation.org/doi/10.1122/1.549971>.
- [233] Bonfanti A, Fouchard J, Khalilgharibi N, Charras G, Kabla A. A Unified Rheological Model for Cells and Cellularised Materials. *Royal Society Open Science*. 2019;7(1):190920. Available from: <https://royalsocietypublishing.org/doi/full/10.1098/rsos.190920>.
- [234] Sollich P, Lequeux F, Hébraud P, Cates ME. Rheology of Soft Glassy Materials. *PHYSICAL REVIEW LETTERS*. 1997;78(10):4. Available from: <https://doi.org/10.1103/PhysRevLett.78.2020>.
- [235] Broedersz CP, MacKintosh FC. Modeling Semiflexible Polymer Networks. *Reviews of Modern Physics*. 2014 Jul;86(3):995–1036. Available from: <https://link.aps.org/doi/10.1103/RevModPhys.86.995>.
- [236] Pritchard RH, Huang YYS, Terentjev EM. Mechanics of Biological Networks: From the Cell Cytoskeleton to Connective Tissue. *Soft Matter*. 2014 Feb;10(12):1864–1884. Available from: <https://pubs.rsc.org/en/content/articlelanding/2014/sm/c3sm52769g>.
- [237] Jaishankar A, McKinley GH. Power-Law Rheology in the Bulk and at the Interface: Quasi-Properties and Fractional Constitutive Equations. *Proceedings of the Royal Society A: Mathematical, Physical and Engineering Sciences*. 2013 Jan;469(2149):20120284. Available from: <https://royalsocietypublishing.org/doi/10.1098/rspa.2012.0284>.
- [238] Schiessel H, Blumen A. Mesoscopic Pictures of the Sol-Gel Transition: Ladder Models and Fractal Networks. *Macromolecules*. 1995 May;28(11):4013–4019. Available from: <https://doi.org/10.1021/ma00115a038>.
- [239] Bochud T, Challet D. Optimal Approximations of Power Laws with Exponentials: Application to Volatility Models with Long Memory. *Quantitative Finance*. 2007 Dec;7(6):585–589. Available from: <http://www.tandfonline.com/doi/abs/10.1080/14697680701278291>.
- [240] Qian B, Goldstein RA. Distribution of Indel Lengths. *Proteins: Structure, Function, and Genetics*. 2001 Oct;45(1):102–104. Available from: <http://doi.wiley.com/10.1002/prot.1129>.

- [241] Winter HH, Chambon F. Analysis of Linear Viscoelasticity of a Crosslinking Polymer at the Gel Point. *Journal of Rheology*. 1986 Apr;30(2):367–382. Available from: <http://sor.scitation.org/doi/10.1122/1.549853>.
- [242] Hawkins DM. The Problem of Overfitting. *Journal of Chemical Information and Computer Sciences*. 2004 Jan;44(1):1–12. Available from: <http://pubs.acs.org/doi/abs/10.1021/ci0342472>.
- [243] Christensen RM. *Theory of Viscoelasticity: An Introduction*. Raymond F. Boyer Library Collection. Academic Press; 1982. Available from: <https://books.google.co.uk/books?id=xkfDQgAACAAJ>.
- [244] Moustache. Expressing Power Law Decay in Terms of Exponentials; 2019. Mathematics Stack Exchange. Available from: [https://math.stackexchange.com/q/3116219\(version:2019-02-17\)](https://math.stackexchange.com/q/3116219(version:2019-02-17)).
- [245] Koeller RC. Polynomial Operators, Stieltjes Convolution, and Fractional Calculus in Hereditary Mechanics. *Acta Mechanica*. 1986 Apr;58(3-4):251–264. Available from: <http://link.springer.com/10.1007/BF01176603>.
- [246] Weisstein EW. Repeated Integral.; Available from: <http://mathworld.wolfram.com/RepeatedIntegral.html>.
- [247] Gorenflo R, Mainardi F. Fractional Calculus: Integral and Differential Equations of Fractional Order. arXiv:08053823 [cond-mat, physics:math-ph]. 2008 May; Available from: <http://arxiv.org/abs/0805.3823>.
- [248] Caputo M. Linear Models of Dissipation Whose Q Is Almost Frequency Independent—II. *Geophysical Journal International*. 1967 Nov;13(5):529–539. Available from: <https://academic.oup.com/gji/article-lookup/doi/10.1111/j.1365-246X.1967.tb02303.x>.
- [249] Baleanu D, Fernandez A. On Some New Properties of Fractional Derivatives with Mittag-Leffler Kernel. *Communications in Nonlinear Science and Numerical Simulation*. 2018 Jun;59:444–462. Available from: <https://linkinghub.elsevier.com/retrieve/pii/S1007570417304240>.
- [250] Scott Blair GW, Coppen FMV. The Subjective Judgement of the Elastic and Plastic Properties of Soft Bodies; the "Differential Thresholds" for Viscosities and Compression Moduli. *Proceedings of the Royal Society of London Series B - Biological Sciences*. 1939 Dec;128(850):109–125. Available from: <https://royalsocietypublishing.org/doi/10.1098/rspb.1939.0046>.
- [251] Scott Blair GW, Coppen FMV. The Subjective Conception of the Firmness of Soft Materials. *The American Journal of Psychology*. 1942;55(2):215–229. Available from: <https://www.jstor.org/stable/1417080>.
- [252] Glöckle WG, Nonnenmacher TF. Fractional Relaxation and the Time-Temperature Superposition Principle. *Rheologica Acta*. 1994;33(4):337–343. Available from: <http://link.springer.com/10.1007/BF00366960>.

- [253] Schiessel H, Metzler R, Blumen A, Nonnenmacher TF. Generalized Viscoelastic Models: Their Fractional Equations with Solutions. *Journal of Physics A: Mathematical and General*. 1995;28(23):6567. Available from: <http://stacks.iop.org/0305-4470/28/i=23/a=012>.
- [254] Garra R, Garrappa R. The Prabhakar or Three Parameter Mittag-Leffler Function: Theory and Application. *Communications in Nonlinear Science and Numerical Simulation*. 2018 Mar;56:314–329. Available from: <http://www.sciencedirect.com/science/article/pii/S1007570417303064>.
- [255] Gorenflo R, Loutchko J, Luchko Y. COMPUTATION OF THE MITTAG-LEFFLER FUNCTION. *Fractional Calculus and Applied Analysis*. 2002;p. 26.
- [256] Kim YR, Lee YC, Lee HJ. Correspondence Principle for Characterization of Asphalt Concrete. *Journal of Materials in Civil Engineering*. 1995 Feb;7(1):59–68. Available from: <http://ascelibrary.org/doi/10.1061/%28ASCE%290899-1561%281995%297%3A1%2859%29>.
- [257] Lee HJ, Kim YR. Viscoelastic Constitutive Model for Asphalt Concrete under Cyclic Loading. *Journal of Engineering Mechanics*. 1998 Jan;124(1):32–40. Available from: <http://ascelibrary.org/doi/10.1061/%28ASCE%290733-9399%281998%29124%3A1%2832%29>.
- [258] Forough SA, Nejad FM, Khodaii A. Comparing Various Fitting Models to Construct the Tensile Relaxation Modulus Master Curve of Asphalt Mixes. *International Journal of Pavement Engineering*. 2016 Apr;17(4):314–330. Available from: <https://doi.org/10.1080/10298436.2014.993190>.
- [259] Bagley RL. Power Law and Fractional Calculus Model of Viscoelasticity. *AIAA Journal*. 1989 Oct;27(10):1412–1417. Available from: <http://arc.aiaa.org/doi/10.2514/3.10279>.
- [260] Mainardi F. On Some Properties of the Mittag-Leffler Function $E_\alpha(-t^\alpha)$, Completely Monotone for $t>0$ with $0<\alpha<1$. *Discrete & Continuous Dynamical Systems*. 2014 Aug;19:2267–2278. Available from: <http://www.aims sciences.org/journals/displayArticlesnew.jsp?paperID=10192>.
- [261] Moresi M, Mancini M, Bruno M, Rancini R. Viscoelastic Properties of Alginate Gels by Oscillatory Dynamic Tests. *Journal of Texture Studies*. 2001;32(5-6):375–396. Available from: <https://onlinelibrary.wiley.com/doi/abs/10.1111/j.1745-4603.2001.tb01243.x>.
- [262] Moresi M, Bruno M, Parente E. Viscoelastic Properties of Microbial Alginate Gels by Oscillatory Dynamic Tests. *Journal of Food Engineering*. 2004 Sep;64(2):179–186. Available from: <http://linkinghub.elsevier.com/retrieve/pii/S026087740300390X>.
- [263] Moresi M, Bruno M. Characterisation of Alginate Gels Using Quasi-Static and Dynamic Methods. *Journal of Food Engineering*. 2007 Oct;82(3):298–309. Available from: <http://linkinghub.elsevier.com/retrieve/pii/S0260877407001227>.

- [264] Nobile MR, Pirozzi V, Somma E, D'Ayala GG, Laurienzo P. Development and Rheological Investigation of Novel Alginate/N-Succinylchitosan Hydrogels. *Journal of Polymer Science Part B: Polymer Physics*. 2008 Jun;46(12):1167–1182. Available from: <https://onlinelibrary.wiley.com/doi/abs/10.1002/polb.21450>.
- [265] Friedrich C. Relaxation and Retardation Functions of the Maxwell Model with Fractional Derivatives. *Rheologica Acta*. 1991 Mar;30(2):151–158. Available from: <http://link.springer.com/10.1007/BF01134604>.
- [266] Deng L, Trepas X, Butler JP, Millet E, Morgan KG, Weitz DA, et al. Fast and Slow Dynamics of the Cytoskeleton. *Nature Materials*. 2006 Aug;5(8):636–640. Available from: <https://www.nature.com/articles/nmat1685>.
- [267] Hoffman BD, Massiera G, Citters KMV, Crocker JC. The Consensus Mechanics of Cultured Mammalian Cells. *Proceedings of the National Academy of Sciences*. 2006 Jul;103(27):10259–10264. Available from: <https://www.pnas.org/content/103/27/10259>.
- [268] Rother J, Büchsenschütz-Göbeler M, Nöding H, Steltenkamp S, Samwer K, Janshoff A. Cytoskeleton Remodelling of Confluent Epithelial Cells Cultured on Porous Substrates. *Journal of The Royal Society Interface*. 2015 Feb;12(103):20141057. Available from: <https://royalsocietypublishing.org/doi/full/10.1098/rsif.2014.1057>.
- [269] Cai P, Mizutani Y, Tsuchiya M, Maloney JM, Fabry B, Van Vliet KJ, et al. Quantifying Cell-to-Cell Variation in Power-Law Rheology. *Biophysical Journal*. 2013 Sep;105(5):1093–1102. Available from: [https://www.cell.com/biophysj/abstract/S0006-3495\(13\)00857-6](https://www.cell.com/biophysj/abstract/S0006-3495(13)00857-6).
- [270] Fabry B, Maksym GN, Butler JP, Glogauer M, Navajas D, Taback NA, et al. Time Scale and Other Invariants of Integrative Mechanical Behavior in Living Cells. *Physical Review E*. 2003 Oct;68(4). Available from: <https://link.aps.org/doi/10.1103/PhysRevE.68.041914>.
- [271] Smith BA, Tolloczko B, Martin JG, Grütter P. Probing the Viscoelastic Behavior of Cultured Airway Smooth Muscle Cells with Atomic Force Microscopy: Stiffening Induced by Contractile Agonist. *Biophysical Journal*. 2005 Apr;88(4):2994–3007. Available from: [https://www.cell.com/biophysj/abstract/S0006-3495\(05\)73351-8](https://www.cell.com/biophysj/abstract/S0006-3495(05)73351-8).
- [272] Cai P, Takahashi R, Kuribayashi-Shigetomi K, Subagyo A, Sueoka K, Maloney JM, et al. Temporal Variation in Single-Cell Power-Law Rheology Spans the Ensemble Variation of Cell Population. *Biophysical Journal*. 2017 Aug;113(3):671–678. Available from: [https://www.cell.com/biophysj/abstract/S0006-3495\(17\)30675-6](https://www.cell.com/biophysj/abstract/S0006-3495(17)30675-6).
- [273] Fredberg JJ, Stamenovic D. On the Imperfect Elasticity of Lung Tissue. *Journal of Applied Physiology*. 1989 Dec;67(6):2408–2419. Available from: <http://www.physiology.org/doi/10.1152/jappl.1989.67.6.2408>.
- [274] Darling EM, Zauscher S, Guilak F. Viscoelastic Properties of Zonal Articular Chondrocytes Measured by Atomic Force Microscopy. *OsteoArthritis Research Society International*. 2006;14:571–579.

- [275] Shahin-Shamsabadi A, Hashemi A, Tahriri M, Bastami F, Salehi M, Mashhadi Abbas F. Mechanical, Material, and Biological Study of a PCL/Bioactive Glass Bone Scaffold: Importance of Viscoelasticity. *Materials Science and Engineering: C*. 2018 Sep;90:280–288. Available from: <http://www.sciencedirect.com/science/article/pii/S092849311733521X>.
- [276] Shen ZL, Kahn H, Ballarini R, Eppell SJ. Viscoelastic Properties of Isolated Collagen Fibrils. *Biophysical Journal*. 2011 Jun;100(12):3008–3015. Available from: <http://www.sciencedirect.com/science/article/pii/S0006349511005625>.
- [277] Fertah M, Belfkira A, montassir Dahmane E, Taourirte M, Brouillette F. Extraction and Characterization of Sodium Alginate from Moroccan *Laminaria Digitata* Brown Seaweed. *Arabian Journal of Chemistry*. 2017 May;10:S3707–S3714. Available from: <http://www.sciencedirect.com/science/article/pii/S1878535214000793>.
- [278] Mancini M, Moresi M, Sappino F. Rheological Behaviour of Aqueous Dispersions of Algal Sodium Alginates. *Journal of Food Engineering*. 1996 May;28(3-4):283–295. Available from: <http://linkinghub.elsevier.com/retrieve/pii/0260877495000682>.
- [279] Liu X, Qian L, Shu T, Tong Z. Rheology Characterization of Sol–Gel Transition in Aqueous Alginate Solutions Induced by Calcium Cations through in Situ Release. *Polymer*. 2003 Jan;44(2):407–412. Available from: <http://www.sciencedirect.com/science/article/pii/S0032386102007711>.
- [280] Serwer P. Agarose Gels: Properties and Use for Electrophoresis. *Electrophoresis*. 1983 Feb;4(6):375–382. Available from: <http://doi.wiley.com/10.1002/elps.1150040602>.
- [281] Marras-Marquez T, Peña J, Veiga-Ochoa MD. Robust and Versatile Pectin-Based Drug Delivery Systems. *International Journal of Pharmaceutics*. 2015 Feb;479(2):265–276. Available from: <http://www.sciencedirect.com/science/article/pii/S0378517314009429>.
- [282] Aime S, Cipelletti L, Ramos L. Power Law Viscoelasticity of a Fractal Colloidal Gel. *Journal of Rheology*. 2018 Nov;62(6):1429–1441. Available from: <http://sor.scitation.org/doi/10.1122/1.5025622>.
- [283] Lidon P, Villa L, Manneville S. Power-Law Creep and Residual Stresses in a Carbopol Gel. *Rheologica Acta*. 2017 Mar;56(3):307–323. Available from: <http://link.springer.com/10.1007/s00397-016-0961-4>.
- [284] Meral FC, Royston TJ, Magin R. Fractional Calculus in Viscoelasticity: An Experimental Study. *Communications in Nonlinear Science and Numerical Simulation*. 2010 Apr;15(4):939–945. Available from: <http://linkinghub.elsevier.com/retrieve/pii/S1007570409002706>.
- [285] Zhang H, zhe Zhang Q, Ruan L, Duan J, Wan M, Insana MF. Modeling Ramp-Hold Indentation Measurements Based on Kelvin–Voigt Fractional Derivative Model. *Measurement Science and Technology*. 2018 Mar;29(3):035701. Available from: <http://stacks.iop.org/0957-0233/29/i=3/a=035701?key=crossref.88b3460a435ac3589a895b340cd72801>.

- [286] Choudhury MD, Chandra S, Nag S, Das S, Tarafdar S. Forced Spreading and Rheology of Starch Gel: Viscoelastic Modeling with Fractional Calculus. *Colloids and Surfaces A: Physicochemical and Engineering Aspects*. 2012 Aug;407:64–70. Available from: <http://www.sciencedirect.com/science/article/pii/S0927775712003378>.
- [287] Bouzid M, Keshavarz B, Geri M, Divoux T, Del Gado E, McKinley GH. Computing the Linear Viscoelastic Properties of Soft Gels Using an Optimally Windowed Chirp Protocol. *Journal of Rheology*. 2018 Jul;62(4):1037–1050. Available from: <https://sor.scitation.org/doi/10.1122/1.5018715>.
- [288] Basak R, Bandyopadhyay R. Formation and Rupture of Ca²⁺ Induced Pectin Biopolymer Gels. *Soft Matter*. 2014 Aug;10(37):7225–7233. Available from: <https://pubs.rsc.org/en/content/articlelanding/2014/sm/c4sm00748d>.
- [289] de Boer DH, Stone M, Lévesque LMJ. Fractal Dimensions of Individual Flocs and Floc Populations in Streams. *Hydrological Processes*. 2000 Mar;14(4):653–667. Available from: <http://doi.wiley.com/10.1002/%28SICI%291099-1085%28200003%2914%3A4%3C653%3A%3AAID-HYP964%3E3.0.CO%3B2-3>.
- [290] Shih WH, Shih WY, Kim SI, Liu J, Aksay IA. Scaling Behavior of the Elastic Properties of Colloidal Gels. *Physical Review A*. 1990 Oct;42(8):4772–4779. Available from: <https://link.aps.org/doi/10.1103/PhysRevA.42.4772>.
- [291] Butera S, Di Paola M. A Physically Based Connection between Fractional Calculus and Fractal Geometry. *Annals of Physics*. 2014 Nov;350:146–158. Available from: <http://www.sciencedirect.com/science/article/pii/S0003491614001791>.
- [292] Ostoja-Starzewski M, Zhang J. Does a Fractal Microstructure Require a Fractional Viscoelastic Model? *Fractal and Fractional*. 2018 Feb;2(1):12. Available from: <http://www.mdpi.com/2504-3110/2/1/12>.
- [293] Belović M, Pajić-Lijaković I, Torbica A, Mastilović J, Pećinar I. The Influence of Concentration and Temperature on the Viscoelastic Properties of Tomato Pomace Dispersions. *Food Hydrocolloids*. 2016 Dec;61:617–624. Available from: <https://linkinghub.elsevier.com/retrieve/pii/S0268005X16302703>.
- [294] RHEOS: Open Source Rheology Data Analysis Software - JuliaRheology/RHEOS.Jl; 2019. JuliaRheology. Available from: <https://github.com/JuliaRheology/RHEOS.jl>.
- [295] DeLano WL. The Case for Open-Source Software in Drug Discovery. *Drug Discovery Today*. 2005 Feb;10(3):213–217. Available from: <http://www.sciencedirect.com/science/article/pii/S135964460403363X>.
- [296] Gentleman RC, Carey VJ, Bates DM, Bolstad B, Dettling M, Dudoit S, et al. Bioconductor: Open Software Development for Computational Biology and Bioinformatics. *Genome Biology*. 2004 Sep;5(10):R80. Available from: <https://doi.org/10.1186/1471-2108-5-10-r80>.
- [297] Ince DC, Hatton L, Graham-Cumming J. The Case for Open Computer Programs. *Nature*. 2012 Feb;482(7386):485–488. Available from: <https://www.nature.com/articles/nature10836>.

- [298] Joppa LN, McInerny G, Harper R, Salido L, Takeda K, O'Hara K, et al. Troubling Trends in Scientific Software Use. *Science*. 2013 May;340(6134):814–815. Available from: <http://www.sciencemag.org/cgi/doi/10.1126/science.1231535>.
- [299] Eklund A, Nichols TE, Knutsson H. Cluster Failure: Why fMRI Inferences for Spatial Extent Have Inflated False-Positive Rates. *Proceedings of the National Academy of Sciences*. 2016 Jul;113(28):7900–7905. Available from: <http://www.pnas.org/lookup/doi/10.1073/pnas.1602413113>.
- [300] Kaplan J, Bonfanti A, Kabla A. RHEOS.Jl – A Julia Package for Rheology Data Analysis. *Journal of Open Source Software*. 2019 Sep;4(41):1700. Available from: <https://joss.theoj.org/papers/10.21105/joss.01700>.
- [301] Bonfanti A, Kaplan JL, Charras G, Kabla AJ. Fractional Viscoelastic Models for Power-Law Materials. *arXiv:200307834 [cond-mat, physics:physics, q-bio]*. 2020 Mar; Available from: <http://arxiv.org/abs/2003.07834>.
- [302] Kaplan JL. API;. Available from: <https://juliarheology.github.io/RHEOS.jl/latest/API/>.
- [303] Messaoud GB, Griel PL, Prévost S, Hermida-Merino D, Soetaert W, Roelants SLKW, et al. Single-Molecule Lamellar Hydrogels from Bolaform Microbial Glucolipids. *Soft Matter*. 2020 Feb; Available from: <https://pubs.rsc.org/en/content/articlelanding/2020/sm/c9sm02158b>.
- [304] JuliaCon 2018;. Available from: <http://juliacon.org/2018/>.
- [305] Seifert J. Python Tools for Analysis of AFM Data.; 2019. Available from: <https://github.com/jcbs/ForceMetric>.
- [306] Johnson SG. The NLOpt Nonlinear-Optimization Package;. Available from: <http://ab-initio.mit.edu/nlopt>.
- [307] Rowan T. Functional Stability Analysis of Numerical Algorithms. University of Texas at Austin; 1990.
- [308] Di Paola M, Fiore V, Pinnola FP, Valenza A. On the Influence of the Initial Ramp for a Correct Definition of the Parameters of Fractional Viscoelastic Materials. *Mechanics of Materials*. 2014 Feb;69(1):63–70. Available from: <http://www.sciencedirect.com/science/article/pii/S0167663613002081>.
- [309] Singh SJ, Chatterjee A. Beyond Fractional Derivatives: Local Approximation of Other Convolution Integrals. *Proceedings of the Royal Society A: Mathematical, Physical and Engineering Sciences*. 2010 Feb;466(2114):563–581. Available from: <https://royalsocietypublishing.org/doi/10.1098/rspa.2009.0378>.
- [310] Diethelm K, Freed AD. An Efficient Algorithm for the Evaluation of Convolution Integrals. *Computers & Mathematics with Applications*. 2006 Jan;51(1):51–72. Available from: <https://linkinghub.elsevier.com/retrieve/pii/S0898122105004438>.
- [311] Amini A, Horn B, Edelman A. Accelerated Convolutions for Efficient Multi-Scale Time to Contact Computation in Julia. *arXiv:161208825 [cs]*. 2016 Dec; Available from: <http://arxiv.org/abs/1612.08825>.

- [312] Chiandussi G, Codegone M, Ferrero S, Varesio FE. Comparison of Multi-Objective Optimization Methodologies for Engineering Applications. *Computers & Mathematics with Applications*. 2012 Mar;63(5):912–942. Available from: <http://www.sciencedirect.com/science/article/pii/S0898122111010406>.
- [313] Bezanson J, Edelman A, Karpinski S, Shah VB. Julia: A Fresh Approach to Numerical Computing. *SIAM Review*. 2017 Jan;59(1):65–98. Available from: <https://epubs.siam.org/doi/10.1137/141000671>.
- [314] Julia 1.0;. Available from: <https://julialang.org/blog/2018/08/one-point-zero>.
- [315] Why We Created Julia;. Available from: <https://julialang.org/blog/2012/02/why-we-created-julia>.
- [316] Musser DR, Hall AE, Stepanov AA, Street J. Generic Programming. In: *International Symposium on Symbolic and Algebraic Computation*; 2005. p. 13. Available from: https://doi.org/10.1007/3-540-51084-2_2.
- [317] Kelly DF. A Software Chasm: Software Engineering and Scientific Computing. *IEEE Software*. 2007 Nov;24(6):120–119. Available from: <http://dx.doi.org/10.1109/MS.2007.155>.
- [318] Merali Z. Computational Science: ...Error. *Nature*. 2010 Oct;467(7317):775–777. Available from: <http://www.nature.com/doifinder/10.1038/467775a>.
- [319] Travis CI - Test and Deploy Your Code with Confidence;. Available from: <https://travis-ci.org/>.
- [320] Continuous Integration and Deployment Service for Windows and Linux;. Available from: <https://www.appveyor.com/>.
- [321] Mainardi F, Masina E, Spada G. A Generalization of the Becker Model in Linear Viscoelasticity: Creep, Relaxation and Internal Friction. *Mechanics of Time-Dependent Materials*. 2018 Feb; Available from: <http://link.springer.com/10.1007/s11043-018-9381-4>.
- [322] Rabinowitz P. On Avoiding the Singularity in the Numerical Integration of Proper Integrals. *BIT*. 1979 Mar;19(1):104–110. Available from: <http://link.springer.com/10.1007/BF01931227>.
- [323] Diethelm K, Ford NJ, Freed AD, Luchko Y. Algorithms for the Fractional Calculus: A Selection of Numerical Methods. *Computer Methods in Applied Mechanics and Engineering*. 2005 Feb;194(6-8):743–773. Available from: <https://linkinghub.elsevier.com/retrieve/pii/S0045782504002981>.
- [324] Zeng F, Li C. Numerical Approach to the Caputo Derivative of the Unknown Function. *Open Physics*. 2013 Jan;11(10). Available from: <http://www.degruyter.com/view/j/phys.2013.11.issue-10/s11534-013-0214-4/s11534-013-0214-4.xml>.
- [325] Taiwo OA OO. An Algorithm for the Approximation of Fractional Differential-Algebraic Equations with Caputo-Type Derivatives. *Journal of Applied & Computational Mathematics*. 2015;04(05). Available from: <https://dx.doi.org/10.4172/2168-9679.1000242>.

-
- [326] Zeng F, Turner I, Burrage K. A Stable Fast Time-Stepping Method for Fractional Integral and Derivative Operators. arXiv:170305480 [math]. 2017 Mar;Available from: <http://arxiv.org/abs/1703.05480>.
- [327] Wang K, Huang J. High Order Fast Algorithm for the Caputo Fractional Derivative. arXiv:170506101 [math]. 2017 May;Available from: <http://arxiv.org/abs/1705.06101>.
- [328] Kaplan JL, Torode TA, Daher FB, Braybrook SA. On Pectin Methyl-Esterification: Implications for In Vitro and In Vivo Viscoelasticity. bioRxiv. 2019 Mar;p. 565614. Available from: <https://www.biorxiv.org/content/10.1101/565614v1>.
- [329] Charrier B, Wichard T, Reddy CRK. Protocols for Macroalgae Research. CRC Press; 2018.

Appendix A

RHEOS Features

A.1 Fitting Rheological Models to Data and Making Predictions

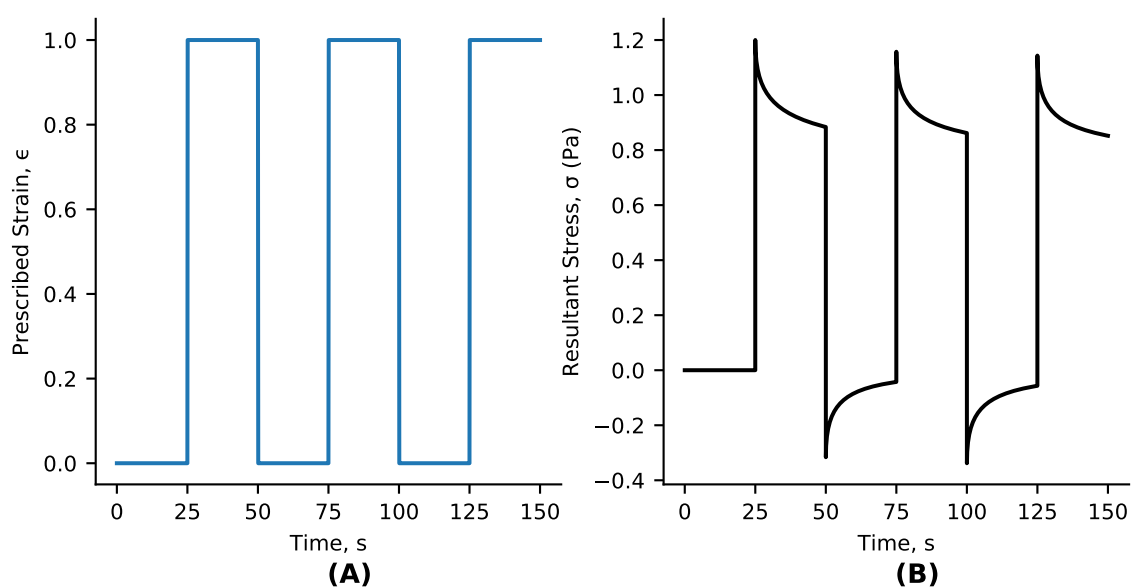


Fig. A.1 A) Imposed strain of the test data used for fitting. B) Resultant stress relaxation curves from the test data. Loading data generated by RHEOS.

This appendix provides an overview of the process of fitting rheological models using RHEOS, and then using those fitted models to test the fit quality and make predictions based on other loading patterns. Firstly, RHEOS has a convenience function for importing data from CSV files. The default column delimiter is a single comma, but an alternative can be specified as a keyword argument. The row delimiter is a newline character (`'\n'`). For

standard viscoelastic testing data RHEOS expects either stress, strain and time data, just stress and time, or just strain and time. All three are required for fitting, whilst at least two are required for prediction. The order of the columns is specified as the first argument in the function *importdata*. The second argument is the directory of the file, as shown below, in which the data file “DataRelaxation.csv” exists in the same directory as the working Julia directory.

```
using RHEOS
```

```
data = importdata(["stress","strain", "time"], "DataRelaxation.csv")
```

Now we have all our data stored in the variable *data* which is of type *RheoTimeData*, an SLS model can be fitted to the data. As the data is known to be strain-controlled relaxation data, we can perform the fitting via the relaxation modulus. (Note that RHEOS uses the convention of *G* for the relaxation modulus whereas this thesis uses *E* for the relaxation modulus and reserves *G* for the shear relaxation modulus.)

```
fitted_SLS_model = modelfit(data, SLS(), :G)
```

The first argument passes the data, the second argument tells RHEOS which model to fit with empty brackets implying that the default parameters will be used as initial guesses, and the final argument tells RHEOS whether to fit the model using a relaxation modulus or creep modulus. The result of this fit is now stored in a *RheoModel* data type. At this stage the best model may not be known, so let us also fit a second model, the fractional SLS model. This time we’ll also add upper and lower bounds on the model parameters. This is recommended for fractional models in particular as values less than 0 or greater than 1 for the spring-pot parameter are unphysical and can lead to numerical issues in the gamma function, or the Mittag-Leffler function for more complicated models.

```
lb = [0.1, 0.01, 0.1, 0.1]
ub = [Inf, 0.99, Inf, Inf]
fractsls_fit = modelfit(data, FractionalSLS(), :G; lo=lb, hi=ub)
```

Note the two keyword arguments used – *lo* and *hi* for the lower and upper parameter boundaries respectively. The special argument *Inf* for the three of the parameters’ upper bounds represent a type of infinity such that the parameters can be as large as required by the optimisation algorithm. For a full list of keyword arguments and features of the *modelfit* function, see the relevant part of the API section [302]. Now we have two models fitted, we

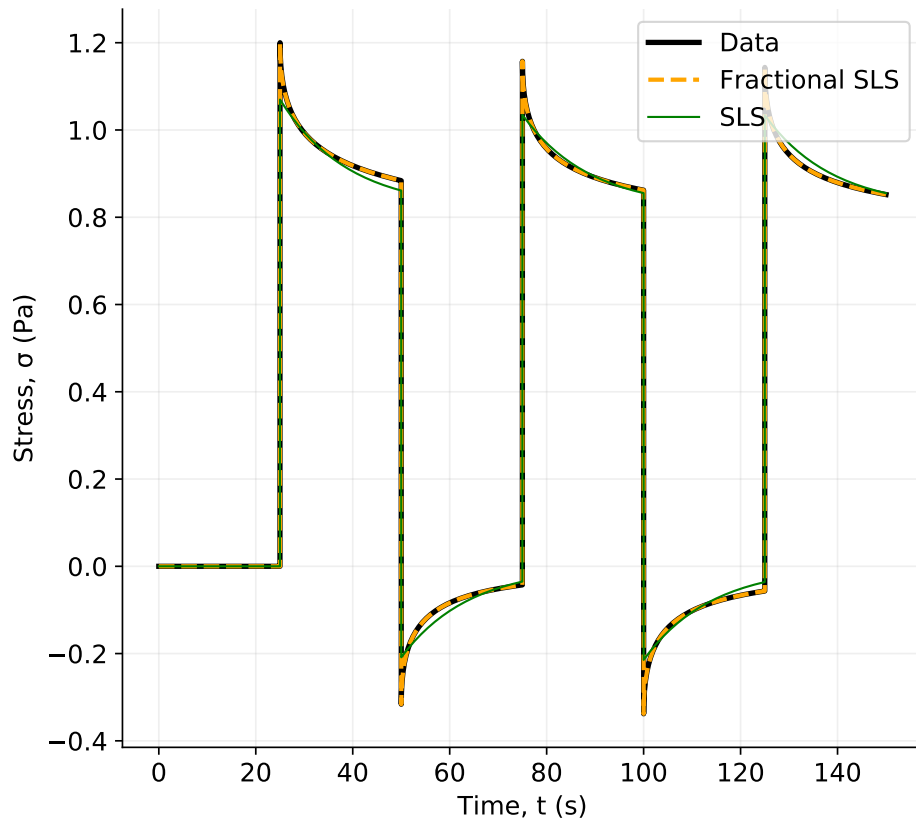


Fig. A.2 Test data fitted to an SLS model and an FSL model.

can qualitatively assess their goodness of fit. First, the fitted models are combined with the original loading data to generate predicted responses.

```
sls_predicted = modelpredict(data, sls_fit, :G)
fractsls_predicted = modelpredict(data, fractsls_fit, :G)
```

Then all that's left to do is plot, which is shown in Figure A.2, where it can be seen that the fit of the fractional model is slightly better. Now, if we have another dataset from the same material but a different loading pattern, we can further test the fitted models by seeing how well they predict the response of this new loading. This is the fit/predict paradigm in action, and our new loading data is analogous to a 'validation' or 'test' set in the language used by machine learning engineers. For the purposes of this example, new data was generated whose loading consisted of a ramp up from $t = 0$ to $t = 40$ seconds, followed by a small step up at $t = 50$ seconds, and a step down $t = 75$ seconds. The code to find the response predicted by both previously fitted models with the new data is the following.

```
sls_predicted2 = modelpredict(newdata, sls_fit, :G)
```

```
fractsls_predicted2 = modelpredict(newdata, fractsls_fit, :G)
```

This result, with comparison to the actual response from the new data, is shown in Figure A.3 in which it can be seen that the FSLS model clearly provides the more accurate prediction.

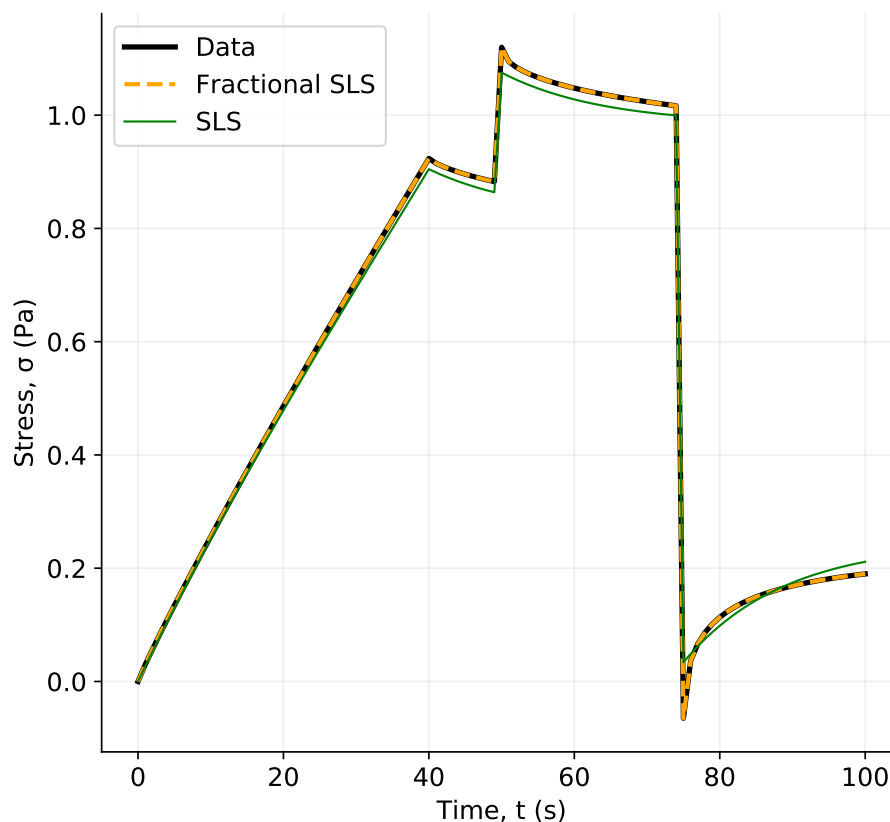


Fig. A.3 Stress relaxation response of the validation compared with that predicted by the two models fitted to the previous data from the same material.

DMA studies do not yield time-series data, but frequency data. This frequency data is either in separate parts of real (storage) modulus and imaginary (loss) modulus, or the absolute value of the complex modulus and the dissipation angle in the complex plane. RHEOS accepts data in the former format – three columns of data, one for frequency, one for the storage modulus and one for the loss modulus. As the two representations of DMA data are easily interchangeable this should not prevent anyone from being able to fit their data, however this is discussed again briefly in the future work section of Chapter 4. Below is a short example demonstrating how models can be fitted to DMA data, and then the response predicted as before but this time using the *dynamicmodelpredict* function.

```

frequency_data = importdata(["Gp", "Gpp", "frequency"], "FrequencyData.csv")

lb = [0.0, 0.01, 0.0, 0.0]
ub = [Inf, 0.99, Inf, Inf]
fitted_fractSLS_model = dynamicmodelfit(frequency_data, FractionalSLS();
    lo=lb, hi=ub, weights="log")

freq_fractSLS_predicted = dynamicmodelpredict(frequency_data,
    fitted_fractSLS_model)

```

The result of this is plotted in Figure A.4.

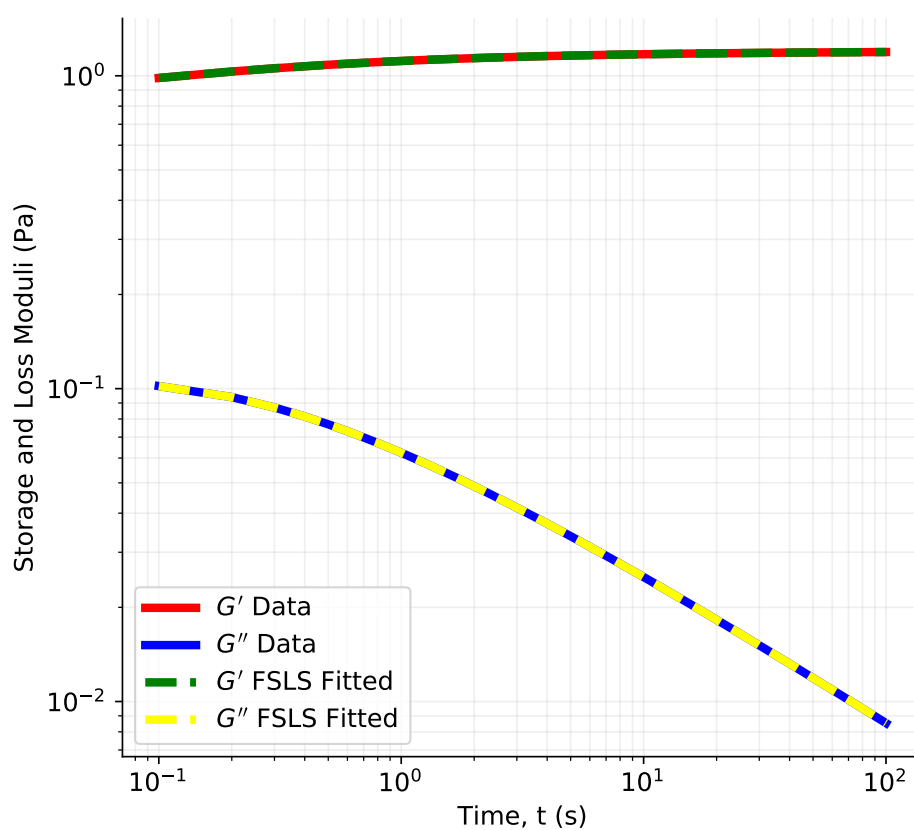


Fig. A.4 Stress relaxation response of the validation compared with that predicted by the two models fitted to the previous data from the same material.

A.2 Arbitrary Loading Generation

It has been mentioned in Chapter 4 that, at the outset, it is not immediately clear how to develop intuition for fractional viscoelastic models. Although Figures 4.5 and 4.7A go a long way in providing model selection heuristics, there are times when more information is required about the models behaviour. Sometimes it is sufficient to just plot the creep/relaxation modulus itself, which is equivalent to a Dirac delta step loading applied. However, many other times it is useful to understand the behaviour of the model under more complex loading. For this reason, RHEOS provides a number of functions for generating step, ramp, oscillatory and noise behaviours which can be added and multiplied to each other. These are demonstrated in this section.

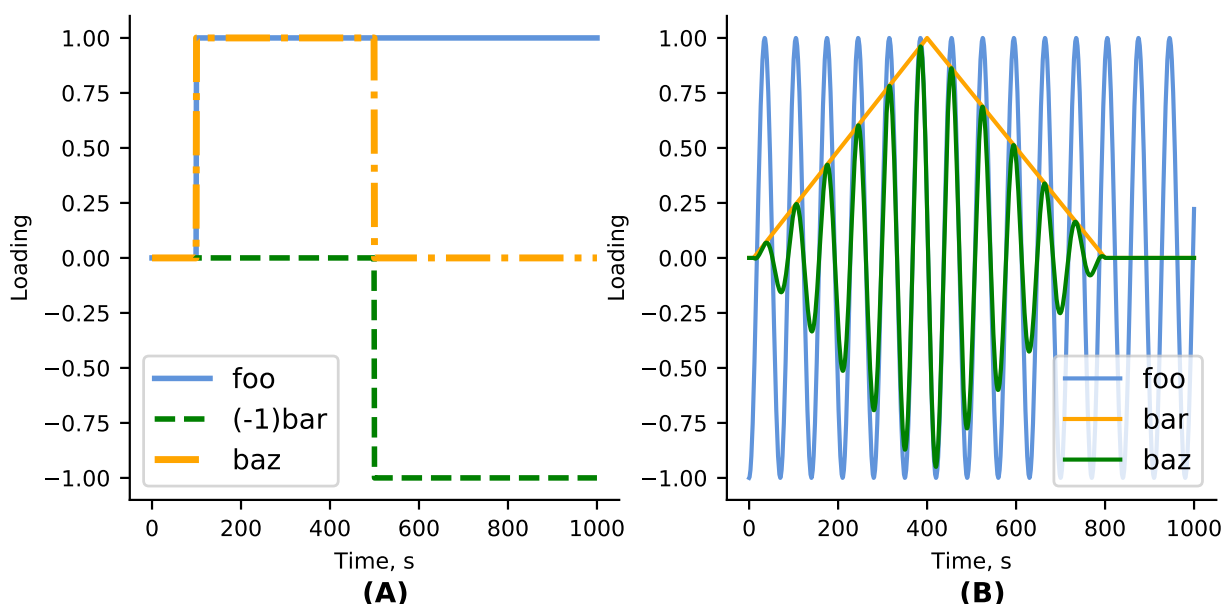


Fig. A.5 A) Two step signals and their additively combined signal, generated using RHEOS convenience functions. B) An oscillatory signal, a ramp signal, and their multiplicative combination, generated using RHEOS convenience functions.

It should be noted that the way these functions are currently implemented, they generate the same loading in both stress and strain with the expectation that users will then use one or other to make predictions, depending on whether they are interested in relaxation or creep behaviour. As all the structs generated are of *RheoTimeData* type, the same addition, subtraction and multiplication overloaded methods can be used for real data. When adding two *RheoTimeData* structs and one is longer than the other (in time), the shorter one will be extended by keeping the last values of that shorter struct's data constant for the rest of

time. Adding, subtracting and multiplying will raise an error if the data do not have the same sample rate.

First, we can try adding and subtracting two step functions to generate a rectangular loading signal. The code below uses *stepgen* to create one step starting at 100 seconds (with total duration of 1000 seconds) and another step starting at 500 seconds lasting the same total duration. The first argument of *stepgen* determines the total length in seconds. The second step is then subtracted from the first to create a new combined loading pattern.

```
foo = stepgen(1000.0, 100.0)
bar = stepgen(1000.0, 500.0)
baz = foo - bar
```

The output of which is plotted in Figure A.5A. The above example uses an instantaneous step. However, a logistic functional transition can be used by adding a non-zero *t_trans* keyword argument. Next we'll generate ramp loading using *rampgen*. The arguments in order are the total time length (as before), the time to start the ramp and the time to stop the ramp. We will also generate oscillatory loading which will be multiplied by the ramp loading. The first argument of *singen* is the total time length, the second is the frequency in hertz, and the keyword argument is phase in radians.

```
foo = singen(1000.0, 1/70; phase = -pi/2)
bar = rampgen(1000.0, 10.0, 400.0) - rampgen(1000.0, 400.0, 800.0)
baz = foo*bar
```

The result of this is plotted in Figure A.5B. Signals can also be repeated. RHEOS provides a convenience function that can loop loading patterns a specified number of times. Similar to the step function, *repeatdata* also offers a *t_trans* keyword argument which determines the transition between the end of one loop and the start of the next. If *t_trans*=0 then the transition is instantaneous, if not the transition occurs by logistic function with approximate transition time *t_trans*. The *repeatdata* function currently only works if the stress and strain arrays contain the same data (as is produced by all the data generation functions). Below we use our most recently defined *baz* variable (the oscillatory loading multiplied by the two ramps) to demonstrate.

```
repeatedbaz = repeatdata(baz, 3)
```

The output of this is plotted in Figure A.6A.

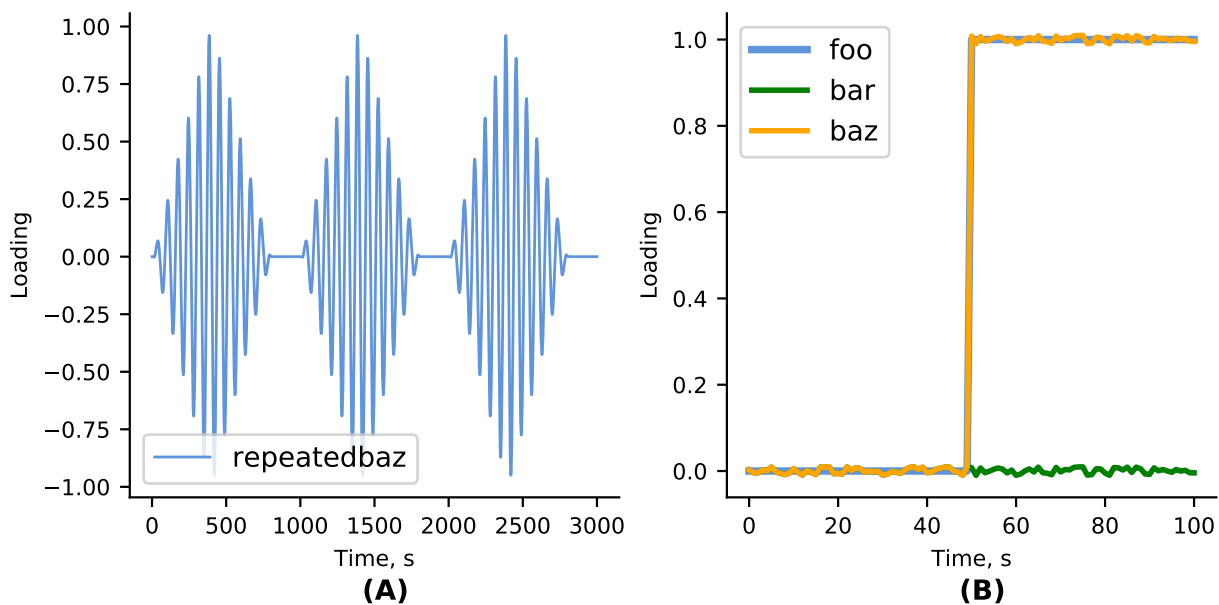


Fig. A.6 A) Previously generated ramp and oscillation multiplicative combination, repeated three times. B) A step signal, a pure noise signal, and their additive combination.

Lastly, RHEOS also features uniform white noise generation function called *noisegen*. The below example demonstrates this on a simple step, and its output is plotted in Figure A.6B.

```
foo = stepgen(100, 50)
bar = 0.01*noisegen(100)
baz = foo + bar
```

A.3 Resampling and Filtering

Preprocessing of experimental data is often important, yet it can be an obstacle for those with less programming experience. For this reason, RHEOS includes a number of commonly used preprocessing functions. This section details their use. Note that the examples use data generated by the data generation functions shown in the previous section. To simply downsample data by taking every *n*th sample, the *downsample* function can be used. In the below example, every 2nd element is taken.

```
foo = stepgen(10, 5)

bar = downsample(foo, [0.0, 10.0], [2])
```

The result of this is shown in Figure A.7A. More than one section of downsampling can be defined. For example, the below code takes every 2nd element from time=0.0 seconds to time=5.0 seconds and after that it takes every element. Note that as there are now two different sample rates, the data set is considered as having ‘variable’ sampling by RHEOS which adds a computational cost to fitting operations.

```
foo = stepgen(10, 5)

bar = downsample(foo, [0.0, 5.0, 10.0], [2, 1])
```

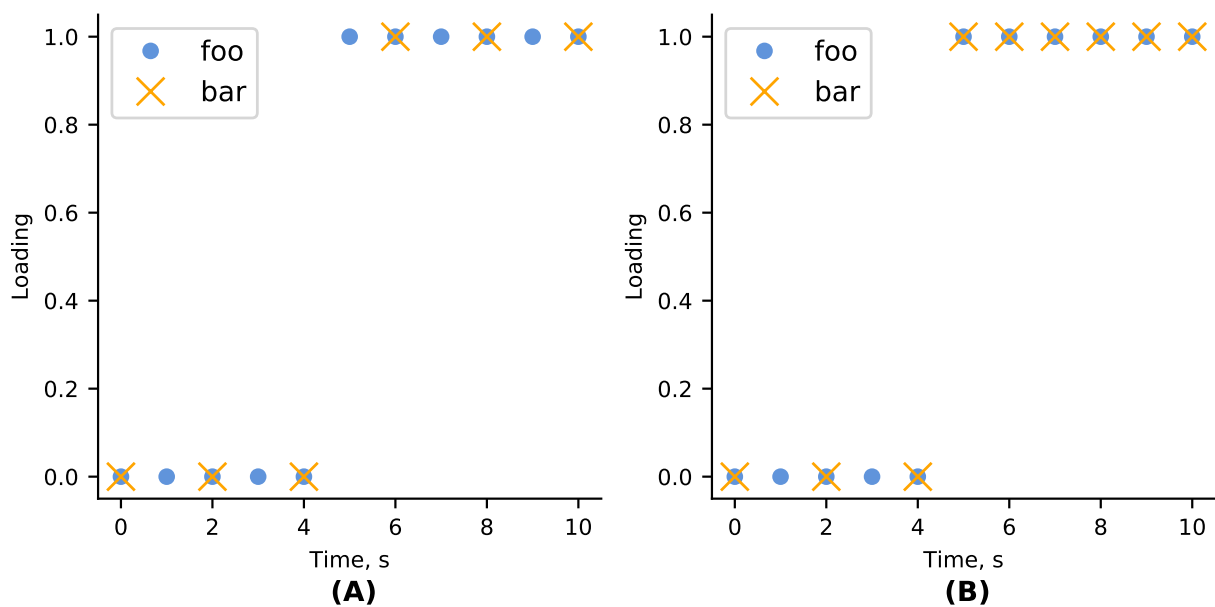


Fig. A.7 A) Step data that has been downsampled over the entire signal by taking every other element. B) Step data that has been downsampled as before but only over the first half of the signal, the second half remains unchanged.

The result of this is plotted in Figure A.7B. The *fixedresample* function is similar to the *downsample* function but also allows for upsampling. The syntax is almost the same but it requires an addition argument to tell RHEOS whether it should upsample or downsample for that section. Below is an example with three distinct sampling regions, the first two regions are downsampled and the third region is upsampled.

```
foo = stepgen(10, 5)

bar = fixedresample(foo, [0.0, 5.0, 8.0, 10.0], [2, 1, 4], ["down", "down",
"up"])
```

The result of this is plotted in Figure A.8A. Lastly, RHEOS provides a smoothing function, *smooth*. The first argument is the data to smooth and the second argument is the approximate time scale of smoothing. (It uses Gaussian smoothing and can be thought of as a low pass filter for information occurring on time scales shorter than the second argument). The padding can be changed using a keyword argument if desired, see API and ImageFiltering.jl documentation for more details. The example below smooths out some noisy data and the before/after data is plotted in Figure A.8.

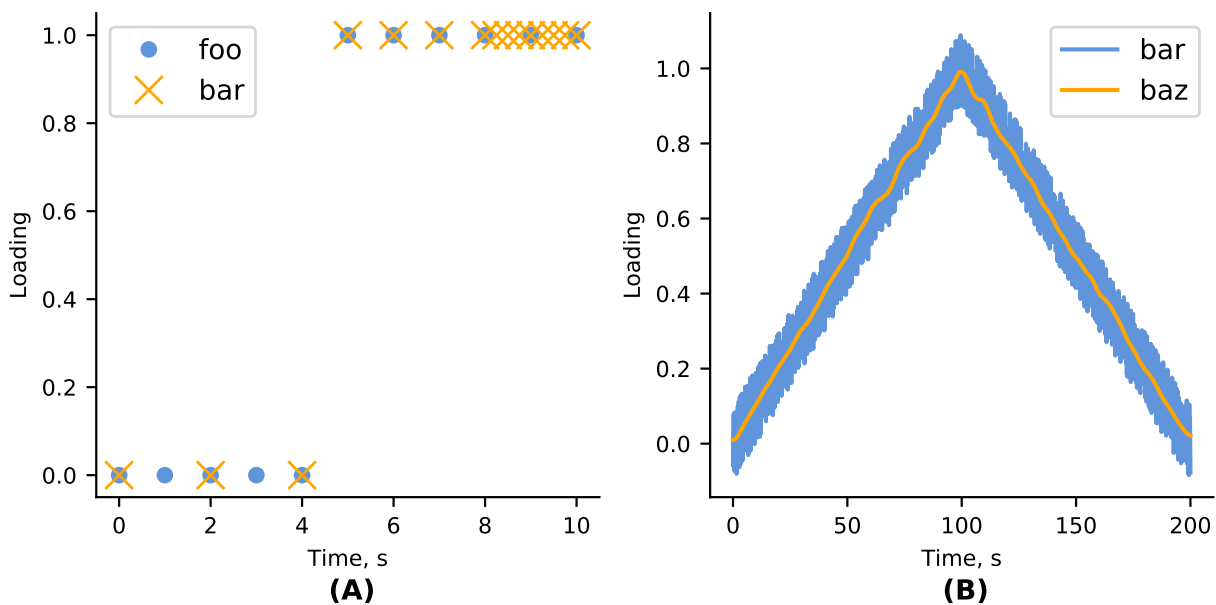
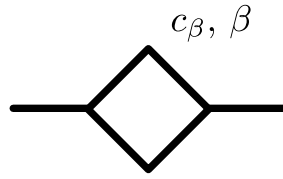


Fig. A.8 A) Step data that has been downsampled and upsampled at different signal times using RHEOS. B) Noisy ramp data that has been smoothed using RHEOS.

Appendix B

Summary of Fractional Viscoelastic Models

B.1 Spring-pot



Constitutive equation

$$\sigma(t) = c_\beta \frac{d^\beta \varepsilon(t)}{dt^\beta} \text{ for } 0 \leq \beta \leq 1$$

Relaxation modulus

$$G(t) = \frac{c_\beta}{\Gamma(1-\beta)} t^{-\beta}$$

Creep modulus

$$J(t) = \frac{1}{c_\beta \Gamma(1+\beta)} t^\beta$$

Complex modulus

$$G^*(\omega) = c_\beta (i\omega)^\beta$$

Storage modulus

$$G'(\omega) = c_\beta \omega^\beta \cos(\frac{\pi}{2}\beta)$$

Loss modulus

$$G''(\omega) = c_\beta \omega^\beta \sin(\frac{\pi}{2}\beta)$$

Special cases

- Spring: $\beta = 0$

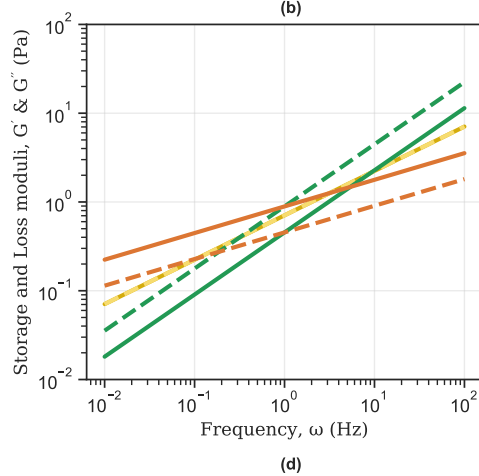
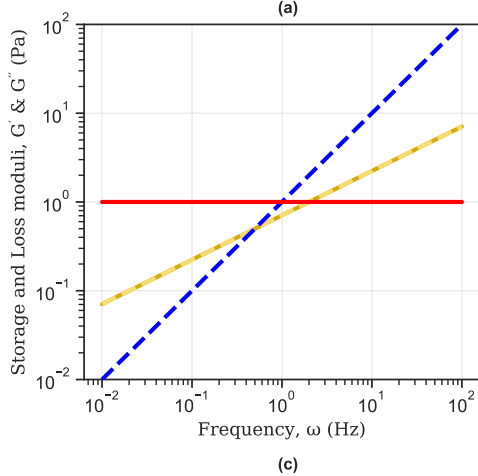
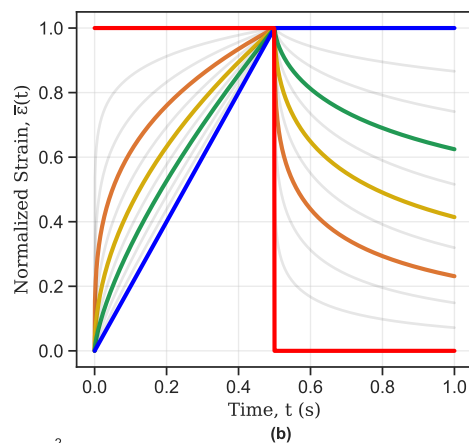
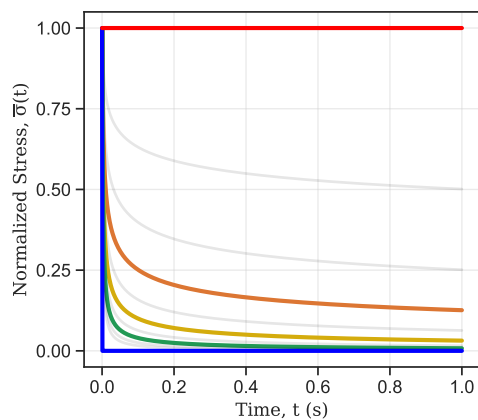
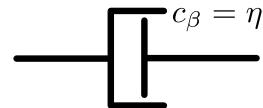
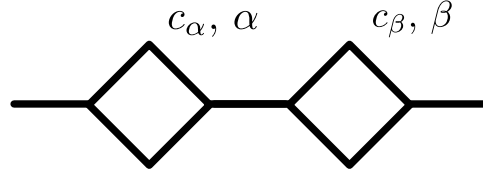


Fig. B.1 Springpot behaviour for varying β in increments of 0.1. Color reference β values are red (0.0), orange (0.3), yellow (0.5), green (0.7) and blue (1.0). (a) Relaxation response to step loading. (b) Creep response to step loading and unloading. (c) and (d) Storage (solid line) and loss (dashed line) moduli for the main values of β with colors ascribed above.

B.2 Fractional Maxwell model



Constitutive equation

$$\sigma(t) + \frac{c_\alpha}{c_\beta} \frac{d^{\alpha-\beta} \sigma(t)}{dt^{\alpha-\beta}} = c_\alpha \frac{d^\alpha \varepsilon(t)}{dt^\alpha}$$

Assuming $0 \leq \beta \leq \alpha \leq 1$

Relaxation modulus

$$G(t) = c_\beta t^{-\beta} E_{\alpha-\beta, 1-\beta} \left(\frac{-c_\beta}{c_\alpha} t^{\alpha-\beta} \right)$$

Creep modulus

$$J(t) = \frac{1}{c_\alpha \Gamma(1+\alpha)} t^\alpha + \frac{1}{c_\beta \Gamma(1+\beta)} t^\beta$$

Complex modulus

$$G^*(\omega) = \frac{c_\alpha (i\omega)^\alpha \cdot c_\beta (i\omega)^\beta}{c_\alpha (i\omega)^\alpha + c_\beta (i\omega)^\beta}$$

Storage modulus

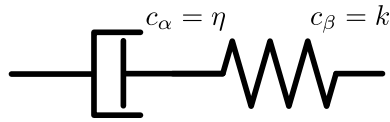
$$G'(\omega) = \frac{(c_\beta \omega^\beta)^2 \cdot c_\alpha \omega^\alpha \cos(\alpha \frac{\pi}{2}) + (c_\alpha \omega^\alpha)^2 \cdot c_\beta \omega^\beta \cos(\beta \frac{\pi}{2})}{(c_\alpha \omega^\alpha)^2 + (c_\beta \omega^\beta)^2 + 2c_\alpha \omega^\alpha \cdot c_\beta \omega^\beta \cos((\alpha-\beta) \frac{\pi}{2})}$$

Loss modulus

$$G''(\omega) = \frac{(c_\beta \omega^\beta)^2 \cdot c_\alpha \omega^\alpha \sin(\alpha \frac{\pi}{2}) + (c_\alpha \omega^\alpha)^2 \cdot c_\beta \omega^\beta \sin(\beta \frac{\pi}{2})}{(c_\alpha \omega^\alpha)^2 + (c_\beta \omega^\beta)^2 + 2c_\alpha \omega^\alpha \cdot c_\beta \omega^\beta \cos((\alpha-\beta) \frac{\pi}{2})}$$

Special cases

- Maxwell model: $\beta = 0$ and $\alpha = 1$



- $\beta = 0$

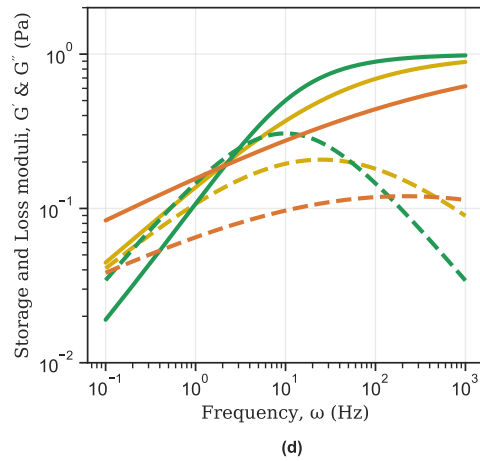
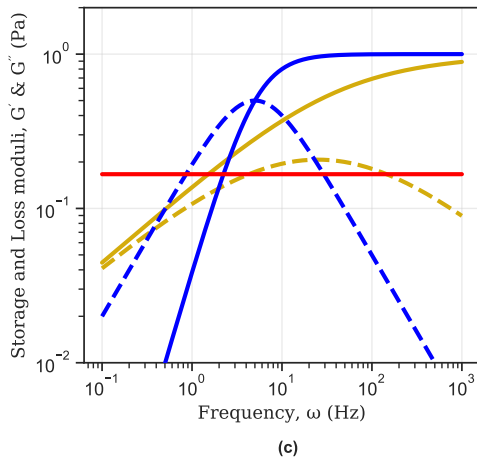
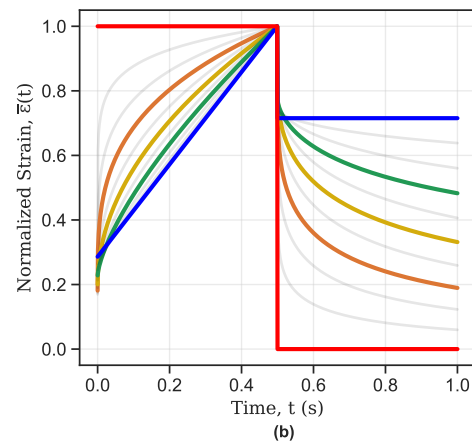
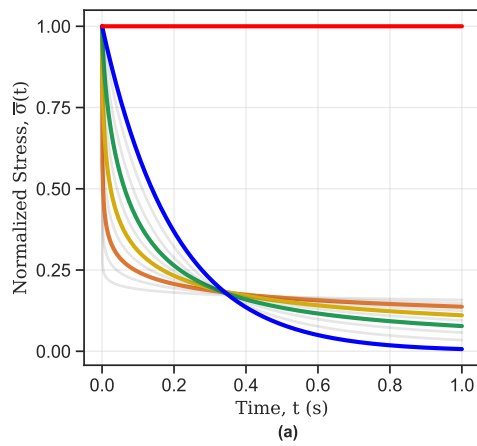
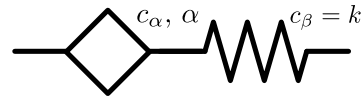


Fig. B.2 Fractional Maxwell behaviour with $\beta = 0$ for varying α in increments of 0.1. Color reference α values are red (0.0), orange (0.3), yellow (0.5), green (0.7) and blue (1.0). (a) Relaxation response to step loading. (b) Creep response to step loading and unloading. (c) and (d) Storage (solid line) and loss (dashed line) moduli for the main values of α with colors ascribed above.

- $\alpha = 1$

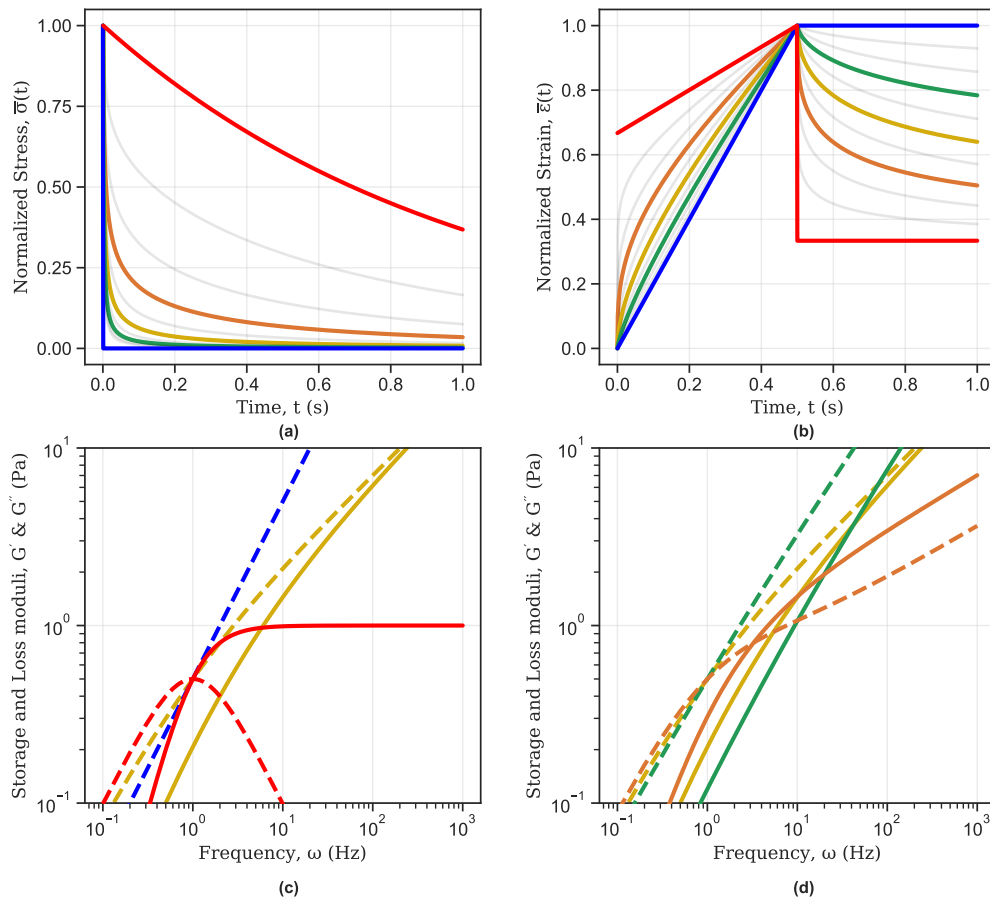
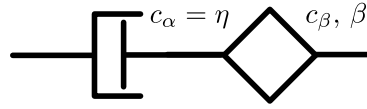
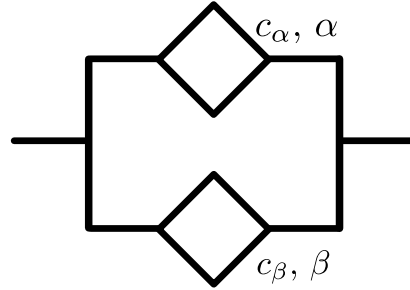


Fig. B.3 Fractional Maxwell behaviour with $\alpha = 1$ for varying β in increments of 0.1. Color reference β values are red (0.0), orange (0.3), yellow (0.5), green (0.7) and blue (1.0). (a) Relaxation response to step loading. (b) Creep response to step loading and unloading. (c) and (d) Storage (solid line) and loss (dashed line) moduli for the main values of β with colors ascribed above.

B.3 Fractional Kelvin-Voigt model



Constitutive equation

$$\sigma(t) = c_\alpha \frac{d^\alpha \varepsilon(t)}{dt^\alpha} + c_\beta \frac{d^\beta \varepsilon(t)}{dt^\beta}$$

Assuming $0 \leq \beta \leq \alpha \leq 1$

Relaxation modulus

$$G(t) = \frac{c_\alpha}{\Gamma(1-\alpha)} t^{-\alpha} + \frac{c_\beta}{\Gamma(1-\beta)} t^{-\beta}$$

Creep modulus

$$J(t) = \frac{t^\alpha}{c_\alpha} E_{\alpha-\beta, 1+\alpha} \left(-\frac{c_\beta}{c_\alpha} t^{\alpha-\beta} \right)$$

Complex modulus

$$G^*(\omega) = c_\alpha (i\omega)^\alpha + c_\beta (i\omega)^\beta$$

Storage modulus

$$G'(\omega) = c_\alpha \omega^\alpha \cos\left(\alpha \frac{\pi}{2}\right) + c_\beta \omega^\beta \cos\left(\beta \frac{\pi}{2}\right)$$

Loss modulus

$$G''(\omega) = c_\alpha \omega^\alpha \sin\left(\alpha \frac{\pi}{2}\right) + c_\beta \omega^\beta \sin\left(\beta \frac{\pi}{2}\right)$$

Special cases

- Kelvin-Voigt model: $\beta = 0$ and $\alpha = 1$
- $\beta = 0$

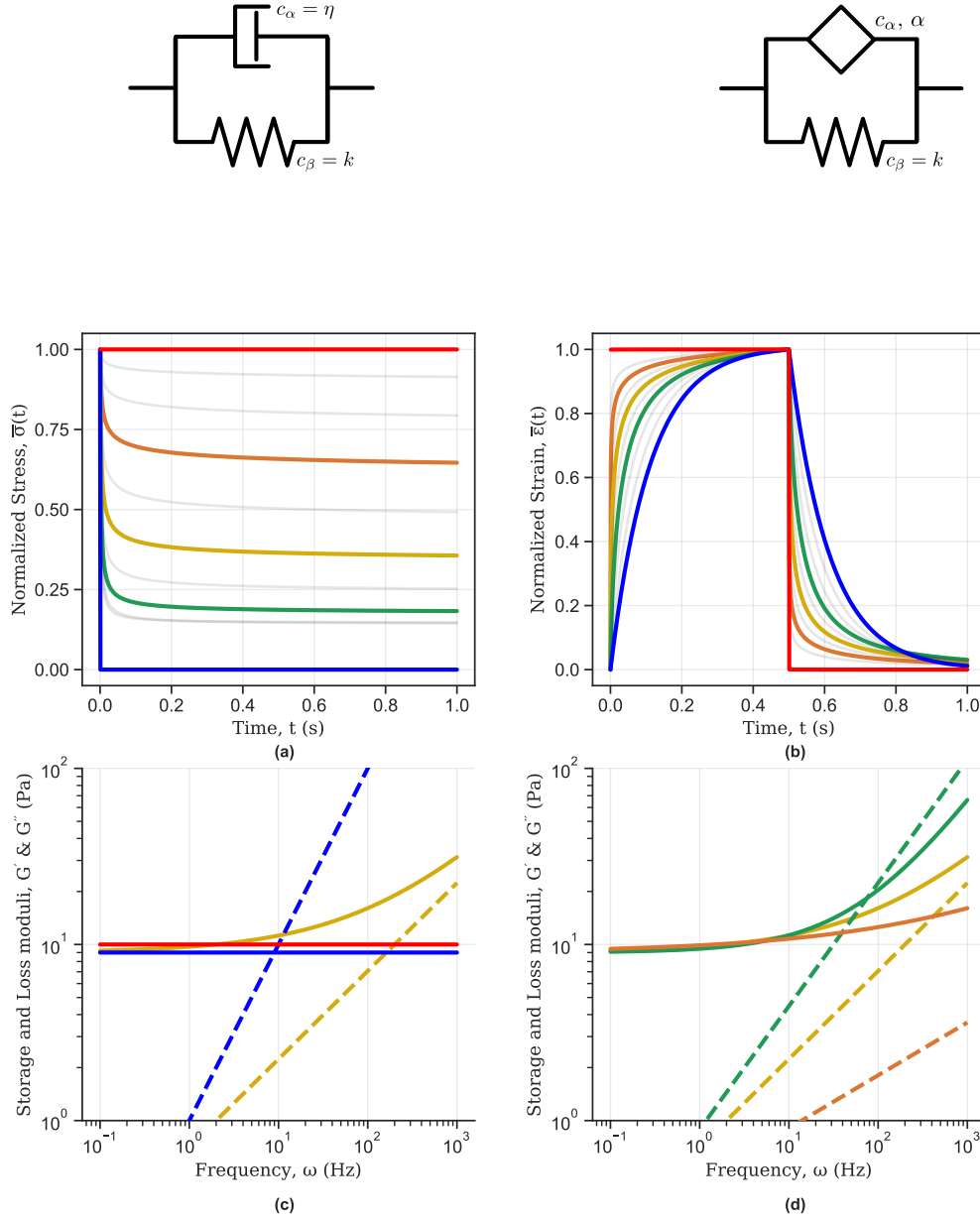


Fig. B.4 Fractional Kelvin-Voigt behaviour with $\beta = 0$ for varying α in increments of 0.1. Color reference α values are red (0.0), orange (0.3), yellow (0.5), green (0.7) and blue (1.0). (a) Relaxation response to step loading. (b) Creep response to step loading and unloading. (c) and (d) Storage (solid line) and loss (dashed line) moduli for the main values of α with colors ascribed above.

- $\alpha = 1$

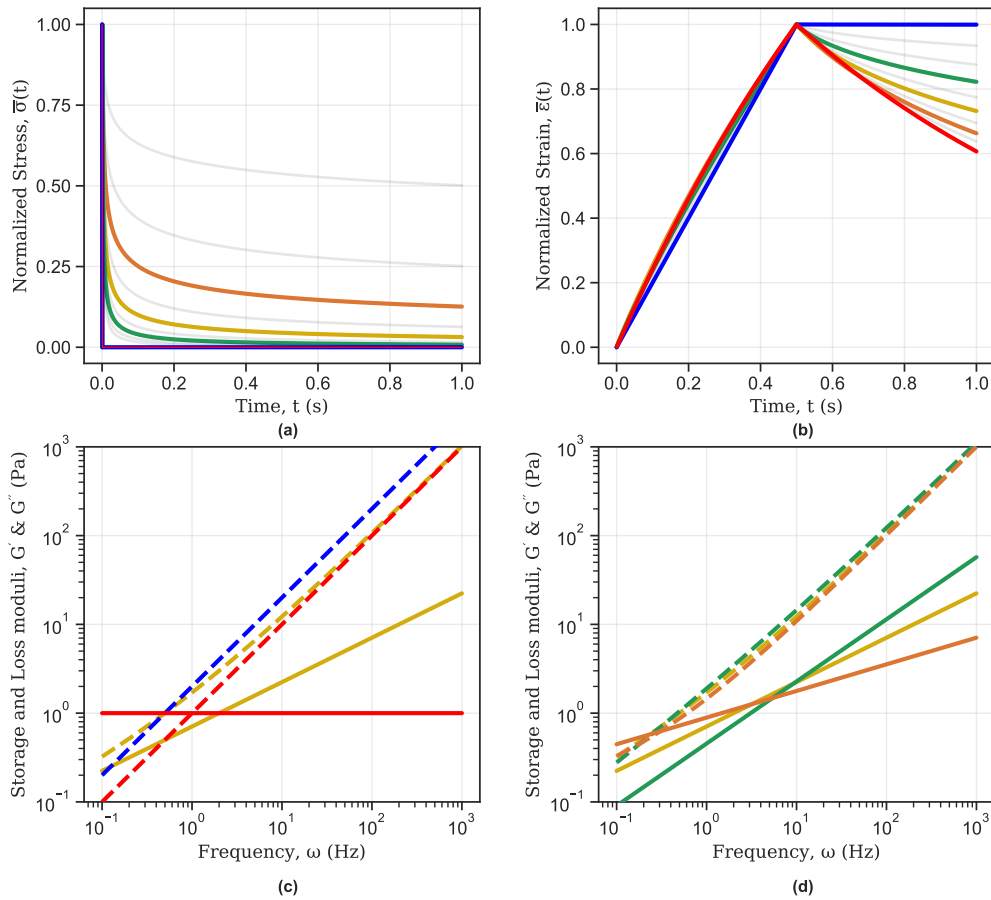
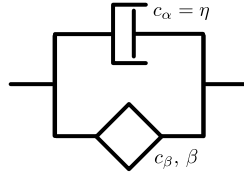
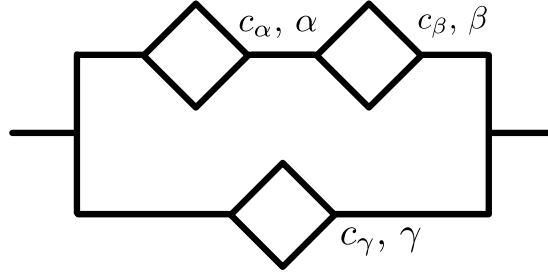


Fig. B.5 Fractional Kelvin-Voigt behaviour with $\alpha = 1$ for varying β in increments of 0.1. Color reference β values are red (0.0), orange (0.3), yellow (0.5), green (0.7) and blue (1.0). (a) Relaxation response to step loading. (b) Creep response to step loading and unloading. (c) and (d) Storage (solid line) and loss (dashed line) moduli for the main values of β with colors ascribed above.

B.4 Fractional Zener model



Constitutive equation

$$\sigma(t) + \frac{c_\alpha}{c_\beta} \frac{d^{\alpha-\beta} \sigma(t)}{dt^{\alpha-\beta}} = c_\alpha \frac{d^\alpha \epsilon(t)}{dt^\alpha} + c_\gamma \frac{d^\gamma \epsilon(t)}{dt^\gamma} + \frac{c_\alpha c_\gamma}{c_\beta} \frac{d^{\alpha+\gamma-\beta} \epsilon(t)}{dt^{\alpha+\gamma-\beta}}$$

Assuming $0 \leq \beta \leq \alpha \leq 1$

Relaxation modulus

$$G(t) = c_\beta t^{-\beta} E_{\alpha-\beta, 1-\beta} \left(-\frac{c_\beta}{c_\alpha} t^{\alpha-\beta} \right) + \frac{c_\gamma}{\Gamma(1-\gamma)} t^{-\gamma}$$

Creep modulus

$$\tilde{J}(s) = \frac{1}{s} \frac{c_\alpha s^\alpha + c_\beta s^\beta}{c_\alpha s^\alpha c_\beta s^\beta + c_\gamma s^\gamma (c_\alpha s^\alpha + c_\beta s^\beta)}$$

Complex modulus

$$G^*(\omega) = \frac{c_\alpha (i\omega)^\alpha \cdot c_\beta (i\omega)^\beta}{c_\beta (i\omega)^\beta + c_\alpha (i\omega)^\alpha} + c_\gamma (i\omega)^\gamma$$

Storage modulus

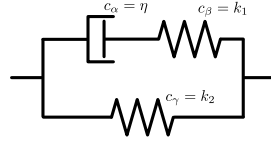
$$G'(\omega) = \frac{(c_\beta \omega^\beta)^2 \cdot c_\alpha \omega^\alpha \cos(\alpha \frac{\pi}{2}) + (c_\alpha \omega^\alpha)^2 \cdot c_\beta \omega^\beta \cos(\beta \frac{\pi}{2})}{(c_\alpha \omega^\alpha)^2 + (c_\beta \omega^\beta)^2 + 2c_\alpha \omega^\alpha \cdot c_\beta \omega^\beta \cos((\alpha - \beta) \frac{\pi}{2})} + c_\gamma \omega^\gamma \cos(\gamma \frac{\pi}{2})$$

Loss modulus

$$G''(\omega) = \frac{(c_\beta \omega^\beta)^2 \cdot c_\alpha \omega^\alpha \sin(\alpha \frac{\pi}{2}) + (c_\alpha \omega^\alpha)^2 \cdot c_\beta \omega^\beta \sin(\beta \frac{\pi}{2})}{(c_\alpha \omega^\alpha)^2 + (c_\beta \omega^\beta)^2 + 2c_\alpha \omega^\alpha \cdot c_\beta \omega^\beta \cos((\alpha - \beta) \frac{\pi}{2})} + c_\gamma \omega^\gamma \sin(\gamma \frac{\pi}{2})$$

Special cases

- Standard Linear Solid model: $\alpha = 1$ and $\beta = \gamma = 0$



- $\beta = \gamma = 0$

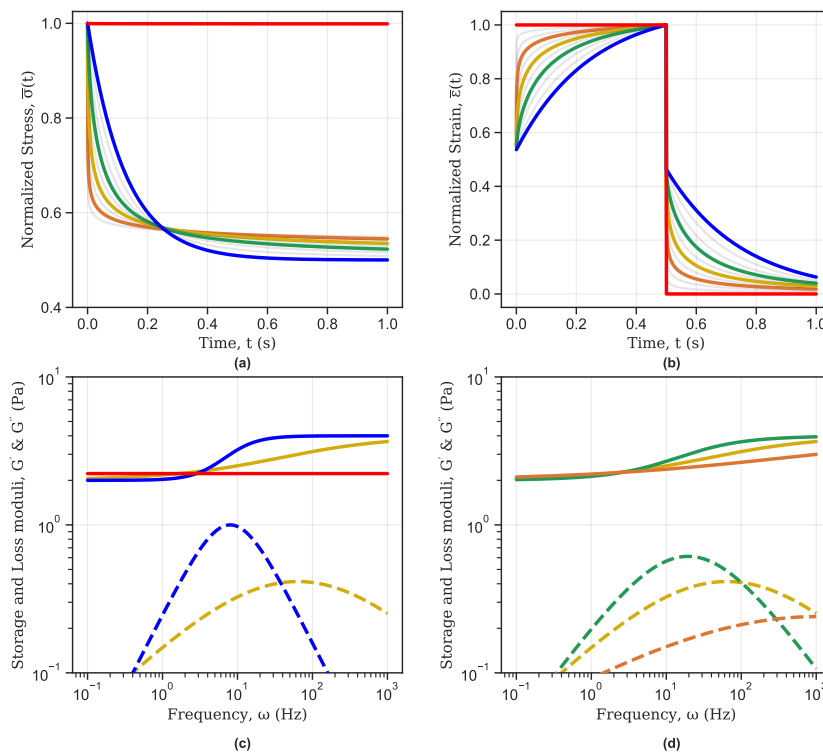
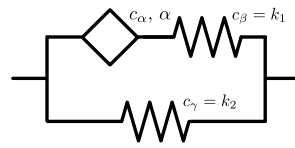
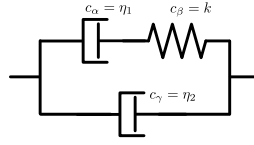


Fig. B.6 Fractional Zener behaviour with $\beta = 0$, $\gamma = 0$ for varying α in increments of 0.1. Color reference α values are red (0.0), orange (0.3), yellow (0.5), green (0.7) and blue (1.0). (a) Relaxation response to step loading. (b) Creep response to step loading and unloading. (c) and (d) Storage (solid line) and loss (dashed line) moduli for the main values of α with colors ascribed above.

- Jeffrey's model: $\alpha = \gamma = 1$ and $\beta = 0$



- $\alpha = \gamma = 1$

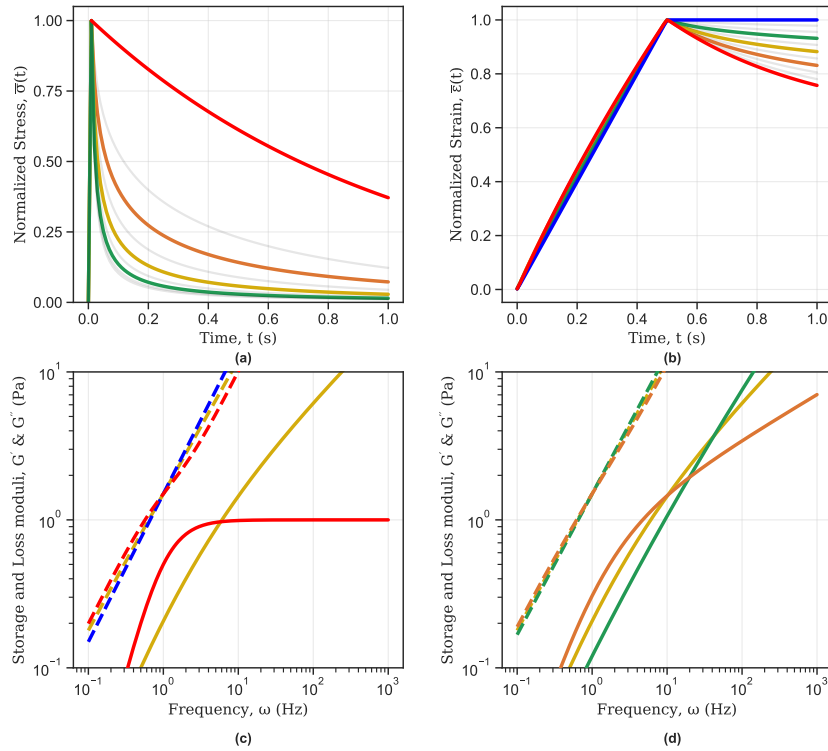
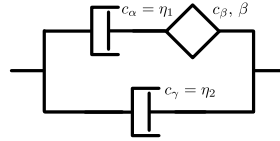


Fig. B.7 Fractional Zener behaviour with $\alpha = 1$, $\gamma = 1$ for varying β in increments of 0.1. Color reference β values are red (0.0), orange (0.3), yellow (0.5), green (0.7) and blue (1.0). (a) Relaxation response to step loading. (b) Creep response to step loading and unloading. (c) and (d) Storage (solid line) and loss (dashed line) moduli for the main values of β with colors ascribed above.

- Fractional BK model: $\alpha = 1$ and $\gamma = 0$

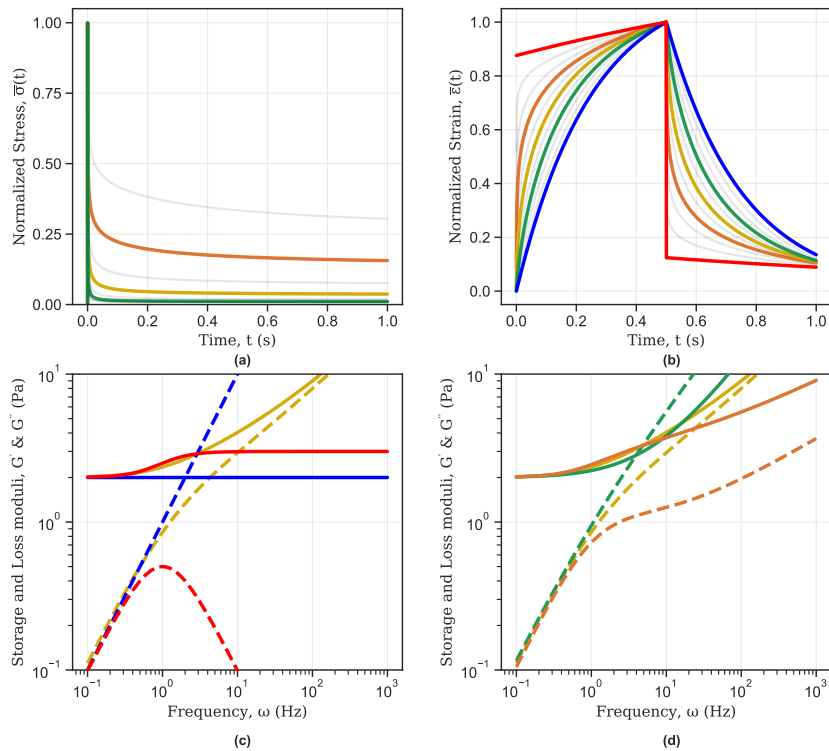
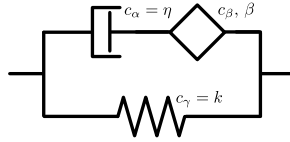


Fig. B.8 Fractional Zener behaviour with $\alpha = 1$, $\gamma = 0$ for varying β in increments of 0.1. Color reference β values are red (0.0), orange (0.3), yellow (0.5), green (0.7) and blue (1.0). (a) Relaxation response to step loading. (b) Creep response to step loading and unloading. (c) and (d) Storage (solid line) and loss (dashed line) moduli for the main values of β with colors ascribed above.

Notes

If we restrict ourself to the cases $\gamma = \alpha$ or $\gamma = \beta$, it is possible to demonstrate that the constitutive equation of the Zener and that of the Poynting-Thomson model presented in the next section are equivalent.

For $\gamma = \alpha$ the constitutive equation of the Zener model is

$$\sigma(t) + \frac{c_{\alpha}^Z}{c_{\beta}^Z} \frac{d^{\alpha-\beta} \sigma(t)}{dt^{\alpha-\beta}} = (c_{\alpha}^Z + c_{\gamma}^Z) \frac{d^{\alpha} \varepsilon(t)}{dt^{\alpha}} + \frac{c_{\alpha}^Z c_{\gamma}^Z}{c_{\beta}^Z} \frac{d^{2\alpha-\beta} \varepsilon(t)}{dt^{2\alpha-\beta}}, \quad (\text{B.1})$$

whereas the constitutive equation of the Poynting-Thomson is

$$\sigma(t) + \frac{c_{\alpha}^{\text{PT}} + c_{\gamma}^{\text{PT}}}{c_{\beta}^{\text{PT}}} \frac{d^{\alpha-\beta} \sigma(t)}{dt^{\alpha-\beta}} = c_{\beta}^{\text{PT}} \frac{d^{\alpha} \varepsilon(t)}{dt^{\alpha}} + \frac{c_{\alpha}^{\text{PT}} c_{\gamma}^{\text{PT}}}{c_{\beta}^{\text{PT}}} \frac{d^{2\alpha-\beta} \varepsilon(t)}{dt^{2\alpha-\beta}}. \quad (\text{B.2})$$

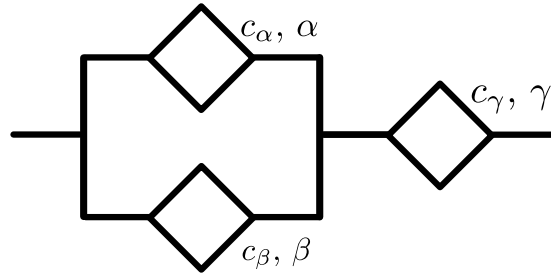
Note that the superscript Z refers to the parameters of the Zener model while PT to those of the Poynting-Thomson model. By equating the coefficients of the terms in equation B.1 and B.2 we can relate the parameters of the Zener model to those of the Poynting-Thomson model

$$\begin{aligned} c_{\alpha}^{\text{PT}} &= \frac{c_{\gamma}^Z (c_{\alpha}^Z + c_{\gamma}^Z)}{c_{\alpha}^Z} \\ c_{\beta}^{\text{PT}} &= \frac{c_{\beta}^Z}{c_{\alpha}^Z} \\ c_{\gamma}^{\text{PT}} &= c_{\alpha}^Z + c_{\gamma}^Z \end{aligned} \quad (\text{B.3})$$

Therefore, we can calculate the creep modulus from the equivalent Poynting-Thomson model.

For $\gamma = \beta$ we simply need to exchange α and β in equation B.3 for both PT and Z parameters.

B.5 Fractional Poynting-Thomson model



Constitutive equation

$$\sigma(t) + \frac{c_\alpha}{c_\gamma} \frac{d^{\alpha-\gamma} \sigma(t)}{dt^{\alpha-\gamma}} + \frac{c_\beta}{c_\gamma} \frac{d^{\beta-\gamma} \sigma(t)}{dt^{\beta-\gamma}} = c_\alpha \frac{d^\alpha \varepsilon(t)}{dt^\alpha} + c_\beta \frac{d^\beta \varepsilon(t)}{dt^\beta}$$

Assuming $0 \leq \beta \leq \alpha \leq 1$

Relaxation modulus

$$\tilde{G}(s) = \frac{1}{s} \frac{c_\gamma s^\gamma \cdot [c_\alpha s^\alpha + c_\beta s^\beta]}{c_\gamma s^\gamma + c_\alpha s^\alpha + c_\beta s^\beta}$$

Creep modulus

$$J(t) = \frac{t^\alpha}{c_\alpha} E_{\alpha-\beta, 1+\alpha} \left(-\frac{c_\beta}{c_\alpha} t^{\alpha-\beta} \right) + \frac{1}{c_\gamma \Gamma(1+\gamma)} t^\gamma$$

Complex modulus

$$G^*(\omega) = \frac{c_\gamma (i\omega)^\gamma \cdot [c_\alpha (i\omega)^\alpha + c_\beta (i\omega)^\beta]}{c_\gamma (i\omega)^\gamma + c_\alpha (i\omega)^\alpha + c_\beta (i\omega)^\beta}$$

Storage modulus

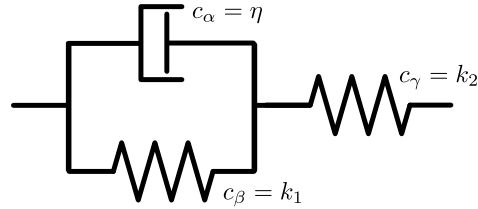
$$G'(\omega) = \frac{c_\gamma \omega^\gamma \cos(\gamma \frac{\pi}{2}) [(c_\alpha \omega^\alpha)^2 + (c_\beta \omega^\beta)^2] + (c_\gamma \omega^\gamma)^2 [c_\alpha \omega^\alpha \cos(\alpha \frac{\pi}{2}) + c_\beta \omega^\beta \cos(\beta \frac{\pi}{2})] + c_\alpha \omega^\alpha \cdot c_\beta \omega^\beta \cdot c_\gamma \omega^\gamma [\cos((\alpha-\beta) \frac{\pi}{2}) + \cos((\beta-\alpha) \frac{\pi}{2})]}{(c_\alpha \omega^\alpha)^2 + (c_\beta \omega^\beta)^2 + (c_\gamma \omega^\gamma)^2 + 2c_\alpha \omega^\alpha \cdot c_\beta \omega^\beta \cos((\alpha-\beta) \frac{\pi}{2}) + 2c_\alpha \omega^\alpha \cdot c_\gamma \omega^\gamma \cos((\alpha-\gamma) \frac{\pi}{2}) + 2c_\beta \omega^\beta \cdot c_\gamma \omega^\gamma \cos((\beta-\gamma) \frac{\pi}{2})}$$

Loss modulus

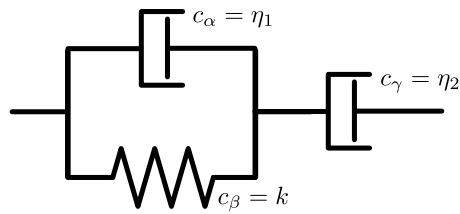
$$G''(\omega) = \frac{c_\gamma \omega^\gamma \sin(\gamma \frac{\pi}{2}) [(c_\alpha \omega^\alpha)^2 + (c_\beta \omega^\beta)^2] + (c_\gamma \omega^\gamma)^2 [c_\alpha \omega^\alpha \sin(\alpha \frac{\pi}{2}) + c_\beta \omega^\beta \sin(\beta \frac{\pi}{2})] + c_\alpha \omega^\alpha \cdot c_\beta \omega^\beta \cdot c_\gamma \omega^\gamma [\sin((\alpha-\beta) \frac{\pi}{2}) + \sin((\beta-\alpha) \frac{\pi}{2})]}{(c_\alpha \omega^\alpha)^2 + (c_\beta \omega^\beta)^2 + (c_\gamma \omega^\gamma)^2 + 2c_\alpha \omega^\alpha \cdot c_\beta \omega^\beta \cos((\alpha-\beta) \frac{\pi}{2}) + 2c_\alpha \omega^\alpha \cdot c_\gamma \omega^\gamma \cos((\alpha-\gamma) \frac{\pi}{2}) + 2c_\beta \omega^\beta \cdot c_\gamma \omega^\gamma \cos((\beta-\gamma) \frac{\pi}{2})}$$

Special cases

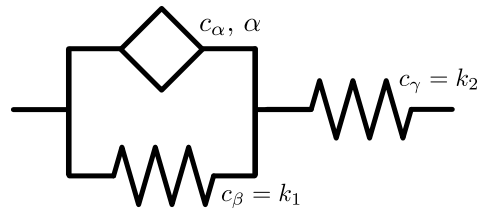
- Standard Linear Solid model: $\alpha = 1$ and $\beta = \gamma = 0$



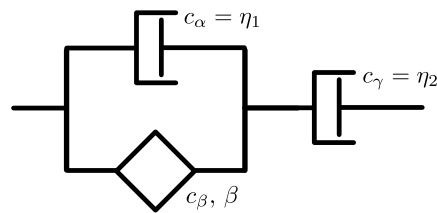
- Jeffrey's model: $\alpha = \gamma = 1$ and $\beta = 0$



- $\beta = \gamma = 0$



- $\alpha = \gamma = 1$



Notes

If we restrict ourselves to the cases $\gamma = \alpha$ or $\gamma = \beta$, it is possible to demonstrate that the constitutive equation of the Poynting-Thomson and that of the Zener model are equivalent.

For $\gamma = \alpha$ the constitutive equation of the Poynting-Thomson model is

$$\sigma(t) + \frac{c_{\alpha}^{\text{PT}}}{c_{\gamma}^{\text{PT}}} \frac{d^{\alpha-\gamma} \sigma(t)}{dt^{\alpha-\gamma}} + \frac{c_{\beta}^{\text{PT}}}{c_{\gamma}^{\text{PT}}} \frac{d^{\beta-\gamma} \sigma(t)}{dt^{\beta-\gamma}} = c_{\alpha}^{\text{PT}} \frac{d^{\alpha} \varepsilon(t)}{dt^{\alpha}} + c_{\beta}^{\text{PT}} \frac{d^{\beta} \varepsilon(t)}{dt^{\beta}}. \quad (\text{B.4})$$

By taking the $(\alpha - \beta)$ th derivative of the equation and multiplying both sides by $c_{\alpha}^{\text{PT}}/c_{\beta}^{\text{PT}}$ we obtain

$$\sigma(t) + \frac{c_{\alpha}^{\text{PT}} + c_{\gamma}^{\text{PT}}}{c_{\beta}^{\text{PT}}} \frac{d^{\alpha-\beta} \sigma(t)}{dt^{\alpha-\beta}} = c_{\beta}^{\text{PT}} \frac{d^{\alpha} \varepsilon(t)}{dt^{\alpha}} + \frac{c_{\alpha}^{\text{PT}} c_{\gamma}^{\text{PT}}}{c_{\beta}^{\text{PT}}} \frac{d^{2\alpha-\beta} \varepsilon(t)}{dt^{2\alpha-\beta}}; \quad (\text{B.5})$$

whereas the constitutive equation of the Zener model becomes

$$\sigma(t) + \frac{c_{\alpha}^{\text{Z}}}{c_{\beta}^{\text{Z}}} \frac{d^{\alpha-\beta} \sigma(t)}{dt^{\alpha-\beta}} = (c_{\alpha}^{\text{Z}} + c_{\gamma}^{\text{Z}}) \frac{d^{\alpha} \varepsilon(t)}{dt^{\alpha}} + \frac{c_{\alpha}^{\text{Z}} c_{\gamma}^{\text{Z}}}{c_{\beta}^{\text{Z}}} \frac{d^{2\alpha-\beta} \varepsilon(t)}{dt^{2\alpha-\beta}}. \quad (\text{B.6})$$

Note that the superscript PT refers to the parameters of the Poynting-Thomson model whilst the superscript Z to those of the Zener model. By equating the coefficients of the terms in equation B.5 and B.6 we can relate the parameters of the Poynting-Thomson model to those of the Zener

$$\begin{aligned} c_{\alpha}^{\text{Z}} &= \frac{(c_{\gamma}^{\text{PT}})^2}{c_{\alpha}^{\text{PT}} + c_{\gamma}^{\text{PT}}} \\ c_{\beta}^{\text{Z}} &= \frac{c_{\beta}^{\text{PT}} (c_{\gamma}^{\text{PT}})^2}{(c_{\alpha}^{\text{PT}} + c_{\gamma}^{\text{PT}})^2} \\ c_{\gamma}^{\text{Z}} &= \frac{c_{\alpha}^{\text{PT}} c_{\gamma}^{\text{PT}}}{c_{\alpha}^{\text{PT}} + c_{\gamma}^{\text{PT}}} \end{aligned} \quad (\text{B.7})$$

Therefore, we can calculate the relaxation modulus from the equivalent Zener model.

For $\gamma = \beta$ we simply need to exchange α and β in equation B.7 for both PT and Z parameters.

Appendix C

Model Fits and Error Analysis

C.1 Overview and Methodology

In this Appendix section, fits for all the data analysed via viscoelastic models are shown in regular and logarithmic scales. The bulk (all group samples) mean and standard deviation of mean-squared-error for each model and dataset is shown in the figure captions. The mean-squared-error for an individual data file is calculated by taking the difference between the predicted and real response at each data point and squaring it, then summing all the squared differences together; the sum is then divided by the number of elements to yield an average mean-squared-error for that data file. The formula is written

$$\frac{1}{N} \sum_i^N (\text{predicted}(i) - \text{real}(i))^2, \quad (\text{C.1})$$

where N is the number of time samples in a particular data file, $\text{predicted}(i)$ $\text{real}(i)$ are the i th samples of the predicted and real response respectively. Note that N varies only slightly between individual data files due to slightly different ramp and hold times during the AFM run. Bulk means and standard deviations reported in the figure captions (e.g. all SLS2 fits to DM33 gels) use these individual data file mean-squared-errors as their input.

C.2 Fits and Errors

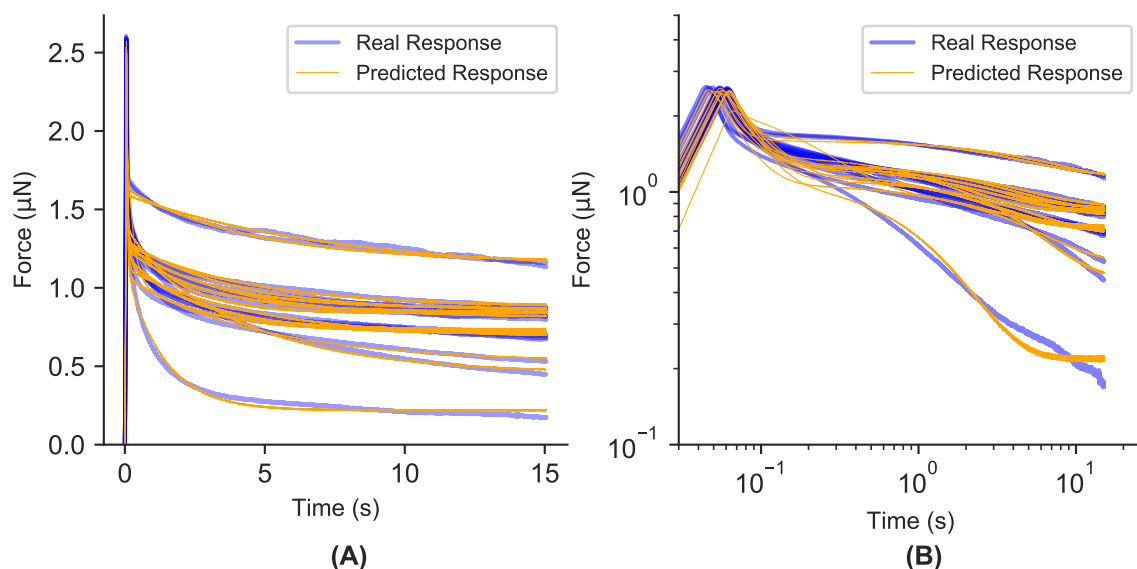
SLS2: DM33 and DM41

Fig. C.1 Real and predicted response of DM33 pectin gels fitted to the SLS2 viscoelastic model. Bulk mean-squared-error: $5.4070\text{e-}16$ (5 s.f.). Bulk standard deviation: $2.4567\text{e-}16$ (5 s.f.). Real response (blue line) has 40% opacity so a stronger blue color indicates greater line density. A) Responses plotted against time in normal scale. B) Same as A but in logarithmic scale.

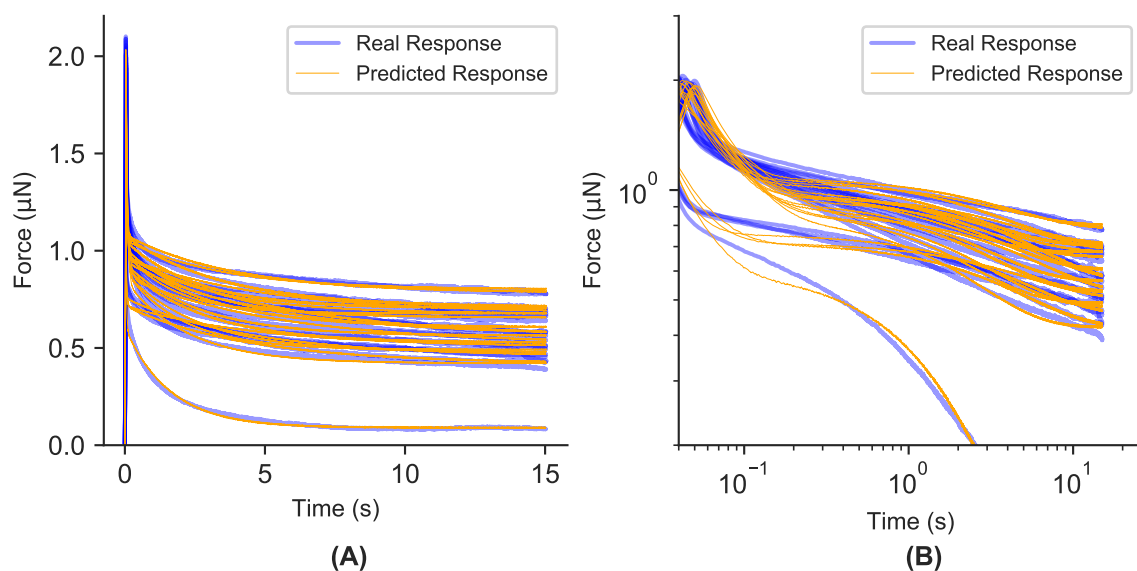


Fig. C.2 Real and predicted response of DM41 pectin gels fitted to the SLS2 viscoelastic model. Bulk mean-squared-error: $3.0784\text{e-}16$ (5 s.f.). Bulk standard deviation: $1.2506\text{e-}16$ (5 s.f.). Real response (blue line) has 40% opacity so a stronger blue color indicates greater line density. A) Responses plotted against time in normal scale. B) Same as A but in logarithmic scale.

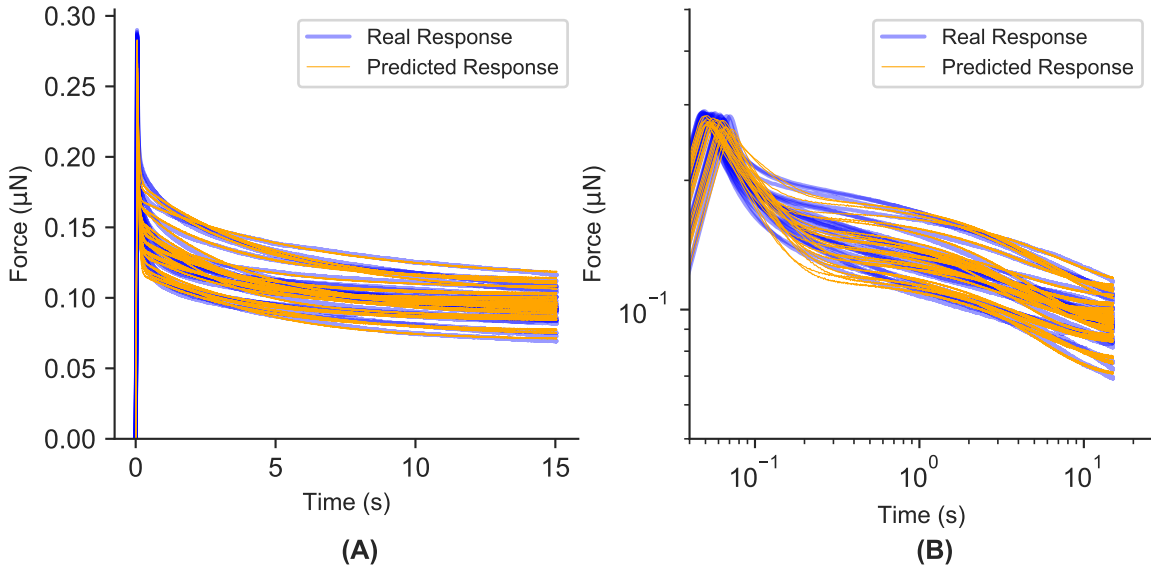
SLS2: DM50 and DM41 (33/50)

Fig. C.3 Real and predicted response of DM50 pectin gels fitted to the SLS2 viscoelastic model. Bulk mean-squared-error: $3.9352\text{e-}18$ (5 s.f.). Bulk standard deviation: $1.0329\text{e-}18$ (5 s.f.). Real response (blue line) has 40% opacity so a stronger blue color indicates greater line density. A) Responses plotted against time in normal scale. B) Same as A but in logarithmic scale.

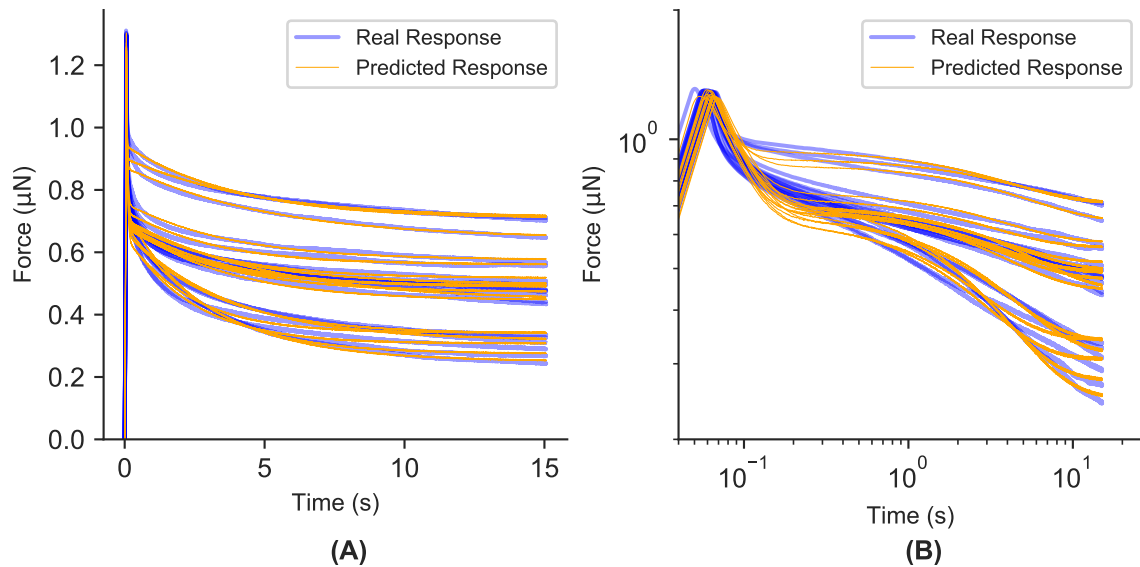


Fig. C.4 Real and predicted response of DM41(33/50) pectin gels fitted to the SLS2 viscoelastic model. Bulk mean-squared-error: $1.1569\text{e-}16$ (5 s.f.). Bulk standard deviation: $4.9029\text{e-}17$ (5 s.f.). Real response (blue line) has 40% opacity so a stronger blue color indicates greater line density. A) Responses plotted against time in normal scale. B) Same as A but in logarithmic scale.

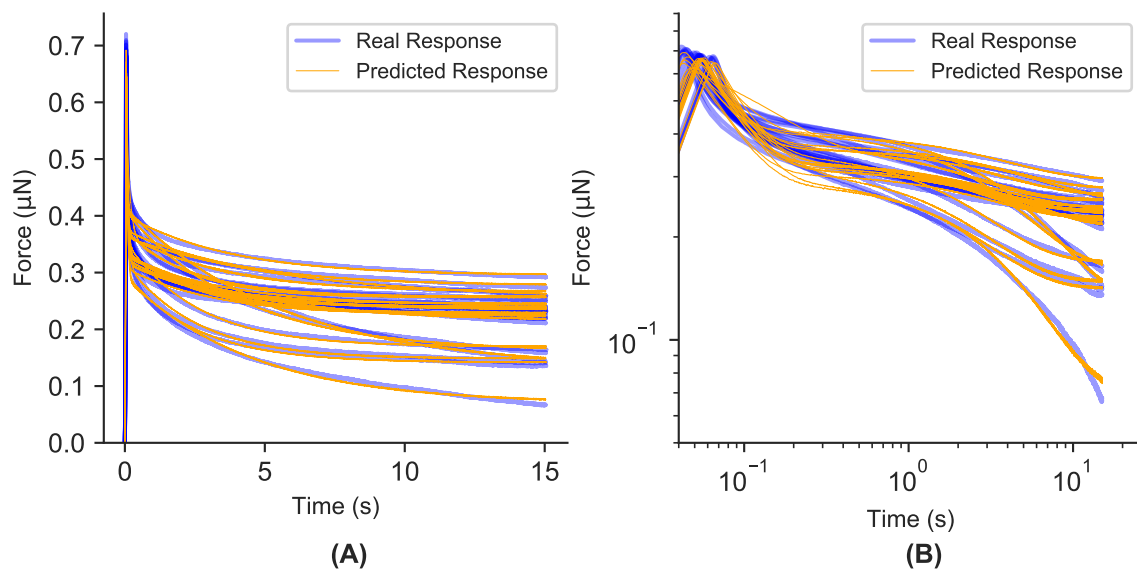
SLS2: DM50 (41/60) and DM50 (33/70)

Fig. C.5 Real and predicted response of DM50(41/60) pectin gels fitted to the SLS2 viscoelastic model. Bulk mean-squared-error: $2.6620\text{e-}17$ (5 s.f.). Bulk standard deviation: $1.0463\text{e-}17$ (5 s.f.). Real response (blue line) has 40% opacity so a stronger blue color indicates greater line density. A) Responses plotted against time in normal scale. B) Same as A but in logarithmic scale.

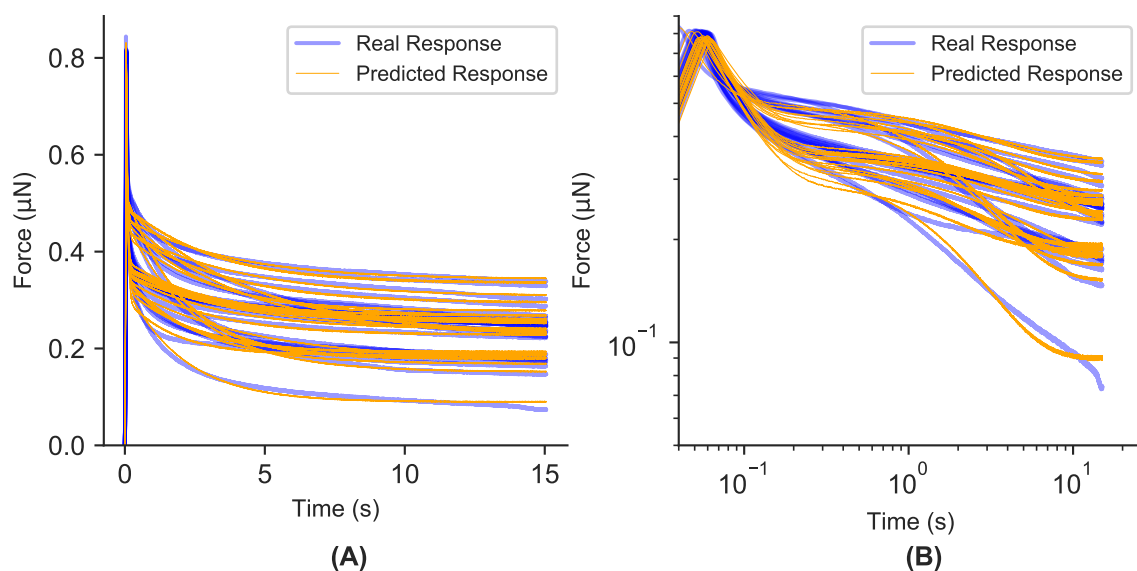


Fig. C.6 Real and predicted response of DM50(33/70) pectin gels fitted to the SLS2 viscoelastic model. Bulk mean-squared-error: $4.2302\text{e-}17$ (5 s.f.). Bulk standard deviation: $1.6586\text{e-}17$ (5 s.f.). Real response (blue line) has 40% opacity so a stronger blue color indicates greater line density. A) Responses plotted against time in normal scale. B) Same as A but in logarithmic scale.

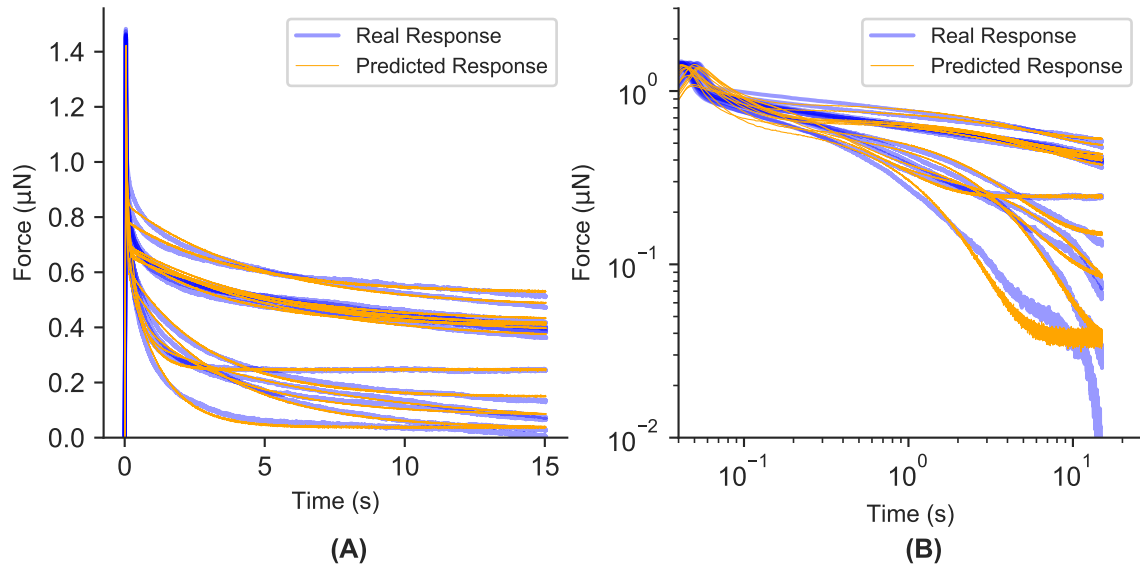
SLS2: DM40 Block and DM40 Random

Fig. C.7 Real and predicted response of DM40 (block) pectin gels fitted to the SLS2 viscoelastic model. Bulk mean-squared-error: 2.5406e-16 (5 s.f.). Bulk standard deviation: 1.0165e-16 (5 s.f.). Real response (blue line) has 40% opacity so a stronger blue color indicates greater line density. A) Responses plotted against time in normal scale. B) Same as A but in logarithmic scale.

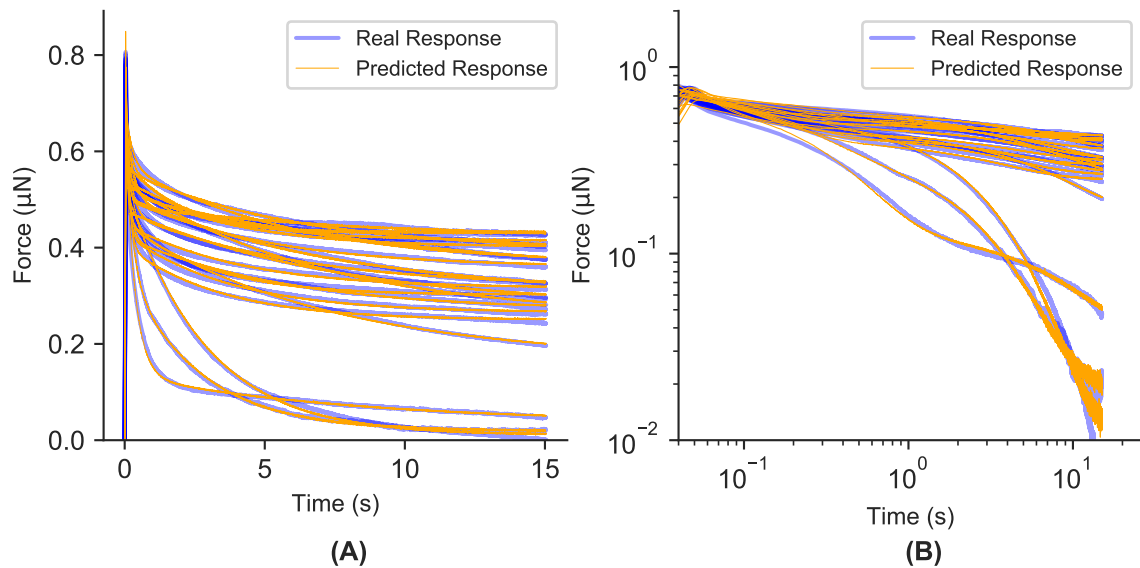


Fig. C.8 Real and predicted response of DM40 (random) pectin gels fitted to the SLS2 viscoelastic model. Bulk mean-squared-error: 5.2624e-17 (5 s.f.). Bulk standard deviation: 1.4564e-17 (5 s.f.). Real response (blue line) has 40% opacity so a stronger blue color indicates greater line density. A) Responses plotted against time in normal scale. B) Same as A but in logarithmic scale.

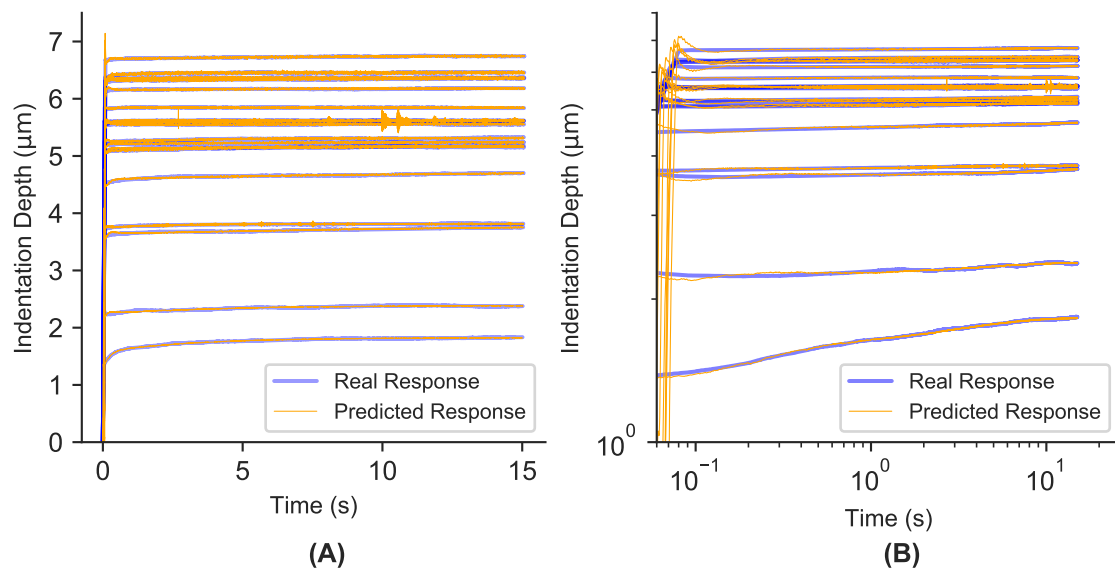
SLS2: *Arabidopsis* Hypocotyl Transverse and Axial Walls

Fig. C.9 Real and predicted response of *Arabidopsis* transverse walls fitted to the SLS2 viscoelastic model. Bulk mean-squared-error: $2.0674\text{e-}14$ (5 s.f.). Bulk standard deviation: $1.2653\text{e-}14$ (5 s.f.). Real response (blue line) has 40% opacity so a stronger blue color indicates greater line density. A) Responses plotted against time in normal scale. B) Same as A but in logarithmic scale.

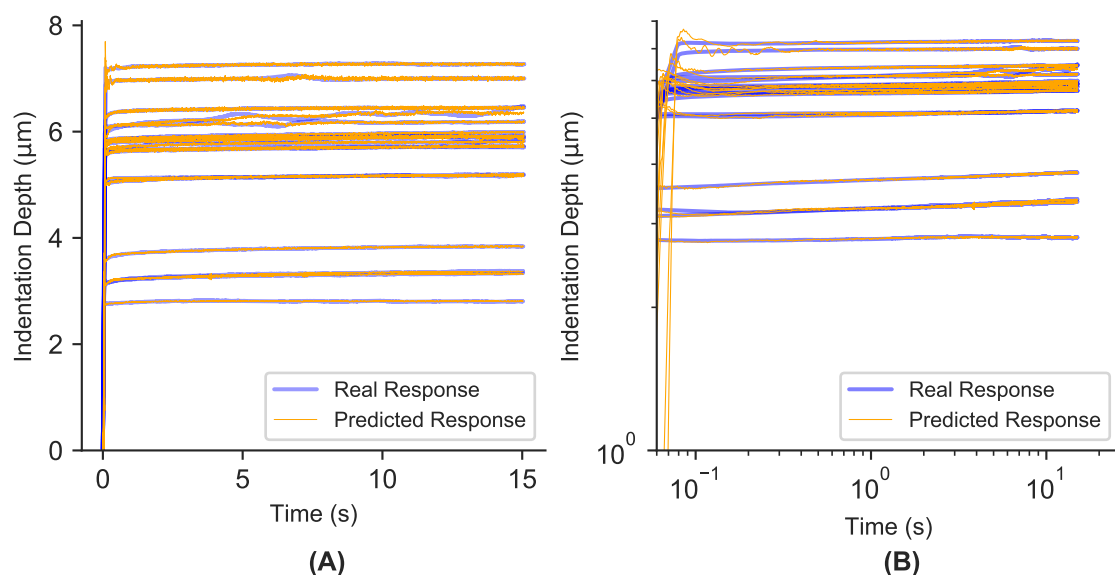


Fig. C.10 Real and predicted response of *Arabidopsis* axial walls fitted to the SLS2 viscoelastic model. Bulk mean-squared-error: $1.7174\text{e-}14$ (5 s.f.). Bulk standard deviation: $1.3187\text{e-}14$ (5 s.f.). Real response (blue line) has 40% opacity so a stronger blue color indicates greater line density. A) Responses plotted against time in normal scale. B) Same as A but in logarithmic scale.

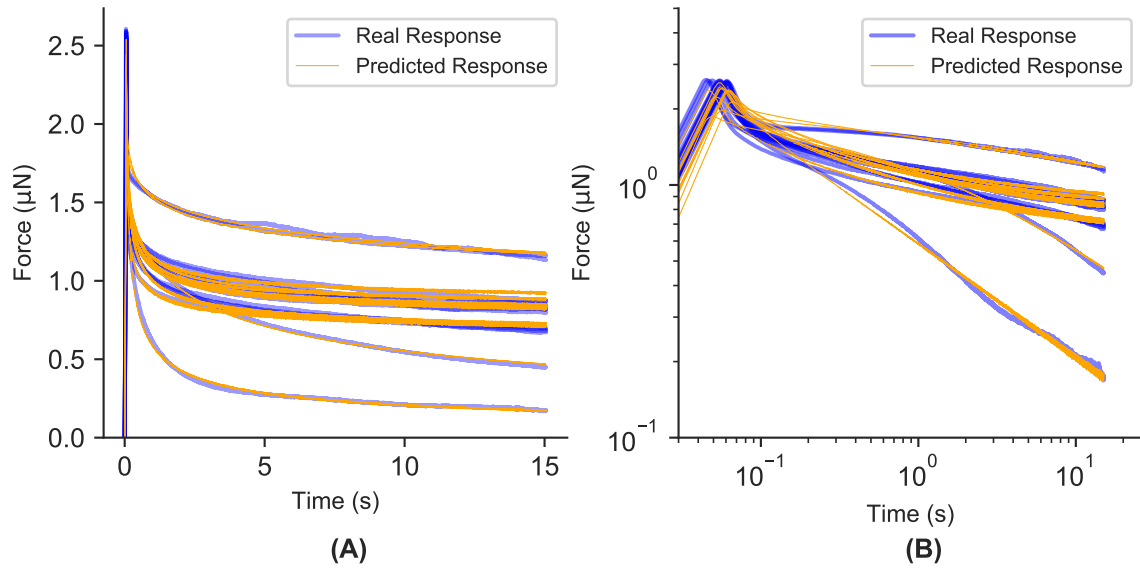
FSLs: DM33 and DM41

Fig. C.11 Real and predicted response of DM33 pectin gels fitted to the FSLs viscoelastic model. Bulk mean-squared-error: $8.4606\text{e-}16$ (5 s.f.). Bulk standard deviation: $4.0028\text{e-}16$ (5 s.f.). Real response (blue line) has 40% opacity so a stronger blue color indicates greater line density. A) Responses plotted against time in normal scale. B) Same as A but in logarithmic scale.

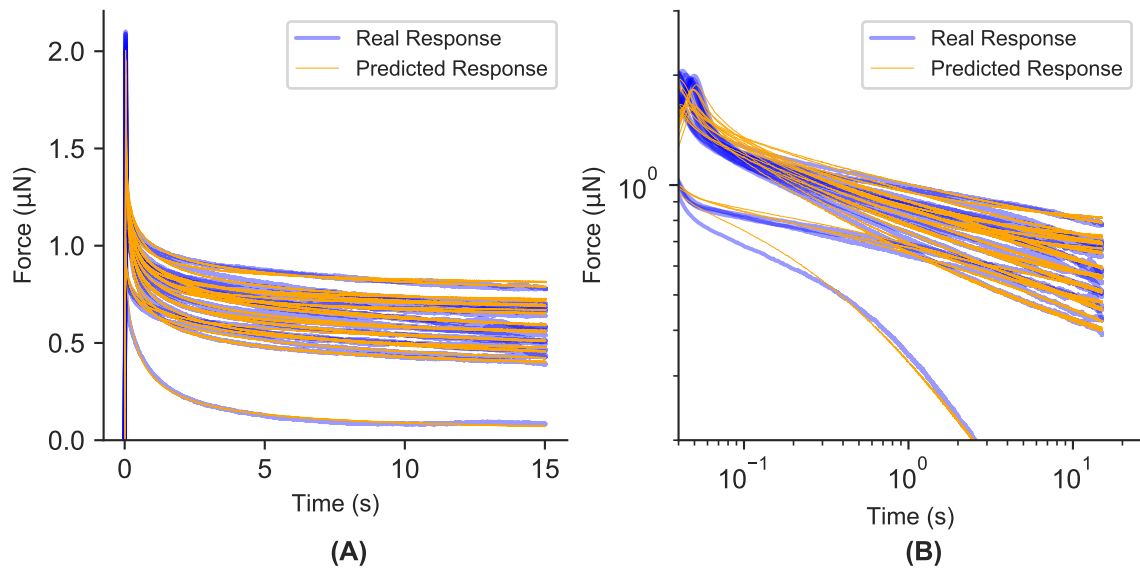


Fig. C.12 Real and predicted response of DM41 pectin gels fitted to the FSLs viscoelastic model. Bulk mean-squared-error: $3.5289\text{e-}16$ (5 s.f.). Bulk standard deviation: $2.0109\text{e-}16$ (5 s.f.). Real response (blue line) has 40% opacity so a stronger blue color indicates greater line density. A) Responses plotted against time in normal scale. B) Same as A but in logarithmic scale.

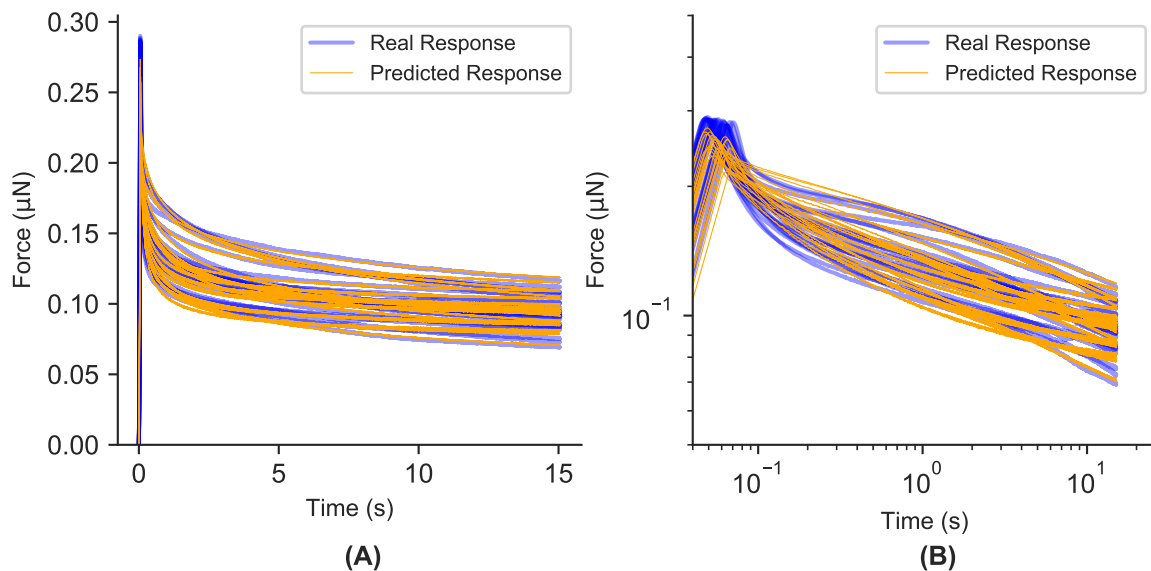
FSLs: DM50 and DM41 (33/50)

Fig. C.13 Real and predicted response of DM50 pectin gels fitted to the FSLs viscoelastic model. Bulk mean-squared-error: $7.8350\text{e-}18$ (5 s.f.). Bulk standard deviation: $4.7708\text{e-}18$ (5 s.f.). Real response (blue line) has 40% opacity so a stronger blue color indicates greater line density. A) Responses plotted against time in normal scale. B) Same as A but in logarithmic scale.

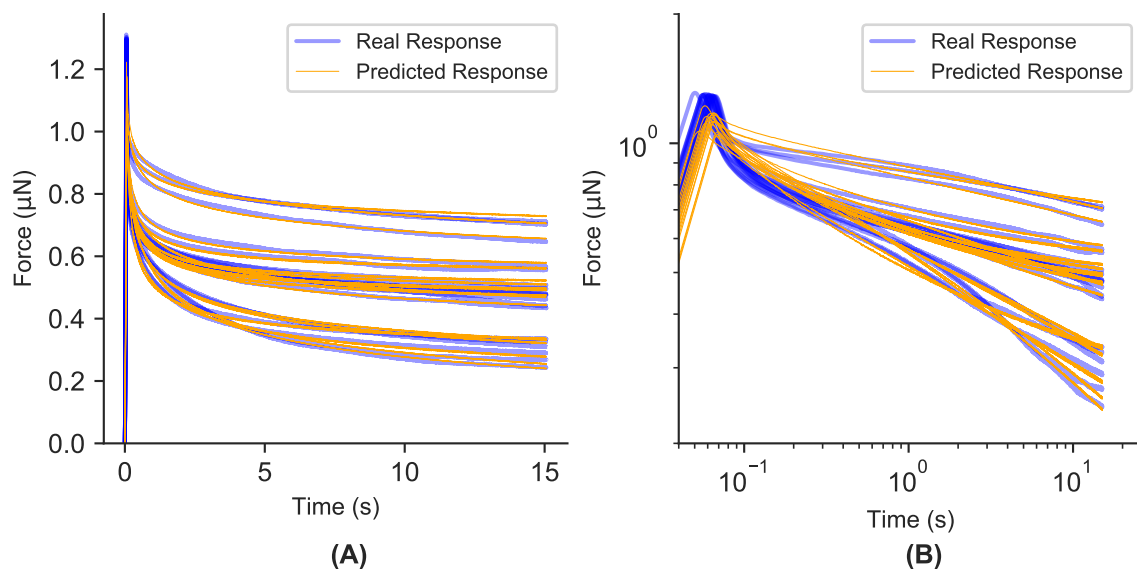


Fig. C.14 Real and predicted response of DM41(33/50) pectin gels fitted to the FSLs viscoelastic model. Bulk mean-squared-error: $1.9054\text{e-}16$ (5 s.f.). Bulk standard deviation: $5.9022\text{e-}17$ (5 s.f.). Real response (blue line) has 40% opacity so a stronger blue color indicates greater line density. A) Responses plotted against time in normal scale. B) Same as A but in logarithmic scale.

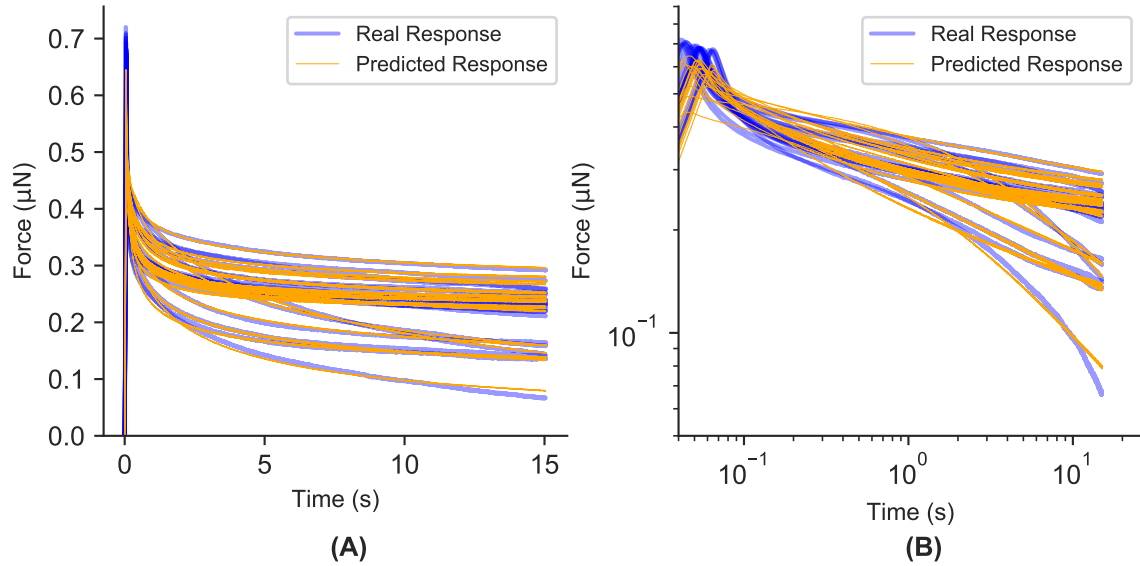
FSLs: DM50 (41/60) and DM50 (33/70)

Fig. C.15 Real and predicted response of DM50(41/60) pectin gels fitted to the FSLs viscoelastic model. Bulk mean-squared-error: 4.1975e-17 (5 s.f.). Bulk standard deviation: 3.4932e-17 (5 s.f.). Real response (blue line) has 40% opacity so a stronger blue color indicates greater line density. A) Responses plotted against time in normal scale. B) Same as A but in logarithmic scale.

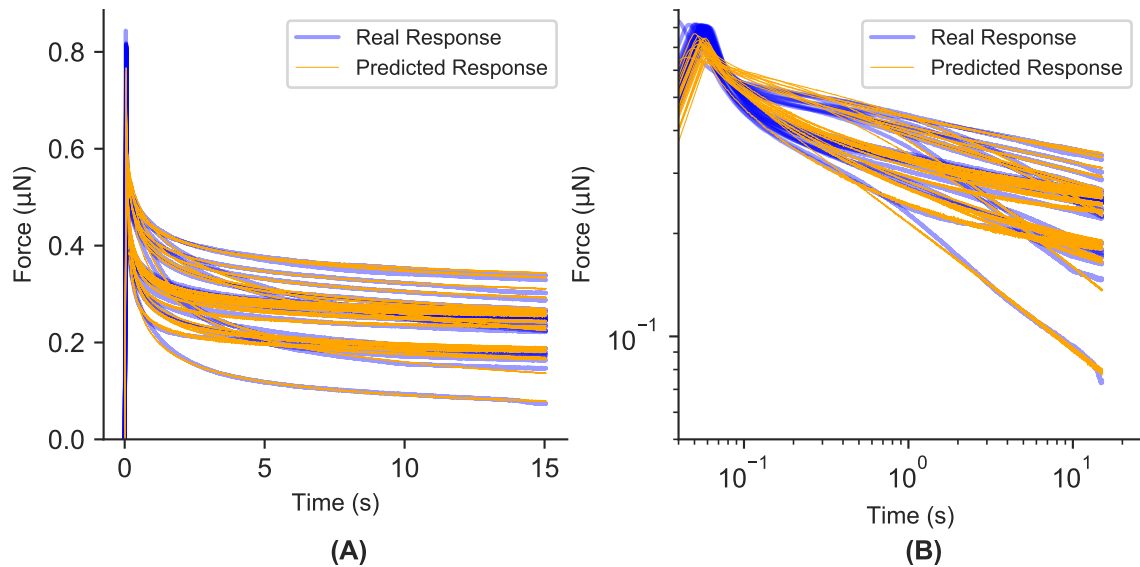


Fig. C.16 Real and predicted response of DM50(33/70) pectin gels fitted to the FSLs viscoelastic model. Bulk mean-squared-error: 6.1739e-17 (5 s.f.). Bulk standard deviation: 2.8291e-17 (5 s.f.). Real response (blue line) has 40% opacity so a stronger blue color indicates greater line density. A) Responses plotted against time in normal scale. B) Same as A but in logarithmic scale.

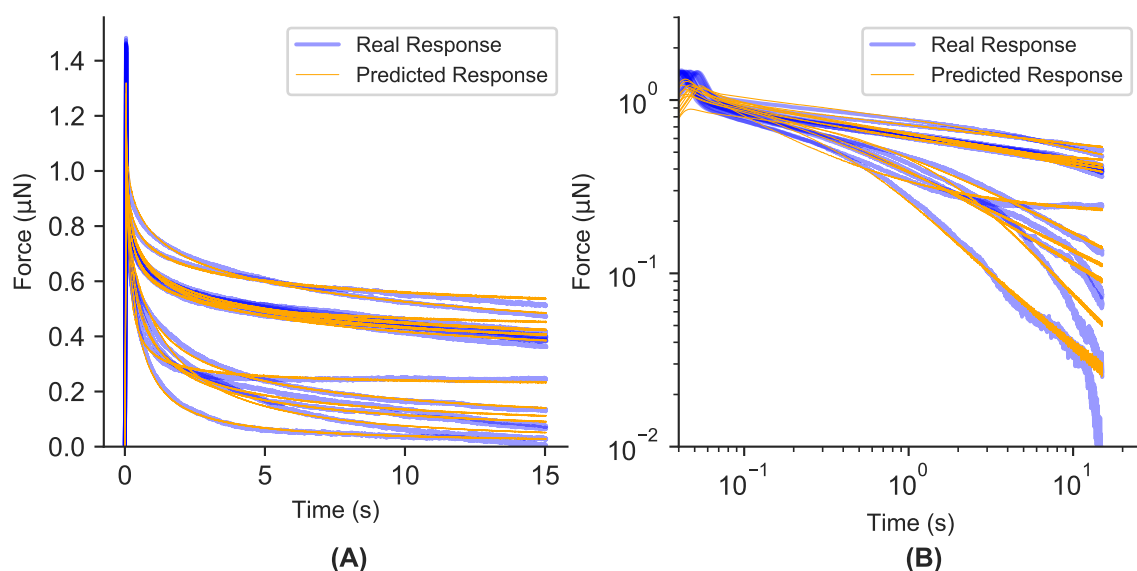
FSLs: DM40 Block and DM40 Random

Fig. C.17 Real and predicted response of DM40 (Block) pectin gels fitted to the FSLs viscoelastic model. Bulk mean-squared-error: $3.5677\text{e-}16$ (5 s.f.). Bulk standard deviation: $1.5222\text{e-}16$ (5 s.f.). Real response (blue line) has 40% opacity so a stronger blue color indicates greater line density. A) Responses plotted against time in normal scale. B) Same as A but in logarithmic scale.

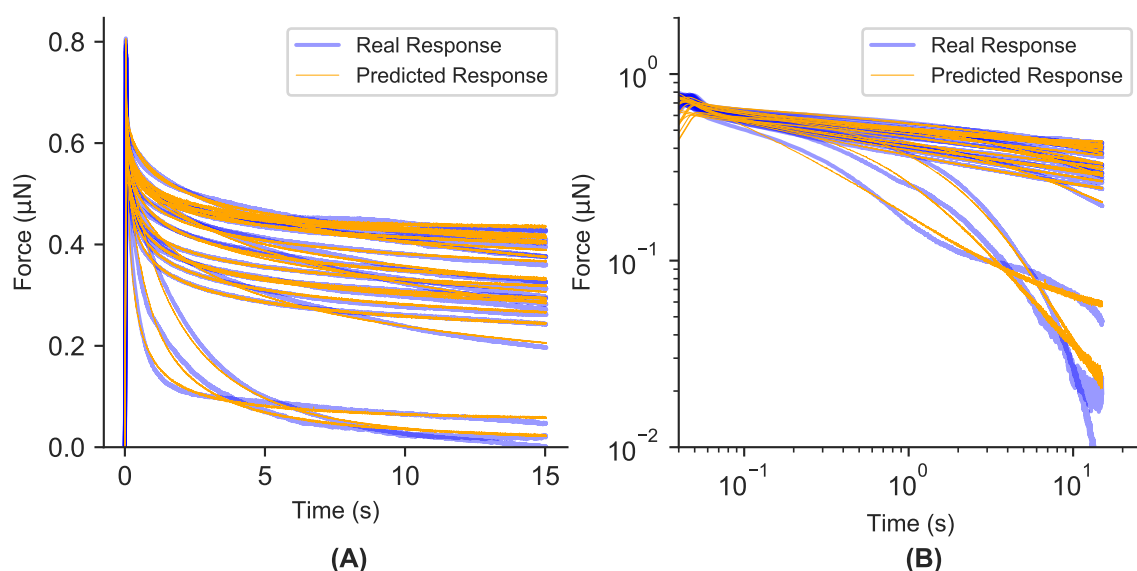


Fig. C.18 Real and predicted response of DM40 (Random) pectin gels fitted to the FSLs viscoelastic model. Bulk mean-squared-error: $6.5486\text{e-}17$ (5 s.f.). Bulk standard deviation: $4.9781\text{e-}17$ (5 s.f.). Real response (blue line) has 40% opacity so a stronger blue color indicates greater line density. A) Responses plotted against time in normal scale. B) Same as A but in logarithmic scale.

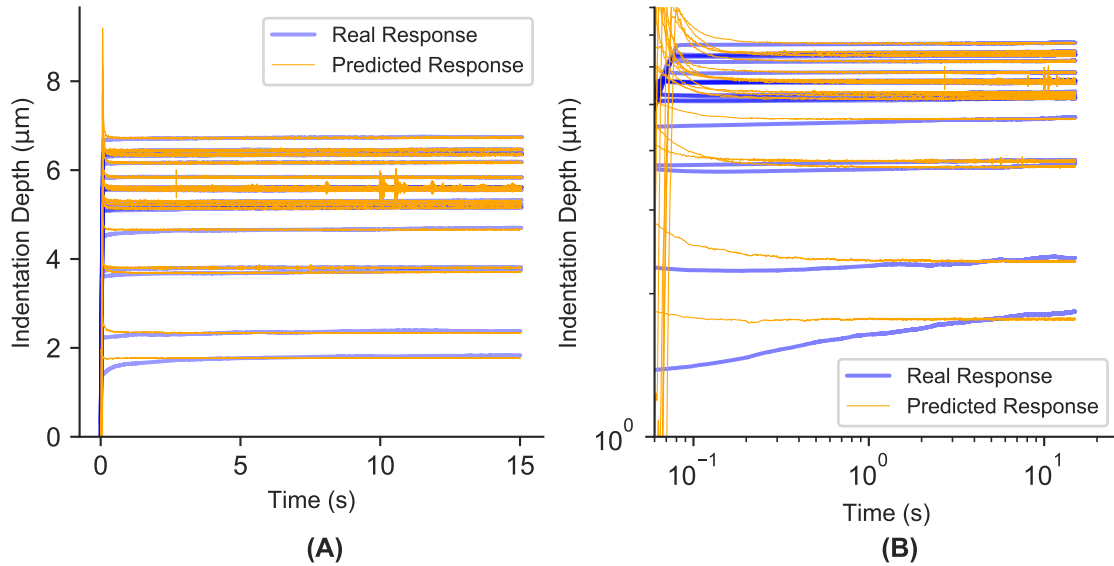
FSLs: *Arabidopsis* Hypocotyl Transverse and Axial Walls

Fig. C.19 Real and predicted response of *Arabidopsis* transverse walls fitted to the FSLs viscoelastic model. Bulk mean-squared-error: 2.2844e-14 (5 s.f.). Bulk standard deviation: 1.1972e-14 (5 s.f.). Real response (blue line) has 40% opacity so a stronger blue color indicates greater line density. A) Responses plotted against time in normal scale. B) Same as A but in logarithmic scale.

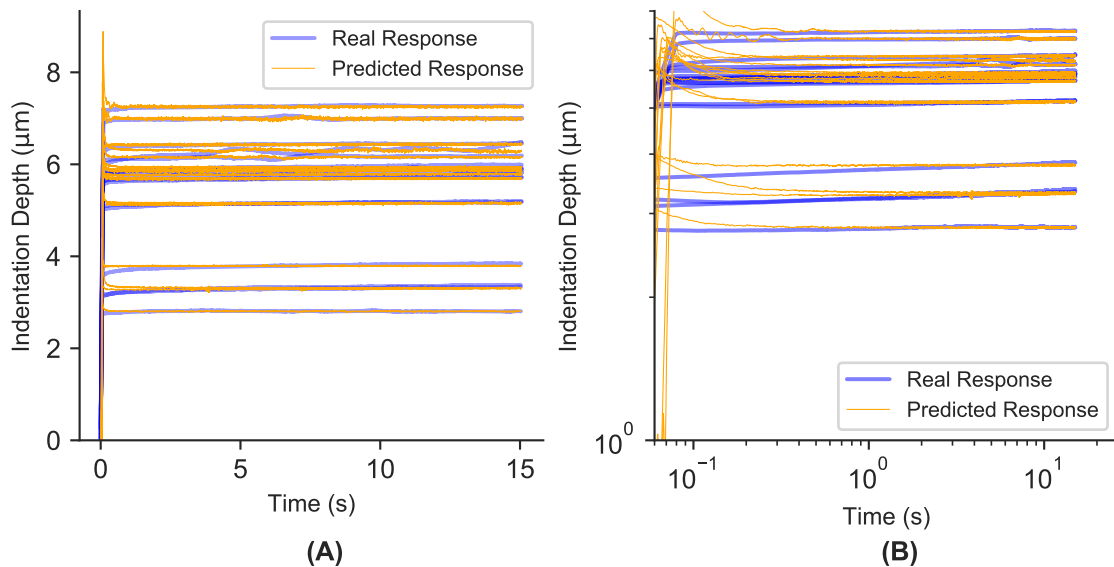


Fig. C.20 Real and predicted response of *Arabidopsis* axial walls fitted to the FSLs viscoelastic model. Bulk mean-squared-error: 1.9197e-14 (5 s.f.). Bulk standard deviation: 1.3413e-14 (5 s.f.). Real response (blue line) has 40% opacity so a stronger blue color indicates greater line density. A) Responses plotted against time in normal scale. B) Same as A but in logarithmic scale.

C.3 Tabulated Error Data

| | SLS2 | FSLs |
|---------------------------|------------|------------|
| DM33 | 5.4070e-16 | 8.4606e-16 |
| DM41 | 3.0784e-16 | 3.5289e-16 |
| DM50 | 3.9352e-18 | 7.8350e-18 |
| DM41 (33/50) | 1.1569e-16 | 1.9054e-16 |
| DM50 (41/60) | 2.6620e-17 | 4.1975e-17 |
| DM50 (33/70) | 4.2302e-17 | 6.1739e-17 |
| DM40 (Block) | 2.5406e-16 | 3.5677e-16 |
| DM40 (Random) | 5.2624e-17 | 6.5486e-17 |
| <i>Arabidopsis</i> Trans. | 2.0674e-14 | 2.2844e-14 |
| <i>Arabidopsis</i> Axial | 1.7174e-14 | 1.9197e-14 |

Table C.1 Summary of bulk mean squared errors for the SLS2 and FSLs models fitted to the gels and plants data.

Appendix D

Summary of Statistics

D.1 Overview and Methodology

In this Appendix section, the pair-wise and group-wise p-values of the experimental data presented in Chapters 3 and 4 are summarised. The pair-wise p-values were calculated using the non-parametric Kolmogorov-Smirnov test in SciPy (`scipy.stats.mstats.ks_twosamp`). The group-wise P-values were calculated using a one-way ANOVA in SciPy (`scipy.stats.f_oneway`).

D.2 SLS2 Parameters

D.2.1 DM33, DM41, DM50 and Mixtures

Instantaneous Shear Stiffness (ISS)

ANOVA P-value: 1.09e-54

| DM | 33 | 41 | 50 | 33/50 | 41/60 | 33/70 |
|-------|----------|----------|----------|----------|----------|----------|
| 33 | - | 6.54e-07 | 1.44e-08 | 9.09e-07 | 3.58e-08 | 1.01e-07 |
| 41 | 6.54e-07 | - | 4.47e-10 | 4.05e-05 | 1.02e-08 | 9.62e-09 |
| 50 | 1.44e-08 | 4.47e-10 | - | 8.40e-10 | 1.37e-10 | 1.06e-11 |
| 33/50 | 9.09e-07 | 4.05e-05 | 8.40e-10 | - | 1.71e-08 | 4.44e-08 |
| 41/60 | 3.58e-08 | 1.02e-08 | 1.37e-10 | 1.71e-08 | - | 1.29e-03 |
| 33/70 | 1.01e-07 | 9.62e-09 | 1.06e-11 | 4.44e-08 | 1.29e-03 | - |

Table D.1 Pairwise P-values of the SLS2 ISS parameters as fitted to DM33, 41, 50 and gel mixtures. Note that the values are symmetric about the diagonal.

Elastic/Viscous (E/V) Ratios

ANOVA P-value: 1.10e-04

| DM | 33 | 41 | 50 | 33/50 | 41/60 | 33/70 |
|-------|----------|----------|----------|----------|----------|----------|
| 33 | - | 3.56e-01 | 4.81e-04 | 1.80e-01 | 3.70e-03 | 1.42e-01 |
| 41 | 3.56e-01 | - | 7.73e-03 | 6.73e-01 | 4.36e-02 | 5.18e-01 |
| 50 | 4.81e-04 | 7.73e-03 | - | 5.87e-02 | 2.49e-01 | 2.65e-05 |
| 33/50 | 1.80e-01 | 6.73e-01 | 5.87e-02 | - | 2.95e-01 | 3.56e-02 |
| 41/60 | 3.70e-03 | 4.36e-02 | 2.49e-01 | 2.95e-01 | - | 5.88e-04 |
| 33/70 | 1.42e-01 | 5.18e-01 | 2.65e-05 | 3.56e-02 | 5.88e-04 | - |

Table D.2 Pairwise P-values of the SLS2 E/V parameters as fitted to DM33, 41, 50 and gel mixtures. Note that the values are symmetric about the diagonal.

Dashpot 1, η_1

ANOVA P-value: 1.07e-27

| DM | 33 | 41 | 50 | 33/50 | 41/60 | 33/70 |
|-------|----------|----------|----------|----------|----------|----------|
| 33 | - | 2.06e-02 | 1.44e-08 | 6.80e-06 | 3.04e-06 | 1.32e-07 |
| 41 | 2.06e-02 | - | 4.47e-10 | 1.68e-06 | 4.53e-07 | 1.65e-08 |
| 50 | 1.44e-08 | 4.47e-10 | - | 8.40e-10 | 8.58e-10 | 1.06e-11 |
| 33/50 | 6.80e-06 | 1.68e-06 | 8.40e-10 | - | 8.99e-04 | 2.21e-05 |
| 41/60 | 3.04e-06 | 4.53e-07 | 8.58e-10 | 8.99e-04 | - | 1.05e-01 |
| 33/70 | 1.32e-07 | 1.65e-08 | 1.06e-11 | 2.21e-05 | 1.05e-01 | - |

Table D.3 Pairwise P-values of the SLS2 Dashpot 1 parameters as fitted to DM33, 41, 50 and gel mixtures. Note that the values are symmetric about the diagonal.

Dashpot 2, η_2

ANOVA P-value: 1.30e-16

| DM | 33 | 41 | 50 | 33/50 | 41/60 | 33/70 |
|-------|----------|----------|----------|----------|----------|----------|
| 33 | - | 5.76e-01 | 1.44e-08 | 5.80e-05 | 3.33e-06 | 1.32e-07 |
| 41 | 5.76e-01 | - | 4.47e-10 | 6.89e-03 | 1.62e-06 | 1.90e-07 |
| 50 | 1.44e-08 | 4.47e-10 | - | 8.40e-10 | 1.53e-04 | 3.41e-07 |
| 33/50 | 5.80e-05 | 6.89e-03 | 8.40e-10 | - | 1.53e-04 | 8.32e-05 |
| 41/60 | 3.33e-06 | 1.62e-06 | 1.53e-04 | 1.53e-04 | - | 5.49e-01 |
| 33/70 | 1.32e-07 | 1.90e-07 | 3.41e-07 | 8.32e-05 | 5.49e-01 | - |

Table D.4 Pairwise P-values of the SLS2 Dashpot 2 parameters as fitted to DM33, 41, 50 and gel mixtures. Note that the values are symmetric about the diagonal.**Time-scale 1, τ_1**

ANOVA P-value: 7.61e-02

| DM | 33 | 41 | 50 | 33/50 | 41/60 | 33/70 |
|-------|----------|----------|----------|----------|----------|----------|
| 33 | - | 4.78e-02 | 5.77e-05 | 9.24e-01 | 2.19e-02 | 1.93e-01 |
| 41 | 4.78e-02 | - | 5.71e-02 | 2.29e-03 | 7.01e-01 | 1.74e-01 |
| 50 | 5.77e-05 | 5.71e-02 | - | 4.71e-06 | 2.28e-03 | 8.92e-06 |
| 33/50 | 9.24e-01 | 2.29e-03 | 4.71e-06 | - | 5.16e-03 | 3.98e-02 |
| 41/60 | 2.19e-02 | 7.01e-01 | 2.28e-03 | 5.16e-03 | - | 4.74e-01 |
| 33/70 | 1.93e-01 | 1.74e-01 | 8.92e-06 | 3.98e-02 | 4.74e-01 | - |

Table D.5 Pairwise P-values of the SLS2 Time-scale 1 parameters as fitted to DM33, 41, 50 and gel mixtures. Note that the values are symmetric about the diagonal.

Time-scale 2, τ_2

ANOVA P-value: 2.42e-02

| DM | 33 | 41 | 50 | 33/50 | 41/60 | 33/70 |
|-------|----------|----------|----------|----------|----------|----------|
| 33 | - | 5.76e-01 | 3.41e-01 | 3.47e-01 | 7.90e-01 | 3.08e-01 |
| 41 | 5.76e-01 | - | 7.11e-01 | 4.64e-02 | 1.99e-01 | 2.98e-02 |
| 50 | 3.41e-01 | 7.11e-01 | - | 3.73e-02 | 1.34e-01 | 1.55e-02 |
| 33/50 | 3.47e-01 | 4.64e-02 | 3.73e-02 | - | 5.41e-01 | 4.91e-01 |
| 41/60 | 7.90e-01 | 1.99e-01 | 1.34e-01 | 5.41e-01 | - | 8.89e-01 |
| 33/70 | 3.08e-01 | 2.98e-02 | 1.55e-02 | 4.91e-01 | 8.89e-01 | - |

Table D.6 Pairwise P-values of the SLS2 Time-scale 2 parameters as fitted to DM33, 41, 50 and gel mixtures. Note that the values are symmetric about the diagonal.

D.2.2 DM40 Block and Random

Instantaneous Shear Stiffness (ISS)

ANOVA P-value: 1.42e-04

Non-parametric KS P-value: 6.94e-03

Elastic/Viscous (E/V) Ratios

ANOVA P-value: 1.28e-04

Non-parametric KS P-value: 5.04e-05

Dashpot 1, η_1

ANOVA P-value: 6.56e-01

Non-parametric KS P-value: 2.07e-01

Dashpot 2, η_2

ANOVA P-value: 7.55e-01

Non-parametric KS P-value: 3.67e-01

Time-scale 1, τ_1

ANOVA P-value: 1.12e-02

Non-parametric KS P-value: 1.07e-03

Time-scale 2, τ_2

ANOVA P-value: 6.75e-02

Non-parametric KS P-value: 9.01e-02

D.2.3 *Arabidopsis* Hypocotyl

Instantaneous Shear Stiffness (ISS)

ANOVA P-value: 1.59e-01

Non-parametric KS P-value: 3.87e-02

Elastic/Viscous (E/V) Ratios

ANOVA P-value: 2.16e-04

Non-parametric KS P-value: 1.19e-02

Time-scale 1, τ_1

ANOVA P-value: 6.31e-03

Non-parametric KS P-value: 4.91e-03

Time-scale 2, τ_2

ANOVA P-value: 2.24e-01

Non-parametric KS P-value: 3.83e-01

Plateau Shear Stiffness (PSS)

ANOVA P-value: 4.18e-01

Non-parametric KS P-value: 2.05e-01

D.3 Fractional SLS Parameters

D.3.1 DM33, DM41, DM50 and Mixtures

Instantaneous Shear Stiffness (ISS)

ANOVA P-value: 1.74e-09

| DM | 33 | 41 | 50 | 33/50 | 41/60 | 33/70 |
|-------|----------|----------|----------|----------|----------|----------|
| 33 | - | 2.78e-01 | 3.80e-08 | 3.86e-03 | 6.99e-07 | 8.22e-06 |
| 41 | 2.78e-01 | - | 3.24e-06 | 9.22e-02 | 3.05e-05 | 5.44e-04 |
| 50 | 3.80e-08 | 3.24e-06 | - | 3.80e-08 | 2.53e-09 | 1.59e-09 |
| 33/50 | 3.86e-03 | 9.22e-02 | 3.80e-08 | - | 1.77e-03 | 2.49e-01 |
| 41/60 | 6.99e-07 | 3.05e-05 | 2.53e-09 | 1.77e-03 | - | 6.14e-02 |
| 33/70 | 8.22e-06 | 5.44e-04 | 1.59e-09 | 2.49e-01 | 6.14e-02 | - |

Table D.7 Pairwise P-values of the FSLs ISS parameters as fitted to DM33, 41, 50 and gel mixtures. Note that the values are symmetric about the diagonal.

Springpot Parameter α

ANOVA P-value: 9.35e-02

ANOVA P-value (without DM33): 3.46e-01

| DM | 33 | 41 | 50 | 33/50 | 41/60 | 33/70 |
|-------|----------|----------|----------|----------|----------|----------|
| 33 | - | 3.42e-02 | 4.00e-01 | 3.66e-02 | 6.18e-02 | 4.43e-01 |
| 41 | 3.42e-02 | - | 2.36e-01 | 7.90e-01 | 3.22e-01 | 1.62e-01 |
| 50 | 4.00e-01 | 2.36e-01 | - | 2.63e-01 | 3.15e-01 | 9.97e-01 |
| 33/50 | 3.66e-02 | 7.90e-01 | 2.63e-01 | - | 9.07e-01 | 2.16e-01 |
| 41/60 | 6.18e-02 | 3.22e-01 | 3.15e-01 | 9.07e-01 | - | 2.27e-01 |
| 33/70 | 4.43e-01 | 1.62e-01 | 9.97e-01 | 2.16e-01 | 2.27e-01 | - |

Table D.8 Pairwise P-values of the FSLs ISS parameters as fitted to DM33, 41, 50 and gel mixtures. Note that the values are symmetric about the diagonal.

D.3.2 DM40 Block and Random

Instantaneous Shear Stiffness (ISS)

ANOVA P-value: 4.51e-01

Non-parametric KS P-value: 9.21e-01

Springpot Parameter α

ANOVA P-value: 4.24e-01

Non-parametric KS P-value: 3.08e-01

Appendix E

Singularity Error Analysis

As mentioned in the text, the error introduced by avoiding the singularity is small but hard to quantify in a general way as it is dependent on the loading applied. In the following a representative, but analytically tractable example is briefly analysed to demonstrate that the error is small. The loading considered is $\varepsilon(t) = 0.5t^2$ and the modulus used is the relaxation modulus of the springpot with $c_\beta = 1$ and $\beta = 0.2$. The exact response can be found to be $\sigma(t) = t^{1.8}/\Gamma(2.8)$. Figure E.1 shows the exact response when compared to two approximations of the singular 0 point, $\Delta t/10$ and $\Delta t/100$, where in the simulation $\Delta t = 1 \times 10^{-2}$. As can be seen from Figure E.1, there is error at the beginning that rapidly decays. Although the error at the beginning is large in relative terms it is very small in absolute terms.

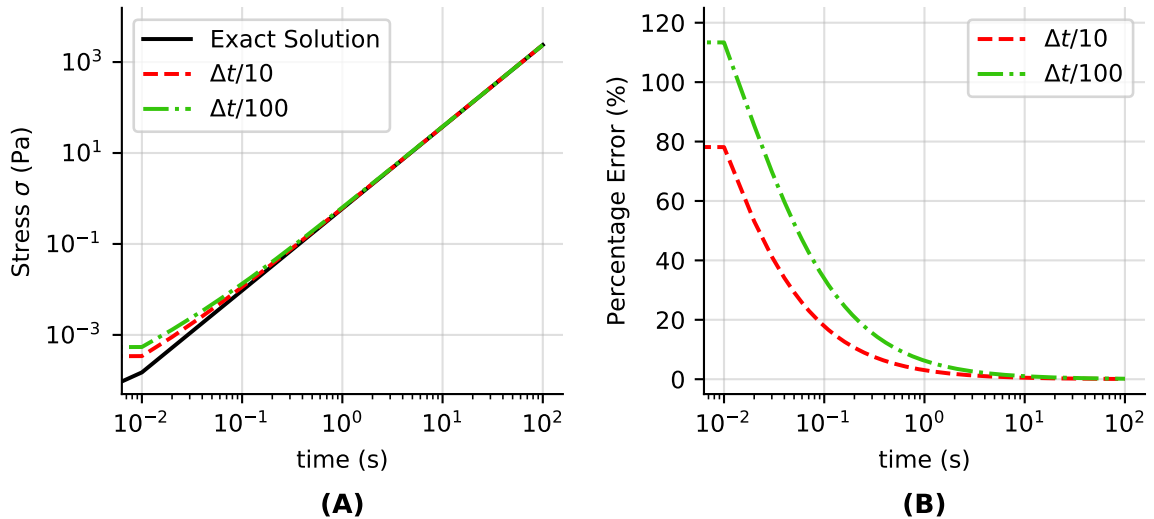


Fig. E.1 A) Exact solution of springpot response with loading $\varepsilon(t) = 0.5t^2$, compared with two different singularity approximations. B) Relative error of the two singularity approximations.

Appendix F

Scientific Output Related to Thesis

- **J L Kaplan**, A Bonfanti, A Kabla. 2019. *RHEOS.jl – A Julia Package for Rheology Data Analysis*. Journal of Open Source Software [300]
- **J L Kaplan**, T Torode, F Bou Daher, S A Braybrook. 2019. *On Pectin Methylesterification: Implications for in vitro and in vivo viscoelasticity*. Under review at Royal Society: Interface. Preprint available on bioRxiv [328]
- **J L Kaplan**, A Bonfanti, A Kabla. 2018. *RHEOS: Making mechanical testing more accessible with Julia*. Presentation at JuliaCon 2018.
Viewable at <https://youtu.be/aMxBchgf0tE>
- A Bonfanti, **J L Kaplan**, G Charras, A Kabla. 2020. *Fractional viscoelastic models for power-law materials*. Accepted with minor corrections at Soft Matter. Preprint available on arXiv [301]
- T Torode, M Linardic, **J L Kaplan**, S A Braybrook. 2018. *Atomic force microscopy based analysis of cell-wall elasticity in macroalgae*. Protocols for Macroalgae Research, Eds. B Charrier, T Wichards, C R K Reddy. CRC Taylor & Francis [329].
- A Gavrin, T Rey, T Torode, J Toulotte, A Chatterjee, **J L Kaplan**, H Takagi, V Charoensawan, R David, E-P Journet, F Debellé, F de Carvalho-Niebel, R Terauchi, S A Braybrook. 2020. *Developmental modulation of root cell wall architecture confers resistance to an oomycete pathogen*. Resubmitted to Nature Plants.

